ulm university universität
uulm

Fakultät für
Naturwissenschaften
Institut für Elektrochemie

Modeling of lithium plating in lithium-ion-batteries

Dissertation zur Erlangung des Doktorgrades Dr. rer. nat. der Fakultät für Naturwissenschaften der Universität Ulm

Vorgelegt von:
Simon Hein aus Schweinfurt, 2017

Dekan:
Prof. Dr. Peter Dürre

Gutachter:
Prof. Dr. Arnulf Latz
Prof. Dr. Axel Groß

Betreuer:
Prof. Dr. Arnulf Latz

08.05.2018

Contents

Kurzfassung v

List of Abbreviations vii

1. Introduction and Motivation 1

2. Theory 3

2.1. Lithium-ion batteries . . . 3
2.2. 3D thermodynamically consistent transport model . . . 7
2.3. Graphite . . . 12
2.4. Potential . . . 14
2.5. Lithium plating . . . 17

3. Implementation and numerics 31

3.1. Modeling of lithium plating and stripping . . . 31
3.2. Discretization and numerical solution . . . 34
3.3. Approaches to numerical challenges . . . 36

4. Simulation setup and parameters 43

4.1. Microstructures . . . 43
4.2. Simulations . . . 48
4.3. Parameters . . . 61

5. Results and discussion 65

5.1. Electrochemical validation of 3D stochastic microstructure model . . . 65
5.2. Time evolution of plating condition . . . 72
5.3. Volume resolved system: Impact of plated lithium on battery . . . 75
5.4. Surface growth: Comparison coupled and decoupled system . . . 81
5.5. Lithium plating through overcharge . . . 87
5.6. Impact of local inhomogeneities on lithium plating . . . 91
5.7. Plating and stripping during operation . . . 98

6. Summary and outlook 103

A. Numerical 107

A.1. Discretization . . . 107

A.2. Numerical solution of nonlinear equation system 110

B. Notes **113**

B.1. Color convention 113

C. Publications and conferences **115**

Bibliography **117**

Curriculum Vitae **136**

Kurzfassung

Lithium-Ionen Akkumulatoren finden in vielen Gebieten Anwendung: Sei es als Netzspeicher, in Unterhaltungs- und Haushaltselektronik oder in der Elektromobilität. Alle Anwendungen haben den Bedarf an hoher Energie- und Leistungsdichte und einer langen Lebensdauer gemein. Die Lebensdauer der energiegeladen Lithium-Ionen Akkumulatoren wird durch verschiedene Degradationsprozesse verkürzt. Einer der prominentesten Effekte ist die Abscheidung von metallischem Lithium auf der Anodenoberfläche. Dieser Prozess tritt vorrangig bei niedrigen Temperaturen und bei hohen Ladeströmen auf. Die metallische Lithiumabscheidung kann zum verstärkten Wachstum der sogenannten SEI-Schicht (engl.: Solid-Electrolyte-Interphase) führen, welche einen irreversiblen Lithiumverlust darstellt. Zudem besteht eine erhöhte Gefahr des elektrischen Kurzschlusses, falls die Lithiumschicht durch den Separator bis zur Kathode vordringt. Im Rahmen dieser Dissertation wird die Lithiumabscheidung mittels elektrochemischer Modellbildung und strukturaufgelösten Simulationen untersucht.

Ein neues elektrochemisches Modell zur Beschreibung der Abscheidung von metallischen Lithium und der Auflösung wurde entwickelt und ist in das Simulationsframework BEST implementiert. Im Gegensatz zu den bestehenden Modellen zur Lithiumabscheidung erlaubt das neue Modell eine Konkurrenz zwischen der Lithiuminterkalation und Lithiumabscheidung. Eine vollständige Bedeckung der Elektrodenoberfläche resultiert in der Blockade der Lithiumeinlagerung im Elektrodenmaterial. Die Kombination des Abscheidungmodells mit einer bestehenden 3D Transporttheorie ermöglicht erstmalig elektrochemische Simulationen eines Lithium-Ionen Akkumulators, in welchem metallisches Lithium entsteht. Bisherige Modelle beinhalten die Mikrostruktur der Elektroden nur als über das Volumen gemittelte Kenngrößen, wie etwa Porosität und Tortuosität.

Während der Entladung eines Lithium-Ionen Akkumulators, welcher metallisches Lithium auf der Anodenoberfläche aufweist, zeigt sich ein charakteristisches Plateau im Zellpotential. Dieses Plateau existiert nur falls metallisches Lithium in der Elektrode vorliegt und sich durch den angelegten Strom in den Elektrolyten auflöst. Elektrochemische Simulationen zeigen, dass die Länge des Plateaus vom angelegten Strom und die Ausgeprägtheit vom Verhältnis zwischen freier und mit Lithium bedeckter Oberfläche abhängen. Zudem ist eine Veränderung des Zellpotentials erkennbar, sobald Lithiummetall abgeschieden wird. Die vollständige Bedeckung der Elektrode führt zu einer porösen Lithiumelektrode und einem konstanten Zellpotential bei einer Halbzellkonfiguration. Die räumlichen Variationen verschiedener elektrochemischer Größen, wie etwa die Reaktionsgeschwindigkeit der Lithiumabscheidung, zeigen einen deutlichen Einfluss auf die räumliche Verteilung und die Homogenität des abgeschiedenen Lithiums. Eine inhomogene Lithiumabscheidung geht mit einer Abschwächung der Veränderungen im Zellpotential einher. Die lokal konzentrierte Lithiumabscheidung kann zu einem lokal beschleunigtem

SEI-Wachstum und somit zu Lithiumverlust führen. Die elektrochemischen Simulationen mit räumlicher Auflösung der Elektrodenstruktur zusammen mit dem Abscheidungsmodell ermöglichen einen Einblick in die elektrochemische Umgebung im Lithium-Ionen Akkumulator und liefern gleichzeitig die Möglichkeit extern messbare Größen mit der Lithiumabscheidung zu korrelieren.

List of Abbreviations

BC	boundary condition, page 9
BEST	Battery and Electrochemical Simulation Tool, page 1
CoRheos	Complex Rheolgy Solver, page 7
CVD	chemical vapor deposition, page 106
DMC	dimethyl carbonate, page 22
dVdQ	differential voltammetry, page 19
EC	ethylene carbonate, page 6
EIS	Electrochemical impedance spectroscopy, page 105
El	Electrolyte or electrolyte phase, page 9
GeoDict	Software for generation of virtual structures and calculation of structural parameters such as diffusion coefficient, page 43
ITWM	Fraunhofer-Institut für Techno- und Wirtschaftsmathematik, page 7
LFP	Lithium Iron Phosphate, page 53
LIB	Lithium-ion battery, page 6
LMO	lithium manganese oxide, page 9
MCMB	meso carbon microbeads, page 12
MULTIBAT	Multiskalenmodelle und Modellreduktionsverfahren zur Vorhersage der Lebensdauer von Lithium-Ionen-Batterien, page 45
NCA	Lithium Nickel Cobalt Aluminium Oxide, page 53
NMC	nickel cobalt oxide, page 43
OCV	Open-circuit voltage, page 12
PC	proylene carbonate, page 6
RT	room temperature, page 19
SEI	solid-electrolyte-interphase, page 2
So	Solid phase of an electrode, page 9
SoC	State of charge, page 14
SVF	Solid Volume Fraction - volume of a phase divided by total amount, page 46

1. Introduction and Motivation

On the road to a society, which relies on less non-regenerative energy sources, lithium-ion batteries can play a vital role. Be it as net storage systems [1, 2], energy storage in consumer electronics or as key component in electro mobility [3]. A high power and energy density is of utter importance. Thus a scale up of battery size, storage capability and lifetime is required. Lithium-ion batteries suffer from different degradation processes. They can decrease the stored amount of charge over usage or can result even in complete loss of functionality. The safe operation of lithium-ion batteries under a broad range of condition has therefor to be ensured: Charging at low temperatures - in the context of lithium-ion batteries, this usually means temperatures around freezing - and high currents would permit a broader and more convenient application inside the frame of electro mobility. The process of *lithium plating* is one of the dominant degradation processes and safety risks inside state-of-the-art lithium-ion batteries. This degradation process leads to the deposition of metallic lithium on the surface of the negative intercalation electrode. The occurrence of metallic lithium furthers the growth of the solid electrolyte interphase, which is another degradation process. Both boost the irreversible loss of cyclable lithium. Lithium plating can even result in a penetration of lithium through the separator potentially leading to a short circuit of the battery.

The focus of this work lays on a better understanding of the process of lithium plating via electrochemical simulations. All existing electrochemical models[4, 5], which describe plating of lithium, lack the possibility to completely block the intercalation reaction in the presence of a fully plated interface. Additionally, they are only applied to volume average transport models, thus not resolving inhomogeneities on the microstructure level. A new electrochemical model was developed, which treats the plated lithium as surface species between the electrolyte and the solid phase. It is included into an existing simulation framework, which uses 3D spatially resolved microstructures as electrodes. The plating model allows a switch of the major charge transfer reaction between the intercalation and the plating reaction. The simulation framework BEST (Battery and Electrochemical Simulation Tool) [6], which is a finite-volume implementation of a thermodynamically consistent transport model [7], is used for the electrochemical simulations.

The geometry for 3D spatially resolved electrochemical simulations is usually based on experimental tomography data [8, 9]. The availability of this type of image data is limited due to the imaging costs. A new stochastic model, which can generate random microstructures with structural parameters based on real tomography data, was introduced by Feinauer *et al.* [10]. The microstructures of the stochastic microstructure model are compared with the real tomography data with respect to their electrochemical performance using the electrochemical simulation tool.

The process of lithium plating is examined using different microstructures at different operation conditions. The time evolution of plating risk in a negative electrode is examined for different applied currents and ambient temperatures. Thus allowing to identify critical regions of the microstructure. The influence of existing plated lithium on the discharge behavior of a graphite electrode is explored. The occurring stripping plateau in the cell voltage is often used to quantify the amount of plated lithium [11]. It will be shown, that the relation between the plateau duration and the amount of plated lithium is influenced by the fraction of active surface covered by plated lithium [12]. The currents flowing through the interface between electrolyte and active material can exhibit unexpected behavior during the stripping process. The developed plating and stripping model is applied to a constant current charge and discharge simulation. Global and local variation of reaction rates yields information regarding inhomogeneous degradation and the influence of the solid-electrolyte-interphase (SEI) on lithium plating.

This short introduction is followed by chapter 2, which contains a short overview of lithium-ion batteries and the transport theory used for the electrochemical simulations. The relevant process for the description of degradation in lithium-ion batteries is introduced. Finally, the developed model for lithium plating presented. A short summary of the steps needed to include the developed plating model into the simulation framework BEST, is given chapter 3. The numerical challenges are also described. Chapter 4 describes the used microstructures and the setup of the completed electrochemical simulations. They are used for the electrochemical validation of a stochastic microstructure model and the investigations of lithium plating. The results are shown in chapter 5. A short outlook regarding possible extensions of the developed model and its applications is given in chapter 6. Additional information is compiled in the appendix (appendix A and appendix B).

2. Theory

This chapter gives the theoretical background and is structured as follows. In the first section (section 2.1) the working principle of a lithium-ion battery is described. The 3D transport model used as framework for this work is shortly reviewed (section 2.2). The important anode material graphite is introduced in section 2.3, followed by a short definition of the relevant potentials in section 2.4. Details about lithium plating and the plating model developed during this thesis are given in section 2.5.

2.1. Lithium-ion batteries

2.1.1. A short history

Luigi Galavani observed in the 1780s that putting two metals in contact with frog legs resulted in a muscle contraction. The Italian professor Alessandro Volta was inspired by this effect and build the first battery. He constructed it in 1799/1800 out of a pile of zinc and copper plates separated by cardboard soaked in salt water. This pile consists of six cells and generates an electromotive force of around 4.65 V. Each of those cells made out of zinc and copper plates separated by cardboard soaked in salt water (brine). This construct represented the first continuous source of electricity and sparked the development of various other batteries. The first rechargeable battery was invented by Gaston Planté several decades later (1859): The lead acid battery. The basic concept can still be found in current car batteries. The construction of the first dry-battery (zinc-carbon) in 1887 and the first alkaline battery (nickel-cadmium) in 1899 opened the field of applications [13, Chapter 2].

Even though first experiments with lithium as battery material were done in the 1910s, it took till the 1970s for the first commercially available lithium battery. These first lithium batteries were single-use batteries. In the year 1983 already several companies offered a variety of primary lithium batteries. Most of the initial systems used lithium metal as anode electrode [14]. But lithium metal posed too many safety risks such as electrical short-circuit [15]. Around 1989 several battery manufacturers had to recall their lithium metal batteries due to battery failures involving the burning of the cells [16]. This prompted the focus of research to alternative materials. The discovery of a new type of cathode material (lithium cobalt oxide - $LiCoO_2$) by John B. Goodenough [17] and graphite as anode material by Rachid Yazami in 1980 [18], lead to the first rechargeable battery using lithium ions as charge carriers in 1985. This type of materials can incorporate lithium reversibly into its lattice. The *lithium-ion battery* was born. With the switch towards graphite some problems, such as formation of dendrites, could be eased. Sony released the first commercial secondary lithium-ion battery in 1991 [19, 20].

2.1.2. Lithium batteries and other batteries

All batteries can be grouped into two categories: *primary* and *secondary* batteries. Primary batteries can only be used for one discharge, since the containing materials undergo irreversibly reactions during the current consumption. Secondary batteries on the other hand can be recharged and hence used again [21, Section 1.3.1]. All batteries, regardless of type, are electrochemical cells comprised of two electrodes, negative and positive, and an electrolyte. An electrochemical cell can convert electrical energy into chemical energy and vice-versa. The electrodes are filled by an electrolyte, which is ionic conductive but isolating for electrons. The lithium based batteries have the advantage of a higher energy densities

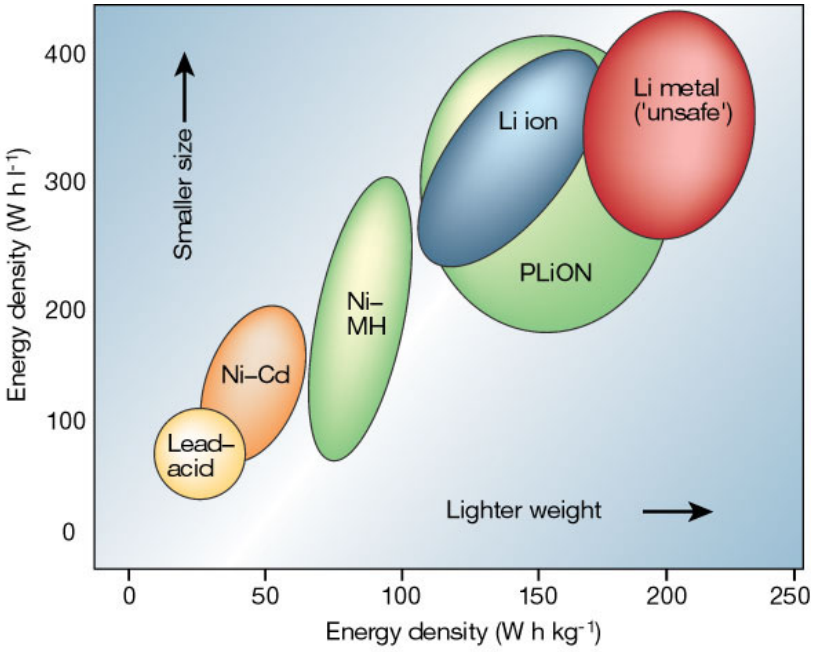

Figure 2.1.: Different battery technologies are compared in terms of volumetric and gravimetric energy density. The higher energy density of lithium-based batteries compared to other common batteries, such as nickel-cadmium, is evident. (reprinted with permission from [22])

as compared to other existing battery systems. In fig. 2.1 the volumetric and gravimetric energy density of different battery technologies are shown. The lithium-ion systems exhibit an energy density, which is around three times higher than common nickel-cadmium-batteries.

The negative and positive electrodes of an electrochemical cell are identified through the terms *anode* and *cathode* respectively. An anode is the electrode, where the oxidation reaction is taking place. The electrode with the reduction reaction is named cathode. The role of an electrode changes depending on the applied external current. In the battery community however the term *anode* and *cathode* identify the negative and positive electrode, regardless of the applied current. The electrode of the reduction reaction during discharge of a battery is called anode. Its counter-electrode is duped cathode. In this work, the terms *negative electrode* and *anode* and the terms *positive electrode* and *cathode* are therefore used interchangeable.

The potential difference measured between the two electrodes of an electrochemical cell is called *cell voltage*. Its value depends on the differences of the electrochemical potentials of reacting species. The electrochemical reaction inside a battery can be written in a general way:

$$\nu_1 \cdot A_1 + \nu_2 \cdot A_2 + \cdots \rightleftharpoons \cdots + \nu_{k-1} \cdot A_{k-1} + \nu_k \cdot A_k \tag{2.1}$$

The cell potential of a battery without any applied current facilitating this reaction can be obtained using the Nernst-equation:

$$E_{\text{cell}} = E^{\theta}_{\text{cell}} + \frac{RT}{zF} \cdot \ln\left(\prod_{i=1}^{k} a_i^{\nu_i}\right) \tag{2.2}$$

where a_i is the activity of the species i, ν_i its stochiometric coefficient and E^{θ}_{cell} the standard cell potential. The amount of charge a battery can contain is given through its *capacity* Q_{bat}. It has the unit Ah. The *theoretical capacity* is the amount of charge a material could reversibly store if all involved processes would be ideal. The *specific capacity* relates the capacity to the mass of the battery system or components:

$$Q^{\text{specific}}_{\text{bat}} = \frac{Q_{\text{bat}}}{m_{\text{comp}}} \tag{2.3}$$

This parameter is used to compare different materials and batteries and has the unit Ah/g. As point of reference one usually selects the amount of pure active material or the amount of all materials needed to achieve a working battery. Other relative parameters are the gravimetric (Wh/kg) or volumetric (Wh/l) energy density (see fig. 2.1). The gravimetric energy density is given with respect to the total weight of the battery system or active components. The energy density with respect to the mass of active material is mostly used in research, since it allows for a direct comparison of different energy materials. This definition ignores auxiliary components, such as current collector. Hence, the energy density with respect to the weight of the complete battery system is preferred for design and construction of weight critical applications such as space and aviation. Applications with restriction due to low battery space pay attention to the volumetric energy density, which is given by the energy density with respect to the volume of the battery system or active components. Larger volumetric energy density, indicates a smaller battery with the same energy density. High energy density batteries are usually achieved through electrodes, which are thicker than their high power complement. These batteries allow for the storage of a large amount of energy. Due to the thickness of the electrodes and the hampered lithium transport in the electrolyte, these batteries are usually only charged and discharged at low currents. High power batteries on the other side can provide a large discharge current and thus a large power. This type of battery has thin electrodes to prevent current limitations due to ohmic losses or ionic resistance in the electrolyte phase.

2.1.3. The working principle and general layout

Lithium-ion batteries (LIB) are of the secondary type. A generalized layout of a LIB is shown in fig. 2.2. The electrode materials used in LIB are intercalation materials [17, 18]. The anode and

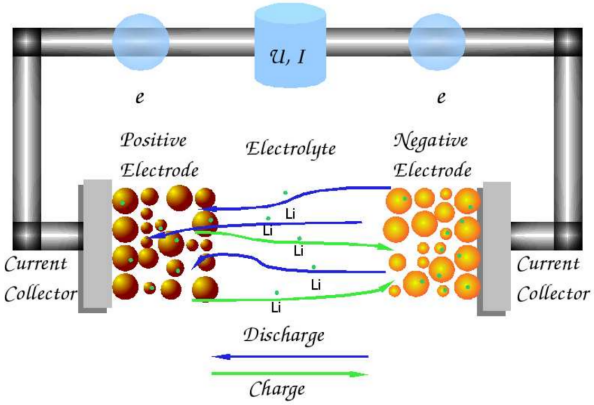

Figure 2.2.: Sketch of a lithium-ion battery (reprinted with permission from [23]). The lithium ions move from the positive electrode into the negative electrode during charge, while electrons get moved through an external circuit.

cathode are porous structures consisting of a mix of active material and auxiliary materials. The active materials store the lithium ions. The auxiliary materials are the current collectors, separator between the electrodes and the battery housing. The porous electrodes are produced from a slurry, which consists of the active material, conductive agents and binder. The conductive agent is added to counteract the often poor electronic conductivity and increase interparticle contact of the active material [24, 25]. Usually a graphite based conductive agent is used. The mechanical stability of the electrode is enhanced by introducing binder into the slurry. The drawback of the binder is, that it can negatively impact the electrochemical performance of the electrodes due to pore blockage. The final electrodes are produced by coating the slurry directly on the current collectors. A elecrical isolating seperator ensures that the positive and negative electrodes are not touching. This separator is a porous structure, which allows for electrolyte penetration and electronic isolation. After assembling the battery sandwich, electrolyte is soaked into the porous structures. The electrolyte consists of a conductive salt, e.g. $LiPF_6$, a solvent mixture and some other additives. The solvent mixture is composed in most cases of different organic compounds. Common electrolyte solvents are carbonates, such as proylene carbonate (PC), ethylene carbonate (EC) and others [26]. The additives are mixed into the electrolyte to increase the ionic conductivity or influence the formation of the solid-electrolyte-interphase [27]. The SEI strongly effects the life-time of LIBs. More information regarding the different types of lithium-ion batteries and the involved materials can be found in [15, 17, 18, 28, 29, 30].

The current flow from one electrode towards the other electrode through the electrolyte is carried by lithium ions. The lithium in a LIB is stored inside the solid phase of the electrodes. The process of bringing lithium ions from the outside of these electrode materials into their lattice is called *intercalation*. During discharge the lithium ions move from the cathode through the electrolyte into the anode. Simultaneously, electrons get transported from the cathode through an external circuit to the

anode. At the cathode the lithium ions are deintercalated and solvated into the electrolyte. The ions then migrate through the porous structures of the electrode and separator to the anode. At this side, the lithium ions shed their solvation-shell and intercalate into the host material. During charge the same steps take place, but in the opposite direction.

The exact steps involved in the desolvation and intercalation of the lithium ions are still subject of research. Several studies suggest, that the intercalation process is split into two separate steps. First, the lithium ions get adsorbed at the electrode surface under partial desolvation. And afterwards a fast diffusion from the surface into the bulk material takes place [31, 32]. Nevertheless, in the electrochemical community a one-step reaction is also used to describe the intercalation. This reaction is modeled by a Butler-Volmer approach [33, 34]. The one-step approach is used in this work. The modification of the transport theory, used in this work, to include a theoretically motivated intercalation process is ongoing research [35].

2.2. 3D thermodynamically consistent transport model

In this thesis the thermodynamically consistent transport theory developed by Latz *et al.* [36, 7] is used as basis. This transport theory was derived using non-equilibrium thermodynamics and fundamental physical relations (mass conservation, Maxwell equitation, ...). The resulting model was transfered to LIB. The microstructure of the electrodes can be resolved in this continuum model. It was implemented in C++ with a finite-volume discretization in the framework CoRheos [37] by the Fraunhofer-Institut für Techno- und Wirtschaftsmathematik (ITWM). The implementation was performed with the assumptions of strict charge-neutrality and pressure independence [7]. The assumption of charge-neutrality is valid as long as the electrochemical double layer at the electrode surfaces is not spatially resolved. The resulting simulation tool is called BEST [6]. More information about the discretization and implementation can be found in chapter 3. In this work we assume an isothermal situation through-out the battery.

The independent quantities of the transport model for the electrolyte phase are chosen to be the lithium ion concentration c_{El} and the electrochemical potential of lithium ions φ_{El} and for solid phases the lithium concentration c_{So} and the electrochemical potential of the electrons ϕ_{So}.The simulation domain for the potentials and concentrations are slightly different. While the potentials are solved in all involved phases (negative current collector, negative electrode, electrolyte, positive electrode and positive current collector), lithium only exists in the electrochemical active components (electrodes and electrolyte). The domain of the different quantities are illustrated in the simplified representation of the spatial simulation domain (see fig. 2.3). The negative-positive electrode direction represents the full cell thickness. This direction is also called *through direction*. In this direction all structural details are resolved. Solving the conservation equations in the respective phases yields the time evolution of

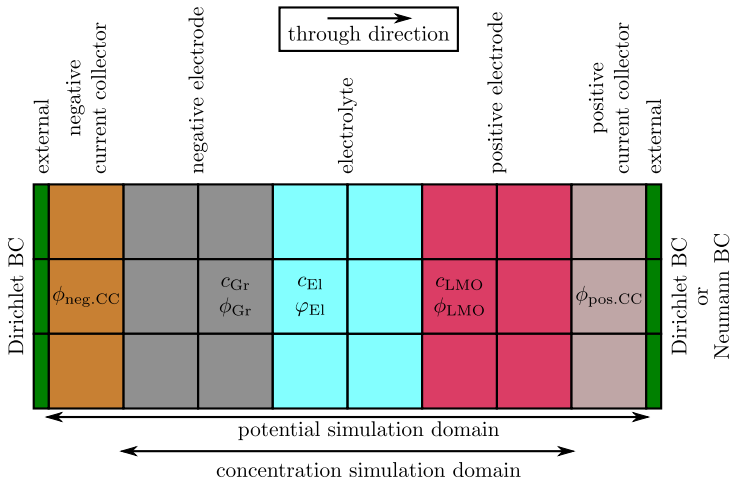

Figure 2.3.: Simplified representation of the spatial simulation domain of the two types of unknowns. Five involved phases are spatially resolved: the two current collectors, the two electrodes and the electrolyte phase.

independent quantities. The governing equations are listed in eqs. (2.4) to (2.7).

$$\frac{\partial\, c_{\mathrm{el}}}{\partial\, t} = -\boldsymbol{\nabla}\cdot\boldsymbol{N}_{\mathrm{el}} \tag{2.4}$$

$$\frac{\partial\, c_{\mathrm{so}}}{\partial\, t} = -\boldsymbol{\nabla}\cdot\boldsymbol{N}_{\mathrm{so}} \tag{2.5}$$

$$\frac{\partial\, \rho_{\mathrm{el}}}{\partial\, t} = 0 = -\boldsymbol{\nabla}\cdot\boldsymbol{j}_{\mathrm{el}} \tag{2.6}$$

$$\frac{\partial\, \rho_{\mathrm{so}}}{\partial\, t} = 0 = -\boldsymbol{\nabla}\cdot\boldsymbol{j}_{\mathrm{so}} \tag{2.7}$$

with $z_+ = 1$ and $\boldsymbol{N}_{\mathrm{i}}$ as the lithium flux in phase i:

$$\begin{aligned}\boldsymbol{N}_{\mathrm{El}} &= -D_{\mathrm{El}}\boldsymbol{\nabla}c_{\mathrm{El}} + \frac{t_+}{F}\boldsymbol{j}_{\mathrm{El}}\\ \boldsymbol{N}_{\mathrm{So}} &= -D_{\mathrm{So}}\boldsymbol{\nabla}c_{\mathrm{So}}\end{aligned} \tag{2.8}$$

and $\boldsymbol{j}_{\mathrm{i}}$ as the current density in phase i:

$$\begin{aligned}\boldsymbol{j}_{\mathrm{El}} &= -\kappa_{\mathrm{El}}\boldsymbol{\nabla}\varphi_{\mathrm{El}} - \kappa_{\mathrm{El}}\frac{1-t_+}{F}\left(\frac{\partial\mu_{\mathrm{El}}}{\partial c_{\mathrm{El}}}\right)\boldsymbol{\nabla}c_{\mathrm{El}}\\ \boldsymbol{j}_{\mathrm{So}} &= -\sigma_{\mathrm{So}}\boldsymbol{\nabla}\phi_{\mathrm{So}}\end{aligned} \tag{2.9}$$

The derivative of the chemical potential with respect to the concentration $\left(\frac{\partial\,\mu_{\mathrm{El}}}{\partial\,c_{\mathrm{El}}}\right)$ is calculated:

$$\frac{\partial\,\mu_{\mathrm{El}}}{\partial\,c_{\mathrm{El}}} = \frac{1}{c_{\mathrm{El}}} + \frac{\partial\,\ln f_{\mathrm{El}}^{\mathrm{Li}^+}}{\partial\,c_{\mathrm{El}}} \tag{2.10}$$

$$= \frac{1}{c_{\mathrm{El}}}\cdot\left(1 + c_{\mathrm{El}}\cdot\frac{\partial\,\ln f_{\mathrm{El}}^{\mathrm{Li}^+}}{\partial\,c_{\mathrm{El}}}\right) \tag{2.11}$$

$$= \frac{1}{c_{\mathrm{El}}}\cdot\left(1 + \frac{\partial\,\ln f_{\mathrm{El}}^{\mathrm{Li}^+}}{\partial\,\ln c_{\mathrm{El}}}\right) \tag{2.12}$$

The definition of the chemical potential is given in section 2.4.1 and eq. (2.30). The different phases in a LIB are in contact at the corresponding interfaces. This is reproduced through different interface conditions for the partial differential equations. The particle and current fluxes at the electrolyte-electrode-interfaces are defined by the exchange currents of the occurring reactions j_{SoEl}. This is represented by the following equations:

$$\begin{aligned} \boldsymbol{j}_{\mathrm{El}} \cdot \boldsymbol{n}_{\mathrm{So-El}} &= j_{\mathrm{SoEl}} & \qquad \boldsymbol{j}_{\mathrm{So}} \cdot \boldsymbol{n}_{\mathrm{So-El}} &= j_{\mathrm{SoEl}} \\ \boldsymbol{N}_{\mathrm{El}} \cdot \boldsymbol{n}_{\mathrm{So-El}} &= N_{\mathrm{SoEl}} & \qquad \boldsymbol{N}_{\mathrm{So}} \cdot \boldsymbol{n}_{\mathrm{So-El}} &= N_{\mathrm{SoEl}} \end{aligned} \tag{2.13}$$

These equations are also called interface conditions, since they specify what is happening at the interfaces between the solid and electrolyte. The normal of the interface area $\boldsymbol{n}_{\mathrm{So-El}}$ is pointing from the solid (So) into the electrolyte (El). The interface current between solid and electrolyte is described by j_{SoEl}. Different reactions and types of interfaces can be framed by using different expression for j_{SoEl}. In this work, a symmetric Butler-Volmer expression (see eq. (2.20)) is used for the interface current between the intercalation material (graphite or lithium manganese oxide (LMO)) and the electrolyte. The reactions will be introduced in more detail in section 2.2.2. For more detailed information and explanations about the underlying theory the reader is referred to [7, 36]. The electrochemical model has been validated in [38]. The properties of the different materials (electrolyte, electrode, ...) are represented by their respective parameters (e.g.: lithium diffusion coefficient inside the anode D_{Anode}).

At the boundaries of the two simulation domains (see fig. 2.3) additional conditions, so called boundary conditions, are applied. The two different boundary conditions are shortly introduced in the following section.

2.2.1. Boundary conditions: operation mode

The two most important operation modes of any battery are the *galavanostatic* and *potentiostatic* operation. Galvanostic operation is the application of defined current $I_{\mathrm{applied}}(t)$ to the battery which results in a certain cell voltage U_{cell}. During potentiostatic operation the battery is hold at a certain voltage $U_{\mathrm{applied}}(t)$ while the resulting current I_{cell} can be negative, zero or positive depending on the location of the applied voltage relative to the equilibrium cell potential. In this work, a negative applied current I_{applied} or cell current I_{cell} indicates a discharging of a full cell and hence a delithiation of the negative electrode and a lithiation of positive electrode. Conversely, a positive applied/cell current signals a charging of a full cell. The operation mode is applied to the simulation domains (see fig. 2.3) through different boundary conditions (BC). The boundary conditions for the potentials are applied at the interface between the current collectors and the external.

Neumann boundary condition

The Neumann boundary condition defines the derivative of the unknown of an ordinary or partial differential equation. In the case of a galvanostatic operation mode the value of the electrical current density $j_{\mathrm{pos.\ CC}} = -\sigma_{\mathrm{pos.\ CC}} \cdot \boldsymbol{\nabla}\phi_{\mathrm{pos.\ CC}}$ at the interface betwen potential simulation domain and

external domain is given by:

$$\nabla \phi_{\text{pos. CC}} \Big|_{\text{pos. CC-external}} = -\frac{j_{\text{applied}}}{\sigma_{\text{pos. CC}}} \tag{2.14}$$

The applied current j_{applied} is given with respect to the area of the current collector $j_{\text{applied}} = I_{\text{applied}}/A_{\text{CC}}$. An isolation Neumann boundary condition is applied at the boundary of the concentration simulation domain. The boundaries are the interface between electrodes and current collectors and electrolyte and current collectors.

$$N_{\text{El}} \Big|_{\text{El-CC}} = 0 \tag{2.15}$$

$$N_{\text{So}} \Big|_{\text{So-CC}} = 0 \tag{2.16}$$

This represents no interaction between the electrolyte and the metal of the current collectors. The metal of the current collectors can react with various electrolytes in a real battery. Depending on the material corrosion, cracking or growth of a metal-electrolyte-interphase can occur [39, 40]. Methods to prevent degradation are the pretreatment of the current collector surface or a protective layer [41, 42]. The interface area between the electrolyte and the current collectors is small compared to the interface between the active material and the electrolyte. Hence, the loss of lithium is small and the degradation of the current collector is neglected in this work.

Dirichlet boundary condition

The Dirichlet boundary condition defines the value of a unknown of an ordinary or partial differential equation. The boundary of the potential simulation domain at the negative electrode is set to a constant potential:

$$\phi_{\text{neg. CC}} \Big|_{\text{neg. CC-external}} = \phi_{\text{initial}}^{\text{Anode}} \tag{2.17}$$

For a potentiostatic operation mode a Dirichlet BC is used. The boundary condition at the positive current collector and the external is the applied voltage with respect to the negative current collector:

$$\phi_{\text{pos. CC}} \Big|_{\text{pos. CC-external}} = \phi_{\text{neg. CC}} \Big|_{\text{neg. CC-external}} + U_{\text{applied}} \tag{2.18}$$

In lateral direction (perpendicular to the through direction - see fig. 2.3) either an isolation Neumann BC or a periodic BC is applied. The selection usually depends on the spatial structure used for the simulation. The periodic boundary condition creates an interface between the top and the bottom (above and below in fig. 2.3) and between the front and the back of the spatial simulation domains.

2.2.2. Reactions

As mentioned earlier, different reactions can take place at the interface between different phases. In the following the processes in an ideal LIB are described. In this degradation-free case only one reaction

exists: the intercalation/lithiation-reaction of the lithium. A sketch of the phases involved in the intercalation can be found in fig. 2.4. A Graphite/LMO-battery is selected as model system. Lithium

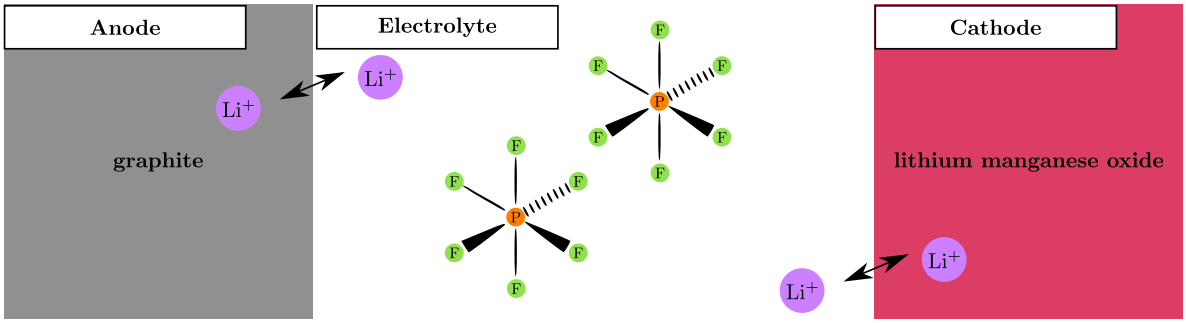

Figure 2.4.: Sketch of the involved phases in a full cell lithium-ion battery. The ideal reaction pathways of lithium ions inside the electrolyte are indicated with the two black arrows.

ions exist in the two active materials and the electrolyte. The positive charge of the lithium ions is shielded by different charge carriers in the different phases. Inside the electrolyte, the positive charge of the lithium ions are shielded through polarized solvents. NMR-, Raman-spectroscopy and molecular dynamics simulations can help to understand the interactions between the salt $LiPF_6$ and different solvents [43, 44, 45, 46, 47]. The lithium ion intercalated into the graphite gets shielded by the free electrons [48]. The lithium ions adsorbed on the metal surface or the active material surface can be shielded by electrons in the solid and solvents in the electrolyte. The ratio of shielding due to electrons and solvent and the dependence on material parameters is still ongoing research [35].

Lithium ions move from the electrolyte into the intercalation material during the intercalation. As mentioned earlier, the exact reaction steps are still subject to research [32, 31, 33, 34]. Here the intercalation reaction is assumed as a one-step process. The intercalation at the anode and cathode is therefore written as follows.

$$\mathrm{Li}^+_{\mathrm{El}} \rightleftharpoons \mathrm{Li}^+_{\mathrm{G}} \qquad \text{(Inter-G)}$$

$$\mathrm{Li}^+_{\mathrm{El}} \rightleftharpoons \mathrm{Li}^+_{\mathrm{LMO}} \qquad \text{(Inter-LMO)}$$

The Gibbs free energy ΔG of the intercalation reaction (e.g. eq. (Inter-G)) is given by the difference of the electrochemical potentials of the involved species:

$$\Delta G_{\mathrm{Inter-G}} = \tilde{\mu}^{\mathrm{Li}^+}_{\mathrm{G}} - \tilde{\mu}^{\mathrm{Li}^+}_{\mathrm{El}} \tag{2.19}$$

The difference of the electrochemical potentials vanishes if the two phases are in thermodynamical equilibrium. The system tries to reach equilibrium through a mass flow between the involved phases. For charged species, as the case with lithium ions, this flow also represents a charge transfer. The flow direction depends on the sign of the energy difference. If the electrochemical potential in the electrolyte $\tilde{\mu}^{\mathrm{Li}^+}_{\mathrm{El}}$ is larger than the one in graphite $\tilde{\mu}^{\mathrm{Li}^+}_{\mathrm{G}}$, lithium ions move from the electrolyte into the graphite. The value of the resulting reaction flux is calculated with a Butler-Volmer-like expression. The relation between flux density and energy difference is modeled according to the theoretical derivation in [34].

The expression of the symmetrical case ($\alpha^{\mathrm{a}}_{\mathrm{Inter-G}} = 0.5$) is given by:

$$N_{\mathrm{Inter-G}} = 2 \cdot N^{00}_{\mathrm{Inter-G}} \sqrt{c_{\mathrm{El}} \cdot c_{\mathrm{G}}} \cdot \sinh\left(\frac{\Delta G_{\mathrm{Inter-G}}}{2\ R\ T}\right) \tag{2.20}$$

where the reaction constant $N^{00}_{\mathrm{Inter-G}}$ contains the reference states $c^{\mathrm{ref}}_{\mathrm{El}}$ and $c^{\mathrm{ref}}_{\mathrm{G}}$:

$$N^{00}_{\mathrm{Inter-G}} = \frac{N^{*}_{\mathrm{Inter-G}}}{\sqrt{c^{\mathrm{ref}}_{\mathrm{El}} \cdot c^{\mathrm{ref}}_{\mathrm{G}}}} \tag{2.21}$$

During the intercalation reaction lithium and charge is transfered through the interface. The current flux density $j_{\mathrm{Inter-G}}$ can therefore be expressed as $j_{\mathrm{Inter-G}} = N_{\mathrm{Inter-G}} \cdot F$. The current $j_{\mathrm{Inter-G}}$ is also called *exchange current*. Another expression used for the Gibbs free energy $\Delta G_{\mathrm{Inter-G}}$ of a reaction is the *overpotential* $\eta_{\mathrm{Inter-G}}$. These two are related through $\Delta G_{\mathrm{Inter-G}} = F \cdot \eta_{\mathrm{Inter-G}}$. The overpotential $\eta_{\mathrm{Inter-G}}$ can be rewritten by introducing the reference state $\hat{\mu}^{\mathrm{ref}}_{\mathrm{Li}}$:

$$\begin{aligned} F \cdot \eta_{\mathrm{Inter-G}} &= \left(\mu^{\mathrm{Li^+}}_{\mathrm{G}} + F \cdot \Phi_{\mathrm{G}}\right) - \tilde{\mu}^{\mathrm{Li^+}}_{\mathrm{El}} - \hat{\mu}^{\mathrm{Li}}_{\mathrm{ref}} + \hat{\mu}^{\mathrm{Li}}_{\mathrm{ref}} && (2.22)\\ &= F \cdot \left(\Phi_{\mathrm{G}} - \frac{\hat{\mu}^{\mathrm{Li}}_{\mathrm{ref}} - \mu^{\mathrm{Li^+}}_{\mathrm{G}}}{F} - \frac{\tilde{\mu}^{\mathrm{Li^+}}_{\mathrm{El}} - \hat{\mu}^{\mathrm{Li}}_{\mathrm{ref}}}{F}\right) && (2.23)\\ &= F \cdot \phi_{\mathrm{G}} - F \cdot U^{\mathrm{G}}_{0} - \varphi^{\mathrm{Li^+}}_{\mathrm{El}} && (2.24) \end{aligned}$$

with the definition of the electrochemical potential $\tilde{\mu}^{\mathrm{Li^+}}_{\mathrm{G}}$, $\tilde{\mu}^{\mathrm{Li^+}}_{\mathrm{El}}$ and $\varphi^{\mathrm{Li^+}}_{\mathrm{El}}$ and the open-circuit voltage U^{G}_{0} in section 2.4.1 and section 2.4.2. The electrical potential Φ_{G} is transformed into the electrochemical potential ϕ_{G} since the reference state contains the chemical potential of the electrons: $\hat{\mu}^{\mathrm{ref}}_{\mathrm{Li}} = \mu^{\mathrm{Li^+}}_{\mathrm{ref}} + \mu^{\mathrm{e^-}}_{\mathrm{ref}}$. The overpotential of the intercalation reaction into the cathode (see eq. (Inter-LMO)) is defined analog to $\eta_{\mathrm{Inter-G}}$:

$$F \cdot \eta_{\mathrm{Inter-LMO}} = F \cdot \phi_{\mathrm{LMO}} - F \cdot U^{\mathrm{LMO}}_{0} - \varphi^{\mathrm{Li^+}}_{\mathrm{El}} \tag{2.25}$$

2.3. Graphite

Nearly all state-of-the-art LIBs use graphite or carbon as negative electrode. Different graphite and carbon materials exist: the spherically shaped meso carbon microbeads (MCMB), the artifical graphite and amorphous carbon [49]. Leading material producers are Hitachi, Toshiba and BASF. A comparison of several different materials can be found in [50]. In this work artificial graphite [51] was considered as negative electrode. The open-circuit voltage (OCV) of artificial graphite is a material property, which is very important for electrochemical simulations. The OCV is defined as the voltage measured between the material and a reference electrode, when they are in thermodynamic equilibrium/rest. A lithium metal electrode is used as reference electrode when obtaining the OCV of lithium intercalation materials. Calculations of the OCV based on theory is quite complex and still topic of ongoing research [52]. Usually specific experiments are used to obtain OCV data. The material is build into a half-cell with a lithium metal counter-electrode. The material is charged with a very low current until a defined

state of charge is reached. Then the cell is allowed to rest for several hours. The resulting cell voltage is the open-circuit voltage of the material for the given state of charge. These steps are repeated until the target voltage window is covered [53]. Electrochemical simulation are not possible without the open-circuit voltage. Therefore different approaches are used to obtain a functional relation between state of charge and open-circuit voltage. In literature different fit functions are used for the various intercalation materials. Ranging from simple polynomial fits to exponential expressions [8, 51, 54, 5]. In this work we use the empirical correlation obtained by [51], which is shown in fig. 2.5(a). Graphite

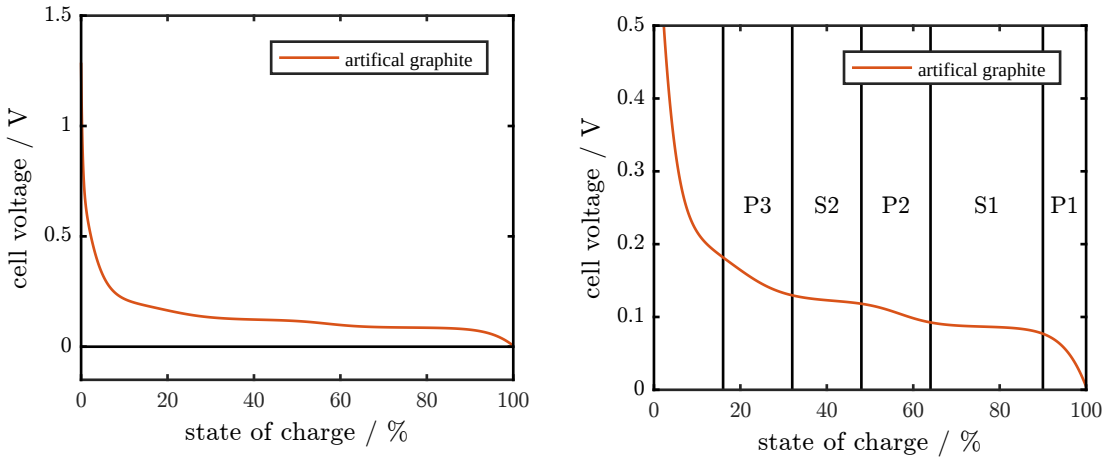

(a) The open-circuit voltage of artificial graphite shows several regions of nearly constant cell potential. The cell voltage is larger zero with respect to lithium.

(b) Some exemplary stages (S) and phases (P) are marked in the OCV of artificial graphite. A voltage plateau S results from the coexistence of multiple phases. The boundaries of the stages/phases are based on [50, 55].

Figure 2.5.: Open-circuit voltage of artificial graphite.

exhibits several potential plateaus during intercalation of lithium. Research indicates, that lithium ions form different phases with the graphite during intercalation. These phases are also called *stages*. The transition from one stage into another one results in a constant potential region [55, 53, 56]. The distinctiveness of the stages varies between the different graphitic battery electrodes. This depends on the purity of the graphite and the existence of other intercalation materials. Lithium can intercalate into added conductive agent and a measured half-cell potential thus shows a convolution of graphite and conductive agent. Dahn *et al.* [55] calculate, that the conductive agent is responsible for around 3.7 % capacity of their investigated material. Also, graphitic materials with more amorphous structures will not exhibit the distinct plateaus, but a more sloped out cell potential [50]. Since the experimental data and material information is not available for the OCV in fig. 2.5(a), only some plateaus are highlighted in fig. 2.5(b) explanatory. The stage S1 is due to the coexistence of phase P1 (Li_xC_6) and phase P2 (Li_xC_{12}). The used OCV shows a smeared out shape in the region below phase P3. Therefore a identification of the different stages and phases is not possible and thus left out. The

function dependence on the state of charge (SoC) of the OCV of artificial graphite is listed in eq. (2.26).

$$\begin{aligned} OCV_{\text{Graphite}}(x) = {} & 0.6379 + 0.5416 \cdot \exp(-305.5309 \cdot x) + 0.044 \cdot \tanh\left(-\frac{x - 0.1958}{0.1088}\right) \\ & - 0.1978 \cdot \tanh\left(\frac{soc - 1.0571}{0.0854}\right) - 0.6875 \cdot \tanh\left(\frac{soc + 0.0117}{0.0529}\right) \\ & - 0.0175 \cdot \tanh\left(\frac{soc - 0.5692}{0.0875}\right) \end{aligned} \tag{2.26}$$

This function was obtained by Safari *et al.* through fitting onto experimental data [51]. During lithiation the graphite undergoes a volume expansion between $5-10\,\%$ [57, 58]. The intercalated lithium increases the spacing between the graphite layers. The inclusion of the volume expansion into the electrochemical simulations posses several challenges. Therefore the volume expansion is neglected in this work.

The state of charge is defined with respect to the maximum lithium concentration $c_{\text{Li,max}}^{\text{material}}$ a material can hold:

$$SoC_{\text{material}} = \frac{c_{\text{Li}}^{\text{material}}}{c_{\text{Li,max}}^{\text{material}}} \tag{2.27}$$

The definition of the maximum lithium concentration posses a challenge for electrochemical simulations. From the theoretical perspective the maximum concentration $c_{\text{Li,max}}^{\text{theo}}$ is defined through the maximum possible amount of lithium inside an ideal intercalation host without changing the lattice irreversibly. In the case of graphite this is assumed to be LiC_6. Experimentally the maximum concentration $c_{\text{Li,max}}^{\text{exp}}$ is defined by the charge transferred while cycling between certain cell voltages. The experimental concentration $c_{\text{Li,max}}^{\text{exp}}$ can differ from the theoretical one $c_{\text{Li,max}}^{\text{theo}}$ due to several reasons, such es inhomogeneities of the material and diffusion limitations. For electrochemical simulations, which are parameterized on dedicated experimental data, one usually selects the value obtained from these parameterizations.

2.4. Potential

2.4.1. Definition

Three seemingly different potentials are of interest: The *chemical* $\mu_{\text{i}}^{\text{p}}$, the *electrical* Φ_{p} and the *electrochemical* $\tilde{\mu}_{\text{i}}^{\text{p}}$ potential. The chemical potential $\mu_{\text{i}}^{\text{p}}$ of a species i in the phase p is defined by the derivative of the free energy f_{i}^{p} with respect to the number of particles of species i n_{i} [59]:

$$\mu_{\text{i}}^{\text{p}} = \left(\frac{\partial\, f_{\text{i}}^{\text{p}}}{\partial\, n_{\text{i}}}\right)_{S,V,n_{i\neq j}} \tag{2.28}$$

If we express the chemical potential as a function of the activity a_{i}^{p} and with respect to an arbitrary reference state Θ we can write the chemical potentials as [33]

$$\mu_{\text{i}}^{\text{p}} = \mu_{\text{i}}^{\text{p},\Theta} + R \cdot T \cdot \log(a_{\text{i}}^{\text{p}}) \tag{2.29}$$

$$\mu_{\text{i}}^{\text{p}} = \mu_{\text{i}}^{\text{p},\Theta} + R \cdot T \cdot \log(f_{\text{i}}^{\text{p}} \cdot c_{\text{i}}^{\text{p}}) \tag{2.30}$$

With $f_{\mathrm{i}}^{\mathrm{p}}$ the molar activity coefficient of species i in phase p. The electrochemical potential of the species i in phase p depends on the chemical and electrical potential and is usually written the following way [60]:

$$\tilde{\mu}_{\mathrm{i}}^{\mathrm{p}} = \mu_{\mathrm{i}}^{\mathrm{p}} + z_{\mathrm{i}} \cdot F \cdot \Phi_{\mathrm{p}} \tag{2.31}$$

This electrochemical potential is with respect to the arbitrary reference state Θ. In the field of LIBs the lithium ion/lithium metal reaction Li^{+}/Li^{0} is the obvious choice as reference state. To allow for easier recognition of the used reference state, the electrochemical potential with respect to the Li^{+}/Li^{0}-reaction is written as $\varphi_{\mathrm{i}}^{\mathrm{p}}$:

$$\varphi_{\mathrm{i}}^{\mathrm{p}} = \tilde{\mu}_{\mathrm{i}}^{\mathrm{p}} - \hat{\mu}_{\mathrm{Li}}^{\mathrm{ref}} \tag{2.32}$$

$$= \mu_{\mathrm{i}}^{\mathrm{p}} - \hat{\mu}_{\mathrm{Li}}^{\mathrm{ref}} + z_{\mathrm{i}} \cdot F \cdot \Phi_{\mathrm{p}} \tag{2.33}$$

The lithium reference state is set to be the sum of the chemical potential of lithium and electrons in the lithium metal:

$$\hat{\mu}_{\mathrm{Li}}^{\mathrm{ref}} = \mu_{\mathrm{Li^{+}}}^{\mathrm{m}} + \mu_{\mathrm{e^{-}}}^{\mathrm{m}} \tag{2.34}$$

As an example, the electrochemical potential of the electrons in phase p is written:

$$\tilde{\mu}_{\mathrm{e^{-}}}^{\mathrm{p}} = \mu_{\mathrm{e^{-}}}^{\mathrm{p}} - F\,\Phi_{\mathrm{p}} \tag{2.35}$$

In this work the electrochemical potential of the electrons is also written as

$$\phi_{\mathrm{p}} = \Phi_{\mathrm{p}} - \frac{\mu_{\mathrm{e^{-}}}^{\mathrm{p}}}{F} = -\frac{\tilde{\mu}_{\mathrm{e^{-}}}^{\mathrm{p}}}{F} \tag{2.36}$$

2.4.2. Open-circuit voltage

With these potentials in mind the open-circuit voltage of a material m is defined. The potential difference between two electrodes is defined by the difference in electrochemical potential of the electrons $\tilde{\mu}_{\mathrm{e^{-}}}^{\mathrm{electrode}}$ in the electrodes [61]:

$$V_{\mathrm{measured}} = -\frac{\tilde{\mu}_{\mathrm{e^{-}}}^{\mathrm{material\ m}} - \tilde{\mu}_{\mathrm{e^{-}}}^{\mathrm{counter}}}{F} \tag{2.37}$$

Using eq. (2.36) this can be brought into a more common form:

$$V_{\mathrm{measured}} = \phi_{\mathrm{material\ m}} - \phi_{\mathrm{counter}} \tag{2.38}$$

The OCV is the measured potential difference between a counter electrode and the material electrode. Two reactions are important to relate the OCV to the relevant potentials of the material. At the

counter electrode the lithium undergoes the following reaction:

$$\mathrm{Li}^+_{\text{electrolyte}} \rightleftharpoons \mathrm{Li}^+_{\text{counter}} \tag{2.39}$$

And at the electrode made from material m the lithium reacts as follows:

$$\mathrm{Li}^+_{\text{electrolyte}} \rightleftharpoons \mathrm{Li}^+_{\text{material m}} \tag{2.40}$$

The change in Gibbs free energy $\Delta G_{\text{reaction}}$ of the reactions is zero, since the OCV is given at thermodynamical equilibrium:

$$\Delta G_{\text{reference}} = \tilde{\mu}^{\text{reference}}_{\mathrm{Li}^+} - \tilde{\mu}^{\text{electrolyte}}_{\mathrm{Li}^+} = 0 \tag{2.41}$$

$$\Delta G_{\text{material m}} = \tilde{\mu}^{\text{material m}}_{\mathrm{Li}^+} - \tilde{\mu}^{\text{electrolyte}}_{\mathrm{Li}^+} = 0 \tag{2.42}$$

Using eq. (2.41) the electrochemical potential $\tilde{\mu}^{\text{electrolyte}}_{\mathrm{Li}^+}$ is replaced in eq. (2.42) and one obtains:

$$\tilde{\mu}^{\text{counter}}_{\mathrm{Li}^+} - \tilde{\mu}^{\text{material m}}_{\mathrm{Li}^+} = 0 \tag{2.43}$$

With the definition of the electrochemical potential in eq. (2.31):

$$\mu^{\text{count}}_{\mathrm{Li}^+} + F \cdot \Phi_{\text{count}} - \mu^{\text{mat m}}_{\mathrm{Li}^+} - F \cdot \Phi_{\text{mat m}} = 0 \tag{2.44}$$

By the addition of zeros ($\tilde{\mu}^{\text{count}}_{\mathrm{e}^-} - \tilde{\mu}^{\text{count}}_{\mathrm{e}^-} = 0$) and with the electrochemical potential of an electron ($\tilde{\mu}^{\text{p}}_{\mathrm{e}^-} = \mu^{\text{p}}_{\mathrm{e}^-} - F\Phi_{\text{p}}$):

$$\left(\tilde{\mu}^{\text{mat m}}_{\mathrm{e}^-} - \tilde{\mu}^{\text{mat m}}_{\mathrm{e}^-}\right) + \left(\tilde{\mu}^{\text{count}}_{\mathrm{e}^-} - \tilde{\mu}^{\text{count}}_{\mathrm{e}^-}\right) = \mu^{\text{count}}_{\mathrm{Li}^+} + F \cdot \Phi_{\text{count}} - \mu^{\text{mat m}}_{\mathrm{Li}^+} - F \cdot \Phi_{\text{mat m}} \tag{2.45}$$

$$-\left(\tilde{\mu}^{\text{mat m}}_{\mathrm{e}^-} - \tilde{\mu}^{\text{count}}_{\mathrm{e}^-}\right) = \mu^{\text{count}}_{\mathrm{Li}^+} + \underbrace{\tilde{\mu}^{\text{count}}_{\mathrm{e}^-} + F \cdot \Phi_{\text{count}}}_{\mu^{\text{count}}_{\mathrm{e}^-}} - \mu^{\text{mat m}}_{\mathrm{Li}^+} - \underbrace{\left(\tilde{\mu}^{\text{mat m}}_{\mathrm{e}^-} + F \cdot \Phi_{\text{mat m}}\right)}_{\mu^{\text{mat m}}_{\mathrm{e}^-}} \tag{2.46}$$

The left hand side is identical to the potential difference measured externally (see eq. (2.37)). Hence, the open-circuit voltage of the material m is defined as

$$U_0^{\text{mat m}} = \frac{\mu^{\text{count}}_{\mathrm{Li}^+} + \mu^{\text{count}}_{\mathrm{e}^-} - \mu^{\text{mat m}}_{\mathrm{Li}^+} - \mu^{\text{mat m}}_{\mathrm{e}^-}}{F} \tag{2.47}$$

The lithium ion at the counter electrode forms together with a electron the reference state (see eq. (2.34)). With the definition of the chemical potential of the lithium ion-electron system inside the material m ($\mu^{\text{mat m}}_{\mathrm{Li}} = \mu^{\text{mat m}}_{\mathrm{Li}^+} + \mu^{\text{mat m}}_{\mathrm{e}^-}$), we can write the OCV as

$$U_0^{\text{mat m}} = \frac{\hat{\mu}^{\text{ref}}_{\mathrm{Li}} - \mu^{\text{mat m}}_{\mathrm{Li}}}{F} \tag{2.48}$$

This expression is identical to the one used in the transport theory [7].

2.5. Lithium plating

LIBs suffer from various degradation processes [62]. The most severe is lithium plating: Instead of intercalation a metallic lithium film forms on the surface of the anode material. This deposition can take place as soon as the so called *plating condition* is met. This condition is defined through the difference in the electrochemical potentials of lithium ions inside the electrolyte and lithium in lithium metal. If this difference is below zero with respect to the Li/Li^+ reaction, plating can occur. This can be expressed by the following inequality

$$\tilde{\mu}^{\mathrm{M}}_{\mathrm{Li^+}} - \tilde{\mu}^{\mathrm{El}}_{\mathrm{Li^+}} < 0 \tag{2.49}$$

The presence of a metallic lithium inside a lithium-ion battery can have several negative effects. The metal-electrolyte surface leads to enhanced growth of a solid-electrolyte-interphase and hence to the loss of cycleable lithium and electrolyte [17, 4, 42, 63]. Repeated plating during the cycling of the battery can result in a large additional SEI growth. The loss of electrolyte and growth of SEI can clog complete pores of the negative electrode. Blocked pores can then prevent the utilization of deeper regions and reducing the electrochemical active electrode surface. Under certain circumstances the metallic lithium phase forms dendrites. Those metallic rods grow towards the positive electrode and can pierce the separator. Upon reaching the cathode material an electrical short circuit is created. This is a process fatal for the battery. It can also start a exothermal reaction of the electrolyte leading to a thermal runaway of the whole battery.

The temporal onset and spatial location of lithium plating is highly dependent on the OCV of the negative electrode [42, 62] and the intercalation kinetics [64]. This is nicely illustrated by Legrand *et al.* [64] in fig. 2.6. In this figure, the plating condition is defined with the overpotential of the intercalation reaction η_{neg}: $|\eta_{\mathrm{neg}}| > |\eta_{\mathrm{lim}}|$. A OCV close to the equilibrium potential of the Li/Li^+-reaction lowers

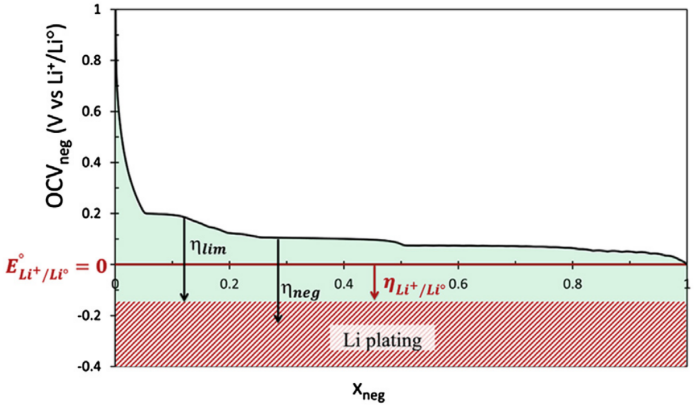

Figure 2.6.: Illustration of the influence of the OCV on the plating condition. (reprinted with permission from [64])

the η_{lim} and hence favors plating. The limiting overpotential is shown as the vertical distance between the OCV (black line) and the plating onset (top of red shaded region) in fig. 2.6. Slow reaction kinetics have an impact on the other side of the plating condition. The rate constant of a intercalation reaction

depends on the electrochemical situation at the active material-electrolyte interface. By modeling the intercalation reaction as a one-step reaction, we implicitly include the influence of the SEI on the lithium intercalation into exchange current constant $i_{00}^{\mathrm{Inter-G}}$ (see eq. (2.20)). The SEI grows during battery operation, thus hindering the lithium ions from moving from the electrolyte into the graphite. This could be expressed through lowering the exchange current constant: $i_{00,\mathrm{aged}}^{\mathrm{Inter-G}} < i_{00}^{\mathrm{Inter-G}}$. Achieving the same current flow through the anode-electrolyte-interface results hence in a larger overpotential η_{neg}. Reduced reaction kinetics also occur at low temperatures, since the reaction rate is dependent on the temperature [63]. (This dependence is usually expressed through the Arrhenius relation.)

Beside these intrinsic battery conditions, the applied current can also lead to lithium plating. Higher current through-put results in a larger current flow through the anode-electrolyte-interface and hence in a larger overpotential η_{neg}. The increased overpotential will then promote lithium plating [63]. Apart from operation conditions, also errors during cell production and cell design can promote lithium plating [65]. Possible production errors are the damaging of the separator or the electrodes during the winding process, misalignment of the electrode and separator. Lithium-ion batteries usually have an excess of the negative electrode material. This should prevent local overcharge of the anode by increasing the active surface area and thus lowering the exchange current density [66].

Artificial graphite exhibits an open-circuit voltage close to zero with respect to $\mathrm{Li/Li^+}$ and is therefore susceptible to lithium plating. Other carboneous materials such as petroleum coke or hard carbon show an OCV with a higher average potential and hence should be less prone to show lithium plating. A downside is the smaller capacity window, where this type of carbon material can be safely operated [42]: The OCV of hard carbon is above zero in the range of $x \in [0, 0.5]$ in $\mathrm{Li_xC_6}$, while artificial graphite allows the facilitation of one lithium atom per six carbon atoms ($\Delta x = 1$) .

2.5.1. Experimental information on lithium plating

In the early years of lithium batteries (1970s/80s) lithium metal were used as metallic anode electrodes. The cycling of these electrodes was usually termed as *lithium plating* and *stripping* [67, 68, 69, 70]. The shift of meaning from *cycling of lithium metal electrode* to *unwanted process in graphitic anodes* [71] took place when the focus from metal lithium electrode changed towards intercalation materials. In [72] it is noted, that the prevention of lithium plating on the graphite is necessary to allow for a safe charging. Bonino *et al.* [70] investigate the efficiency of wanted deposition on "vitreous carbon" (glassy carbon). They state that the poor reversibility of the lithium plating is probably due to the formation of a lithium carbide phase. This "phase" is related to the intercalation stages of graphite used nowadays. With the origin of the term *lithium plating* in mind, the usage of it with regard to the degradation process seems inconsistent. Nevertheless, in the recent years this term is used in the scientific community to describe the degradation process. Hence, in this work *lithium plating and stripping* refers to the degradation process of lithium deposition on the surface of an intercalation material as negative electrode in lithium-ion batteries.

It is quite difficult to see experimentally whether lithium plating is taking place. The detection of already plated lithium is relatively easy. During the discharge of a LIB, which contains plated lithium,

the distinct voltage plateau at the start of discharge is a result of the potential independent stripping process. In fig. 2.7(a) the cell voltage of an experimental cell exhibiting this stripping plateau is shown. The cell voltages during discharge after charging at room temperature (RT) and −20 °C are compared. The differential voltage (dVdQ) [74, 11, 75] of the cell potentials exhibits a peak for lower transferred

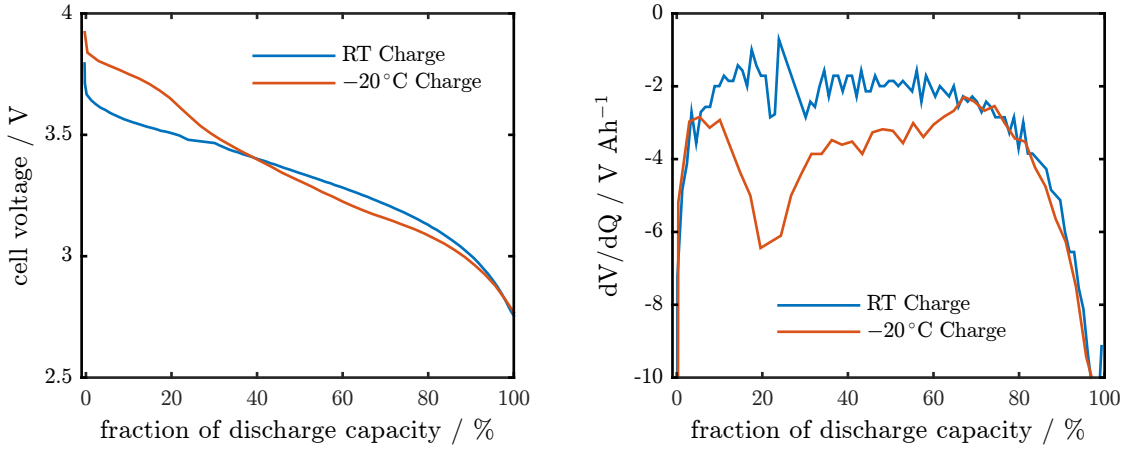

(a) Experimental cell voltage (data extracted from figure 7 in [73]) during discharge at −20 °C after charging at room temperature (RT) (blue) and at −20 °C. After charging at low temperature a voltage plateau can be seen during discharging the battery.

(b) Differential voltage calculated from fig. 2.7(a). The end of the voltage plateau is visible as a dip in the differential voltage curve at 20 % discharge capacity (red).

Figure 2.7.: Experimental cell voltage for discharge after different prior charging conditions (obtained from figure 7 in [73]).

charges if stripping did occure. This method can only detect lithium plating after this process already took place. The differential voltage is calculated for the experimental data in fig. 2.7(a) as an example and shown in fig. 2.7(b). It can clearly be seen, that the voltage plateau results in a dip in the differential voltage at the corresponding transferred charge. A more direct approach to detect if lithium is getting plated is the use of an additional reference electrode [76, 77]. The introduction of a third electrode, usually lithium metal, as reference electrode enables the measurement of the potential difference between the reference electrodes and the two battery electrodes. The potential difference measured between the reference electrode and the negative electrode can be approximated by $E_{\mathrm{Ref-neg.}} \approx \Phi_{\mathrm{neg.}} - \varphi_{\mathrm{El}}^{@\mathrm{neg.}}$. This measurement is only feasible in the laboratory. Another direct method is the use of an in-situ optical microscope [78]. This method is restricted to lab-scale cells and need a special housing. Based on reference electrode measurements, the plating condition is defined experimentally through half-cell potential of the anode [79]: $E_{\mathrm{Ref-neg.}} < 0$. This definition is approximatly correct, if the reference electrode is a lithium metal electrode and the distance between the reference electrode and the anode is very small. This will be shown in section 2.5.4. Tippmann *et al.* [5] uses a slightly different condition to indicate the plating and degradation regime. Their definition only depends on the electrical potential in the solid phase of the anode $\phi_{\mathrm{s,a}} < 0$ (see equation 26 in [5]). This definition is thermodynamically only valid, if the electrolyte potential $\varphi_{\mathrm{El}}^{@\mathrm{neg}}$ is zero with respect to the $\mathrm{Li/L^+}$-reaction. This assumption is not stated in their electrochemical simulation study. Hence their degradation factor Θ_I^{norm} either underestimates or overestimates the amount of degradation depending on the electrolyte potential.

The majority of the available detection methods can only really be applied in the lab scale. They are either restricted by very precise measurement instruments (high precision coulometry [80]), expensive and large facilities (Neutron diffraction [81]) or destructive methods (GD-OES [82, 83]).

Apart from the challenges of detecting and investigating lithium plating experimentally, the shape and structure of the lithium deposit is not easy to define. Depending on the resolution used to create an image of a plated region, a smooth film can look like a aggregation of needle-like structures. Needle-like structures out of metal are called *dendrites*. The formation of lithium dendrites is usually only shown for lithium metal electrodes [84, 85, 86, 78, 87]. Dendrite formation is seldom seen for graphite with lithium plating [53]. Nevertheless, LIBs sometimes exhibit an electrical short-circuit. They can result from the dissolution of current collector material [42] or the formation of a lithium dendrite [88]. Different approaches exist, which try to describe their growth and dissolution [89, 90].

2.5.2. The lithium plating reactions and other side reactions

We will introduce the different side-reactions of lithium ions inside the lithium-ion battery in this section. The different phases, which are of relevance in the deposition of metallic lithium, are the electrolyte, the supporting active material, the solid-electrolyte-interphase and the plated lithium. In fig. 2.8 a sketch shows the different involved phases and possible reaction pathways of plated lithium. The plated lithium

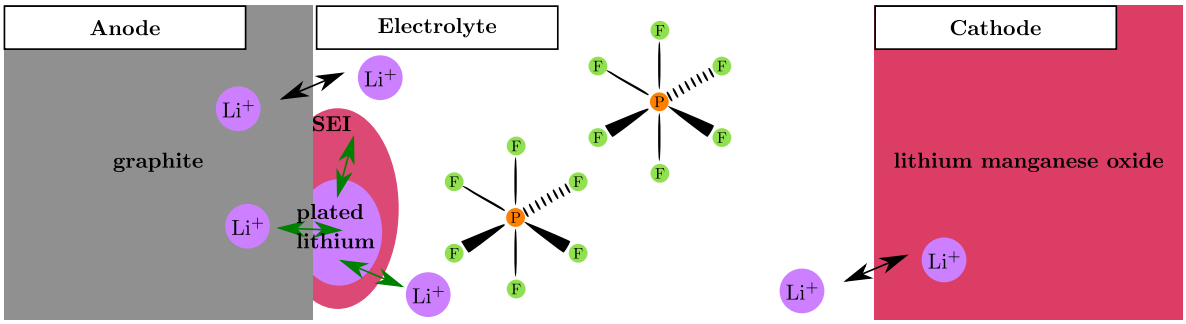

Figure 2.8.: The ideal lithium-ion battery (see fig. 2.4) is extended by possible side reactions. Plated lithium is shown as purple area on the surface of the graphite electrode. This metallic lithium phase can form the SEI, chemical intercalated into the graphite or strip into the electrolyte. These side reactions are indicated by the green arrows.

phase can vanish during discharge and appear during charge of a LIB. The solid-electrolyte-interphase grows at two interfaces. The interface between the graphite and the electrolyte and the interface between the metallic lithium and the electrolyte. The lithium salt in the sketch consists of $LiPF_6$.

2.5.2.1. Plating reaction

The deposition of metallic lithium on the surface of the intercalation material is the main plating reaction:

$$Li^+_{El} \rightleftharpoons Li^0_{Pl} + e^- \qquad \text{(Pl/St)}$$

The difference in electrochemical potentials of the lithium ions can be written as

$$F \cdot \eta_{\mathrm{Pl/St}} = \tilde{\mu}^{\mathrm{So}}_{\mathrm{Li^+}} - \tilde{\mu}^{\mathrm{El}}_{\mathrm{Li^+}} \tag{2.50}$$

$$\eta_{\mathrm{Pl/St}} = \phi_{\mathrm{Li}} - \varphi^{\mathrm{Li^+}}_{\mathrm{El}} \tag{2.51}$$

with the electrochemical potential inside the plated lithium phase and the electrochemical potential of the lithium ions inside the electrolyte. Lithium metal is a very good electron conductor. Hence one can approximate the electrochemical potential of the electrons ϕ_{Li} in the metal through the electrochemical potential of the electrons in the supporting electrode: $\phi_{\mathrm{Li}} \approx \phi_{\mathrm{So}}$. Following the general definition of an exchange current of a reaction [34], we express the lithium flux due to the plating reaction the following way:

$$N_{\mathrm{Pl/St}} = N^{00}_{\mathrm{Pl/St}} \cdot \left(c^{\mathrm{El}}_{\mathrm{Li^+}}\right)^{\alpha_{\mathrm{a}}^{\mathrm{Pl/St}}} \cdot \left(\exp\left[\frac{\alpha_{\mathrm{a}}^{\mathrm{Pl/St}} F}{R\,T} \cdot \eta_{\mathrm{Pl/St}} \right] - \exp\left[-\frac{\alpha_{\mathrm{c}}^{\mathrm{Pl/St}} F}{R\,T} \cdot \eta_{\mathrm{Pl/St}} \right] \right) \tag{2.52}$$

with the reaction rate constant $N^{00}_{\mathrm{Pl/St}} = \frac{N^{*}_{\mathrm{Pl/St}}}{\left(c^{\mathrm{ref}}_{\mathrm{El}}\right)^{\alpha_{\mathrm{a}}^{\mathrm{Pl/St}}}}$ and $\alpha_{\mathrm{a}}^{\mathrm{Pl/St}}$ the anodic transfer number of the reaction and $\alpha_{\mathrm{c}}^{\mathrm{Pl/St}} = 1 - \alpha_{\mathrm{a}}^{\mathrm{Pl/St}}$. For the case of a symmetric reaction ($\alpha_{\mathrm{a}}^{\mathrm{Pl/St}} = 0.5$) this results in a symmetric exchange current:

$$N_{\mathrm{Pl/St}} = 2 \cdot N^{00}_{\mathrm{Pl/St}} \cdot \sqrt{c^{\mathrm{El}}_{\mathrm{Li^+}}} \cdot \sinh\left(\frac{F}{2\,R\,T} \cdot \eta_{\mathrm{Pl/St}} \right) \tag{2.53}$$

The plating and stripping reaction is, similar to the intercalation reaction, a charge transfer reaction. Hence, the current flux density $j_{\mathrm{Pl/St}}$ through the reaction interface is given as $j_{\mathrm{Pl/St}} = r_{\mathrm{Pl/St}} \cdot F$. The expression for the plating and stripping reaction (eq. (2.52)) can be used as exchange current for the counter-electrode in a half-cell-geometry. In certain cases the current can be further simplified to minimize the influence of the counter electrode on the cell voltages:

$$N^{00}_{\mathrm{Pl/St}} = N^{*(\mathrm{const})}_{\mathrm{Pl/St}} \tag{2.54}$$

As long as no lithium depletion inside the electrolyte close to the counter-electrode occurs, the simplification above can be used. The rate constant $N^{00}_{\mathrm{Pl/St}}$ and the anodic transfer number $\alpha_{\mathrm{a}}^{\mathrm{Pl/St}}$ are important factors for electrochemical simulations. There is not a lot of literature regarding the determination of these parameters [91, 92]. Both parameters depend on the electrolyte composition [73, 93]. Possible approaches to obtain these parameters will be sketched in chapter 6.

2.5.2.2. Chemical intercalation

The plated lithium phase is not in a thermodynamic equilibrium with the supporting electrode. A possible reaction is the intercalation into the host lattice:

$$\mathrm{Li}^0_{\mathrm{Pl}} \rightleftharpoons \mathrm{Li}^0_{\mathrm{So}} \qquad \text{(Chem. Int.)}$$

This reaction is named *chemical intercalation*. It is assumed, that this reaction does not result in a charge transfer between the plated lithium and the intercalated lithium. The plated lithium can intercalate into the underlying electrode with the free energy difference:

$$\eta_{\text{Chem.Int}} = -U_0^{\text{G}} \tag{2.55}$$

The following lithium flux generated by the chemical intercalation is used to study the basic effects:

$$N_{\text{Chem.Int}} = N_{\text{Chem.Int}}^{00} \cdot \left(c_{\text{Li+}}^{\text{So}}\right)^{\alpha_{\text{c}}^{\text{Chem.Int}}} \cdot \left(\exp\left(\frac{\alpha_{\text{a}}^{\text{Chem.Int}} F}{R\,T} \cdot \eta_{\text{Chem.Int}}\right) - \exp\left(-\frac{\alpha_{\text{c}}^{\text{Chem.Int}} F}{R\,T} \cdot \eta_{\text{Chem.Int}}\right)\right) \tag{2.56}$$

with $N_{\text{Chem.Int}}^{00} = \frac{N_{\text{Chem.Int}}^{*}}{\left(c_{\text{So}}^{\text{ref}}\right)^{\alpha_{\text{c}}^{\text{Chem.Int}}}}$ and $\alpha_{\text{c}}^{\text{Chem.Int}} = 1 - \alpha_{\text{a}}^{\text{Chem.Int}}$. The author is not aware of any literature regarding the determination of this parameter. Possible approaches to get better foundation for the exchange rate constant are described in chapter 6. Under the assumption of a charge-neutral-reaction, the current flux density $j_{\text{Chem.Int}} = 0$ is vanishing.

2.5.2.3. The growth of a solid-electrolyte-interphase

The lithium ions can react with the solvent molecules to form the *solid-electrolyte-interphase*. This reaction is a degradation process. The time scale of this process is, apart from the formation cycle, in the range of days and hence assumed to be negligible slow compared to lithium plating. During this reaction lithium ions, electrons and solvent molecules (e.g. ethylene carbonate (EC) or dimethyl carbonate (DMC)) react at the surface of the negative electrode to form a porous surface layer. The SEI is roughly $10 - 100\,\text{nm}$ thick, depending on the exact electrolyte composition and battery age. The growth of the SEI can also occur at a fresh interface between metallic lithium and the electrolyte:

$$\text{Li}_{\text{Pl}}^{+} + \text{Electrolyte} \rightarrow \text{SEI} \tag{SEI}$$

Hence, repeated cycling of a battery, where plating occurs, will result in an increased SEI formation. In this work model development and simulations are done in the frame of the simplified situation, where only reversible processes are relevant. The addition of irreversible processes like growth of SEI are extensions for future research (see chapter 6). More information about the influences of this layer on the battery performance can be found elsewhere [62, 94].

2.5.3. Reversible stripping of plated lithium

The metallic lithium, which is deposited at the surface of the negative electrode, can be reintroduced into the reversible lithium cycle along two possible pathways. Either the deposited lithium is stripped and dissolved into the electrolyte (along eq. (Pl/St)) during the discharging of the battery, from where it can either intercalate into the anode (along eq. (Inter-G)) or cathode (along eq. (Inter-LMO)). Or the plated lithium-ion battery is held at rest until the plated lithium can electro-neutrally intercalate

into the anode (along eq. (Chem. Int.)). These two paths are not equivalent under non-equilibrium conditions, even though the final states are thermodynamically, i.e. in equilibrium, identical. The direct chemical intercalation (eq. (Chem. Int.)) is a process independent from the electrical potential ϕ_{Anode} in the anode phase (eq. (2.55)). Hence the changes in the cell potential are purely due to the increase of the state of charge of the anode. During the coexisting stripping and delithiation reaction, an anode with plated lithium exhibits a mixed potential. The value of this potential lays between the potential of a pure anode-delithiation and pure lithium stripping, since the electrochemical process of lithium stripping (eq. (Pl/St)) has an equilibrium potential vs. a lithium reference of zero. When a plated lithium-ion battery is driven with a stripping current, plated lithium gets stripped into the electrolyte. This newly dissolved lithium ion has a chemical potential which also allows the intercalation into the anode. Hence it can directly intercalate into the anode, before even being transported to the cathode electrode. These steps of stripping and intercalation into the anode material results in a globally electro-neutral process, since the electrons freed during the lithium dissolution are consumed during the intercalation process in the anode. This cycle exhibits different energy barriers than for the direct chemical intercalation and thus the overpotentials and the dependence on the applied current will be different.

2.5.4. Relation between half-cell potentials and plating condition

Lithium plating is often investigated with a full-cell containing an additional reference electrode. The layout of a three-electrode-cell is sketched in Fig. 2.9. In this sketch lithium metal is used as reference electrode. The half-cell voltage of the anode is measured with respect to the reference electrode and is

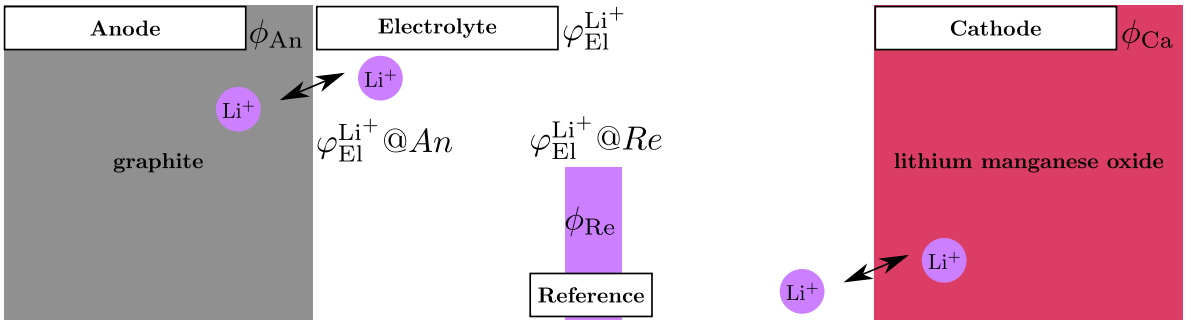

Figure 2.9.: Sketch of a full-cell setup with reference electrode. The different potentials important for the measurement of the electrode potentials are included.

defined as [79]

$$E_{\text{Anode}} = \phi_{\text{An}} - \phi_{\text{Re}} \tag{2.57}$$

The introduction of a reference electrode is done such, that the anode-cathode-system should not be influenced. The potential difference is measured through a high resistance in such a way, that no current is flowing from the reference electrode into the electrolyte. The overpotential of the lithium reaction at

the reference electrode is hence zero:

$$\eta_{\text{Reference}} = 0 \tag{2.58}$$

In the following subsections we will investigate, how two different types of reference electrodes influence the measurement of the plating condition. The experimental plating condition is defined as [79]

$$E_{\text{Anode}} < 0 \tag{2.59}$$

$$\phi_{\text{An}} - \phi_{\text{Re}} < 0 \tag{2.60}$$

The plating condition as defined through the plating reaction eq. (Pl/St):

$$\phi_{\text{An}} - \varphi_{\text{El}}^{\text{Li}^+} @An < 0 \tag{2.61}$$

where $\varphi_{\text{El}}^{\text{Li}^+} @An$ is the electrochemical potential of lithium ions in the electrolyte $\varphi_{\text{El}}^{\text{Li}^+}$ close to the Anode-Separator-Interface.

2.5.4.1. Case 1: Intercalation material as reference electrode

The overpotential for the intercalation reference electrode is expressed by

$$\eta_{\text{Reference}}^{\text{Intercalation}} = \phi_{\text{Re}} - U_0^{\text{Re}} - \varphi_{\text{El}}^{\text{Li}^+} @Re \tag{2.62}$$

The open-circuit-potential of the reference electrode is constant $U_0^{\text{Re}}(c_{\text{Re}}) = const$, since the concentration inside the reference electrode is constant $c_{\text{Re}} = const$. The vanishing overpotential of the reference electrode allows to express the electrical potential of the reference electrode through the electrochemical potential inside the electrolyte and the open-circuit potential of the reference electrode:

$$\phi_{\text{Re}} = U_0^{\text{Re}} + \varphi_{\text{El}}^{\text{Li}^+} @Re \tag{2.63}$$

For a reference electrode close to the anode, we can neglect the potential drop in the electrolyte due to the ionic resistance. Hence we can approximate the electrochemical potential in the electrolyte at the different positions as follows:

$$\varphi_{\text{El}}^{\text{Li}^+} @Re \approx \varphi_{\text{El}}^{\text{Li}^+} @An \tag{2.64}$$

Substituting eq. (2.63) and eq. (2.64) in the experimental plating condition (see eq. (2.59)) yields:

$$\phi_{\text{An}} - \varphi_{\text{El}}^{\text{Li}^+} @An - U_0^{\text{Re}} < 0 \tag{2.65}$$

This expression obviously differs from the plating condition as shown in Eq. 2.61. Therefore, the experimental expression (Eq. 2.59) is more strict than needed. The thermodynamically correct condition

would be in the case of an intercalation reference electrode

$$E_{\text{Anode}} < U_0^{\text{Re}} \tag{2.66}$$

2.5.4.2. Case 2: Lithium metal as reference electrode

If a lithium metal is used as reference electrode, the overpotential at the reference electrode is

$$\eta_{\text{Reference}}^{\text{Li-metal}} = \phi_{\text{Re}} - \varphi_{\text{El}}^{\text{Li}^+}@Re \tag{2.67}$$

This overpotential is also zero and hence we can express the electrical potential of the reference as

$$\phi_{\text{Re}} = \varphi_{\text{El}}^{\text{Li}^+}@Re \tag{2.68}$$

The experimental plating condition (Eq. 2.59) together with the approximation for the electrolyte potential (Eq. 2.64) and the reference overpotential (Eq. 2.68) can be written as:

$$\phi_{\text{An}} - \varphi_{\text{El}}^{\text{Li}^+}@An < 0 \tag{2.69}$$

This expression is identical to the plating condition taken from the theoretical work (see Eq. 2.61), as long as the assumption in Eq. 2.64 is valid. In the case that $\varphi_{\text{El}}^{\text{Li}^+}@Re \approx \varphi_{\text{El}}^{\text{Li}^+}@An$ one needs to modify the plating condition in Eq. 2.59 to

$$E_{\text{Anode}} < \Delta\varphi_{\text{El}}^{\text{Li}^+} \tag{2.70}$$

with $\Delta\varphi_{\text{El}}^{\text{Li}^+}$ being the difference in electrochemical potential at the anode and reference electrode:

$$\Delta\varphi_{\text{El}}^{\text{Li}^+} = \left(\varphi_{\text{El}}^{\text{Li}^+}@Re - \varphi_{\text{El}}^{\text{Li}^+}@An\right) \tag{2.71}$$

During charge, when lithium plating is usually taking place, this difference has a positive value:

$$\Delta\varphi_{\text{El}}^{\text{Li}^+} > 0 \tag{2.72}$$

2.5.4.3. Conclusion

The usage of the electrode potential E_{Anode} as indication for the plating condition $E_{\text{Anode}} < 0$ is more strict than needed for both cases. Both configurations include a shift due to the resistance of the electrolyte between the reference electrode and the investigated electrode (see section 2.5.4.2). The intercalation reference electrode (see section 2.5.4.1) has an additional offset due to the open-circuit potential of the intercalation reference. The usage of a lithium metal electrode as reference electrode with the smallest possible distance to the investigated electrode is suggested.

2.5.5. Literature review of lithium plating models

The types of models and simulation to describe the plating of lithium are manifold. While most work focuses on the possible structural growth mechanisms (diffusion limited, field gradients) [89, 95, 96, 97, 98], only one model so far was used to investigate the effect of lithium plating on the performance of a full lithium ion battery in the framework of a pseudo-2D-transport theory. The most prominent electrochemical model regarding lithium plating and stripping is the model from Arora *et al.* [4]. This model was constructed in the framework of the porous electrode theory of Newman [54, 99]. The model system consists of graphite in the form of MCMB 2528 and lithium-manganese-oxide $Li_xMn_2O_4$ emerged in $LiPF_6$ in plasticized EC/DMC electrolyte. This model describes the deposition of plated lithium and the irreversible loss of lithium due to growth of an SEI. The degradation processes of lithium deposition and SEI growth are described using only one Butler-Volmer current. The distribution of the lithium ions into the plated lithium phase or the SEI phase is done according to defined parameters (z_{Li} and $z_{\mathrm{Li_2CO_3}}$). Arora *et al.* [4] were able to show, that the amount of excess negative electrode capacity is vital for the suppression of lithium plating during overcharge. The model of Arora was the basis for some extension: Tang *et al.* [65] applied the model to a pseudo 3D (2D+1D) domain to investigate the effect of mismatched electrodes. Perkins *et al.* [100] used model order reduction schemata to enable a possible implementation of the plating model into a micro-controller used for battery management systems. A close investigation presented some shortcomings and vagueness about the exact operation of the model. The Arora model does not clearly state, what the exact conditions for the onset of the plating reactions are. Before the plating condition ($\Phi_1 - \Phi_2 < 0$) is reached, the plating current seems to be set to zero. Also, as soon as a film of plated lithium is formed and the whole active surface is covered by lithium, one would expect the intercalation reaction to be blocked. But the figures in the publication show, that the intercalation at the negative electrode/separator-interface is still taking place after the formation of a plated surface. The only influence on the intercalation reaction is the rising resistance R_{film} in the overpotential. The film resistance corresponds to the sum of ionic conductivity in the SEI and the electronic conductivity in the lithium metal. This indicates, that the current in the SEI has lithium ions as charge carriers, while in the plated lithium electrons are the charge carriers. Hence one would expect the interface between the plated lithium and the SEI to be the reaction area of the intercalation. The excellent electron conductivity of lithium leads to a dominance of the SEI. This critique on the Arora-model lead to the development of a new lithium plating and stripping model in the framework of a spatially resolved transport model. The resulting model, which will be described in the following section, allows for the complete blockage of the direct intercalation path.

2.5.6. Modeling of lithium plating and stripping

The newly developed lithium plating model will be introduced in the following section. The model describes the growth of a lithium film on the surface of an anode. Three reactions are relevant: the intercalation reaction between electrolyte and graphite, the metallic lithium deposition and a charge-neutral reaction between the plated lithium and the supporting graphite. Without the presence of plated lithium, lithium ions can intercalate from the electrolyte into the graphite. During plating the

lithium ions get deposited from the electrolyte on the surface of the anode and form a neutral lithium atom. Prolonged deposition results in an growing lithium phase on the surface. The presence of a large lithium phase can prevent the intercalation from the electrolyte into the graphite. The metallic lithium on the surface is not thermodynamically stable. It can either react with the electrolyte to form the solid-electrolyte-interphase or intercalate charge neutral into the supporting graphite. To model the growth of an SEI is a complex topic itself [62, 101]. Hence the SEI growth is not included in the plating model presented in this work. The extension of the presented model to include SEI growth is subject of future development. The shape of the lithium deposition is characterized through a simplified morphology in this model. Experimental investigations of the deposition of lithium on lithium metal electrodes showed, that after an initial thickness growth different morphologies, such as "bushy" or "dense", exist [78]. The conditions, which lead to the development of one phase or the other one, are not fully understood. The exact local electrochemical situation at the lithium-electrolyte-interface needed for the growth of different morphology is not known. Hence, the amount of plated lithium on a given surface is identified in this model through the average thickness of the lithium film and the amount of surface covered by it. As an result of these simplifications, the active surface area between the metallic lithium and the electrolyte is smaller than the surface of a porous structure with the same amount of lithium. But due to increasing electrolyte depletion towards the surface and tip effects, it is expected, that only the fraction of a porous surface furthest away from the supporting electrode is electrochemical active [89, 98]. This fraction scales with the fraction of the projected surface covered by the porous lithium film. The assumption of a flat reactive surface should therefor be a good approximation. The plated lithium, the electrolyte and the active particle are connected through different reactions. Some possible reaction pathways are sketched in Fig. 2.10. The irreversible formation

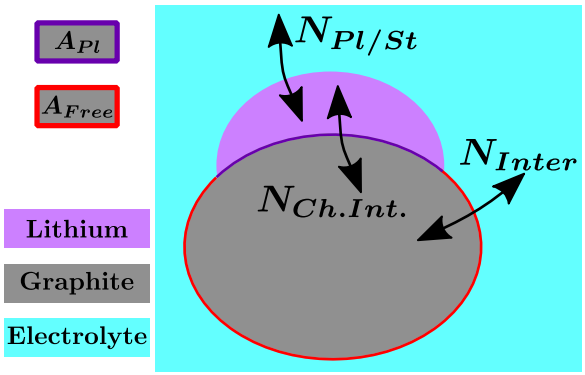

Figure 2.10.: A graphite particle (grey ellipse) has part of its surface A_{Pl} (dark purple) covered by a metallic lithium phase (purple). The dissolved lithium in the electrolyte (light blue), the plated lithium (purple) and the intercalated lithium (grey) can react along the three shown paths. The interface between graphite and electrolyte A_{Free} (red) is relevant for the direct intercalation N_{Inter}.

of the solid-electrolyte-interphase (SEI) is omitted, since it is not included in this model. The SEI would be located at the graphite-electrolyte-interface (A_{Free}) and the plated lithium-electrolyte-interface.

It is assumed, that lithium ions from the electrolyte adsorb at the surface of graphite and form a neutral lithium atom. These adsorbed atoms are the building blocks of a lithium phase on the surface of a

graphite particle. The metallic lithium either stays at the surface or intercalates into the supporting graphite. The amount of plated lithium depends on the reactions with its surroundings (see Eq. Pl/St and Eq. Chem. Int.). The temporal change of the amount of lithium plated n_{Pl} at the surface is therefore described by a conservation equation:

$$\frac{\partial n_{\mathrm{Pl}}}{\partial t} = \left(N_{Ch.Int.} - N_{Pl/St}\right) \cdot A_{\mathrm{Pl}} \tag{2.73}$$

with n_{Pl} the amount of substance of the adsorbed lithium with the unit *mol*. The active surface for the plating and chemical intercalation reaction is the amount of surface covered A_{Pl}. The adsorbed lithium could also react with the electrolyte to form the solid-electrolyte-interphase (SEI). A possible approach to describe the SEI growth is sketched in chapter 6.

The plated lithium in this work is described using two parameters: the amount of surface covered by plated lithium A_{Pl} and the average thickness of the plated lithium d_{Pl}. The exact shape of the plated lithium is not resolved in this model. Instead the plated lithium is represented as a solid film with the average thickness d_{Pl}. Without the resolution of the surface roughness of the plated lithium, the area between the plated lithium and the electrolyte is assumed to be identical in size as the area between the plated lithium and the graphite A_{Pl} (see fig. 2.11(a)). The lithium thickness of the case in fig. 2.11(a) would be below the thickness of a monolayer of lithium $d_{\mathrm{Li}}^{\mathrm{ML}}$. A rough lithium surface, as seen in

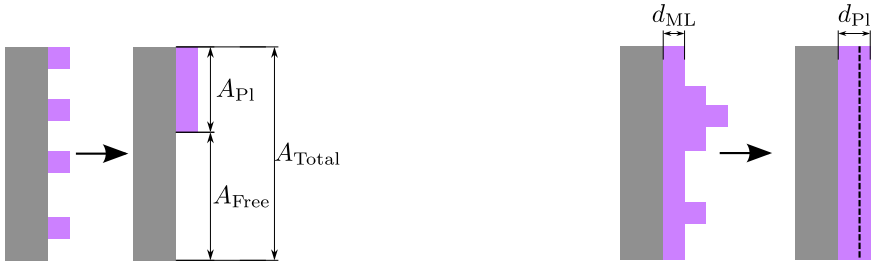

(a) The spatial distribution of the adsorbed lithium atoms is not resolved. This plating stage is represented only through the amount of surface covered A_{Pl}.

(b) Structure of plated lithium (left) is approximated through a solid film with an average thickness d_{Pl} (right). The thickness of a monolayer d_{ML} is shown as dashed line in the right picture.

Figure 2.11.: Explanatory illustrations of the assumptions concerning the distribution of plated lithium in the framework of this model. Lithium (purple) and graphite (grey) are colored according to the general color scheme in this work (see appendix B.1).

fig. 2.11(b), is expressed in the model through a solid film as shown right. The direct intercalation from the electrolyte into the graphite proceeds in parallel to the lithium deposition and chemical intercalation. As long as the surface is not completely covered by plated lithium, direct intercalation of lithium ions from the electrolyte into the graphite (eq. (Inter-G)) can take place. The amount of surface area available for intercalation is given through:

$$A_{\mathrm{free}} = A_{\mathrm{Total}} - A_{\mathrm{Pl}} \tag{2.74}$$

and is also indicated in fig. 2.11(a). As mentioned earlier the volume of graphite can change during intercalation of lithium. This can result in cracking or other irreversible structural changes. In general

the total surface area A_{total} should therefor be a variable, which depend on the battery operation in the past and the current state of charge. For simplification it is assumed, that the variation of total surface area can be neglected and is hence treated as a constant. The developed model should easily be modified to allow for changes, should the need arise to include the volume changes. During the deposition of metallic lithium the surface of the active material is covered. At the same rate as lithium is plated on the surface, the amount of surface area covered by these lithium atoms A_{Pl} is increasing:

$$\frac{\partial\ A_{\text{Pl}}}{\partial\ t} = \frac{\partial\ n_{\text{Pl}}}{\partial\ t} \cdot a_{\text{Li}} \tag{2.75}$$

The covered surface area increases by a_{Li} per mol lithium atom (m^2/mol). This increase takes place as long as there exists free surface A_{Free}. The change in surface area directly depends on the change of the amount of substance and the presented model therefor only allows thickness growth after the complete given surface A_{Total} is covered. Due to the direct dependence of the surface coverage on the amount of plated lithium, only one independent variable is needed to describe the surface system: n_{Pl}. The theory behind the expressions of the exchange currents (eq. (2.52) and eq. (2.56)) assumes non-depleting reaction species. Since the plated lithium atoms do not represent a infinite phase, the vanishing of the lithium phase needs to be included. The approach used in this work is the extension of the overpotential by a dissolution overpotential η_{dis}. The additional overpotential represents an energy barrier for the dissolution of lithium atoms on the surface below a certain surface coverage. The dissolution energy barrier is incorporated into the part of the exchange current representing the consumption of adsorbed lithium:

$$N_{\text{PlEl}} = N^0_{PlEl}\left[\exp\left(\frac{\alpha^a_{PlEl}F}{R\ T}\left(\eta_{\text{PlEl}} + \eta_{\text{dis}}\right)\right) - \exp\left(-\frac{\alpha^c_{PlEl}F}{R\ T}\eta_{\text{PlEl}}\right)\right] \tag{2.76}$$

$$N_{\text{SoPl}} = N^0_{SoPl}\left[\exp\left(\frac{\alpha^a_{SoPl}F}{R\ T}\eta_{\text{SoPl}}\right) - \exp\left(-\frac{\alpha^c_{SoPl}F}{R\ T}\left(\eta_{\text{SoPl}} - \eta_{\text{dis}}\right)\right)\right] \tag{2.77}$$

The impact of the dissolution on the deposition reaction should vanish when a certain amount of adsorbed lithium is present. The overpotential due to the dissolution hindrance is less or equal to zero: $\eta_{\text{dis}} \leq 0$. In section 3.3.2 more information regarding the exact definition of the factor is given.

3. Implementation and numerics

This chapter revolves around the implementation of the introduced lithium plating model into the simulation framework BEST. Numerical approximations and solutions to numerical problems are also introduced and shown.

3.1. Modeling of lithium plating and stripping

The important reactions, potential dependencies and conservation equation of lithium plating and stripping were defined in the previous sections. In this section the inclusion of this process into the framework of the 3D transport model is described. The implementation into the framework BEST and investigation of the lithium plating model was done in two steps. Figure 3.1 illustrates the two different approaches. Due to the historical structure of the framework the plating and stripping model

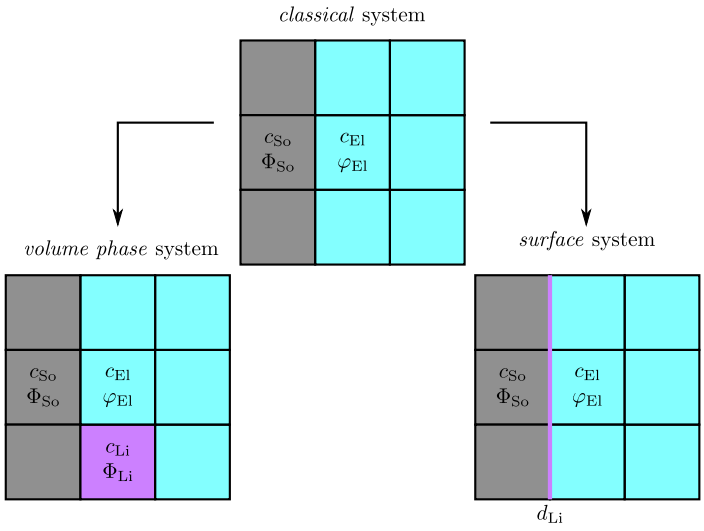

Figure 3.1.: The two different approaches to include lithium into the simulation framework. The *volume phase* approach describes a plated lithium phase via an additional volume phase inside the anode electrode, and the *surface* system allows for the definition of a plated lithium film as a pure surface species.

was first adopted as a dedicated volume phase (see section 3.1.1). This allowed for first investigations on the influence of a plated lithium phase on the battery performance and the electrochemical situation inside the battery. A further generalization of the framework BEST in cooperation with the ITWM allowed for the definition of variables on the surface between two discretization volumes. This extension of the software framework enabled the implementation of the plating model as surface equation

(see section 3.1.2). The simulation of lithium plating and stripping became possible through this development.

3.1.1. Volume phase

As first approach the plating model was implemented as a volume phase model, where the plated lithium is represented as a dedicated volume inside the 3D battery microstructure. The MBE of the amount of plated lithium is set as the governing equation of the volume phase. The volume phase model describes an additional phase inside the anode microstructure which represents a metallic lithium phase. This lithium phase allows for lithium dissolution into the electrolyte. The additional phase is included into the cell geometry as sketched in the lower left of fig. 3.1. The two reversible reactions are set as interface conditions for the lithium flux $\boldsymbol{N}_\mathrm{i}$ at their respective interfaces. The chemical intercalation is taking place between the anode phase (grey in fig. 3.1) and the plated lithium phase (purple in fig. 3.1). And the plating reaction is active at the interface between plated lithium phase (purple in fig. 3.1) and the electrolyte (light blue in fig. 3.1). The electrical potential is assumed to be continuous between the electrode and the plated lithium and is hence represented by a continuous flux boundary. The lithium flux $\boldsymbol{N}_\mathrm{i}$ at that interface is given through the chemical intercalation. At the interface between the plated lithium and the electrolyte, the current density has the plating current as boundary condition. The interface conditions are listed in the following equations in the shape of the ideal lithium-ion battery (see eq. (2.13)):

$$\boldsymbol{j}_\mathrm{Pl} \cdot \boldsymbol{n}_\mathrm{Pl-El} = \boldsymbol{j}_\mathrm{El} \cdot \boldsymbol{n}_\mathrm{Pl-El} \quad = j_\mathrm{Pl/St} \tag{3.1}$$

$$\boldsymbol{N}_\mathrm{Pl} \cdot \boldsymbol{n}_\mathrm{Pl-El} = \boldsymbol{N}_\mathrm{El} \cdot \boldsymbol{n}_\mathrm{Pl-El} = N_\mathrm{Pl/St} \tag{3.2}$$

$$\boldsymbol{j}_\mathrm{So} \cdot \boldsymbol{n}_\mathrm{So-Pl} = \boldsymbol{j}_\mathrm{Pl} \cdot \boldsymbol{n}_\mathrm{So-Pl} \quad = -\sigma_\mathrm{So,Pl} \boldsymbol{\nabla} \phi_\mathrm{So,Pl} \tag{3.3}$$

$$\boldsymbol{N}_\mathrm{So} \cdot \boldsymbol{n}_\mathrm{So-Pl} = \boldsymbol{N}_\mathrm{Pl} \cdot \boldsymbol{n}_\mathrm{So-Pl} = N_\mathrm{Ch.Int.} \tag{3.4}$$

This model was applied to a half-cell geometry to investigate the influence of a present plated lithium phase on the electrochemical situation. This was published in the journal *Electrochimica acta* [12]. The study is included in this thesis. The different simulations are described in section 4.2.3 and the results are discussed in different parts of chapter 5.

3.1.2. Surface growth

The disadvantage of the volume phase model is, that the simulation of plating is only possible, if a dedicated phase for the plated lithium is already defined before the simulation is started. Hence, one can not investigate at which locations and how plated lithium would form. This dedicated phase can only be used as plated lithium storage and not as active material. Conversely, during stripping simulations the lithium phase acts as passivated active material as soon as the lithium is fully dissolved. A different approach to lithium plating and stripping was therefor needed. The simulation framework could initially only solve for unknowns in the volume discretization. It was extended to allow for unknowns to exist

on the interfaces between the discretization volumes. These unknowns represent quantities without a spatial dimension. This extension allowed for a new implementation of a lithium growth process.

The amount of plated lithium n_{Pl} was selected as new surface variable. The governing equation of the surface system is eq. (2.73). During the plating process a switch from direct intercalation towards pure lithium plating can take place. Therefor the interface conditions between the electrolyte and the anode need to be adjusted. In fig. 3.2 the different reactions and their respective active surfaces are illustrated. The lithium ions in the electrolyte can either react along the plating reaction $r_{\mathrm{Pl/St}}$ or along the direct

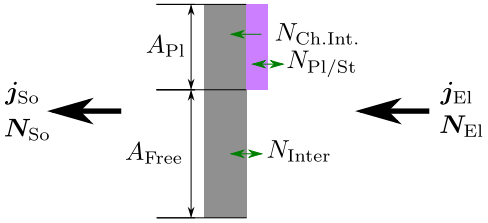

Figure 3.2.: The condition at the interface between anode and electrolyte while part of the surface is covered with plated lithium. The three reactions at the interface are indicated through green arrows.

intercalation reaction r_{Inter}. The new interface conditions will be developed in the following for the case of lithium ion flux from the electrolyte into the solid phase. The total flux of lithium ions out of the electrolyte can be obtained from an integration over the surface. This results in the following relation:

$$N_{\mathrm{El}}\Big|_{@\ \mathrm{So\text{-}El}} = \left(A_{\mathrm{Pl}} \cdot N_{\mathrm{Pl/St}} + A_{\mathrm{Free}} \cdot N_{\mathrm{Inter}}\right) \cdot A_{\mathrm{Total}}^{-1} \tag{3.5}$$

The charge flowing out of the electrolyte $J_{\mathrm{El}}\Big|_{@\ \mathrm{So\text{-}El}}$ results directly from $N_{\mathrm{El}}\Big|_{@\ \mathrm{So\text{-}El}}$, since both reactions are charge-transfer reactions:

$$J_{\mathrm{El}}\Big|_{@\ \mathrm{So\text{-}El}} = N_{\mathrm{El}}\Big|_{@\ \mathrm{So\text{-}El}} \cdot F \tag{3.6}$$

The sources of lithium ions in the solid phase are the direct intercalation N_{Inter} and the chemical intercalation $N_{\mathrm{Ch.Int.}}$.

$$N_{\mathrm{So}}\Big|_{@\ \mathrm{So\text{-}El}} = \left(A_{\mathrm{Pl}} \cdot N_{\mathrm{Ch.Int.}} + A_{\mathrm{Free}} \cdot N_{\mathrm{Inter}}\right) \cdot A_{\mathrm{Total}}^{-1} \tag{3.7}$$

The chemical intercalation leads to no net charge transfer from the plated lithium into the anode. Hence the charge flowing into the solid phase result to be

$$F_{\mathrm{So}}\Big|_{@\ \mathrm{So\text{-}El}} = \left(A_{\mathrm{Pl}} \cdot j_{\mathrm{Pl/St}} + A_{\mathrm{Free}} \cdot j_{\mathrm{Inter}}\right) \cdot A_{\mathrm{Total}}^{-1} \tag{3.8}$$

The relations developed above are also valid for the inverse flow of lithium ions. These relations can be expressed as interface conditions for the current flux density $\boldsymbol{j}_\mathrm{i}$ and lithium flux density $\boldsymbol{N}_\mathrm{i}$:

$$\boldsymbol{j}_\mathrm{El}\Big|_{@\ \mathrm{So\text{-}El}} = \Theta_\mathrm{A}^\mathrm{Pl} \cdot j_\mathrm{Pl/St} \quad + \left(1 - \Theta_\mathrm{A}^\mathrm{Pl}\right) \cdot j_\mathrm{Inter} \tag{IC-J-El}$$

$$\boldsymbol{N}_\mathrm{El}\Big|_{@\ \mathrm{So\text{-}El}} = \Theta_\mathrm{A}^\mathrm{Pl} \cdot N_\mathrm{Pl/St} \quad + \left(1 - \Theta_\mathrm{A}^\mathrm{Pl}\right) \cdot N_\mathrm{Inter} \tag{IC-N-El}$$

$$\boldsymbol{j}_\mathrm{So}\Big|_{@\ \mathrm{So\text{-}El}} = \Theta_\mathrm{A}^\mathrm{Pl} \cdot j_\mathrm{Pl/St} \quad + \left(1 - \Theta_\mathrm{A}^\mathrm{Pl}\right) \cdot j_\mathrm{Inter} \tag{IC-J-So}$$

$$\boldsymbol{N}_\mathrm{So}\Big|_{@\ \mathrm{So\text{-}El}} = \Theta_\mathrm{A}^\mathrm{Pl} \cdot N_\mathrm{Ch.Int.} + \left(1 - \Theta_\mathrm{A}^\mathrm{Pl}\right) \cdot N_\mathrm{Inter} \tag{IC-N-So}$$

with $\Theta_\mathrm{A}^\mathrm{Pl} = \frac{A_\mathrm{Pl}}{A_\mathrm{Total}}$ and $\Theta_\mathrm{A}^\mathrm{Free} = 1 - \Theta_\mathrm{A}^\mathrm{Pl}$. As long as only part of the surface area is plated ($\Theta_\mathrm{A}^\mathrm{Pl} < 1$) lithium ions can still intercalate or deintercalate from the supporting electrode.

The area covered by one lithium atom is estimated as follows. We assume, that a block of lithium metal is made out of cubic lithium atoms. The lithium metal has a molar mass of $M_\mathrm{Li} = 6.94$ [102] and a density of $\rho_\mathrm{Li} \approx 0.534\,\mathrm{g/cm^3}$ [103]. The lithium concentration in lithium metal is therefore $c_\mathrm{Li} = \rho_\mathrm{Li}/M_\mathrm{Li} = 0.076945\,\mathrm{mol/cm^3}$. The number of lithium atoms in a volume of $1\,\mathrm{cm^3}$ is

$$N_\mathrm{Li} = 0.076945\,\mathrm{mol} \cdot N_\mathrm{A} \approx 4.634 \cdot 10^{22} \tag{3.9}$$

The side length of one atom is hence:

$$d_\mathrm{Li} = \frac{1\,\mathrm{cm}}{\sqrt[3]{N_\mathrm{Li}}} = 2.784 \times 10^{-10}\,\mathrm{m} \tag{3.10}$$

and the surface area covered by one lithium atom:

$$a_\mathrm{Li} = d_\mathrm{Li}^2 \tag{3.11}$$

The simulation conducted with the surface plating system are described in section 4.2.4.

3.2. Discretization and numerical solution

In this section a short overview of the discretization process and the calculation of the numerical solution used in BEST is given. The more detailed intermediate steps are shown in appendix A. The transport model was implemented by the Fraunhofer-Institut für Techno-und Wirtschaftsmathematik (ITWM) using finite-volume discretization. The resulting modeling framework is called Battery and Electrochemical Simulation Tool (BEST) [6]. The principle of the finite-volume discretization used in BEST is illustrated solely on a mass balance equation in the shape of eq. (2.5). The mass balance of the concentration c is defined using the lithium flux $\boldsymbol{N} = -D\boldsymbol{\nabla} c$:

$$0 = \frac{\partial\, c}{\partial\, t} - \boldsymbol{\nabla} \boldsymbol{N} \tag{3.12}$$

This equation is defined on a 1D domain Ω, which consist of two different subdomains Ω_1 and Ω_2. The main domain is discretized by cell centered finite volumes: The spatial domain Ω is divided into a polygonal mesh ($\Omega = \Sigma_{i=1}^{N} e_i$) with each cell e_i being a polyhedron. In fig. 3.3 the discretization of the simple 1D domain is shown. The different terms used to describe the discretization process are shown explanatory in this figure. The two subdomains are split into several discretization volumes, where

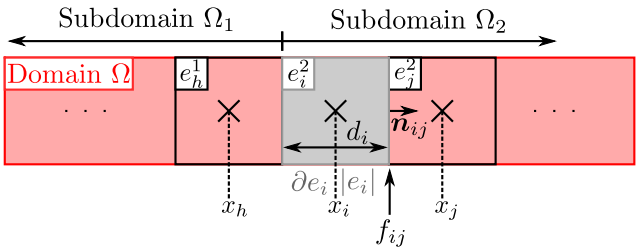

Figure 3.3.: Cell centered finite volumes for a simple 1D domain Ω (red). The cell e_i^2 (grey) is specified by the center x_i, the outer surface ∂e_i and the volume $|e_i|$. The interface between neighboring cells (e.g. e_i^2 and e_j^2) is denoted by f_{ij} with the surface normal $\boldsymbol{n}_{ij}$.

e_n^p indicates a nth volume in the subdomain p. In fig. 3.3 e_h^1 is part of the domain Ω_1 and e_j^2, e_j^2 in Ω_2. The discretization cell e_i is described by the center x_i, the thickness in one direction d_i, the outer surface ∂e_i and the volume $|e_i|$. The interface area between cell e_i and a neighboring cell e_j is named f_{ij} and has a surface normal $\boldsymbol{n}_{ij}$, which points from i into j.

The mass balance equation (eq. (3.12)) is integrated over the volume of a cell e_i and the time t:

$$0 = \int_{t_n}^{t_{n+1}} \int_{e_i} \left[\frac{\partial\, c}{\partial\, t} + \boldsymbol{\nabla} \boldsymbol{N} \right] dx\ dt \tag{3.13}$$

Using the divergence theorem, a backward Euler method and the interface conditions between the subdomains (see Eq. 2.13) we obtain the following expression:

$$0 = |e_i| \frac{C(x_i) - c(x_i)}{\Delta t} - \sum_{j \in \Omega_2}^{\text{same D.}} f_{ij} \cdot D_{\frac{i+j}{2}} \frac{c(x_j, t) - c(x_i, t)}{x_j - x_i} + \sum_{h \in \Omega_1}^{\text{dif. D.}} f_{ih} \cdot \mathcal{N}\left(c_h, c_i\right) \tag{3.14}$$

This equation represents the fully discretized system $\boldsymbol{F}$. The system is influenced by the strong nonlinear nature of the system and hence a linearization is applied to the system. The system $\boldsymbol{F}$ is extended using the first order of the Taylor series around the point $\boldsymbol{x}_0$:

$$\boldsymbol{F}(\boldsymbol{x}) \approx \boldsymbol{F}(\boldsymbol{x}_0) + \boldsymbol{J}(\boldsymbol{x}_0) \cdot (\boldsymbol{x} - \boldsymbol{x}_0) \tag{3.15}$$

with $\boldsymbol{J}(\boldsymbol{x}_0)$ being the Jacobian matrix of the system $\boldsymbol{F}(\boldsymbol{x}) = (f_1, ..., f_n)$ with the unknowns $\boldsymbol{x} = (x_1, ..., x_n)$. The Jacobian matrix is defined as:

$$\boldsymbol{J} = \frac{d\, \boldsymbol{F}}{d\, \boldsymbol{x}} = \left[\frac{\partial\, \boldsymbol{F}}{\partial\, x_1} \ ... \ \frac{\partial\, \boldsymbol{F}}{\partial\, x_n} \right] = \begin{pmatrix} \frac{\partial\, F_1}{\partial\, x_1} & \cdots & \frac{\partial\, F_1}{\partial\, x_n} \\ \vdots & \ddots & \vdots \\ \frac{\partial\, F_n}{\partial\, x_1} & \cdots & \frac{\partial\, F_n}{\partial\, x_n} \end{pmatrix} \tag{3.16}$$

The next step is the determination of the solution. Newton's method [104] is applied to find the root of the algebraic equations. In general the initial values for the unknowns $\boldsymbol{x}_0$ do not fulfill the system. Hence the iterative Newton's method is used. The next solution $\boldsymbol{x}_1$ is calculated to satisfy the following equation:

$$\boldsymbol{F}(\boldsymbol{x}_0) + \boldsymbol{J}(\boldsymbol{x}_0) \cdot (\boldsymbol{x}_1 - \boldsymbol{x}_0) = 0 \tag{3.17}$$

This equation can be solved by obtaining the inverse of the Jacobian matrix, which is a computational very expensive step [105]. Instead one can gain a valid solution through calculation of the root for the following linear equation:

$$\boldsymbol{J}(\boldsymbol{x}_0)\,\Delta\boldsymbol{x} = -\boldsymbol{F}(\boldsymbol{x}_0) \tag{3.18}$$

In this case the Jacobian matrix $\boldsymbol{J}(\boldsymbol{x}_0)$ and the vector $-\boldsymbol{F}(\boldsymbol{x}_0)$ are known. With the result of the Newton iteration $\Delta\boldsymbol{x}$ one can estimate the solution via

$$\boldsymbol{x}_1 = \boldsymbol{x}_0 + \Delta\boldsymbol{x}\,. \tag{3.19}$$

The accuracy of the solution $\boldsymbol{x}_1$ is checked for acceptance. Should the result for the values $\boldsymbol{x}_1$ not satisfy the accuracy need, one repeats the Newton iteration with $\boldsymbol{x}_i = \boldsymbol{x}_{i-1}$ until a suitable result is obtained. This iterative process is illustrated in the red box of fig. 3.4(a). To obtain a time transient solution for a given system the accepted result of the Newton iterations is used as basis for a new solution after increasing the time of the system. In fig. 3.4(a) the general flow diagram for the solution of the *classical* system is shown. After setting all concentrations to their initial values, the pure potential system is solved to obtain a consistent potential distribution. Now the transient simulation starts with the first time step. Every time step follows the same rule: Solve eq. (3.18) and test the result for convergence according to selected accuracy. After success increase the time and repeated until target time is reached. In the simulation framework BEST two different checks are used to test if the numerical solution of a system is acceptable: The relative difference in the norm of the solution $\Delta\boldsymbol{x}_{j+i}$ to the norm of the previous iteration $\frac{|\Delta\boldsymbol{x}_{j+1}|}{|\boldsymbol{x}_j|}$ and the absolute norm $|\boldsymbol{F}(\boldsymbol{x}_{j+1})|$ of the system $\boldsymbol{F}$. The norm is calculated via the quadratic norm $|\boldsymbol{v}| = \sqrt{\sum_{i=1}^{N} v_i^2}$. The relative solution tolerance is set to at least 10^{-8}.

3.3. Approaches to numerical challenges

Important challenges are the boundaries of the open circuit voltage, the vanishing of a species and the spanning of multiple orders of magnitude for different equations and unknowns. All these problems have impact on the numerical stability of the solution process, thus leading to an increase in Newton iterations or resulting in an earlier stop of the simulation. In this section the different methods used to overcome or dampen their impact are introduced.

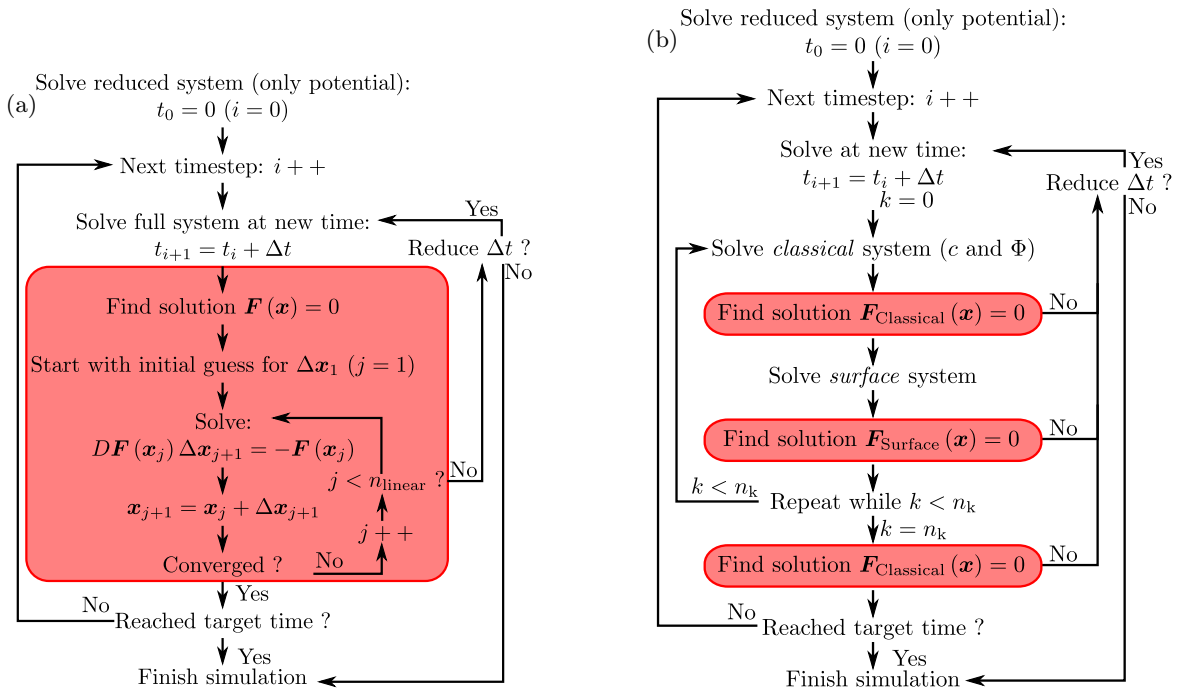

Figure 3.4.: (a) Flow diagram for the *classical* and coupled surface system. (b) Flow diagram for the decoupled surface system.

3.3.1. Modification of open-circuit voltage

To ensure a better divergence close to fully lithiated artificial graphite the second hyperbolic tangent in the OCV (eq. (2.26)) was replaced with a slightly modified hyperbolic tangent (eq. (3.21)).

$$\begin{aligned} ocv_{\text{Graphite}}(x) = {} & 0.6379 + 0.5416 \cdot \exp(-305.5309 \cdot x) + 0.044 \cdot \tanh\left(-\frac{x - 0.1958}{0.1088}\right) \\ & - 0.1978 \cdot \tanh_{\text{mod}}\left(\frac{soc - 0.99}{0.05}\right) - 0.6875 \cdot \tanh\left(\frac{soc + 0.0117}{0.0529}\right) \\ & - 0.0175 \cdot \tanh\left(\frac{soc - 0.5692}{0.0875}\right) \end{aligned} \tag{3.20}$$

$$\tanh_{\text{mod}}(x) = \frac{\exp(20 \cdot x) - \exp(-x)}{2 \cdot \cosh(x)} \tag{3.21}$$

The parameters in the modified hyperbolic tangent were chosen in such a way, that the deviation between the original OCV and the modified OCV is minimal for a state of charge lower than 95 %. In fig. 3.5 the two different OCVs are plotted. The inset shows that the deviation between the modified and the original open-circuit potential is larger than 0.1 V for a state of charge larger than 98 %. The modified OCV reaches zero potential with respect to zero close to 98.1 % state of charge.

3.3.2. Approximation of vanishing species/phase

A new challenge for the simulation of lithium plating and stripping is the fact, that the lithium phase is not always existing and most of the theoretical description is done with non-depleting phases and

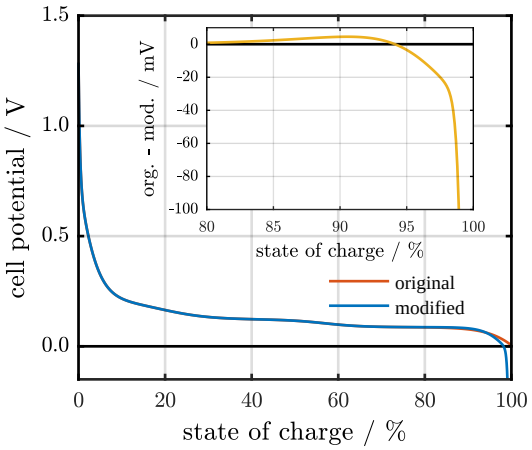

Figure 3.5.: The open-circuit voltage of artificial graphite is slightly modified to increase the divergence behavior close to maximal lithiated graphite. The original and modified OCV are compared.

non-vanishing species. The Butler-Volmer and similar interface current expressions are derived under the assumptions of non-depleting phases. Hence the exchange current expression in eq. (2.52) is only valid, if the reaction does not lead to the vanishing of the phase. The complete consumption of one of the phases involved in the electrochemical processes requires additional considerations. The plated lithium phase exists on the surface of the anode electrode. The occurrence and vanishing of a new phase at the interface between two other phases can be described through nucleation theory [106]. In this work the overpotential of the dissolution part of a reaction is modified. This reaction part, which corresponds to a positive lithium flux, is extended by a dissolution overpotential η_{dis}.

$$N_{\text{PlEl}} = N^0_{PlEl}\left[\exp\left(\frac{\alpha^a_{PlEl}F}{R\,T}\left(\eta_{\text{PlEl}}+\eta_{\text{dis}}\right)\right)-\exp\left(-\frac{\alpha^c_{PlEl}F}{R\,T}\eta_{\text{PlEl}}\right)\right] \tag{3.22}$$

$$N_{\text{SoPl}} = N^0_{SoPl}\left[\exp\left(\frac{\alpha^a_{SoPl}F}{R\,T}\eta_{\text{SoPl}}\right)-\exp\left(-\frac{\alpha^c_{SoPl}F}{R\,T}\left(\eta_{\text{SoPl}}-\eta_{\text{dis}}\right)\right)\right] \tag{3.23}$$

The energy barrier of the dissolution η_{dis} will increase for vanishing amount of plated lithium. And it should approach zero above a critical surface coverage. A process, which is switched off at a certain point, can be described mathematically by the Heaviside step function $H\left(x\right)$ (eq. (3.24)). This function is zero below a limit and one otherwise.

$$H\left(x,x_0\right) = \begin{cases} 0, x < x_0 \\ 1, \text{otherwise} \end{cases} \tag{3.24}$$

Adopting this function $H\left(x,x_0\right)$ for $f\left(d_{\text{Li}},d_0\right)$ in eq. (2.73) introduces a singularity into the equation system. If the lithium thickness d_{Li} vanishes while solving the equation system, numerical instabilities occur, which can prevent a further computation. A regularization technique of singularities in source terms is applied to prevent or at least minimize the influence on the numerical stability [107]. Instead

of the Heaviside step function, a numerically stable choice was found to be

$$f\left(d, d_0\right) = \frac{d^4}{d_0^4 + d^4} \tag{3.25}$$

The constant value d_0 defines the smoothness of the step from zero to one. The shape of the energy barrier was therefor selected as follows

$$\eta_{\mathrm{dis}} = k \cdot \ln\left(\frac{d_{\mathrm{Pl}}^4}{d_{\mathrm{Pl},0}4 + d_{\mathrm{Pl}}4}\right) \tag{3.26}$$

Figure 3.6 shows the dissolution energy barrier with eq. (3.25) as a functional dependence on the amount of plated lithium. The constant value d_0 defines the location, were the factor η_{dis} reaches

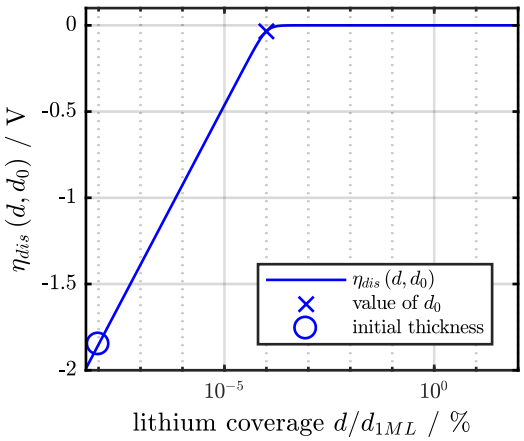

Figure 3.6.: The value of dissolution overpotential η_{dis} as a function of lithium coverage for $\alpha_{\mathrm{Pl/St}}^{\mathrm{a}} = 0.5$. The initial thickness $d_{\mathrm{Pl}}^{\mathrm{init}}$ and the constant value d_0 are highlighted.

$k \ln\left(\frac{1}{2}\right)$. Zero is approximately reached at $d_{\mathrm{Pl}} \approx 10 \times d_0$. Under consideration of increased runtime with smaller d_0-values and impact on the lithium thickness and plating onset, the constant value is set to $d_0 = 10^{-6}$ in this work. In section 5.4.1 the result of the sensitivity analysis are given. The plated lithium phase is approximated as vanished for a d_0-value below the coverage of 10^{-5} or 0.001%.

3.3.3. Scaling of plating conservation equation

In the implementation of the classical system, the concentrations and the potentials are represented by numerical variables. The potentials are given in the unit V and are therefore usually in the range of $-0.2\,\mathrm{V}$ till $5\,\mathrm{V}$. The lithium concentration is internally handled in $\mathrm{mol/cm^3}$ and thus is roughly in the range of $0.001\,\mathrm{mol/cm^3}$ (electrolyte concentration) till $0.03\,\mathrm{mol/cm^3}$ (fully lithiated solid). The plating system is represented by the amount of substance of the plated lithium n_{Pl}. The thickness of plated lithium is expected to be in the range of nm to μm. The surface of a discretization volume is around $1\,\mu\mathrm{m}^2$. Therefore the amount of lithium in a film of a thickness of 100 nm is roughly $7.7 \cdot 10^{-15}\,\mathrm{mol}$. As explained earlier, the acceptance of the numerical solution is based on the norm of the system $|\boldsymbol{F}\left(\boldsymbol{x}_{j+1}\right)|$ or the norm of the difference of the solution $\frac{|\Delta \boldsymbol{x}_{j+1}|}{|\boldsymbol{x}_j|}$. Obtaining an accurate solution for the

surface system is therefor limited, if the values of the different unknowns span a large range. A common approach is scaling different variables of a numerical system into the same value range [108]. Here we use a simple approach to scale the plating model (see section 2.5.6). In this section the transformation used for the implementation of the plating model is introduced. The plated lithium can only cover as much area as is available, hence there exists an upper limit for the covered area A_{Pl}:

$$A_{\mathrm{Pl}} \in [0, A_{\mathrm{Total}}] \tag{3.27}$$

This can be transformed into the range between zero and one by dividing the plated area by the total area:

$$\Theta_{\mathrm{A}}^{\mathrm{Pl}} = \frac{A_{\mathrm{Pl}}}{A_{\mathrm{Total}}} \in [0, 1] \tag{3.28}$$

The term $\Theta_{\mathrm{A}}^{\mathrm{Pl}}$ describes the fraction of the surface area plated by lithium, or short *plated area fraction*. The amount of plated lithium, on the other side, has in general no upper limit:

$$n_{\mathrm{Pl}} \in [0, \infty[\tag{3.29}$$

Similar to the plated area a reference for the amount of plated lithium is defined. As reference the amount of lithium in a monolayer thick film is selected $n_{\mathrm{Pl}}^{\mathrm{1ML}}$:

$$n_{\mathrm{Pl}}^{\mathrm{1ML}} = A_{\mathrm{Total}} \cdot d_{\mathrm{Li}} \cdot c_{\mathrm{Li}} \tag{3.30}$$

The amount of plated lithium n_{Pl} can then be transformed to the dimensionless quantity $\Theta_{\mathrm{n}}^{\mathrm{Pl}}$ with

$$\Theta_{\mathrm{n}}^{\mathrm{Pl}} = \frac{n_{\mathrm{Pl}}}{n_{\mathrm{Pl}}^{\mathrm{Ref}}} = \frac{n_{\mathrm{Pl}}}{n_{\mathrm{Pl}}^{\mathrm{1ML}}} \tag{3.31}$$

With this definition the mass balance equation for the amount of plated lithium (eq. (2.73)) can be rewritten

$$\frac{\partial\, \Theta_{\mathrm{n}}^{\mathrm{Pl}}}{\partial\, t} = \left(N_{\mathrm{Ch.Int.}} - N_{\mathrm{Pl/St}}\right) \cdot A_{\mathrm{Pl}} \cdot \frac{1}{F \cdot A_{\mathrm{Total}} \cdot d_{\mathrm{Li}} \cdot c_{\mathrm{Li}}} \tag{3.32}$$

$$= \left(N_{\mathrm{Ch.Int.}} - N_{\mathrm{Pl/St}}\right) \cdot \Theta_{\mathrm{A}}^{\mathrm{Pl}} \cdot \frac{1}{F \cdot d_{\mathrm{Li}} \cdot c_{\mathrm{Li}}} \tag{3.33}$$

The resulting equation above is implemented in the framework BEST and used for the electrochemical simulations.

3.3.4. Inclusion of surface unknowns: Coupled and decoupled system

The way BEST obtains the numerical solution to a given differential equation systems allows for two different implementations of the plating model as surface equation. Either the new system, consisting of lithium concentration in the electrolyte and electrodes, potential in the electrolyte and the electrodes and the amount of plated lithium, is solved simultaneously by inclusion of surface unknowns in the same

Jacobian matrix as the concentrations and potentials (see section 3.2) or the concentration-potential system (called *classical* system in this work) and the *plating* system (represented by the eq. (2.73)) are solved with separate Jacobi matrices. In the later case the amount of plated lithium n_{Pl} is set constant for the solution of the classical system and the concentration and potential constant for the solution of the plating system. The first case is named *coupled system* and the second case *decoupled system* in this work. The different steps for obtaining a numerical solution of these systems are shown in fig. 3.4(a) and fig. 3.4(b). The approach of decoupling one variable from the others is used in the framework BEST for the thermal battery model. There the temperature is solved sequentially after the concentration-potential-system.

4. Simulation setup and parameters

The electrochemical simulations in the framework BEST need material parameters such as the diffusion coefficient D_{El} and the microstructures of the electrodes. In this chapter the different sources of microstructures, the used electrochemical parameters and the different simulations presented in this work are listed.

4.1. Microstructures

One can obtain 3D microstructures using two ways: Either one measures the microstructures via different tomography methods or constructs geometries on a computer using model based or random generators. X-ray tomography [9, 109] and FIB-SEM [110] are the most used experimentally methods. The resulting microstructure data will be called *real* microstructure in this work. *Virtual* microstructures are often constructed through random distribution of particles (e.g. using GeoDict [111]). Recently stochastic models for generation of microstructures were applied to lithium-ion batteries [10].

4.1.1. Cathode - based on literature

The microstructure of the cathode material used for the full-cell investigations is based on the open-data of Ebner *et al.* [9]. The cathode materials investigated by Ebner *et al.* are $\mathrm{LiNi_{1/3}Mn_{1/3}Co_{1/3}O_2}$ (NMC)-based cathodes. These show similar particle sizes and distribution as lithium maganese oxide (LMO). Without any other sources for cathode tomography data, these microstructures are adopted for the material LMO. This approximation is motivated due to the similar particle size distribution of LMO and NMC. The particle size distribution for LMO was measured by the Japanese precision instrument manufacture [112] and is compared to the particle size distribution of NMC [9] in fig. 4.1. Additionally, Park *et al.* [113] use a particle diameter of 10 µm and spherical particle shapes for simulation of stress in LMO. A spherical particle shape for LMO was also found by Huang *et al.* [114]. Hence, a microstructure representation is constructed on the basis of experimental tomographic image data [9]. The data set for 60 wt % and 600 bar is selected. The side of the microstructure, which is in contact with the current collector, is cut to a flat surface. The cut position is chosen such, that the solid volume fraction of the resulting surface is close to the average solid volume fraction of the electrode bulk. In fig. 4.2 the resulting 3D structure is shown. A major challenge of cathode materials used in lithium-ion batteries is their relatively low electronic conductivity. Hence conductive agents, usually a carbon based materials, are added during electrode production. This additional materials are smaller in size than the cathode

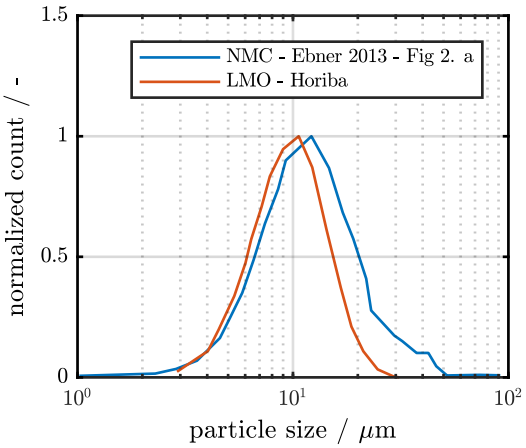

Figure 4.1.: The particle size distribution of LMO (extracted from [112]) and NMC (extracted from [9]) show quite similar mean particle sizes and a similar distribution.

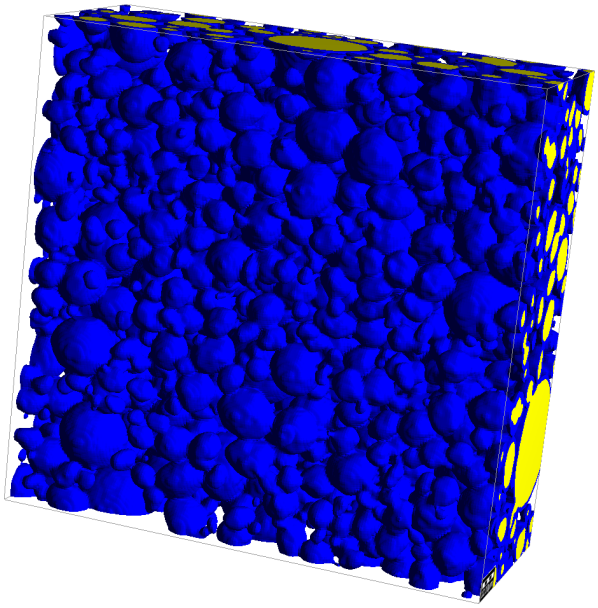

Figure 4.2.: The microstructure used for the LMO-cathode as obtained from [9]. The interface between electrolyte and active material is identified with an additional phase (blue) to allow for an effective conductivity as a result of the conductive agent.

particles. The conductive agents are also not resolved in the tomography data due to the reduced sensitivity with respect to carbon based materials. The combination of EDX with FIB-SEM allows to identify the carbon black and binder phases in the porous part of an electrode[115]. Their small size is beyond the resolution of the microstructures used for the electrochemical simulation. The extension of the simulation framework BEST to allow for a porous phase inside the electrolyte, which is electronic conductive, is ongoing work. To include the impact of carbon black on the cathode conductivity, the interface of the cathode with the electrolyte is therefor modified to represent a mixture of active material and conductive agent. This is done by using two phase identifiers, where the one on the interface between electrolyte phase and solid phase describes a cathode phase with effective conductivity. Ebner

et al. obtained the microstructure data for NMC through X-ray tomography using a synchrotron as radiation source. They published the results as open source in the supporting information [9].

4.1.2. Anode

Several different microstructures were used as negative electrode in the electrochemical simulations. They can be split into two groups: computer generated and experimentally obtained. At the start of this work, no microstructures based on real 3D image data were available. Hence, the first investigations were done using computer generated microstructure. As first basis a symmetric geometry (see section 4.1.2.1) was generated using the software GeoDict [111]. The electrochemical simulations revealed, that the region at the interface between the separator and the negative electrode is important for lithium plating. A microstructure with a surface closer to real microstructure surfaces was therefor created (see section 4.1.2.2). Through cooperations in the frame of a federally funded project (BMBF - MULTIBAT[116]), 3D image data of graphite electrodes became available (see section 4.1.2.3). This microstructures were used by a project partner to develop a stochastic microstructure model, which can generate random structures with similar structural parameters as the experimentally obtained microstructures [10]. The resulting microstructures (see section 4.1.2.4) and the real structures were checked for electrochemical similarity.

4.1.2.1. Symmetric electrode - GeoDict generated

The microstructure generation was done with GeoDict. The resulting microstructure is shown in fig. 4.3. The microstructure consists of particles with prismatic/planar polyhedrons as particle shape [12]. The

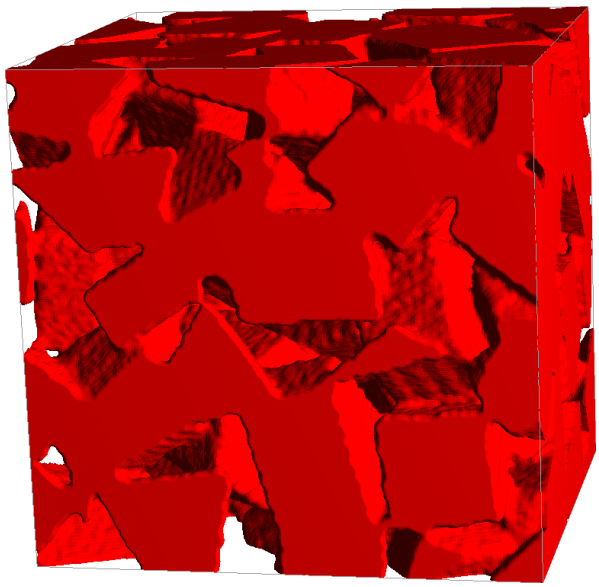

Figure 4.3.: The 3D representation of the symmetric microstructure. The dimensions are $180 \times 200 \times 200$ voxels with a size of $0.37\,\mu m$.

geometric parameters are listed in table 4.1. The target parameters are based on literature values. This

Table 4.1.: The resulting structure data of symmetric anode, used in [12].

Phase	Parameter	Value
Active material	Solid volume fraction	0.5311
	Particle size	20 µm
Binder	Solid volume fraction	0.0343 [a]
Conductive agent	Solid volume fraction	0.0346 [a]

a - attribute to the active material phase.

geometry was used to investigate the influence of operation conditions, like applied current or ambient temperature, on the plating condition.

4.1.2.2. Rough separator interface - GeoDict generated

In section 5.2 the anode-separator-interface is identified as crucial point regarding the first occurrence of plated lithium [12]. Optical experiments by Harris *et al.* [78] revealed that the graphite particles at the anode-separator-interface seem to lithiate inhomogeneous. This prompted the generation of a graphite microstructure, which has a non-flat anode-separator-interface. The resulting structure can be found in fig. 4.4. The structure is slightly thinner in through direction than the symmetric microstructure

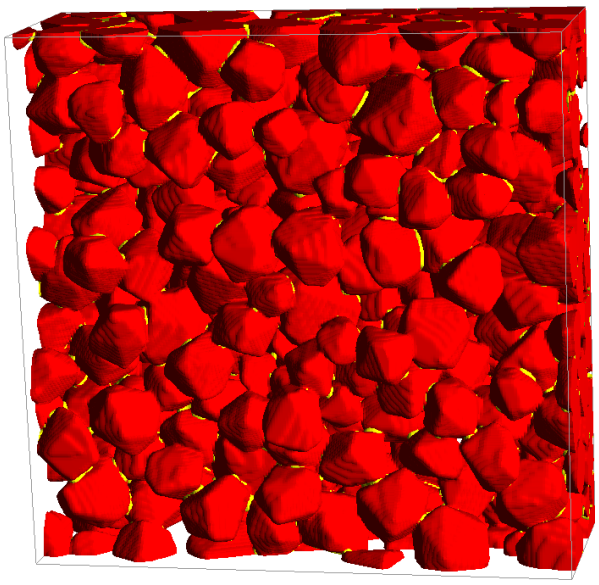

Figure 4.4.: The anode structure (red) with a rough separator interface and binder (yellow). The dimensions are $70 \times 200 \times 200$ voxels with a size of 0.74 µm.

(see fig. 4.3), but is larger in lateral size. The structure was generated using the "Pile"-function of the "SinterGeo"-module of the software GeoDict. Particles with a convex polyhedron shape are piled into a box from the separator-side with periodic boundaries in the lateral directions. The dimensions of these particles are based on experimental data (see table 4.2). The box was filled till the first particle hit the side where the particles are piled from. This resulted in a total solid volume fraction of 53.1 %. In fig. 4.5(a) the local and average solid volume fraction (SVF) along the through direction of the resulting geometry is shown.

Table 4.2.: Particle size used for the creation of a non-flat microstructure. As a distribution function a simple Gaussian was selected.

particle size	value
mean	20 µm
standard deviation	4 µm
size range	[10; 30] µm

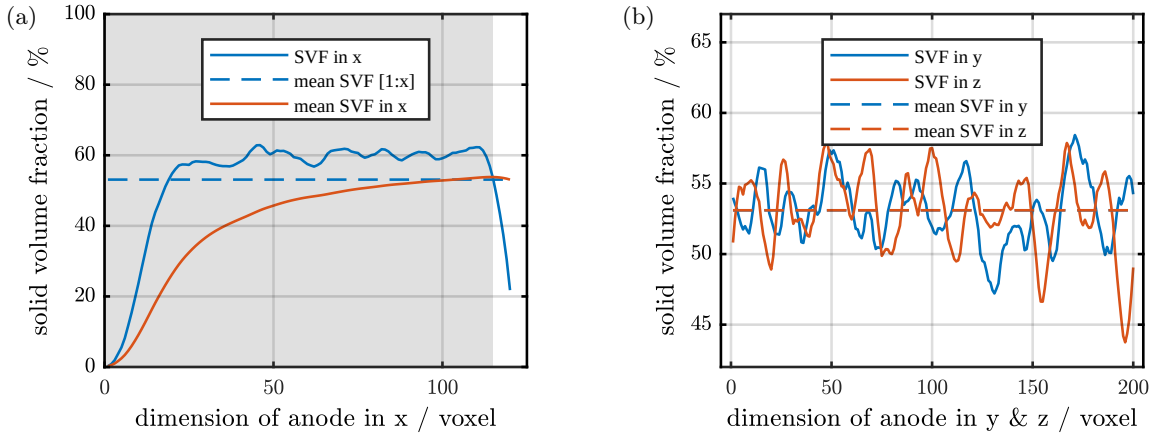

Figure 4.5.: (a) Solid volume fraction along the x-direction. The used part of the microstructure is marked with the grey box. (b) Local and average SVF along the lateral directions (y- and z-direction).

Along the lateral directions the local solid volume fractions vary around the mean SVF (see fig. 4.5(b)). The microstructure at the separator side has a rough surface with a decreasing number of particles towards the boundary. Thus, the existence of a single particle highly impacts the local solid volume fraction. Additionally to the rough separator surface a phase, which represents binder, was added to the microstructure. This additional phase allows to include electrochemical inactive regions in the electrochemical simulations. The binder was added using the Geodict-function "Add Binder" of the "ProcessGeo"-module with periodic boundaries in the lateral directions. The program GeoDict than adds the binder phase at contact regions and close regions between different particles. The binder phase is visible as yellow regions in fig. 4.4. The particle shape for this structure was changed from prismatic/planar polyhedrons to convex polyhedrons. The analysis of different SEM images of anode particles and input from experimentalists indicated, that this particle structure is more realistic.

4.1.2.3. Experimentally obtained

This PhD thesis was part of the BMBF project MULTIBAT [116], which had the development of a lithium plating theory, its implementation and numerical efficient simulations as topic. In this context a stochastic model was developed by a project partner [10], which is able to create different 3D microsturctures based on experimental structure data. The microstructure created through this model were compared to the real microstructures for electrochemical identity. The description of simulations

can be found in section 4.2.1. In fig. 4.6(a) a cut-out from the real structure data used for simulations is shown.

4.1.2.4. Stochastic microstructure model

The stochastic microstructure model [10] was implemented by Feinauer *et al.* as a java-tool, which can create random realizations with the structural parameters as obtained from the experimental data. In fig. 4.6(b) an exemplary microstructure produced with the java-tool is opposed to an experimentally obtained microstructure (see fig. 4.6(a)).

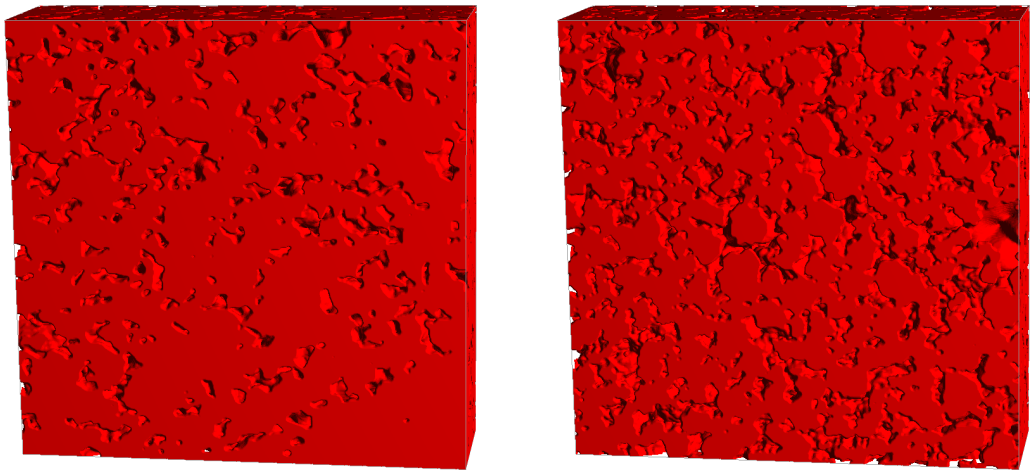

(a) Cut-out of real anode electrode obtained experimentally [117].

(b) Realization of microstructure obtained using 3D stochastic microstructure model [10]

Figure 4.6.: Two of the 3D microstructures used for the electrochemical validation of the 3D stochastic microstructure model with a base area of 400x400 voxels with 0.44 µm as voxel dimension.

4.2. Simulations

In this section the parameters and the setup of the different simulations in this work are listed.

4.2.1. Electrochemical validation of 3D stochastic microstructure model

One of the major drawbacks of 3D microstructure based electrochemical simulations is the need for spatially resolved microstruture data. This data is quite costly to obtain, since electrodes need to be produced, tested and then characterized. Each of these steps is time and cost extensive. Additionally, imaging methods have a low sensibility for some materials of interest and it is therefore hard to achieve the needed and wished resolution and image quality. Using microstructures model to describe the 3D morphology of electrochemical materials is a way to surmount this hindrance. For explanatory models see [118, 119, 120]. These models are parametrized using real tomographic image data. Afterwards they can be used as a tool to generate virtual structures without the need of experimental effort, such as

production of materials and electrodes in a laboratory. The variation of selected model parameters could allow for the creation of new and unique microstructures. In this section a already geometrically validated 3D stochastic microstructure model [10] is investigated regarding its electrochemical behavior using the electrochemical simulation framework. The virtual structures, generated from an implementation of the stochastic model, are compared to real structures, obtained from synchrotron x-ray tomography [117]. For more information about the 3D stochastic microstructure model the reader is referred to the references [10, 121]. The term *virtual* in this setting refers to the structures generated the stochastic model using a computer, while the term *real* microstructure refers to structural data obtained using x-ray tomography. In fig. 4.6 an example of a microstructure of the two different sources is shown. For the investigations a total of 20 structures of the same size of each source (virtual and real) are used as simulation domain.

The electrochemical parameters of the solids and the reactions used for the validation simulations are listed in table 4.3. The electrolyte parameters are listed in table 4.18. The initial conditions used for

Table 4.3.: Material and kinetic parameters used for the electrochemical validation simulations. [121]

	Graphite		Li metal	
Parameter/Unit	Value	Ref	Value	Ref
c_{max} / kmol/m^3	26.39	[122]		
σ / S/m	1000	[122, 123, 54][a,b]		
D_{So} /10^{-13} $\frac{\mathrm{m}^2}{\mathrm{s}}$	3.9	[122, 124]		
U_0 / V	$0.63 + ...$	[51]		
N^{00}_{Inter}/10^{-5} $\frac{\mathrm{Am}^{5/2}}{\mathrm{mol}^{3/2}}$	0.088	[54][c]		
N^{00}_{Plat} / $\frac{\mathrm{A}}{\mathrm{mol}^{1/2}\mathrm{m}^{1/2}}$			0.364	[125][b]
E^{D}_{act} / kJ/mol	53.1	[124]		
$E^{i_{00}}_{act}$ / kJ/mol	68	[126]	0	[d]
E^{σ}_{act} / kJ/mol	0	[a]		

[a] Conductivity too large to have effect on Φ, therefore assumed to be constant in T [b] Literature values vary, this value selected [c] estimated from literature for initial conditions [d] no temperature dependence needed, since simulation only at one temperature and counter electrode is identical for all simulations

the concentration and potential in the different phases are given in table 4.4.

Table 4.4.: Initial values of the concentration and potentials for the electrochemical validation simulations.

Parameter	Phase				
	CC Anode	Anode	Electrolyte	Counter electrode	CC CE
concentration	-	25.0705 kmol/m^3 [a] 13.195 kmol/m^3 [b]	1.200 mol/l	-	-
potential	Φ^0_{An}	$\Phi^0_{\mathrm{An}} = U_{0,\mathrm{An}}\left(c^0_{\mathrm{An}}\right)$	0	$\Phi^0_{\mathrm{Ca}} = 0$	Φ^0_{Ca}

[a] For full delithiation simulations (see fig. 4.8) [b] For short pulse high current simulations (see section 5.1)

The interfaces of the structures with the separator or current collector seem to be different for the real and virtual microstructures (see the large front in fig. 4.6). This becomes more obvious when one looks at the SVF along the through direction in fig. 4.7. The real microstructures have a slightly higher

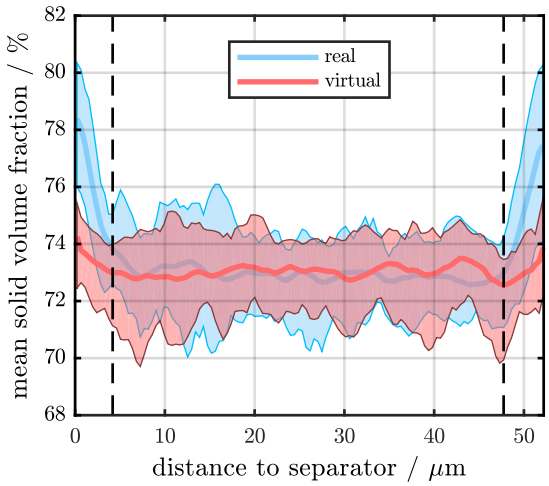

Figure 4.7.: Comparison of solid volume fraction (based on [121]). The SVF along the through direction is average over the 20 different cut-outs for each of the structure sources.

volume fraction close to the separator and current collector interface. This is due to the production process of the electrode layers and the involved pressing of the electrode sheets. This feature is so far not represented by the 3D stochastic microstructure model. The geometrical parameters of the non-voxelized structures are taken from [10] and are listed in table 4.5 for referencing. Geometrical

Table 4.5.: Geometrical parameters of the real and virtual microstructures (taken from [10]).

	Real	Virtual
Volume fraction	0.734	0.732
Specific surface area (voxel^{-1})	303842.2	299305
Mean tortuosity of pore space	1.577	1.569

parameters of the real and virtual electrodes are calculated for the voxelized (see table 4.5) and a smooth representation (see table 4.6) of the same structures. The surface area exhibits a different trend for the voxelized structures compared to the smooth structures.

Table 4.6.: Statistics of surface area and solid volume for the real and virtual microstructures obtained from the voxelized datasets. (reprinted with permission from [121])

quantity	type	mean	std	unit
surface area	real	7.72	0.34	$\times 10^{-7}\,\mathrm{m}^2$
	vir	7.80	0.40	$\times 10^{-7}\,\mathrm{m}^2$
solid volume	real	1.190	0.013	$\times 10^{-12}\,\mathrm{m}^3$
	vir	1.185	0.005	$\times 10^{-12}\,\mathrm{m}^3$
electrolyte volume	real	0.704	0.013	$\times 10^{-12}\,\mathrm{m}^3$
	vir	0.710	0.005	$\times 10^{-12}\,\mathrm{m}^3$

These deviations are a result of the voxelization process, which converts smooth geometries into structures consisting of cubic voxels. Additionally to the geometrical parameters the effective diffusion coefficient D_{eff} and the effective conductivity σ_{eff} in through-direction were calculated for the full through-direction and the region without the outer 10 voxels using the software GeoDict [111]. The results of the diffusion calculations are listed in table 4.7.

Table 4.7.: Statistics of effective diffusion coefficient and effective conductivity for the real and virtual microstructures in throught direction obtained from the voxelized datasets. The thinner microstructures are the one, which are reduced by 10 voxels on each side in through direction. (reprinted with permission from [121])

quantity	type	mean (std)	
		complete microstructures	thinner microstructures
effective diffusion coefficient	real	0.0644 (0.0049)	0.0697 (0.0037)
	virt	0.0788 (0.0065)	0.0713 (0.0058)
effective conductivity	real	46.1 (2.9)	45.3 (2.8)
	virt	48.3 (0.7)	48.0 (0.9)

First tests of the two different sources were done using a constant current delithiation. The delithiation starts at a state of charge of 95 % and is done using a constant current of 20 $\mathrm{A/m^2}$. The resulting cell potentials of the real and virtual microstructures are plotted in fig. 4.8. The cell potentials are quite

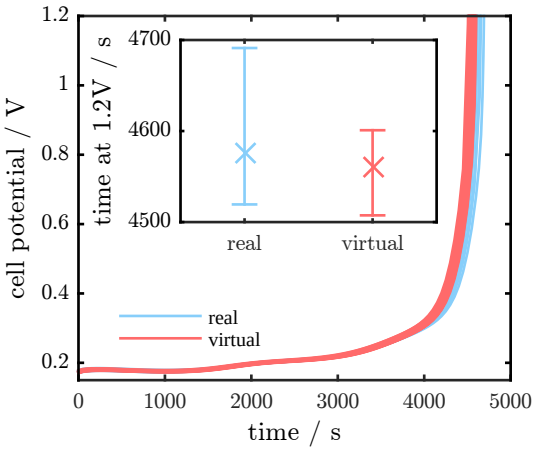

Figure 4.8.: (main) Cell voltage of all microstructures for a full delithation with a constant current. The real and virtual microstructure are quite overlaying. (inset) The mean time when the cell voltage reached 1.2 V is shown together with the distance to the minimum and maximum time.

incident. Still, some deviations between the two sources exist. In the inset of fig. 4.8 the average time of the simulations needed to reach a cell voltage of 1.2 V is plotted. The two sources show a quite close average value, but the real microstructures show a slightly larger stretch. Hence the decision was made to investigate the geometries using only short current pulses. With a pulse duration of 10 s the anode material was delithiated in half-cell setup. The initial concentration and the electrochemical parameters

of the electrodes and the electrolyte can be found in section 4.3.3. Three different currents were chosen as applied currents (see table 4.8). The results of the electrochemical validation are investigated with

Table 4.8.: The three different applied current density magnitudes used in the electrochemical validation simulations. The current density is with respect to the area of the current collector.

name	value	C-rate
current h	$200\,\mathrm{mAm^{-2}}$	$\approx 10\,\mathrm{C}$
current m	$20\,\mathrm{mAm^{-2}}$	$\approx 1\,\mathrm{C}$
current l	$10\,\mathrm{mAm^{-2}}$	$\approx$ C/2

respect to possible differences. See section 5.1 for the presentation and discussion.

4.2.2. Time evolution of plating condition

Knowing and understanding which location and at what time during battery operation lithium plating is taking place is an important task. The investigation of the influences on the time evolution of the plating condition is conducted using the symmetric electrodes (see fig. 4.9) [12]. To describe a

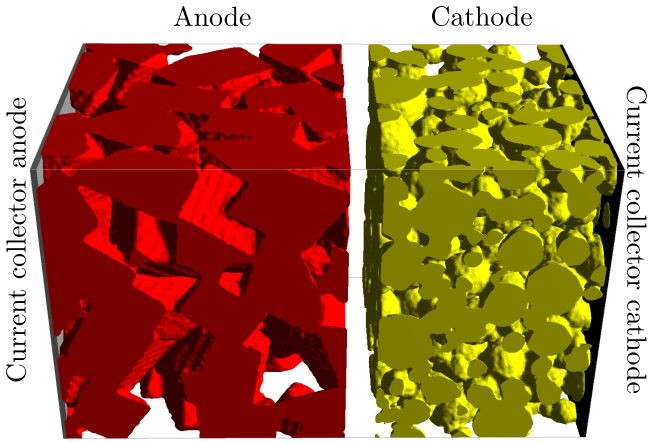

Figure 4.9.: Geometry of full cell used for electrochemical simulations (reprinted with permission from [12]). As anode the symmetric electrode structure and as cathode the microstructure from Ebner *et al.* were taken.

microstructure two directions need to be defined: The direction from one current collector through the electrodes and separator to the current collector on the opposite side is called *through direction*. The directions perpendicular to the through direction is named *lateral direction*. The through direction is addiationally sometimes called *x-direction*.

The electrochemical parameters of the solids and the reactions used for the validation simulations are listed in table 4.9. The electrolyte parameters are listed in table 4.18. The initial conditions used for the concentration and potential in the different phases are given in table 4.10.

Table 4.9.: Material and kinetic parameters used for the electrochemical validation simulations. (reprinted with permission from [121])

	Graphite		LMO		Li metal	
Parameter/Unit	Value	Ref	Value	Ref	Value	Ref
c_{max} / kmol/m^3	26.39	[122]	23.671	[38]		
σ / S/m	1000	[122, 123, 54][a,b]	3.8	[122] [a]		
D_{So} /10^{-13} $\frac{\mathrm{m}^2}{\mathrm{s}}$	3.9	[122, 124]	10	[122, 54]		
U_0 / V	$0.63 + ...$	[51]	$4.06 + ...$	[38, 127]		
N^{00}_{Inter}/10^{-5} $\frac{\mathrm{Am}^{5/2}}{\mathrm{mol}^{3/2}}$	0.088	[54][c]	0.8	[54][c]		
N^{00}_{Plat} / $\frac{\mathrm{A}}{\mathrm{mol}^{1/2}\mathrm{m}^{1/2}}$					0.364	[125][b]
E^{D}_{act} / kJ/mol	53.1	[124]	53.1	[d]		
$E^{i_{00}}_{act}$ / kJ/mol	68	[126]	50	[126][e]	0	[f]
E^{σ}_{act} / kJ/mol	0	[a]	0	[a]		

[a] Conductivity too large to have effect on Φ, therefore assumed to be constant in T
[b] Literature values vary, this value selected [c] estimated from literature for initial conditions
[d] no literature value, assumed since cathode does not strongly influence plating condition
[e] no literature value, approximated out of LFP (Lithium Iron Phosphate) and NCA (Lithium Nickel Cobalt Aluminium Oxide) [f] no temperature dependence needed, since stripping simulation only at one temperature

Table 4.10.: Initial values of the concentration and potentials for the electrochemical simulations with the volume phase model.

Parameter	Phase				
	CC Anode	Anode	Electrolyte	Cathode	CC Cathode
concentration	-	$1.3195\,\mathrm{kmol/m^3}$ [a]	$1.200\,\mathrm{mol/l}$	$20.574\,\mathrm{kmol/m^3}$ [a]	-
	-	$18.473\,\mathrm{kmol/m^3}$ [b]		- [c]	-
potential	Φ^0_{An}	$\Phi^0_{\mathrm{An}} = U_{0,\mathrm{An}}\left(c^0_{\mathrm{An}}\right)$	0	$\Phi^0_{\mathrm{Ca}} = U_{0,\mathrm{Ca}}\left(c^0_{\mathrm{Ca}}\right)$ [a] $\Phi^0_{\mathrm{Ca}} = 0$ [b]	Φ^0_{Ca}

[a] For full-cell simulations
[b] For half-cell simulations [c] Lithium counter electrode used for half cell simulations

The A/C-ratio with respect to available room for lithium is roughly 2.0. This indicates a highly unbalanced battery with a large excess of anode capacity. In lithium-ion batteries the A/C-ratio is usually in the range of $1.1 - 1.2$ [4, 128, 129]. Hence one would expect lithium plating only to appear very unlikely for the test full-cell. The full cell is operated at three different ambient temperatures and four different charging currents. In table 4.11 the different operation conditions are listed.

4.2.3. Impact of existing lithium metal phase using the volume resolved model

The cell voltage during discharge of a lithium-ion battery, which contains plated lithium, exhibits at the start a plateau of constant voltage value. This is the result of the stripping reaction which is independent of the current state of charge of the supporting and surrounding anode material. In this section the impact of a plated lithium phase on the cell voltage and as well as intrinsic parameters are investigated. The geometry used for the time evolution of the plating condition is modified by a explicit lithium phase (see fig. 4.10(a)). The anode (red) is extended by a flat plated lithium sheet at

Table 4.11.: Operation conditions applied for the plating condition investigations. The current density is with respect to the area of the current collector.

Ambient Temperature	Applied current Value A/m^2	C-Rate
295	1.6	1/10
295	16	1
295	48	3
295	160	10
285	16	1
275	16	1

the anode-separator-interface (green). The cell voltage of a discharge simulation exhibits the stripping plateau and is compared to the unplated full cell geometry and experimental data (see fig. 4.10(b)). It

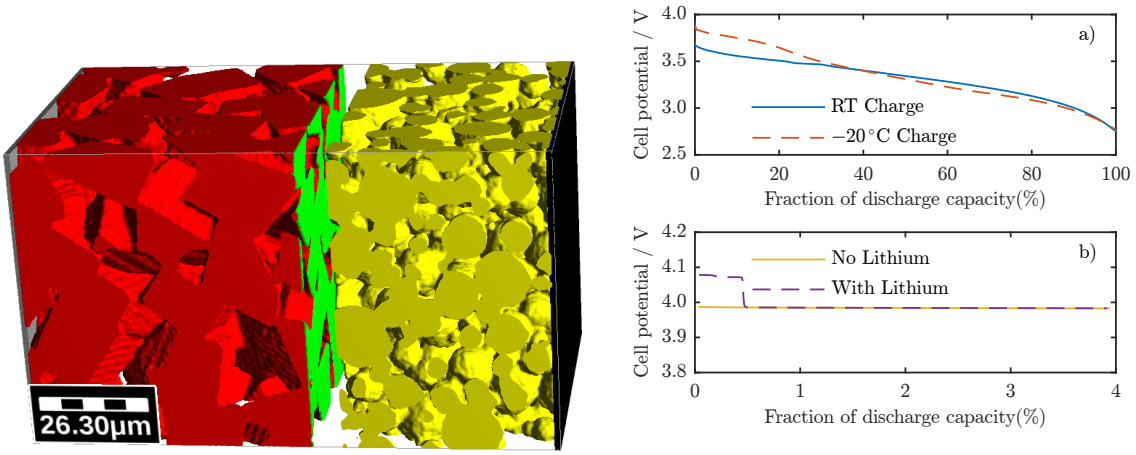

(a) A thin lithium film is added to the full cell geometry (see fig. 4.9) at the anode-separator-interface.

(b) Cell potential during discharge of full cell with plated lithium. Compared to experimental observations. (reprinted with permission from [12])

Figure 4.10.: Stripping simulations using a plated full cell geometry.

can be seen that the cell potential of the plated full cell shows a plateau at the beginning of discharge. A similar observation can be made when looking at the experimental data. The initial cell potential differ, because the cathode material used for experiments is NCO ($LiNi_{0.8}Co_{0.2}O_2$), compared to LMO in the simulations, and the initial concentrations and C/A-ratio of the experiments is not known. Nevertheless a qualitative comparison is possible. The most probable location for plated lithium is usually the interface between anode and separator (see section 5.2). Most experiments can only show postmortem that a mostly uniform lithium film exists at that interface (see figure 7 in [74]). With electrochemical simulations we are able to investigate how plated lithium at different locations inside the negative electrode influence the lithium-ion battery as a whole. Therefore the graphite electrode (see fig. 4.3) is modified to contain a volumetric lithium metal phase at its active surface. This is approached as follows: The geometry partitioned into 96 sectors with a size of $30 \times 50 \times 50$ voxels and thus the microstructure is divided into six slabs in x-direction which are themselve also divided into 16 equally sized parts. On the interface between solid phase and electrolyte of a sector an additional phase is created by dilating the

solid phase by a thickness of one voxel. The dilation is either replacing pore volume or anode volume. One modified and the other 95 sectors are recombined into one microstructure, where this new volume phase is to be the plated lithium for the stripping simulations, and thus creating 192 microstructures with one plated sector. In fig. 4.11 the half-cell geometery for one of the modified structures is shown. The unmodified part of the graphite material is shown in red, while the modified sector is highlighted

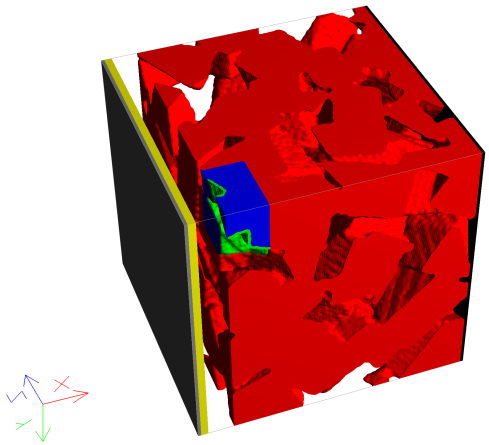

Figure 4.11.: S(1/0/0) Geometry of half cell simulations (reprinted with permission from [12])

in blue. The additional phase is shown in green. To the left of the anode phase the counter electrode (yellow) is separated by a void space representing the separator. On the far left and right the grey and black sheets are the current collectors of the respective electrodes. The different microstructures are identified by the location of the plated sector and the phase (**S**olid or **E**lectrolyte), which was not partially replaced by lithium. E.g. S(1/0/0) points to the microstructure with a modified sector, where the plated lithium replaced electrolyte volume, located at the lower left corner at the anode-separator interface. The different sectors are combinations of $x \in (1, 31, 61, 91, 121, 151)$, $y \in (0, 50, 100, 150)$ and $z \in (0, 50, 100, 150)$.

The parameters used for the stripping simulations are identical to the ones used for the time evolution (see table 4.9 and table 4.10). The plated half-cells were delithiated (discharged in full-cell term) using three different currents, which are listed in table 4.12. With this different currents we were able to

Table 4.12.: The three different applied current density magnitudes used in the stripping simulations. The current density is with regard to the area of the current collector.

Name	Value	C-Rate
Current 1	$20\,\mathrm{A/m^2}$	≈1C
Current 2	$10\,\mathrm{A/m^2}$	≈C/2
Current 3	$5\,\mathrm{A/m^2}$	≈C/4

check if the applied current has an influence on the amount of plated lithium as estimated by the dQdV-method (see section 2.5.1).

Dissolution barrier constant

As mentioned in section 3.1.1, a new challenge while simulating lithium stripping is the vanishing of the phase. The influence of the exact value of d_0 used for the dissolution energy barrier was investigated by comparing the simulation results for four different values (0.48 nm, 0.24 nm, 0.048 nm and 0.0048 nm). The thickness of a lithium metal monolayer would be 0.28 nm. The choice of smaller value for d_0 still has meaning as a numerical approximation for the Heaviside function (jump from one to zero at the monolayer thickness). In fig. 4.12 the cell potential during a stripping simulation (no chemical intercalation enabled) with applied constant current as function of time for the four different prefactors is shown. It can bee seen, that the shape of the cell potential is not influenced by the exact value of the

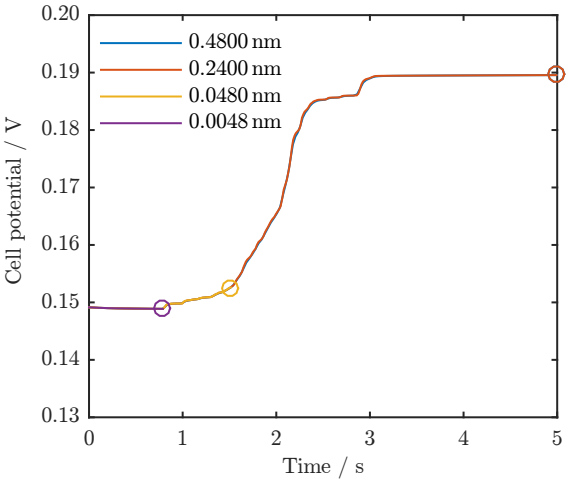

Figure 4.12.: The influence of the prefactor on the cell potential for a stripping simulation for the S(1/0/0) half-cell. The location when the simulation stopped, is marked with a colored circle. The simulation with 0.24 nm stops just before the 5 s. Smaller values increase the numerical instability and hence the runtime of the simulation. Larger numerical instabilities force the solver to complete more iterations to reach a stable solution of the system. (reprinted with permission from [12])

prefactor. Smaller prefactors force the solver to calculate more iteration steps, when the lithium phase is depleting. Each iteration step also take more time and therefor prolonging the total simulation time. The investigation showed, that smaller prefactor values increased the simulation time significantly and at the same time not yielding any additional information from the simulations. To minimize computational cost the value of the prefactor was therefore set to be 0.48 nm for the stripping simulations in this work. The investigation of the influences on the electrochemical situation inside the negative electrode with an existing plated lithium phase of a lithium-ion battery was published in [12]. The results are discussed in section 5.3.

4.2.4. Surface growth

The advantage of the surface growth model over the volume phase model is, that the anode surface can allow for the different states during one simulation. The intercalation can be suppressed if plated

lithium exists and the stripping of plated lithium does not leave an electrochemical inactive surface (opposed to the volume phase model) behind.

4.2.4.1. Comparison coupled and decoupled system

The implementation of the surface growth model lead to the question if the system should best be solved together or separated into the *classical* system and the new surface system. The differences in the process of solution are explained in section 3.3.4. To investigate the differences a small geometry was used since this allowed a faster comparison. The geometry is shown in fig. 4.13 and consists of a anode and cathode. The total size of this system is $69 \times 16 \times 16$ cubic discretization units and therefor

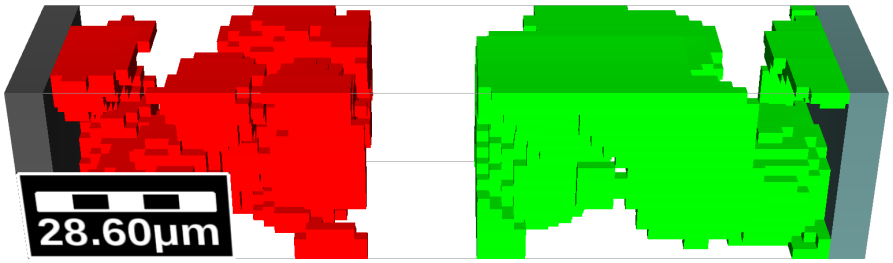

Figure 4.13.: Simple geometry used for the comparison of coupled and decoupled system.

the equation system consists of 33792 volume unknowns and 2752 surface unknowns. The comparison was done for a case, where lithium plating will take place for certain. This was achieved by setting the anode concentration not far away from the maximum concentration. As reference a charge without the surface variables is conducted. The resulting cell potential is shown in fig. 4.14(a). Roughly 300 s after

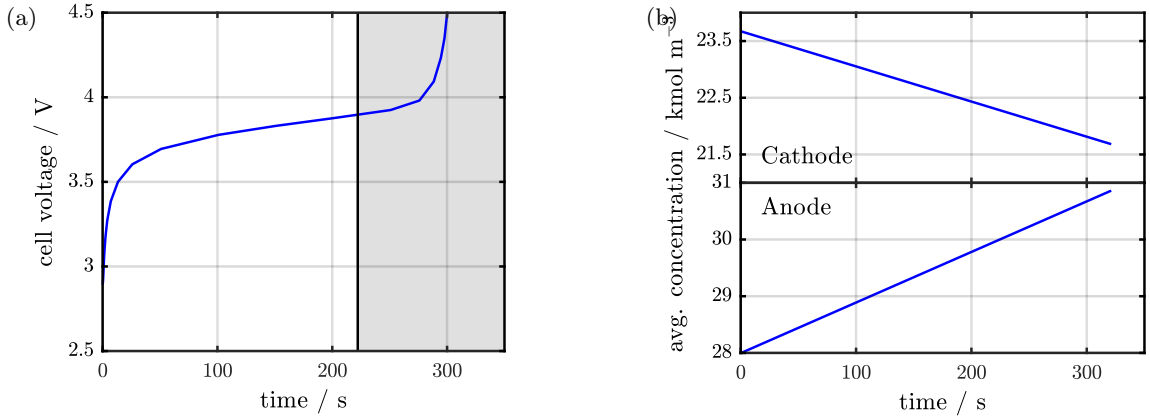

Figure 4.14.: (a) Cell potential of charge simulation for the reference case (without surface variables). The region, where the plating condition is met is marked with a solid black line and grey background. (b) Average concentration in the solid part of the anode and cathode.

start of charge, the anode reaches maximum concentration and hence exhibits a diverging open-circuit voltage (see eq. (3.20)). This divergence is also visible in the cell potential (see fig. 4.14(a)). The average concentration inside the electrodes is a parameter used to check the surface model for physical consistence. The average concentration inside the electrodes exhibits a linear slope for a simple charge

with constant current (see fig. 4.14(b)). The growth of the lithium surface phase should take place when the plating condition is fulfilled. In fig. 4.15 the time evolution of the plating condition at the separator-anode-interface is shown. The switch from positive to negative value is around 222 s. During

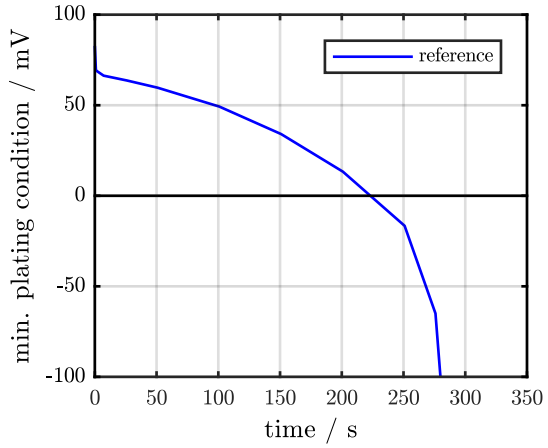

Figure 4.15.: Minimum value of the plating condition at the separator-anode-interface. The plating condition is fulfilled around $t = 222\,\mathrm{s}$.

a simulation, which includes the plating side reactions, one would expect to see the onset of plating around that time. This time value is selected as a critical factor to control if an implementation of a plating model behaves as assumed. The simulation results obtained from the coupled and decoupled implementations (see section 3.3.4) are investigated and discussed in section 5.4. It shall be briefly mentioned, that the coupled system is selected as basis for further investigations due to the results of the previously described investigation.

The electrochemical parameters of the solids and the reactions used for the validation simulations are listed in table 4.13. The electrolyte parameters are listed in table 4.18. The initial conditions used for the concentration and potential in the different phases are given in table 4.14.

4.2.4.2. Impact of the dissolution barrier constant

The overpotential of the dissolution barrier η_{diss} was included into the plating reaction $N_{\mathrm{Pl/St}}$ to allow for the vanishing of a species (see section 3.3.2). The impact of the dissolution barrier constant d_0 is investigated in this section. The decoupled system was selected as a result of the previous section. The value of d_0 was varied between 10^{-9} and 10^{-4} with the geometry of the previous section. The electrochemical parameters are identical to the previous section. The results are shown in section 5.4.1.

4.2.4.3. Influences on the plating onset and the spatial distribution of plated lithium

Post-mortem analysis of degraded lithium-ion batteries showed inhomogeneous lithium deposition on the negative electrode [131]. The impact of local inhomogeneities of electrochemical parameters on the lithium deposition is therefor investigated. The electrode is modified to be able to define different

Table 4.13.: Material and kinetic parameters used for the comparison of coupled and decoupled surface system and the investigations of the dissolution barrier constant.

		Graphite		LMO		Plated Li	
Parameter	/Unit	Value	Ref	Value	Ref	Value	Ref
c_{max}	/ kmol/m^3	31.370	[51]	23.671	[38]		
σ	/ S/m	1000	[122, 123, 54][a,b]	3.8	[122] [a]		
D_{So}	/10^{-13} $\frac{\mathrm{m}^2}{\mathrm{s}}$	3.9	[122, 124]	10	[122, 54]		
U_0	/ V	$0.63 + ...$	section 3.3.1	$4.06 + ...$	[38, 127]		
N^{00}_{Inter}	/10^{-2} $\frac{\mathrm{Am}}{\mathrm{mol}}$	0.0657	[130][c]	0.197	[130][c]		
E^{D}_{act}	/ kJ/mol	53.1	[124]	53.1	[d]		
$E^{N^{00}_{\mathrm{Inter}}}_{act}$	/ kJ/mol	70	[130]	70	[130]		
$T^{N^{00}_{\mathrm{Inter}}}_{act}$	/ K	294.15	[130][X]	294.15	[130] [X]		
E^{σ}_{act}	/ kJ/mol	0	[a]	0	[a]		
$N^{00}_{\mathrm{Pl/St}}$	/ $\frac{\mathrm{A}}{\mathrm{mol}^{1/2}\mathrm{m}^{1/2}}$					0.631	[91]
$E^{N^{00}_{\mathrm{Ch.Int.}}}_{act}$	/ kJ/mol					35	[91]
$T^{N^{00}_{\mathrm{Ch.Int.}}}_{act}$	/ K					294.15	[91][X]

[a] Conductivity too large to have effect on Φ, therefore assumed to be constant in T [b] Literature values vary, this value selected [c] estimated from literature for initial conditions [d] no literature value, assumed since cathode does not strongly influence plating condition [f] no temperature dependence needed, since stripping simulation only at one temperature [X] assumed, since no specific information is given

Table 4.14.: Initial values of the concentration and potentials for the comparison of coupled and decoupled surface system and the investigations of the dissolution barrier constant.

Parameter			Phase		
	CC Anode	Anode	Electrolyte	Cathode	CC Cathode
concentration	-	28.0 kmol/m^3	1.200 mol/l	23.670 kmol/m^3	-
potential	Φ^0_{An}	$\Phi^0_{\mathrm{An}} = U_{0,\mathrm{An}}\left(c^0_{\mathrm{An}}\right)$	0	$\Phi^0_{\mathrm{Ca}} = U_{0,\mathrm{Ca}}\left(c^0_{\mathrm{Ca}}\right)$	Φ^0_{Ca}

spatial values of the electrochemical parameters. The graphite electrode with rough interface (see section 4.1.2.2) is divided into two regions. Several parameters are varied between these two regions. Their impact on the plating condition and the spatial distribution of the plated lithium is analyzed. In fig. 4.16 the modified microstructure is shown. The outer region (red) will be called *bulk* or *outer region* and the inner region (green) will be called *inner* or *modified region*. Different parameters of the solid phase in the inner region will be modified and the response of the cell will be investigated. table 4.15 contains selected geometrical properties of the modified electrode. Only the surfaces between the inner and outer region and the electrolyte are electrochemical active. The solid-electrolyte-surface of the binder is inactive, since the binder is assumed to be electrochemical inactive.

Two different types of plating simulations were done with this modified graphite electrode. First, the electrode was forced into plating by applying a high current pulse to a nearly lithiated half-cell. The initial state of charge of the graphite was set to 95.3 % so the cell potential of the half-cell at rest was 0.05 V. Second, the empty graphite, which has an initial state of charge of 0.01 % and corresponds to 1.27 V cell voltage, was lithiated with different currents between 10 and 90 A/m^2 at an ambient temperature 298.15 K. The lithiation is stopped at 400 nAh. For the highest applied current (90 A/m^2)

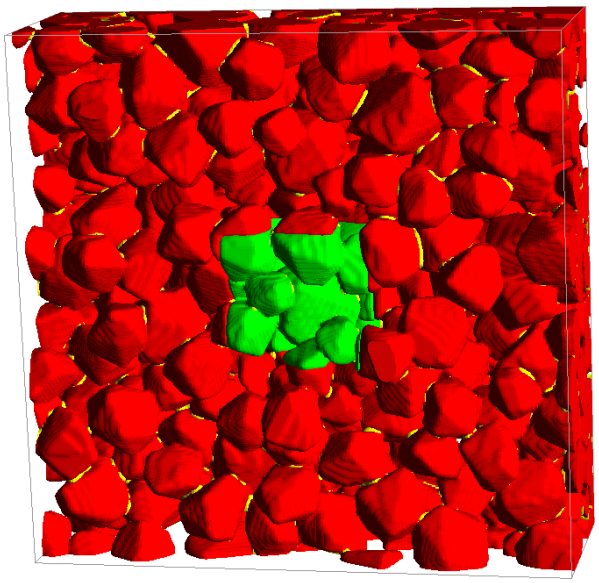

Figure 4.16.: The geometry of the anode with rough separator interface is split into two regions: a outer region (red) and an inner region (green).

Table 4.15.: Fraction of solid phase on total electrode volume and active surface area for the inner and outer region of the electrode with rough surface.

region	Solid volume fraction of total volume	Solid volume fraction of solid volume	solid-electrolyte-surface fraction
Inner region	3.1 %	5.9 %	15.8 %
Outer region	46.6 %	88.7 %	79.1 %
Binder	2.8 %	5.4 %	5.1 %

the lithiation and plating operation is followed by a delithiation step. The delithiation is done with the same current density and is ended as soon as the cell voltage reaches 1 V. At the start of delithiation the plated lithium will be stripped. The switch from lithiation to delithation occurs at $t = 730\,\mathrm{s}$. The rate constants of the intercalation reaction ($N^{00}_{\mathrm{Inter-G}}$ in eq. (2.20)) and of the plating reaction ($N^{00}_{\mathrm{Pl/St}}$ in eq. (2.52)) were modified for the whole electrode and only the inner part. These variations allow for some insight how an electrode with inhomogeneities on the microscale behaves under plating conditions. The results are discussed in section 5.5.

The electrochemical parameters of the solids and the reactions used for the validation simulations are listed in table 4.16. The electrolyte parameters are listed in table 4.18. The initial conditions are listed in table 4.17. The prefactor of exchange currents for the direct intercalation is set to $\sqrt{c_{\mathrm{El}} \cdot c_{\mathrm{So}}}$ based on [34]. It is assumed, that the temperature dependence of all rate constants N^{00}_{r} can be expressed through an Arrhenius law :

$$N^{00}_{\mathrm{r}}\left(T\right) = N^{00}_{\mathrm{r}}\left(T = T^{\mathrm{Inter}}_{\mathrm{act}}\right) \cdot exp\left[-\frac{E^{\mathrm{Inter}}_{\mathrm{act}}}{R}\left(\frac{1}{T} - \frac{1}{T^{\mathrm{Inter}}_{\mathrm{act}}}\right)\right] \tag{4.1}$$

Table 4.16.: Material and kinetic parameters used for plating simulations with the surface model for the modified geometry.

Graphite parameters			Plated lithium parameters		
Parameter/Unit	Value	Ref	Parameter/Unit	Value	Ref
c_{max} / kmol/m^3	31.370	[51]	$N^{00}_{\mathrm{Pl/St}}$ / $\frac{\mathrm{A}}{\mathrm{mol}^{1/2}\mathrm{m}^{1/2}}$	0.631	[91]
σ / S/m	1000	[122, 123, 54][a,b]	$E^{N^{00}_{\mathrm{Pl/St}}}_{act}$ / kJ/mol	35	[91]
D_{So} /10^{-13} $\frac{\mathrm{m}^2}{\mathrm{s}}$	3.9	[122, 124]	$T^{N^{00}_{\mathrm{Pl/St}}}_{act}$ / K	294.15	[91][X]
U_0 / V	$0.63 + ...$	section 3.3.1	$N^{00}_{\mathrm{Ch.Int.}}$ / $\frac{\mathrm{A}}{\mathrm{mol}^{1/2}\mathrm{m}^{1/2}}$	10^{-8}	[Y]
N^{00}_{Inter} /10^{-2} $\frac{\mathrm{Am}}{\mathrm{mol}}$	0.0657	[130][c]	$E^{N^{00}_{\mathrm{Ch.Int.}}}_{act}$ / kJ/mol	70	[X]
E^{D}_{act} / kJ/mol	53.1	[124]	$T^{N^{00}_{\mathrm{Ch.Int.}}}_{act}$ / K	294.15	[X]
$E^{N^{00}_{\mathrm{Inter}}}_{act}$ / kJ/mol	70	[130]			
$T^{N^{00}_{\mathrm{Inter}}}_{act}$ / K	294.15	[130][X]			
E^{σ}_{act} / kJ/mol	0	[a]			

[a] Conductivity too large to have effect on Φ, therefore assumed to be constant in T [b] Literature values vary, this value selected [c] estimated from literature for initial conditions [X] assumed, since no specific information is given [Y] estimated, since no literature value known. See section 4.3.2.

Table 4.17.: Initial values of the concentration and potentials for the electrochemical simulations with the surface model.

Parameter	Phase				
	CC Anode	Anode	Electrolyte	Counter electrode	CC CE
overcharge simulation					
concentration	-	29.896 kmol/m^3	1.200 mol/l	-	-
potential	Φ^0_{An}	$\Phi^0_{\mathrm{An}} = U_{0,\mathrm{An}}\left(c^0_{\mathrm{An}}\right)$	0	$\Phi^0_{\mathrm{CE}} = 0$	Φ^0_{CE}
lithiation and lithiation-delithiation simulation					
concentration	-	3.137 kmol/m^3	1.200 mol/l	-	-
potential	Φ^0_{An}	$\Phi^0_{\mathrm{An}} = U_{0,\mathrm{An}}\left(c^0_{\mathrm{An}}\right)$	0	$\Phi^0_{\mathrm{CE}} = 0$	Φ^0_{CE}

4.3. Parameters

The electrochemical parameters needed and used for the simulations in this work are listed and explained in this section.

4.3.1. Approximation of the maximum lithium concentration

Artificial graphite changes from pure graphite C_6 to fully lithiated graphite LiC_6 during intercalation. Under the assumption of non-existent defects in the graphite lattice and a complete lithium depletion and intercalation at the two ends of the state of charge, the maximal lithium concentration inside

artificial graphite can be calculated from the material parameters of graphite:

$$\begin{aligned} \rho_{\text{Graphite}} &= 2.26\,\text{g/cm}^3 \\ M_{\text{Graphite}} &= 12.01\,\text{u} \\ c_{\text{C}} &= \frac{\rho_{\text{Graphite}}}{M_{\text{Graphite}}} = 0.18817\,\text{mol/cm}^3 \end{aligned} \tag{4.2}$$

At full lithiation six carbon atoms correspond to one lithium atom and hence the maximal lithium concentration is

$$c_{\text{Li,graphite}}^{\text{max}} = 0.03136\,\text{mol/cm}^3 \tag{4.3}$$

or expressed as maximum weight capacity:

$$\begin{aligned} Q_{\text{Li,graphite}}^{\text{max}} &= \frac{F}{M_{\text{Graphite}} \cdot 6} \\ &= 371.9\,\text{mAh/g} = 371.9\,\text{Ah/kg} \end{aligned} \tag{4.4}$$

The calculations above result in the theoretically possible lithium concentration in graphite. In a real battery the amount of lithium, which actually can be stored reversibly in the graphite electrodes is smaller due to different constraints. The active material usually consists of graphite with local impurities or lattice defects, which can hinder the lithium storage in their vicinity. The diffusion of lithium inside the active material is relatively small. For the complete active volume to achieve the maximum concentration the lithiation and delithiation would need to be done with very small applied current. It is therefor common to treat the maximum concentration as a fitting variable, when parameterizing the electrochemical model on experimental data. A common approach is the determination of the maximum concentration through the maximum transferred charge during a slow lithiation or delithation experiment. When the amount of active material in the experimental cell is known, one can estimate the maximum experimental concentration as follows:

$$Q_{\text{Li,graphite}}^{\text{max,exp}} = \frac{Q_{\text{charge}}^{\text{max,exp}}}{m_{\text{graphite}}^{\text{electrode}}} \tag{4.5}$$

with mAh/g as unit. This can be translated into the needed maximum concentration $c_{\text{Li,graphite}}^{\text{max,exp}}$ by multiplication with the density of graphite ρ_{Graphite}. In this study the theoretical capacity is used, since it is also used as reference point by the source of the open-circuit potential [51]. The majority of the presented investigations are done in half-cell layout and thus neglects the cathode. A smaller actual maximum concentration would only result in a compression of all time dependent results along the time or transferred charge axis. The results and the conclusions will stay the same. The exact maximum concentration has a large impact on the creation of a balanced full cell. Some simulation studies use a maximum concentration roughly two-thirds of the theoretically possible concentration [34]

4.3.2. Approximation of the rate constant of the chemical intercalation

The rate constant of the chemical intercalation reaction is not known. Hence, the value of the constant is approximated under the assumption, that the chemical intercalation proceeds with the same speed as the electrochemical intercalation, when averaged over the whole state of charge range of the negative electrode:

$$\int_0^{c_{\mathrm{Li}}^{\mathrm{Max}}} N_{\mathrm{Inter-G}}\left(c_{\mathrm{Li}}^{\mathrm{G}}\right) dc_{\mathrm{Li}}^{\mathrm{G}} = \int_0^{c_{\mathrm{Li}}^{\mathrm{Max}}} N_{\mathrm{Chem.Int.}}\left(c_{\mathrm{Li}}^{\mathrm{G}}\right) dc_{\mathrm{Li}}^{\mathrm{G}} \tag{4.6}$$

$$N_{\mathrm{Inter-G}}^{00} \cdot \sqrt{c_{\mathrm{El}}} \int_0^{c_{\mathrm{Li}}^{\mathrm{Max}}} \left(\sqrt{c_{\mathrm{G}}} \cdot \sinh\left(\beta \cdot \eta_{\mathrm{Inter-G}}\right)\right) dc_{\mathrm{Li}}^{\mathrm{G}} = N_{\mathrm{Chem.Int.}}^{00} \int_0^{c_{\mathrm{Li}}^{\mathrm{Max}}} \left(\sqrt{c_{\mathrm{G}}} \cdot \sinh\left(\beta \cdot \eta_{\mathrm{Chem.Int.}}\right)\right) dc_{\mathrm{Li}}^{\mathrm{G}} \tag{4.7}$$

with the assumption of a symmetric factor for the chemical intercalation ($\alpha_{\mathrm{a}}^{\mathrm{Chem.Int}} = 0.5$) and $\beta = \frac{F}{2\ R\ T}$. This can be reformulate to

$$N_{\mathrm{Chem.Int.}}^{00} = N_{\mathrm{Inter-G}}^{00} \cdot \sqrt{c_{\mathrm{El}}} \cdot \frac{\int_0^{c_{\mathrm{Li}}^{\mathrm{Max}}} \left(\sqrt{c_{\mathrm{G}}} \cdot \sinh\left(\beta \cdot \eta_{\mathrm{Inter-G}}\right)\right) dc_{\mathrm{Li}}^{\mathrm{G}}}{\int_0^{c_{\mathrm{Li}}^{\mathrm{Max}}} \left(\sqrt{c_{\mathrm{G}}} \cdot \sinh\left(\beta \cdot \eta_{\mathrm{Chem.Int.}}\right)\right) dc_{\mathrm{Li}}^{\mathrm{G}}} \tag{4.8}$$

With the assumption, that the currents are in average equal over the SoC range from 0.1 % and 98 %, the exchange current constant is calculated to be $N_{\mathrm{Chem.Int.}}^{00} \approx 8 \cdot 10^{-10}\ \frac{\mathrm{A}}{\mathrm{cm}^{1/2}\mathrm{mol}^{1/2}}$. A plated lithium layer usually exists for high state of charge, hence the exchange current constant is also calculated in the state of charge range from 90 % to 98 %: $N_{\mathrm{Chem.Int.}}^{00} \approx 2 \cdot 10^{-6}\ \frac{\mathrm{A}}{\mathrm{cm}^{1/2}\mathrm{mol}^{1/2}}$. The exchange current constant of the intercalation reaction $N_{\mathrm{Inter-G}}^{00}$ was set to 0.0657 Acm/mol.

4.3.3. Electrochemical parameters of the used Electrolyte

All simulations in this work use the same electrolyte $LiPF_6$ in PC:EC:DMC as measured and described by Valøen *et al.* [132]. The parameters are listed in table 4.18.

Table 4.18.: Electrochemical parameters of the used electrolyte $LiPF_6$ in PC:EC:DMC.

Parameter/Unit	Value	Ref
t_+ /—	0.399	[132]
$f_\pm$ /—	Eq. 6 in	[132]
κ / S/cm^2	Eq. 17 in	[132]
D_{El}/ cm^2/s	Eq. 14 in	[132]

5. Results and discussion

5.1. Electrochemical validation of 3D stochastic microstructure model

The electrochemical validation of the stochastic microstructure model of interest is the topic of this section. As described in the simulations section, the different microstructures are delithiated with a short current pulse. Three different current magnitudes were selected. The analysis of the resulting data showed, that any given microstructure behaves quite similar for the different currents. The lithium distribution inside the electrolyte at the different currents is shown exemplary in fig. 5.1(a). On the first glance the distribution (inset in figure) seems quite different for the three currents. The curve for the highest applied current (current h) shows the largest separation between the two peaks and also finer resolved features. Scaling the curves such, that the maxima lay at the same x-value, the near identity of the features seen for the different currents becomes obvious. Apart from the quite similar shape of the peaks, the features between the peaks, like the shoulder left of the smaller peak, resemble each other. Other quantities, like current density inside the electrolyte, exhibit similar trends

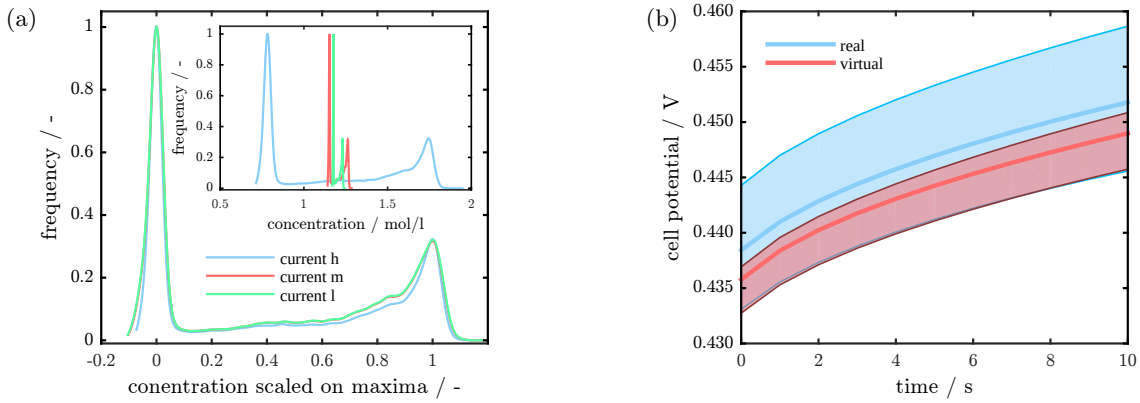

Figure 5.1.: (a) (inset) The histogram of the lithium concentration in the electrolyte for the different applied delithiation currents. (main) Scaling of the concentration distribution such that the position of the peaks coincide. This illustrates that the three different curves exhibit the same behavior. (reprinted with permission from [121]) (b) The average cell potential of the real and virtual microstructures for a delithiation pulse of 10 s. (reprinted with permission from [121])

and shapes when compared for the three applied currents. Hence the further discussion and comparison of the real and virtual microstructures are completed using the data for the highest current (current h).

In the rest of this section electrochemical simulation data of the real microstructures are indicated by the color blue, while the results of the virtual microstructures are shown in red. The areas, shaded in the respective color, represent the range between the 5 % and 95 %-quantile. One of the only quantities available externally to compare different battery cells, regardless of the materials, is the cell voltage. Hence as a first step, it is compared for the different microstructure sources. In fig. 5.1(b) the average cell voltages for high current are shown. The deviations between the average cell voltage of real and virtual microstructures are less than 1 % or 5 mV. Thus indicating a good agreement.

Electrolyte concentration

The first spatial resolved quantity to be investigated is the lithium concentration inside the electrolyte. The evolution of the concentration in time is strongly dependent on the exact 3D microstructure. Hence the comparison of this quantity for real and virtual microstructures is sensitive to possible deviations.

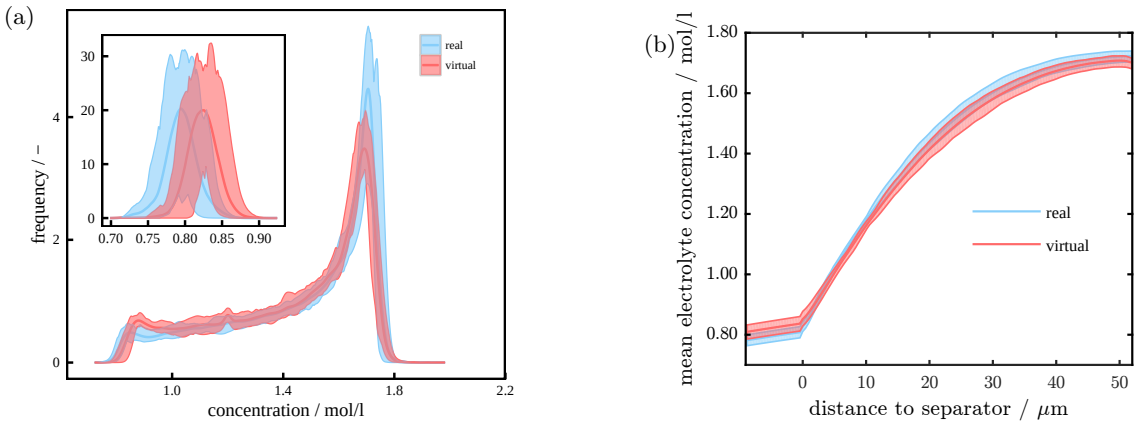

Figure 5.2.: (a) The distribution of the electrolyte concentration is separated into two regions. The pore space inside the electrode is shown in the main plot, while the distribution inside the separator space is displayed in the inset. The densities are normed to unity area. (reprinted with permission from [121]) (b) The average lithium concentration in the electrolyte is plotted as a function of distance to the separator. The shape and height are quite identical and both curves overlap within the 5 %- and 95 %-quantiles. The shape is also in general agreement with results from porous electrode theory [7, 54]. (reprinted with permission from [121])

The distribution of the lithium concentration in the electrode pore space at the end of the discharge pulse is shown in fig. 5.2(a). The distribution inside the separator space is shown separately in the inset of fig. 5.2(a). The concentration in the electrode pore space exhibits a small peak around the initial concentration of 1.2 mol/l. This results from a certain amount of pore volume which is not connected to the main pore space. In real microstructures those unconnected volume would not be filled with electrolyte but with void and thus would be electrochemical inactive. In the simulations these volumes were filled with electrolyte, but still stayed electrochemical inactive. As a result they will not change their initial concentration and therefor appear as small peak at initial concentration. The virtual microstructures generated by the investigated 3D stochastic microstructure model contain more

unconnected volume compared to the real microstructures. This could be the result of the connection rules of the particles used in the stochastic model [121]. Another feature of the concentration distribution inside the pore space (main of fig. 5.2(a)) is the slightly lower maxima position for the virtual structures as compared to the real microstructures. This can also be seen in the two explanatory 3D-spatial distribution shown in fig. 5.3. The virtual structures exhibit an overall smaller spread between maximum and minimum concentrations. Hence, the electrolyte concentration inside the separator space also shows a higher concentration (see inset in fig. 5.2(a)). This actuality is attributed to the slightly large total electrolyte volume of the virtual microstructures compared to the real microstructures (see table 4.6) and the accordingly minor spatial concentration gradients. The average lithium concentration along the through direction is displayed in fig. 5.2(b). The virtual and real microstructures exhibit a nearly identical shape for their distribution functions. Both exhibit a nonlinear gradient of the concentration inside the electrode, which is due to the superposition of lithium delithiation and lithium transport. At the region close to the current collector the concentration of the real structures is somewhat higher than for the virtual structures. The linear concentration gradient inside the separator space is rooted in the lithium diffusion and migration, since there is not any lithium source inside the separator. It is obvious, that the real microstructure shows a larger spread between minimum and maximum concentration than the virtual microstructures, as can also be seen in the functional distribution (see fig. 5.2(a)). The small differences between the concentration functions for real and virtual structures is attributed to the small differences in electrolyte volume (see table 4.6) and the inhomogeneous distribution of the solid volume fraction (see fig. 4.7). The shape of the spatial distribution of the mean electrolyte concentration is quite similar to what is usually obtained as a result of porous electrode theory [7, 54]. An advantage of

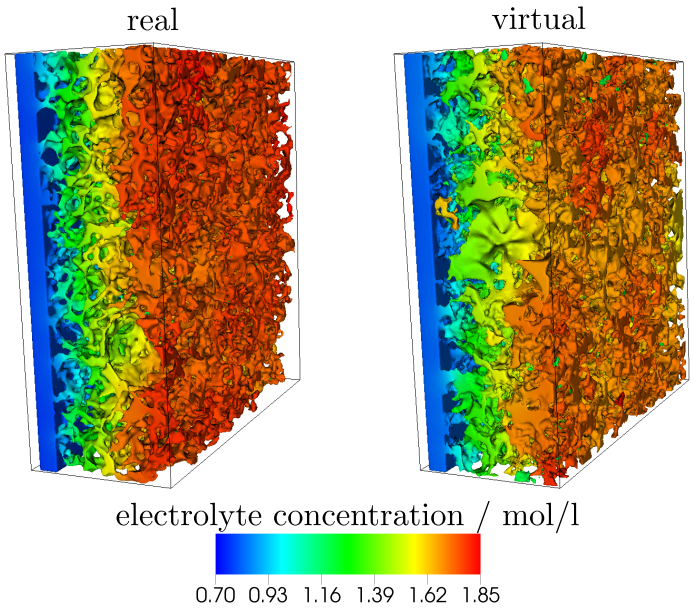

Figure 5.3.: The spatial distribution of the electrolyte concentration for two cut-outs. The real (left) and virtual (right) microstructures have the same color scale (shown below the cut-outs). Pores with less-than-average connectivity to the main pore space can be seen in both structures: (virtual) Orange sector close to the separator (blue) and a dark read region at the upper corner for the real structure. (reprinted with permission from [121])

3D resolved electrochemical simulations is that spatially localized effects can be resolved without the need for any additional assumptions. This can be easily seen in fig. 5.3 where the 3D spatial distribution of the electrolyte concentration for two cut-outs of real and virtual microstructures is shown. Both cut-outs contain pores which have a lower-than-average connection to the main pore network. For example the virtual microstructure has a small orange/yellow pore close to the separator. This pore is not an unconnected pore, since its concentration is above the initial 1.2 mol/l, but shows a higher concentration than the surrounding pore space. The real microstructure displays a dark red section at the upper current collector interface which also contains a higher concentration compared to its surroundings. The real microstructure exhibits an overall higher concentration (more dark red) at the current collector interface compared to the virtual microstructure.

Current density

The degradation inside a lithium-ion battery is influenced by the current density. SEI growth and electrolyte decomposition are highly dependent on the local strength of the current flow [62]. High applied currents increase the local and total temperature of batteries, since a large applied current need to be transferred from the solid into the electrolyte and the resulting irreversible Joule heat leads to a temperature rise at the surfaces [7]. An increase in cell temperature favors the local decomposition of the SEI and in the worst case starts an exothermic reaction which can lead to thermal runaway [133]. The current density in the electrolyte and solid phase is defined in eq. (2.9). In this work it is assumed that the charge carriers inside the electrolyte are lithium ions and electrons inside the solid phase.

Electrolyte phase

The current densities in the whole electrolyte phase of the real and virtual microstructures show a nearly identical behavior, as can be seen in fig. 5.4(a). For higher local current densities, which are potentially critical for SEI decomposition, no significant differences between the two microstructure sources could be seen. The virtual microstructure show slightly higher amount of smaller current densities. This indicates, that the virtually generated microstructures are electrochemically very similar to the real structures. The agreement between virtual and real structures looks different when the spatial distribution of the current density in the electrolyte is plotted (see fig. 5.5(b)). The current density increases from the current collector towards the separator, because the main charge transport phase switches from the solid into the electrolyte. For most parts a good overlap exists between the spatial distribution of the current density for real and virtual microstructures, except close to the separator. There the current density of the virtual structures is lower than for the real ones and also shows a smaller spread between the 5 %- and 95 %-quantile. Close to the separator the current density of the real microstructures is roughly 10 % higher than the values for the virtual structures. This deviation is attributed to the different behavior of the solid volume fraction close to the separator (see fig. 4.7). The increase of the SVF for the real structures close to the separator and current collector is not yet resembled by the stochastic structure model. The higher solid volume fraction (SVF) results in a smaller pore space available for the lithium transport and current flux. Hence, for the same amount

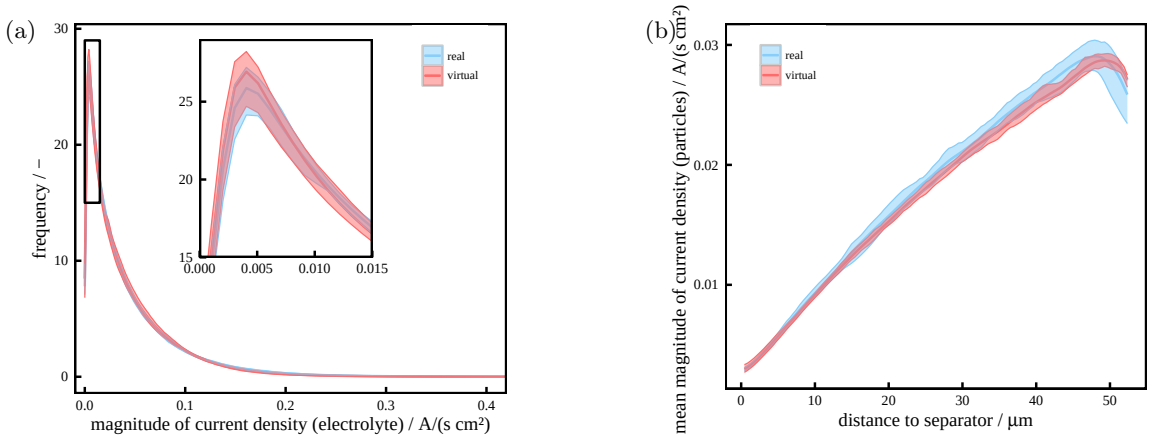

Figure 5.4.: (a) Histogram of the current density inside the electrolyte for the high applied current after 10 s. (b) The spatial distribution of the average current density inside the solid phase. The deviation close to the current collector is attributed to the inhomogeneous solid volume fraction (see fig. 4.7). (reprinted with permission from [121])

of current to be transported from the bulk of the electrode into the separator a larger current density is needed.

Solid phase

The histogram for the current density inside the solid phase is shown in fig. 5.5(a). Both structure sources show abroad peak which is toped with two smaller peaks as features. The top of the broad peak is shown zoomed in the inset of fig. 5.5(a). Again, the current density of virtual and real mcirostructures display a good agreement. The spatial distribution of the current density inside the solid phase along the through direction exhibits the reverted slop of the electrolyte phase, because closer to the separator more and more charge gets transported through the electrolyte phase (see fig. 5.4(b)). Similar to the

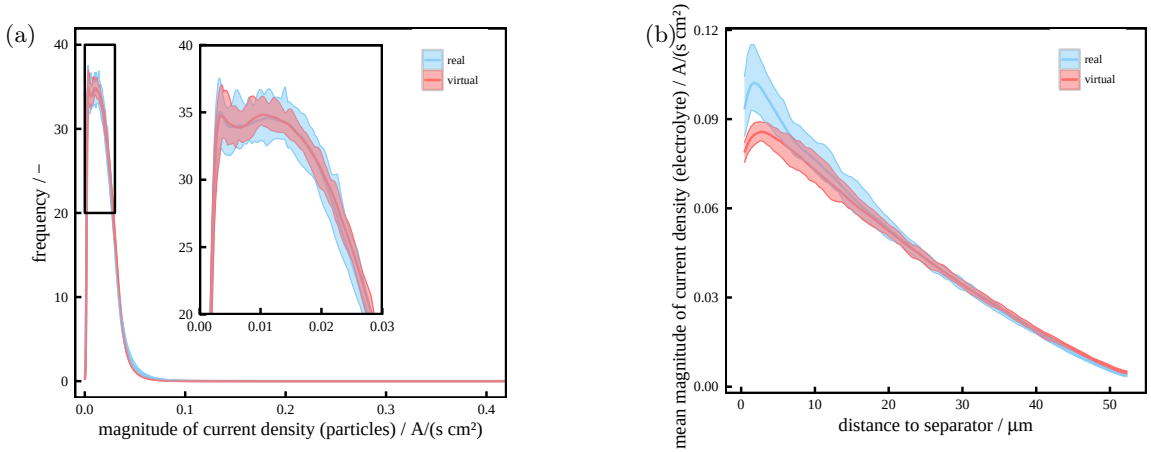

Figure 5.5.: (a) Histogram of the current density inside the solid phase for the high applied current after 10 s. (b) The spatial distribution of the average current density inside the electrolyte phase. The large deviation close to the separator is attributed to the inhomogeneous solid volume fraction (see fig. 4.7).

current density in the electrolyte phase, the real microstructures deviate from the virtual structures close to the boundary of the electrode. In the solid case it is the region close to the current collector. In this region two features are visible: the average current density in the solid phase increases for some distance (around 5 µm). At the same time, the values for the real structures are smaller than for the virtual ones. As soon as the current density begins to decline, the values of the real structures are larger again. Both features are accounted on the spatial variance of the solid volume fraction (see fig. 4.7). The decrease of the SVF away from the current collector leads to an increase in the current density, since the same current needs to travel through a smaller cross section. The real structures have a 5 % larger contact area between electrode and current collector as compared to the virtual microstructures. Hence the initial current density is smaller, as can be seen in fig. 5.4(b), for the real microstructures.

The current density in the two relevant phases show a good agreement between the real and virtual microstructures.

Overpotential

The distribution of the overpotential of the intercalation reaction into the electrode $\eta_{\mathrm{So-El}}$, as defined by eq. (2.24), is plotted in fig. 5.6(a). A similar behavior for real and virtual microstructures can

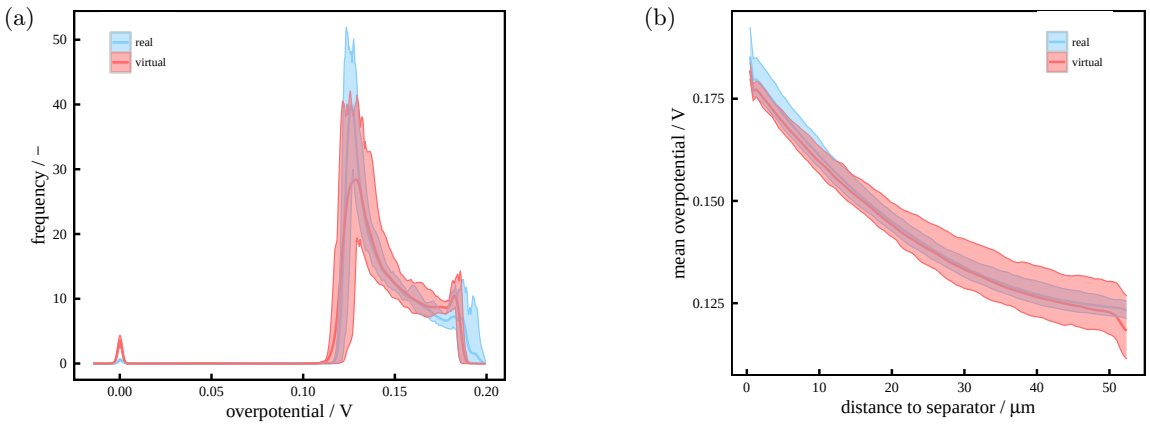

Figure 5.6.: (a) Histogram of the overpotential of the intercalation reaction. (b) Spatial distribution of the overpotential along the through direction.

be seen. A positive overpotential indicates deintercalation of lithium ions from the graphite into the electrolyte. Throughout the graphite electrode only deintercalation is taking place. The peaks at 0 V are the result of interfaces between the solid phase and electrolyte pores, which are not connected to the main pore space. As mentioned earlier, these interfaces are electrochemical inactive. The different heights of the peaks show that the virtual structures contain more unconnected electrolyte volume compared to the real structures. This is in agreement with fig. 5.2(a). There is also a larger peak with a broad shoulder towards higher overpotentials in the frequency plot. The virtual structures exhibit a lower mean feature compared to the real microstructures. The real structure, on the other side, reach slightly larger overpotentials with a small shoulder. This additional shoulder is due to the increased solid volume fraction close to the current collector (see fig. 4.7). This can be seen in the larger value for

the overpotential close to the separator when looking at the spatial distribution of the overpotentials as displayed in fig. 5.6(b). The overpotential as a function of distance in through-direction increases from the current collector towards the separator. This indicates an increase of current flowing from the solid through the interface into the electrolyte. An increase of the overpotential by 50 % would lead to an increase of the average interface current of roughly 100 %, due to the non-linear relation between overpotential and exchange current.

The spatial distribution of the overpotential is quite similar for real and virtual structures. The virtual microstructures show a larger spread for most parts compared to the real ones. The kink close to the current collector is attributed to the small morphological difference between virtual and real structures as described before. The larger overpotential at the separator-electrode interface correlates to an increased deintercalation. The strong nonlinear relation between overpotential and exchange current leads to a highly raised exchange current. This can be seen in the spatial distribution of the lithium flux inside the solid phase, which is discussed in the following section.

Distribution of lithium flux

The spatial distribution of the lithium ion flux inside the electrolyte (see fig. 5.7(a)) is identical for real and virtual structures. A larger part of the lithium ions get transported with a small flux density. The

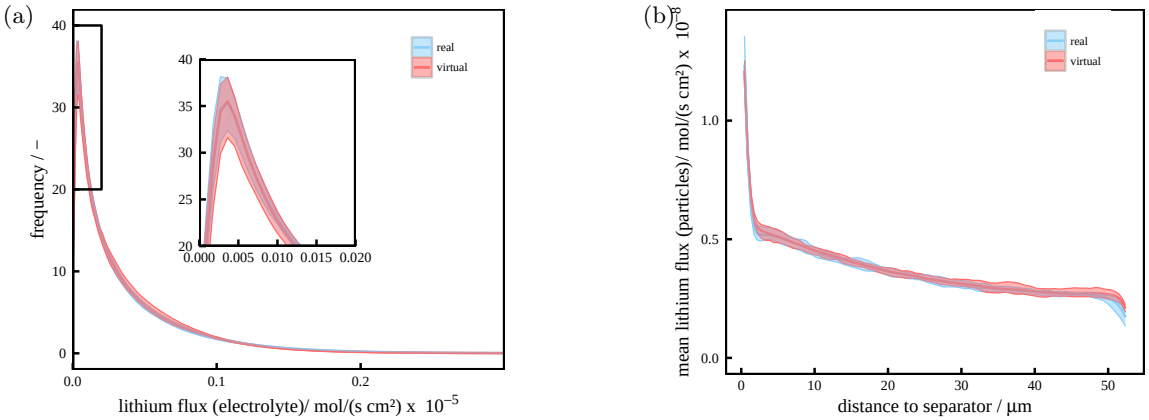

Figure 5.7.: (a) Histogram of the lithium ion flux density inside the electrolyte phase for the high applied current. (b) The spatial distributions of the lithium flux inside the solid phase exhibit a good agreement. The real microstructures show a slightly lower lithium flux close to the current collector.

spatial distribution of the lithium flux inside the solid phase is shown in fig. 5.7(b). The electrode has a flat surface at the separator interface and therefore a locally increased active surface. As a result an increased lithium flux can cross from the solid into the electrolyte phase. The increase in lithium flux is more abrupt for the real structures than the virtual ones. In the region close to the current collector (on the other side in through-direction) the real microstructures exhibit an earlier decrease and a smaller value at the interface to the current collector. Both features are a result of the difference in the solid volume fractions close to the current collector and separator.

Conclusion and outlook

Overall a good agreement between the real and virtual microstructures from the electrochemical point of view has been found. The main deviations are rooted in the differences in the solid volume fraction. The increase of the SVF close to the surfaces in through-direction are likely caused by the calendaring process [134, 135]. This is to be addressed in a new version of the stochastic structure model. The electrochemical validated structure model was used for a publication, which illustrates the workflow achieved in the scope of the MULTIBAT project [136]. The separator-electrode interface of microstructures, which are based on the electrochemical validated stochastic microstructure model [10], are modified using a simple algorithm such, that a plated lithium phase is included. These modified structures are used to apply a Model Order Reduction scheme to the full electrochemical equation system. This method reduces the amount of calculations needed to find the solution for the system. The method of electrochemical validation was also applied in a rudimentary form to a 3D stochastic microstructure model, which describes the anode structure of lithium-ion power cells. This model shows also a promising agreement between the real and virtual structures. More information about the stochastic model for high power cells can be found in [119].

5.2. Time evolution of plating condition

It is well known, that the ambient temperature and the applied current influences the onset of lithium plating inside a lithium-ion battery. These effects are investigated using the *classical* battery model applied to a full-cell geometry during charging. In fig. 5.8(a) the cell potential of the various operation conditions is shown. It can be seen, that an increase in applied current or the lowering of ambient

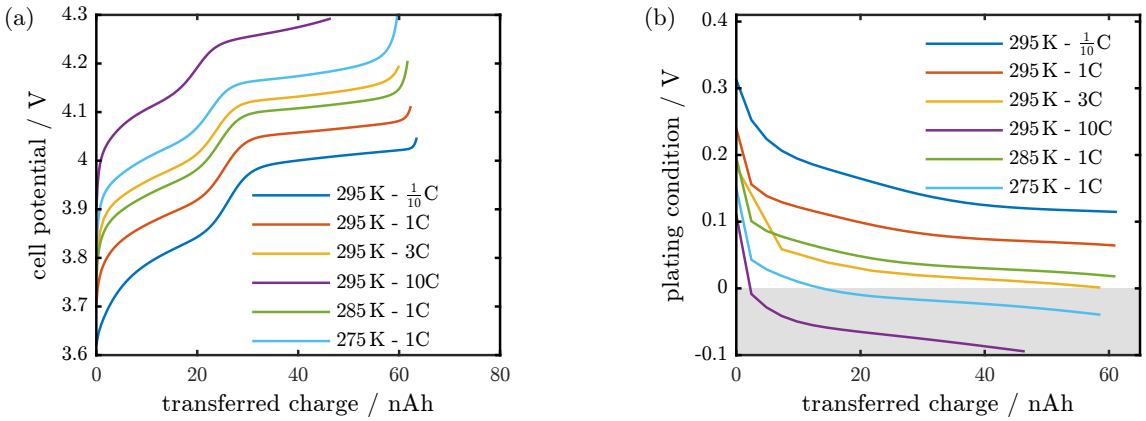

Figure 5.8.: (a) Cell voltage for the different charging operation conditions. (b) The time evolution of the minimum plating condition for the different operation conditions at the separator-anode-interface. (reprinted with permission from [12]).

temperature results in an increased overpotential inside the battery and hence in a shift of the cell voltage towards higher values. The different end potentials are a result of the simulations. The open circuit potential is calculated for each discretization volume inside the microstructure. If one of these

volumes reaches the maximum allowed concentration, as defined by the state of charge range of the open circuit function, the simulation ends. This is highly influenced by the size of discretization due to the solid diffusion coefficient, which is temperature dependent. Together with the effect of the applied current, these "cut-off" potentials vary between the different operation conditions. A more correct calculation and determination of the cut-off potential was not focus of these simulations and hence no optimization of the behavior towards the end of charge is done. The plating simulations, which are presented in latter sections, require an OCV that exhibits diverging features at the limits of the SoC range. The OCV is therefore extend as described in section 3.3.1. The increase of applied current or decrease of ambient temperature leads to a higher cell potential. It can be noted, that these effects result in a similar cell voltage for the charging with 3C at 295 K and 1C at 285 K. The cell voltage itself allows no conclusions regarding the plating condition: neither globally nor locally. But, the 3D simulation generates spatial and temporal information on the concentration and potential landscape. In fig. 5.9 the spatial distribution of the plating condition for the highest charging current at room temperature after a transferred charge of 10 nAh is displayed. It can be clearly seen, that the plating condition is

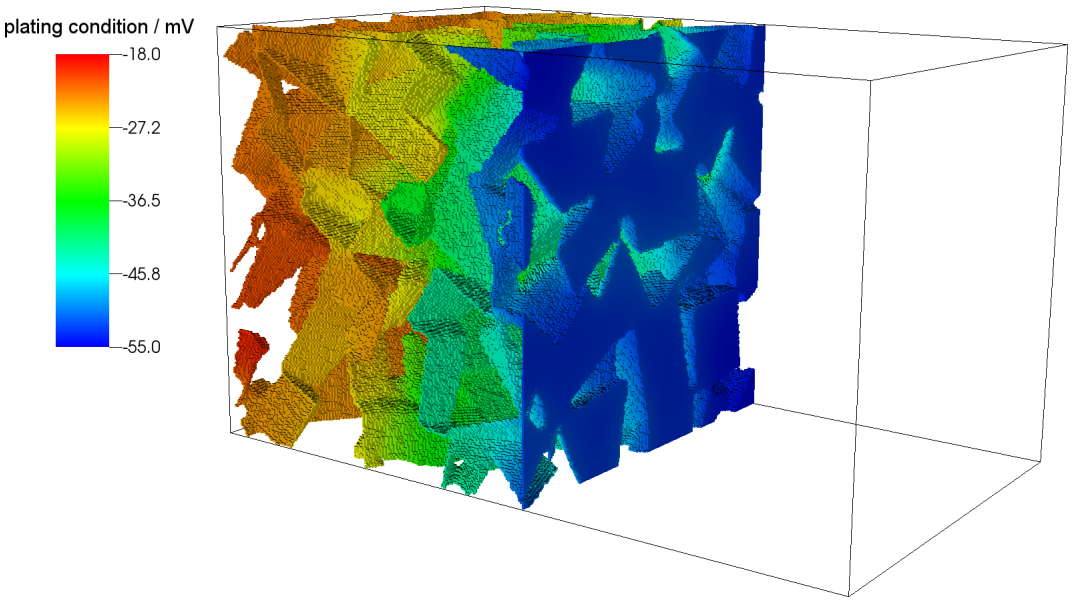

Figure 5.9.: The spatial distribution of the plating condition at 10 nAh exhibits the lowest value at the separator-anode-interface. This indicates a high probability, that lithium will be plated at that position.

fulfilled over the whole anode surface with the lowest value close to the separator. The simulations shown here do not include any side reactions and hence no feedback of a possible plating reaction on the potential landscape is resolved. The impact of plating onset on the potential inside the lithium-ion battery will be discussed in section 5.6. This indicates, that one could expect the complete surface of the anode to being covered with plated lithium. As a result of a lithium film covering the surface, it is expected, that the overpotential stays fairly constant, since during constant current operation the plating and stripping reaction is fixed to a constant value. This feedback and situation is observed using the surface growth model (see section 5.4). The temporal evolution of the plating condition is extracted at the separator-anode-interface and shown in fig. 5.8(b). As expected, the plating condition

is fulfilled the earliest during charging with high currents or at low temperatures. These observations conform to experiments for the simulated materials, where lithium plating is taking place during high current charging or low temperatures [77]. Under the assumption, that lithium plating will start as soon as it is thermodynamically possible, the largest amount of plated lithium is expected for an early plating onset. The surface growth model (see section 3.1.2) is later used to investigate how the actual formation of a plated lithium phase influences the potential landscape inside the batteries. The plating condition for the different operation conditions in fig. 5.8(b) is obtained the following way from the 3D data: For every output-timestep the plating condition is calculated for every voxel. For this calculation, the average overpotential of all active interfaces is used. Afterwards a histogram is generated for every timestep. In fig. 5.10(a) the resulting histograms of the 10C charging data are displayed as a contour plot. The plating condition stretches as a band across the lower part of the figure. Two different regions are identified: The position of the maximum count in the histogram (**max count**) and the position of the lowest plating condition (**min PC**). The stretch between the minimum plating condition value and

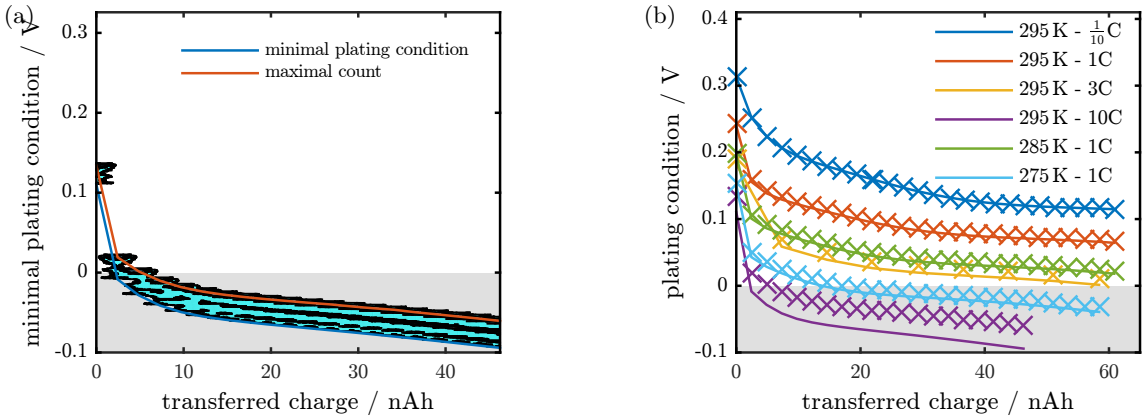

Figure 5.10.: (a) Histogram of plating condition for the different operation conditions for 10C and 298K. (b) Comparison of the **min PC** and **max Count** condition.

the maximum count indicates, that for the 10C discharge the electrode exhibits a very inhomogeneous electrochemical condition. The region, where the minimum value occurs, can be identified as the electrode-separator-interface. The two different features are compared in fig. 5.10(b). This reveals that the differences for small currents ($\leq 1C$) are nearly negligible. The part of the electrode, where the plating condition is fulfilled first, is the most probable area for plating onset. It is therefor suggested to use the minimum plating condition as critical indicator, as it is done in the rest of this work. The deviation between minimum condition and maximum count also has indications regarding the usage of a reference electrode in a three-electrode setup. The voltage E_{An} measured between the negative electrode and the reference electrode is often used as indication of lithium plating (see section 2.5.4 and [79]). When only a small fraction of the electrode experiences lithium deposition, the signal E_{An} could still be dominated by the majority of unplated regions. Thus E_{An} would not correctly display the plating risk.

5.3. Volume resolved system: Impact of plated lithium on battery

Using the volume resolved model, the influence of an existing plated lithium phase on the performance of the lithium-ion battery is investigated. As described in section 4.2.3, the structure of the anode (see fig. 4.9) is taken and slightly modified to include a dedicated plated lithium phase (see fig. 4.11). These modified geometries are then delithiated with a constant current. The cell potential during this operation for different locations along the through-direction is plotted in fig. 5.11(a). Due to the large

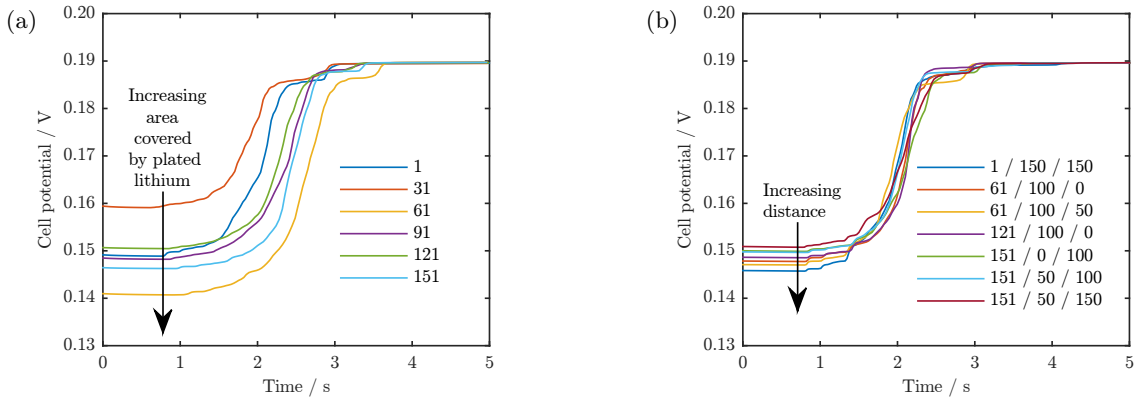

Figure 5.11.: (a) The cell potential of half-cells during a constant current charge with a plated sector along the x-axis with $y = 0/z = 0$. The arrow indicates the direction of increasing surface area covered by the plated lithium phase. (b) Cell potential of half-cells with a lithium covered surface of $8.50 \cdot 10^{-6} - 8.75 \cdot 10^{-6}\,\mathrm{cm}^2$. The arrow indicates the direction of increasing distance of the plated lithium sector from the current collector. (reprinted with permission from [12]). The coordinates of the plated sector are given in the figure legend.

amount of simulations, only the cell potentials for the sectors along the x-axis with $y = 0$ and $z = 0$ are shown. The other sectors behave similarly. The cell voltage exhibits a plateau at the beginning of delithiation. Which is followed by a first slow and then faster increase of the potential. The cell voltage afterwards is identical for all investigated half-cells. The voltage level of 0.19 V is the cell potential of graphite at a state of charge of 70 % shifted by the overpotential of a constant current charging. The initial potential plateau is due to the stripping process, which takes place at constant potential. The strong increase of the cell potential can be seen as soon as the plated lithium is nearly completely consumed. To simplify the analysis of the cell potential during stripping, it is approximated by three consecutive linear fits. This approach is used due to artifacts in the cell potential. The cell potential is separated into three regions: initial potential level, section with biggest change and final potential level. Each regime is fitted with straight lines (eq. (5.1)).

$$g\,(t, m, t_0) = t_0 + m \cdot t \tag{5.1}$$

In fig. 5.12 the three linear fits are shown on the blue curve in fig. 5.11(a). The intersections between the three lines are marked as "point 1" (t_1, V_1) and "point 2" (t_2, V_2). It is assumed, that at the x coordinate t_2 all lithium would be stripped if no potential artifacts existed. Thus, one could use this

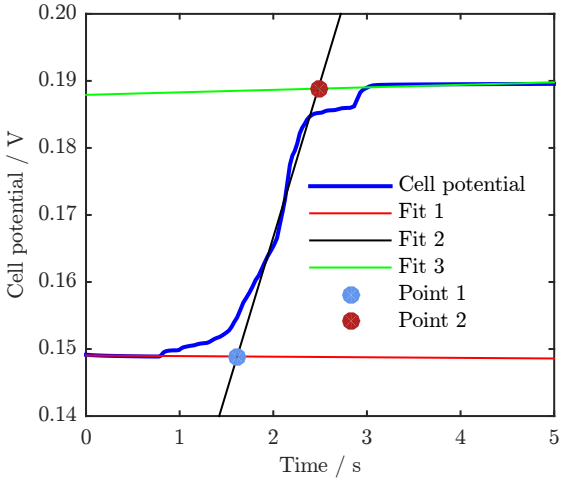

Figure 5.12.: The linear fits to the three regions of the stripping cell potential of sector S(1/0/0) used to estimate the plateau duration and size of potential difference. (reprinted with permission from [12])

point t_{strip} to estimate the amount of plated lithium.

$$t_{\text{strip}} = t_2 \tag{5.2}$$

The height of the voltage drop due to the stripping process is approximated using the differences in the y coordinates:

$$\Delta U_{\text{Plateau}} = V_2 - V_1 \tag{5.3}$$

Using the shown approximations the average potential jump of all 192 simulations is $\Delta\bar{U}_{\text{Plateau}} = 44.5\,\text{mV}$ with a standard deviation of 5.6 mV. The average stripping duration is $\bar{t}_{\text{strip}} = 2.48\,\text{s}$ with a standard deviation of 0.25 s. This corresponds to a charge of 0.07 nAh. The concentration distribution of the lithium ions inside the electrolyte for three different locations of the plated lithium phase are displayed at two different times in fig. 5.13. Local concentration maxima can be seen while lithium is stripped (upper row in fig. 5.13). These features are spatially localized to the pore space above the surface of the plated lithium phase. The peakedness of a maximum depends on the pore connectivity close to the plated phase, where a smaller pore leads to a higher concentration (see sector S(91/0/0)). After the plated lithium is completely dissolved, the concentration maxima slowly degenerated due to the lithium diffusion inside the electrolyte. The electrolyte concentration profile of a plated cell will then relax to the profile of an unplated cell, where the lowest concentration is close to the anode current collector and the highest concentration close to the cathode current collector. Cells with a plated sector close to the anode current collector will take more time to reach the profile of an unplated cell. This is visible for the lower right picture in fig. 5.13. The zoning behavior of the concentration maxima can not be resolved in a 1D+1D-Newman-type simulation, since the concentration in the electrolyte in the lateral

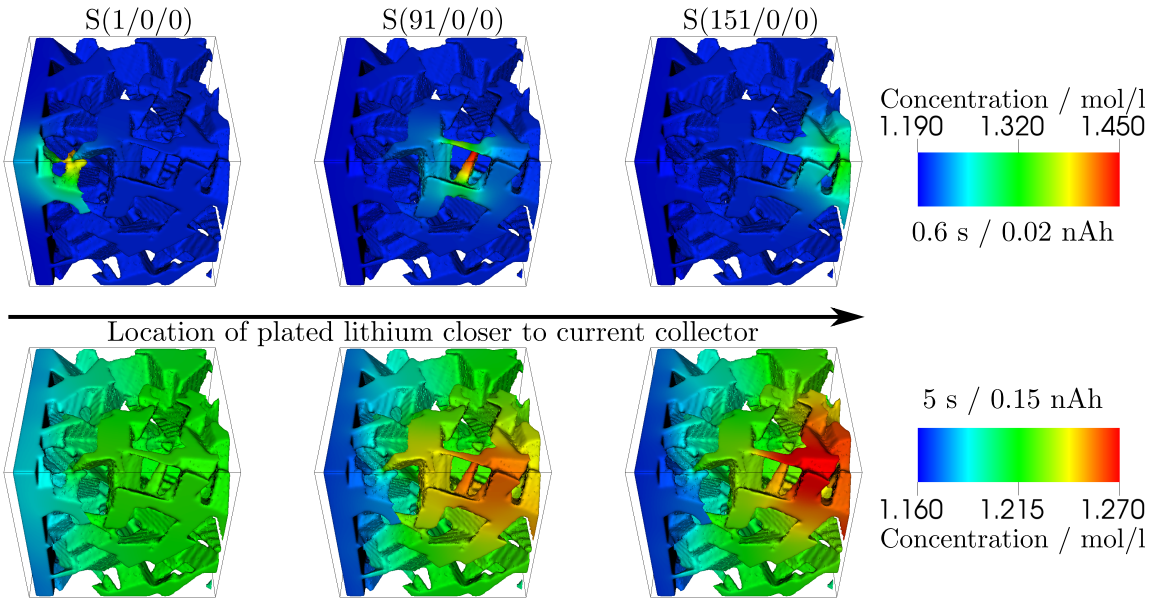

Figure 5.13.: The spatial distribution of the lithium concentration in the electrolyte phase for three different locations of plated lithium at 0.6 s (upper row) and 5 s (lower row). While the plated lithium phase still is stripped, a local maxima close to its location is found. At the end of simulation these maxima are nearly dissipated and hence are less distinctive.

direction is not resolved. Furthermore, other spatially in lateral directions localized effects can also be resolved with this 3D transport theory.

Influences on the potential plateau

All microstructures used for the half-cell stripping simulation have the same thickness of lithium, namely 50 nm. The surface area onto which the lithium is added differs between the modified structures and hence also the total amount of lithium added. The initial cell potential and the duration of the stripping plateau depend on the amount of plated lithium and the size of the plated surface. Hence the cell potentials shown in fig. 5.11(a) exhibit some variation in initial level and stripping duration.

With an increasing surface area covered by plated lithium the stripping plateau is lowered towards the Li/Li^+ redox potential. The covered surface area of the sectors $x = 31$ and $x = 61$ (as seen in fig. 5.11(a)) is $5.8 \cdot 10^{-6}\,cm^2$ and $12.7 \cdot 10^{-6}\,cm^2$ respectively. The cell potential of these two exhibits an initial potential level of 159 mV (potential jump of 30 mV) and 141 mV, respectively (potential jump of 49 mV). In this example, an increase of 112 % in surface coverage results in a lowering of the plateau level by 63 %. The larger the coverage of the surface area with plated lithium, the further the initial cell potential is lowered. For the case of the whole surface area of the graphite be covered by a lithium film, an effective lithium/lithium-cell is created. If so the difference between the stripping plateau and the Li/Li^+ potential would purely given by the overpotential due to the applied current.

Apart from the surface coverage, also the distance of the plated lithium sector relative to other battery components, such as current collector or counter electrode, could influence the cell potential. Thus, it is investigated, if the distance from the plated sector towards the current collector has any correlation

visible in the cell potential. As shown in the previous paragraph, the amount of surface area covered by plated lithium has a large impact on the cell potential. Therefore we selected plated sectors where the surface coverage lay within a thin region ($8.50 \cdot 10^{-6}\,\mathrm{cm}^2$ and $8.75 \cdot 10^{-6}\,\mathrm{cm}^2$). The cell potentials of such sectors is sorted according to their distance to the current collector and are shown in fig. 5.11(b). It can be seen, that an ordering of the cell potentials took place. The plateau height for the selected simulations changes about 5 mV for a distance of roughly 66 µm. This small distance dependence is not based only on the electrolyte resistance. For a constant electrolyte concentration, which exists e.g. at the start of delithiation before the lithium had time to respond, the electrochemical potential in the electrolyte decreases by around 1 mV over a distance of 70 µm.

The fraction of surface area covered by plated lithium has a greater impact on the plateau height than the distance of the plated sector from the current collector. Additionally to the influence on the potential level, an increase in covered surface area also increases the stripping duration and thus the amount of charge transferred. This is not only a result of an increase in the amount of metallic lithium, since the transferred charge will also depend on the ratio of the intercalation exchange current amplitude and the plating exchange current magnitude, as is discussed in more detail in the next section.

The interface currents during lithium stripping

The 3D simulation of a lithium-ion battery allows to investigate the distribution of quanitites, which can not experimentally be obtained. The currents at the interfaces are of great importance during stripping. In fig. 5.14(a) the stripping current and the graphite intercalation current for one plated sector during stripping operation with the different applied currents are shown. To allow for an easier comparison, they are normalized to the applied current. The net charge transferred during the stripping

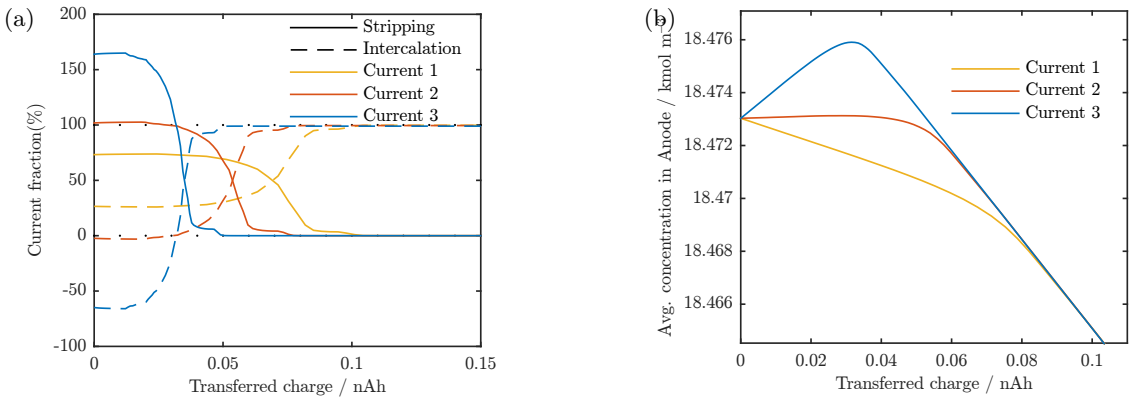

Figure 5.14.: (a) Temporal distribution of the total current on the two reactions inside the graphite electrode during stripping against the transferred charge. The current composition during the stripping process depends on the applied currents (see table 4.12). (b) The average concentration in graphite during stripping of plated lithium in sector S(91/0/0) with three different applied currents. Shown for the lithium in sector S(91/0/0). (reprinted with permission from [12]).

plateau is smaller for smaller applied currents. A subtle competition between the local oxidation of

plated lithium and the reduction of lithium ions during the intercalation into graphite is the root of this finding. It emerges that for low currents the oxidative stripping of the metallic lithium film results in an effective surplus of lithium ions in the adjacent electrolyte (see fig. 5.13). These lithium ions are then available for the intercalation into the graphite. Thus, the total intercalation current between the graphite and the electrolyte can either be positive, zero or negative. The sign convention used with regard to the interface currents is such, that a positive value indicates stripping or deintercalation, while a negative interface current represents intercalation or lithium plating. During the stripping a negative interface current is only observed between the electrolyte and the uncovered graphite. Hence, for the higher current (current 1) the lithium deintercalates from the graphite and for the lowest current (current 3) lithium intercalates into the graphite. The resulting change in the lithium concentration inside the graphite is visible in fig. 5.14(b). The lowest current clearly results in an increase of the average lithium concentration during the stripping of the plated lithium. This lithium accumulation is followed by a net deintercalation. Only at large currents, an overall deintercalation from the start of delithiation is observed for all times. In fig. 5.15 the spatial distribution of the sign of the interface currents for the three different applied currents is overlayed on the surface of the 3D structure. Please

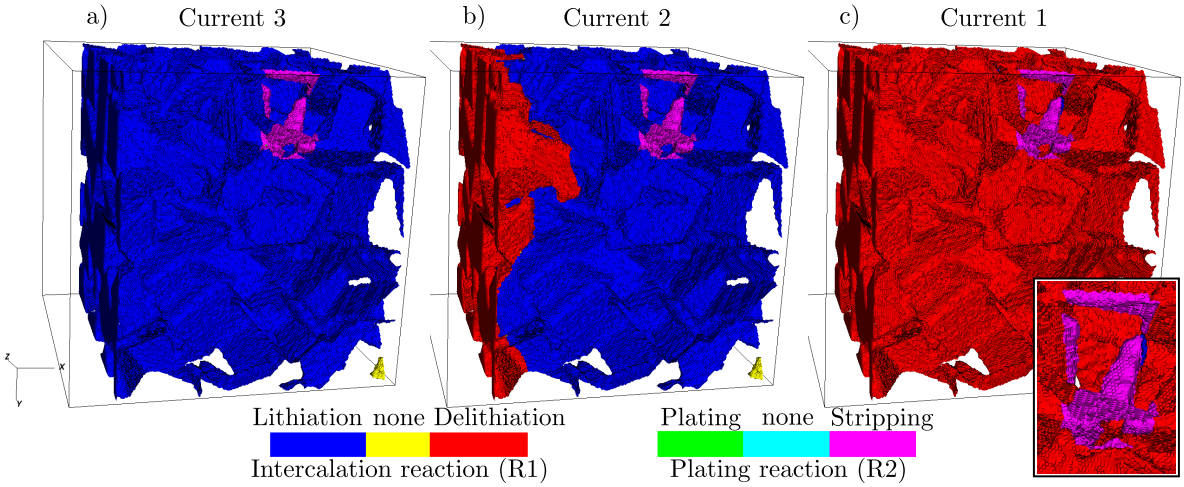

Figure 5.15.: The sign of the interface currents for three different applied currents in 3D representation during delithiation at 0.02 nAh. Blue indicates intercalation at the graphite-electrolyte-interface and red delithiation. A green colored electrolyte-plated lithium-interface represents plating, while a pink colored one means stripping. For all the currents, the plated lithium is stripped, whereas the graphite either intercalates or deintercalates lithium depending on the applied current. The microstructure with a lithium sector S(91/0/0) is shown. (based on [12])

note, that only the solid voxels sharing an interface with the electrolyte are visible. All other parts (counter electrode, electrolyte, ...) are transparent. Areas of lithiation or delithiation (eq. (Inter-G)), plating or stripping (eq. (Pl/St)) are shown color coded. The plated sector is visible as pink region for all currents, which indicates that lithium stripping is taking place. It is clearly visible, that for the smallest current (fig. 5.15 a)), lithium only enters the electrolyte through the lithium stripping reaction, while lithium is intercalated from the electrolyte into the graphite. For the second current (fig. 5.15 b)) a mixed state can be seen: At the separator-electrode-interface the graphite only deintercalates lithium, while the other region still intercalates. For the highest current (fig. 5.15 c)) the graphite exhibits

delithiation nearly everywhere, except for a small portion close to the plated sector (shown in inset in lower right corner). Noteworthy is also the small yellow region in the lower right corner of the 3D structure. The yellow color indicates, that this surface is not electrochemical active. This is due to the neighboring electrolyte pore being unconnected to the main electrolyte body.

Estimation of amount of plated lithium

Even though the estimation of the amount of plated lithium and with this the severity of this degradation process can be done after things have gone wrong, it is nevertheless an important information. One method of choice is the differential voltage, as described in [74]. Based on the potential drop in the discharge cell potential the amount of plated lithium is estimated. The interpretation of the potential drop duration as a marker for the amount of plated lithium is supported by neutron diffraction measurements [81]. For the differential capacity the derivative of the cell potential with respect to the transferred current Q is calculated. The position of highest change is selected for the lithium amount estimation. The 3D resolved simulations allow for a more detailed investigation of the potential and limitations of the proposed method. The differential capacity for the simulations in fig. 5.14(a) at the three different applied currents is plotted in fig. 5.16. The total amount of charge transferred

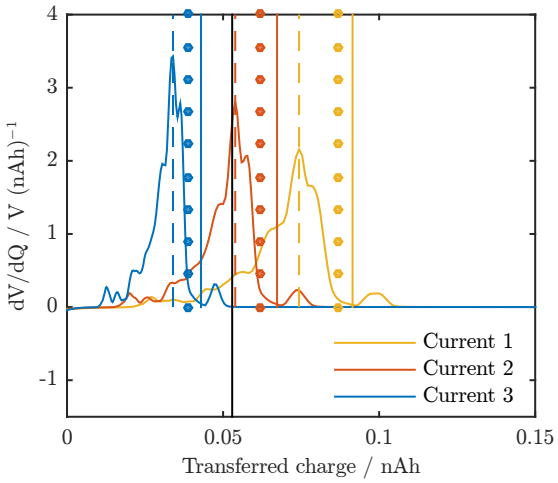

Figure 5.16.: The differential capacity calculated from the cell potential for sector S(91/0/0) for the three different currents. The amount of plated lithium estimated using different methods are highlighted with colored vertical lines.

by converting the plated lithium layer into lithium ions is marked as solid black line. The amounts estimated using different methods are shown as dashed, dotted or colored solid lines. Applying the differential voltage method on the simulation results yields then estimations shown as dashed lines. The dotted line represents the amount obtained via "point 2" of the line fits (see eq. (5.2)). The solid colored line represents the position, when the average thickness of the plated lithium in the system is less than 0.48 nm. For any of the applied currents, the estimated amounts are not the same for the different methods. A dependency on the applied current is clearly visible. Even though it could happen, that for a certain current the estimated amount of a method is the same as the exact amount of lithium,

one cannot experimentally prove if that is the case. Depending on the applied current the amount of plated lithium can be overestimated or underestimated. So, with the differential capacity method only a rough approximation of the plated lithium can be obtained. Table 5.1 lists the deviations of the estimated amount of lithium from the real amount of lithium for the three different analysis methods.

Table 5.1.: Difference between correct amount of plated lithium and estimated. (reprinted with permission from [12])

Current	Error of method in %		
	dVdQ (dashed)	Fits (dotted)	avg. thickness (solid)
Current 1	36	26	19
Current 2	-2	-17	-27
Current 3	-41	-64	-73

5.4. Surface growth: Comparison coupled and decoupled system

The developed model for lithium plating and stripping can be included into the simulation framework BEST two ways. As addition to the mass balance and charge conservation equation, thus resulting in one large system. Or as additional system, which is solved after the classical system. In this section the two approaches are investigated. The coupled and decoupled system are solved with the same material and numerical parameters. The cell voltages of the constant current charge are plotted in fig. 5.17(a). Both, coupled and decoupled, deviate visible from the classical case. The system with

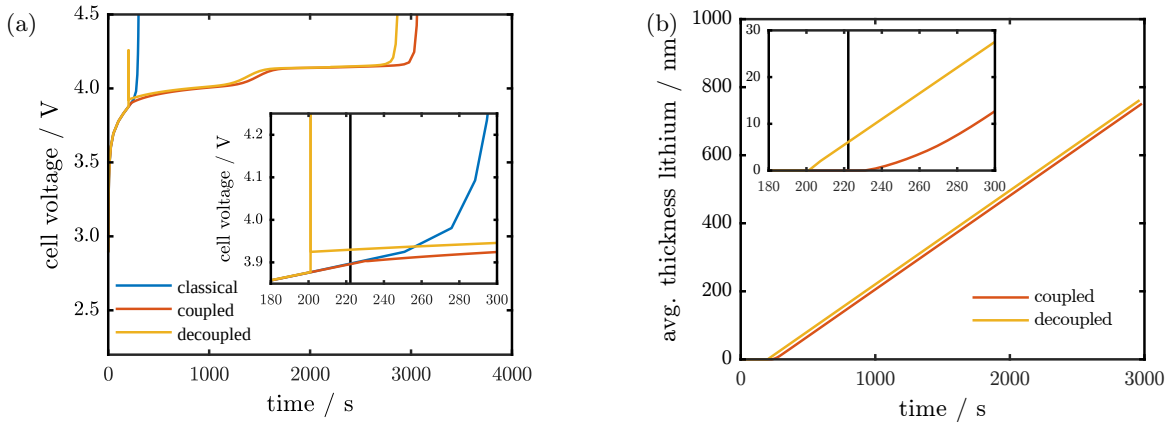

Figure 5.17.: (a)(main) The cell voltages of the coupled and decoupled system show a clear deviation from the classical system. (inset) Close up of the cell voltage where the plating condition (black line) was fulfilled for the classical system. The decoupled system (yellow) exhibits a voltage jump around 200 s. (b) Average thickness of plated lithium in the coupled and decoupled system. (inset) The coupled system shows a smooth transition from unplated to plated.

lithium plating changes from a anode dominated cell potential to a pure cathode cell potential. The point in time, where this takes place differs between the coupled and decoupled system. The region

around the fulfillment of the plating condition in the classical system is shown as inset in fig. 5.17(a). The decoupled system exhibits a strong overshoot at the point, where it switches from not plated to fully plated. This feature is a first indication, that the decoupled system is exhibiting unphysical behavior and thus not being a good choice for plating simulations. The average thickness of plated lithium (see fig. 5.17(b)) starts to increase at the same time, when the cell potentials exhibit the deviation from the classical case. The beginning of lithium deposition exhibits a different behavior for the coupled and decoupled system. The average lithium thickness for the decoupled system shows a discrete change in slope (see inset in fig. 5.17(b)). The lithium thickness of the coupled system features a slow increase until a constant slope is reached. After the initial region both system exhibit the identical slope. The slope is directly proportional to the applied current. The constant slope indicates, that all current reaching the negative electrode is leading to growth of the plated lithium phase. The average thickness amounts to nearly 0.8 µm after over 2700 s of plating.

A look at the average concentration inside the electrodes reveals unphysical behavior of the decoupled system. The concentration of the anode and cathode (see fig. 5.18(a)) exhibit a jump at the position of the cell potential overshoot. Nevertheless, the total amount of lithium in the system is conserved. The

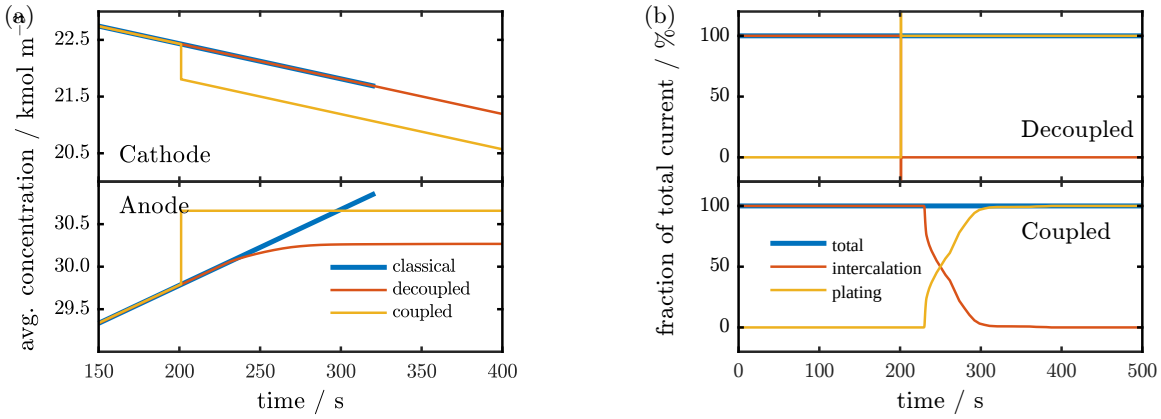

Figure 5.18.: (a) The average concentration in the solid electrodes. The decoupled system exhibits a discrete change in anode and cathode concentration. (b) The distribution of the interface current onto the direct intercalation and plating path.

concentration inside the anode for the coupled system changes from a monotonic increase to a constant value. This represents the change from direct intercalation towards the plating reaction as main reaction at the anode. The cathode concentration for the coupled system exhibits no visible deviation from the constant slope and is incident with the classical case. These findings are interpreted such, that the coupled system yields a physically consistent solution. The impact of numerical parameters on the solution of the coupled and decoupled system was tested further. At first the impact of the relative solution tolerance on the temporal location and the number of numerical iteration needed is studied. This tolerance is used as the numerical convergence criteria (see section 3.2), . The cell voltage of the two systems show no visible dependence on the relative solution tolerance. Only the lowest tested solution tolerance results in small deviations for the coupled system. In fig. 5.19 the impact of the relative solution tolerance on the cell voltage of the coupled and decoupled systems is visible. A zoom

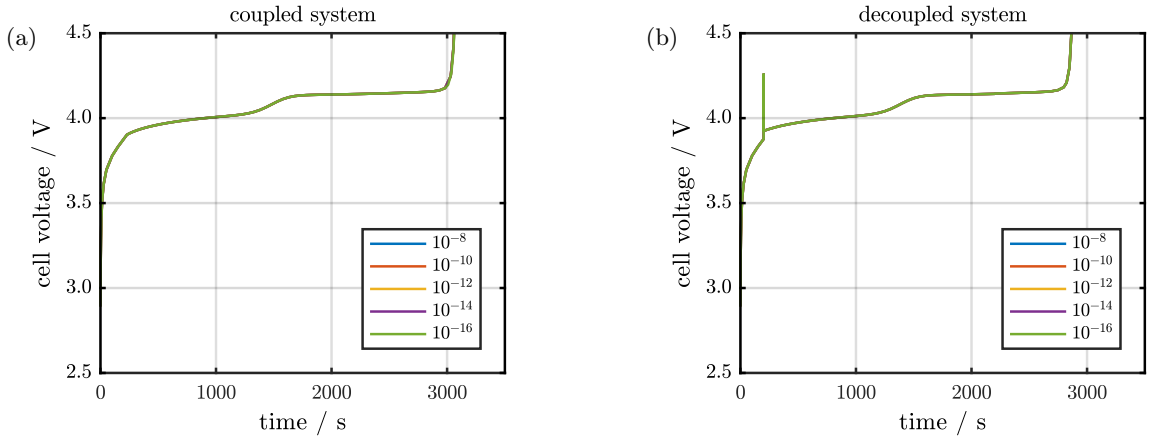

Figure 5.19.: The variation of the relative solution tolerance has no large impact on the cell voltage of the (a) coupled and (b) decoupled system.

at the regions around the plating onset (see fig. 5.20) reveals some small deviations. Each successful simulation time step is marked by a circle, thus allowing to see variations in the time steps. The result of the decoupled case is unaffected by the tolerance variation (see fig. 5.20(b)). The coupled case (see fig. 5.20(a)) exhibits a variation in the time steps and a slightly smaller voltage variation for the smallest relative solution tolerance. Overall no strong impact of the solution tolerance on the cell

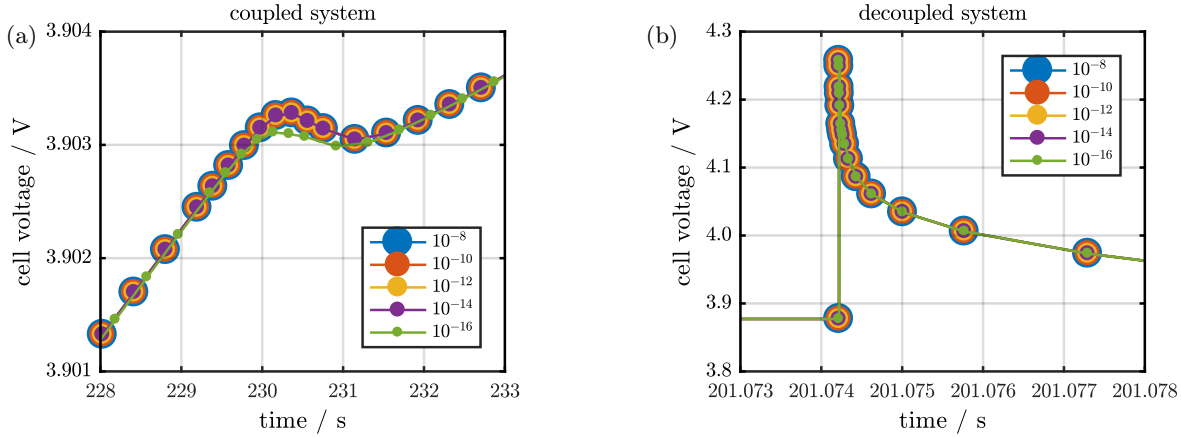

Figure 5.20.: A zoom on the region around 200 s of fig. 5.19: While the coupled system shows a small variation for the smallest relative tolerance (a), no influence can be seen for the decoupled system (b).

voltage could be found. Apart from the electrochemical results the amount of time the simulation needs to complete one full simulation is used to judge the numerical performance of the coupled or decoupled system. The runtime until the simulation reaches 2500 s is plotted (see fig. 5.21) for the coupled and decoupled system as a function of relative solution tolerance. The decoupled system exhibits a nearly constant amount of time, while the coupled system shows an increase towards smaller tolerances. If both systems would return the same result for electrochemical situation inside the battery system, one would prefer the decoupled system.

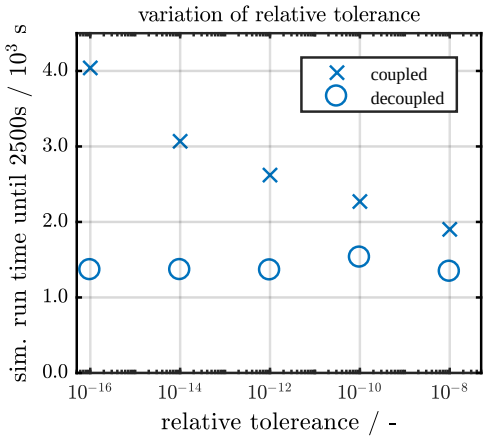

Figure 5.21.: The duration of the simulation to reach 2500 s in the simulation time frame.

The average thickness of plated lithium for the coupled and decoupled system in fig. 5.22 show the same trends as seen in the cell potentials. The coupled system exhibits a slight variation for the lowest

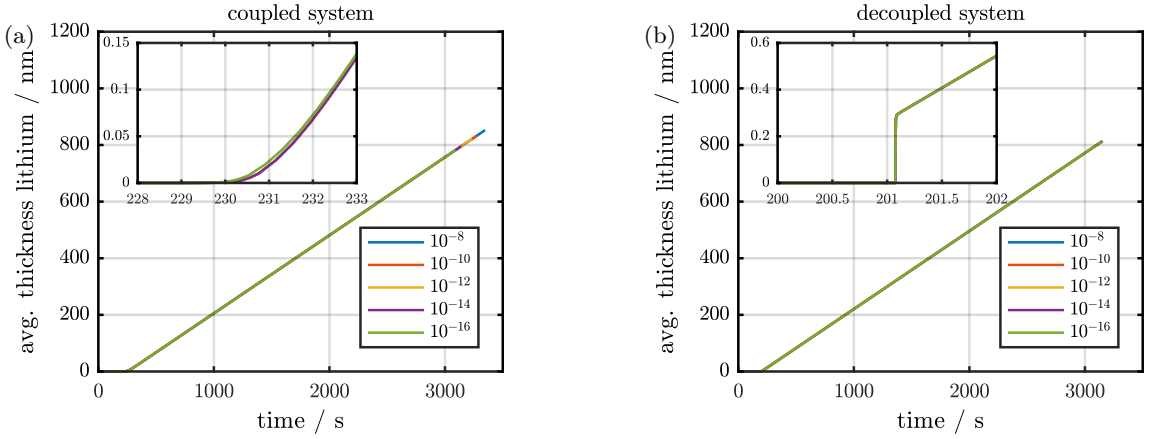

Figure 5.22.: The average thickness of the plated lithium for the (a) coupled and (b) decoupled system.

solution tolerance, while the curves retain similar shape.The jump in thickness for the decoupled case corresponds to a complete switch from unplated to plated active surface. The concentration inside the anode and cathode phases are nearly identical to the ones shown in fig. 5.18(a) and are therefore omitted.

A relative solution tolerance of 10^{-14} is selected as basis for the study how the maximum allowed time step size Δt influences the simulation result. The maximum time step of the previously shown simulations was set to 50 s. The result of the variation study with $\Delta t \in [1, 2, 5, 10, 25, 50]$ s is presented in the following. The decrease of maximum time step has a immense impact on the cell voltage for the decoupled system (see fig. 5.23(b)) and a minor shift for the coupled system (see fig. 5.23(a)). The decrease in maximum time step leads to a shift of the plating feature for the coupled system by roughly 2 s, while preserving the shape and height of the feature. The situation of the decoupled system is more complex. At first glance one will notice the decreasing sharpness of the discrete jump in the cell potential. The cell potential around the plating feature still exhibits an erratic behavior. The change

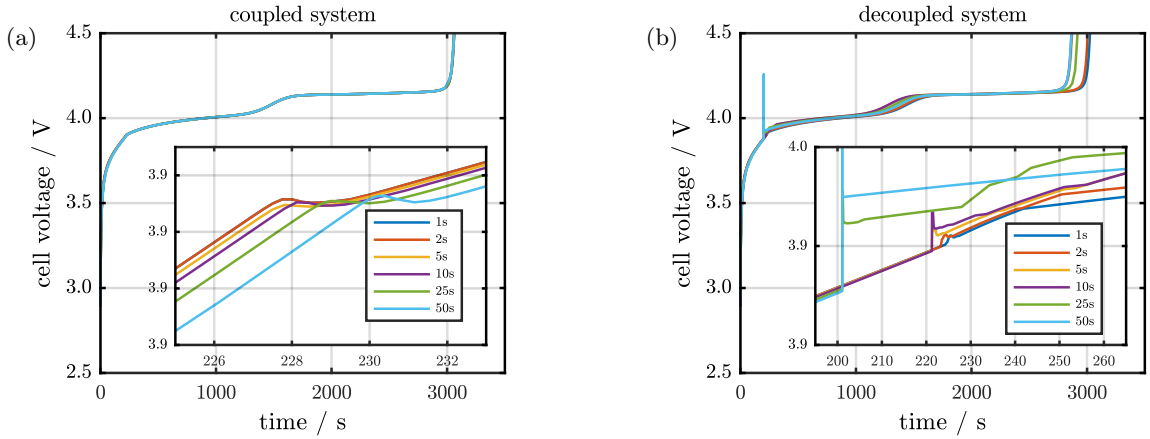

Figure 5.23.: The cell voltage for the (a) coupled and (b) decoupled system with different maximum time steps.

from anode limited to cathode limited operation for the decoupled system moves closer to the time region, where the coupled system exhibits this change. The average lithium concentration inside the cathode (see fig. 5.24(a)) for the decoupled system reveals, that even for the maximum time step set to 1 s unphysical behavior exists. The decrease in the maximum time step has an larger impact on the

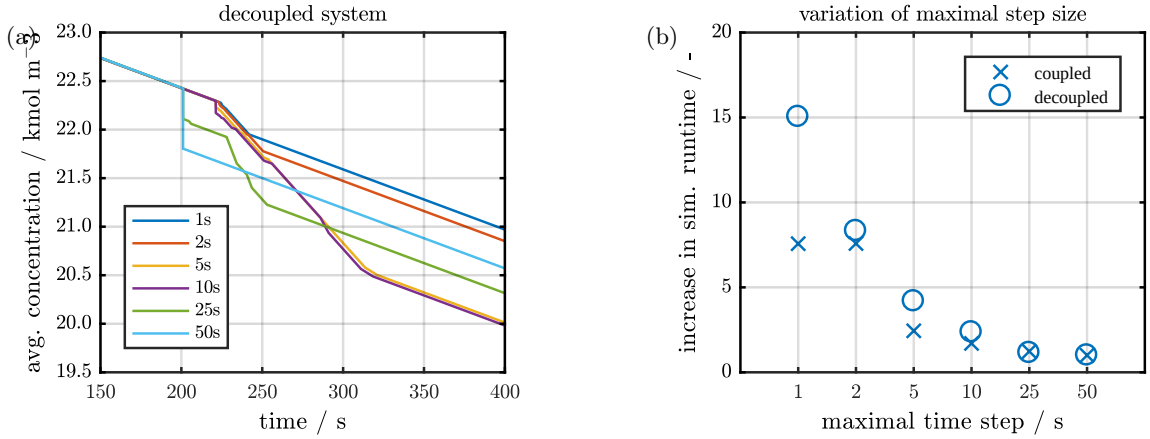

Figure 5.24.: (a) The average concentration in the cathode for the decoupled system. (b) The impact of maximum time step on the simulation runtime with respect to the runtime at 50 s step size.

simulation runtime than the variation of the relative solution tolerance. A side effect of the decreased step size is the increase of simulation runtime, as can be seen in fig. 5.24(b). There the increase in runtime with respect to the runtime at 50 s as maximum step size is given for the coupled and decoupled system. Both system exhibit similar behavior. The runtime of the coupled system increases slightly less than the decoupled system. Due to the physically consistent results of the coupled system, it is selected as basis for the further investigations of lithium plating.

5.4.1. Impact of the dissolution barrier constant

The influence of the dissolution barrier constant d_0 was investigated in this section. Its value was varied between 10^{-9} and 10^{-4}. Varying the barrier constant allows to investigate, how the dissolution barrier impacts the growth of a plated lithium film. The cell voltages for the variation of the dissolution barrier constant d_0 are shown in fig. 5.25(a). The different curves overlap quite good for the majority of the simulation. The only visible difference can be found around the time, when lithium deposition due to the plating reaction begins until the majority of charge transfer is completed by the plating reaction. A

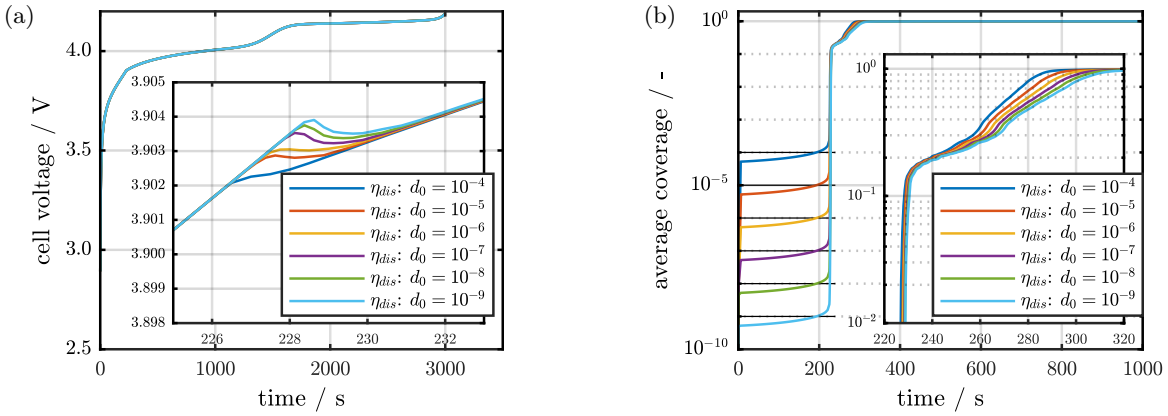

Figure 5.25.: (a) The cell voltage of the test system exhibits more pronounced dip for smaller constants d_0. (b) The average coverage reveals, that for all constants the plating onset is at nearly the same time. 20 % coverage is achieved simultaneous.

more pronounced local maximum appears for smaller constants. Although the different cell voltages are nearly coincident shortly after the feature of plating onset, the average surface coverage (see fig. 5.25(b)) reveals, that it takes roughly 90 s to achieve full coverage. In fig. 5.25(b) the fraction of the total surface covered by plated lithium is displayed. The different values of the barrier constant are included as horizontal black lines. All simulations reached an average coverage equal to the barrier constant at the same time. Shortly afterwards the surface coverage starts to increase rapidly. The largest increase of surface coverage is nearly identical for all tested values. The main difference between the different barrier simulations is the total time needed from the unplated surface until complete coverage with the largest constant ($d_0 = 10^{-4}$) being the fastest.

In the following we try to identify, how the variation of barrier constant results in the variation of the cell voltage feature as seen in the inset of fig. 5.25(a). Let assume, that a change of dominant reaction took place, thus resulting in a different potential dependence and reaction rate. Before the onset of plating, all charge transfer between the anode and the electrolyte is sustained by the direct intercalation (see eq. (Inter-G)). After plating onset a superposition of direct intercalation and lithium plating exists. The exact contributions of the two reactions towards the total current is shown in fig. 5.26(a). The complete charge transfer is done by the plating reaction roughly around $t = 350$ s. The largest deviations in the current fractions for the varied barrier constants occur after the plating current corresponds to over 50% charge transport, with smaller barrier constant taking more time to

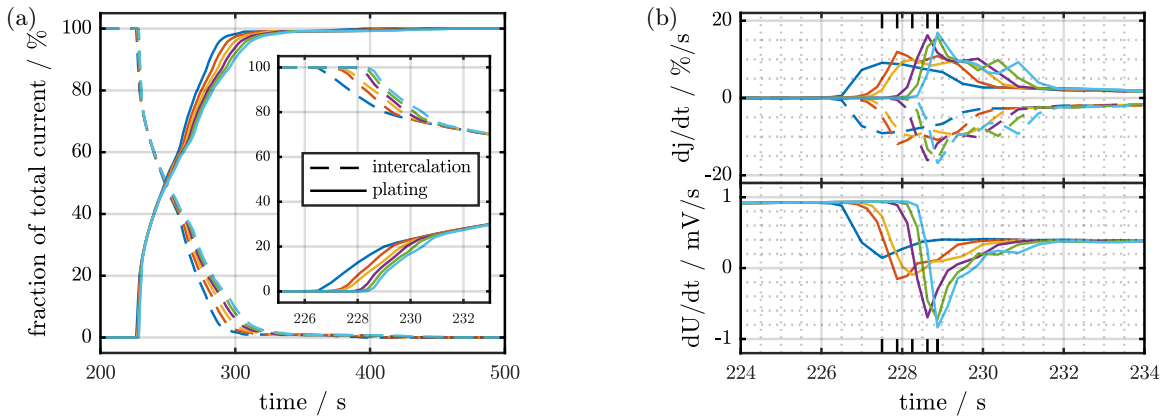

Figure 5.26.: (a) The distribution of total current on the intercalation and plating reaction. The color assignment is identical to fig. 5.25. The dashed curves represent the direct intercalation (see eq. (Inter-G)) and solid lines the plating reaction (see eq. (Pl/St)). (b) The time derivative of (upper) the current fraction (see fig. 5.26(a)) and (lower) the cell voltage (see fig. 5.25(a)).

achieve full plating. The inset in fig. 5.26(a) examines the time region of the plating feature in the cell voltage. The zoom of the plating onset show, that the current fractions also vary slightly in that region. A larger constant d_0 lead to a earlier plating onset. The overall variance spans roughly 2 s and is therefor quite small. The smallest constant d_0 results in the fastest change in the plating current after the onset, as can be seen in the time derivative in the upper part of fig. 5.26(b). The time derivative of the cell voltage is plotted in the lower part of fig. 5.26(b). The position of maximum change is marked by six black lines, but only five are visible, since the lines of the two smallest constants overlap. A current flux is given as external boundary condition. The cell voltage is the response to the applied current and the internal electrochemical situation. The distribution of the current flux onto the two different reaction paths depends on the electrochemical situation at the electrode-electrolyte-interface. The different potential dependence of the intercalation and plating reaction result in different responses in the cell voltage. A quicker change in current flux leads to an stronger signal in the cell voltage as seen in fig. 5.25(a).

5.5. Lithium plating through overcharge

A well defined situation, where lithium plating will take place, is the lithiation of an already nearly lithiated graphite. The open circuit potential of graphite should approach 0 V with respect to lithium, when the maximum acceptable lithium content at the surface region is reached. The initial state of charge for the following half-cell simulation was set such, that the cell voltage is at 50 mV. The cell voltage of a constant current overcharge simulation (see fig. 5.27(a)) begins with an further decrease of the cell voltage. At a certain point (roughly 34 s) a change towards a constant cell voltage takes place. The constant voltage is at a slightly higher value than before the change. The open circuit potential of the anode would be around 22 mV at $t = 40$ s if no plating would occur. The feature in

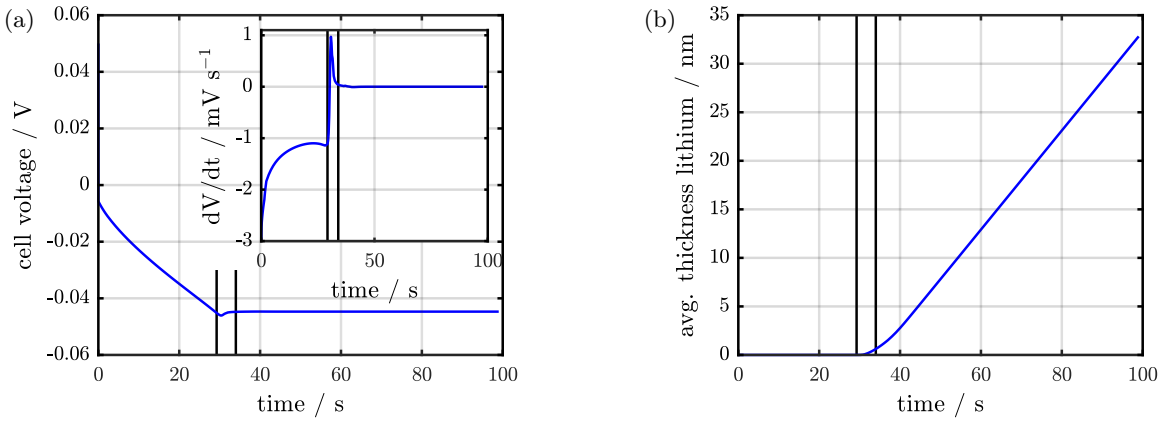

Figure 5.27.: (a) The cell voltage of the overcharge simulation exhibits a switch from decreasing voltage towards a constant cell voltage. The time derivative of the cell voltage is shown in the inset. (b) The mean thickness of plated lithium exhibits a increase with increasing slope until the complete electrode surface is covered with plated lithium.

the cell voltage is a dip. The exact shape of the dip seems to depend on the prefactor constant d_0 as shown in section 5.4.1. The start of the dip and the position where the cell voltage reaches a nearly constant value are marked by black lines. The time derivative of the cell voltage is shown as inset in fig. 5.27(a). As long as no plated lithium exists the cell voltage is monotonically decreasing. The switch towards plating is present as variation from a decreasing to a increasing regime. beyond the second black line the time derivative is close to zero and nearly constant. The time derivative of the cell voltage dV/dt is proportional to the differential voltage dV/dQ due to the constant applied current. The method of differential voltage analysis (DVA) is used to identify the degradation state of battery electrodes. The differential voltage of a fullcell consists of the differential voltage of the anode and the cathode. The presented simulations exhibit a unique feature in the dVdQ. The questions arises, if such a feature could be seen in experimental data. A dip in the cell voltage is similar to the feature observed by D. Guyomard and J. Tarascon [137]. They discharged a petroleum-coke electrode with a constant current until the half-cell voltage reached $-0.045\,\mathrm{V}$ vs Lithium. Every cycle after the initial formation cycle exhibits a dip in the cell voltage (see fig. 5.28). By using an *in situ* XRD the change in spacing of the (002)-lattice plane of the petroleum-coke could be observed. The spacing stayed constant as soon as the dip in the half-cell voltage was observed. Thus they identified this feature as the onset of lithium plating. The average thickness of the plated lithium in the half-cell simulations (see fig. 5.27(b)) starts to increase as soon as the dip formed in the cell potential. The two black vertical lines are at the same time as in fig. 5.27(a). The lithium starts to deposit on the surface when the dip starts to form. The lithium thickness growth is linear after the active surface is completely covered. A plating dip in the cell voltage and a stripping plateau in the subsequent delithiation of a carbon cell was also found by Liu *et al.* [138]. But no indications in the dVdQ of a full-cell was found reported. A possible explanation is, that usually no homogeneous and full plating coverage occurs in experiments. The impact of inhomogenous lithium deposition is investigated in section 5.6.

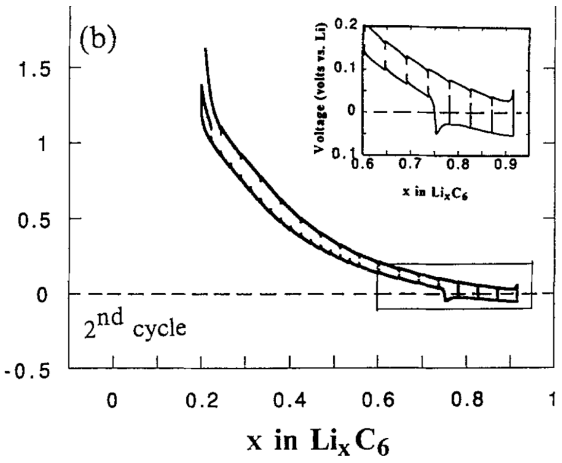

Figure 5.28.: The cell voltage vs Lithium for the constant current overcharge experiment done by Guyomard *et al.* . Reprinted with permission from [137]. Copyright 1992, The Electrochemical Society.

The cell potential and the average lithium thickness indicate, that a change from direct intercalation towards lithium plating as major reaction at the graphite surface is taking place. The direct intercalation and the plating reaction both transfere a certain amount of current from the electrolyte into the graphite electrode. The time evolution of those two, as shown in fig. 5.29(a), clarifies that the start of the dip is the beginning of lithium plating and thus the increase of current transfered by plating. When

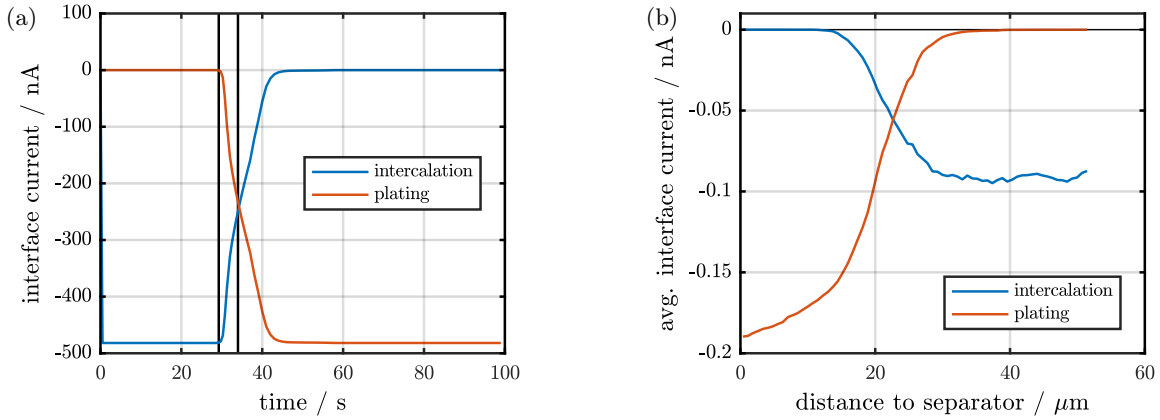

Figure 5.29.: (a) The current flow through the electrode-electrolyte-interface divides into intercalation or plating. (b) Spatial distribution of the interface current at $t = 34\,\mathrm{s}$. The spatial distribution of the interface current is averaged with respect to the number of interfaces.

the plating reaction carries the majority of charge the cell voltage starts to level into the constant regime, as marked with the right black line. The spatial distribution of the two currents along the through-direction of the electrode (see fig. 5.29(b)) shows a split of the electrode into two regions. Close to the separator the charge transfer is completed purely by the plating reaction. At the other side of the electrode only intercalation is taking place. As a result of this spatial variation of the plating current one can expect a thicker lithium film at the separator. There is also a region of roughly 10 µm, where both reactions coexist. Figure 5.30(a) shows the plated lithium on the surface of the microstructure.

The blue color close to the current collector indicates that no lithium is plated in this region. At the

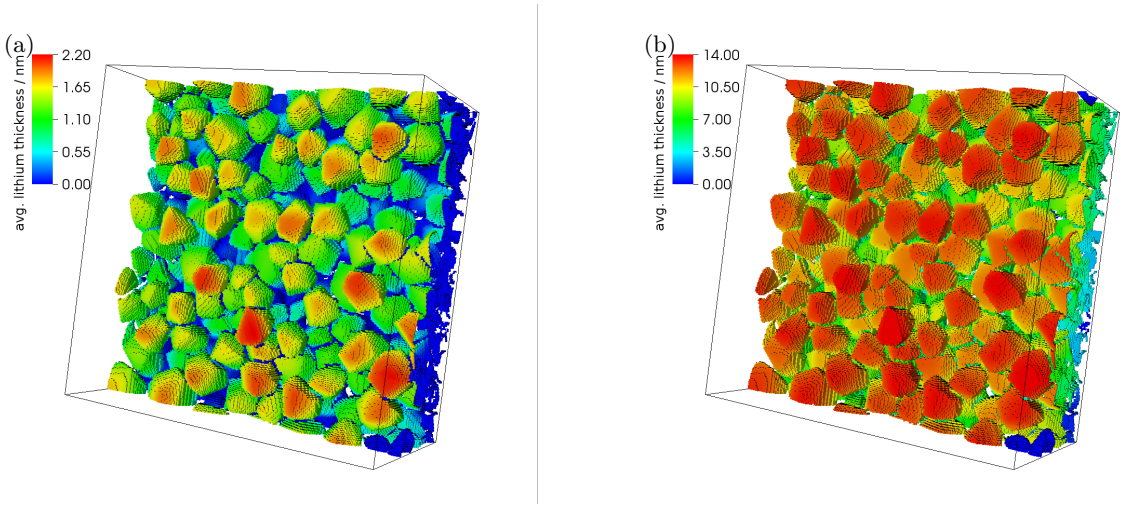

Figure 5.30.: The spatial distribution of the plated lithium after (a) 36 s and (b) 60 s. The color scale is in nm.

later time of 50 s (see fig. 5.30(b)) nearly the complete surface of the graphite is covered with lithium. Only electrically unconnected particles, e.g. in the lower right corner, are left without plated lithium. At both times do some particles at separator interface show slightly different plating amount. This is similar to the observations of Harris *et al.* [78] through a optical microscope. The thickness of lithium differs, since a much larger lithium amount is needed to be visible optically.

The rate constant $N^{00}_{\mathrm{Pl/St}}$ of the plating reaction is a crucial parameter. Literature values are only known for one electrolyte [125]. To understand how the rate constant impacts the findings, the rate constant of the plating reaction N^{00}_{PLEL} was varied by one magnitude in both directions. In fig. 5.31(a) the resulting cell voltage of these simulations is shown. For a faster plating reaction the transition from direct intercalation towards lithium plating takes place at higher cell voltage. If the plating reaction is slowed down, the thermodynamic condition for lithium deposition is undercut by over 20 mV before the majority of the electrode is covered with plated lithium (see fig. 5.31(b)). It appears, that the exact timing of the plating onset is highly dependent on the rate of the plating reaction. The observed dip and the following plateau could possibly be used to validate the proposed lithium plating model. The comparison of an experimentally overcharged negative electrode and the presented simulations should allow for an estimation of the plating reaction rate. The overcharge simulations indicated, that a slower plating reaction lets the negative electrode withstand a more negative potential difference before the plating reaction actually takes place. Thus hindering this reaction through electrolyte additives could help reducing the amount of plated lithium. An other result is, that an early plating onset does not result in a fully plated electrode. As long as a fraction of the surface is not plated direct intercalation can take place. This can be seen in the distribution of the interface current shown in fig. 5.32. While a fast plating reaction favors an early start of lithium deposition, it also allows for an long coexistence of plated and unplated regions. A slower plating reactions leads to a nearly instantaneous switch from direct intercalation to fully plated electrode. Attributing the voltage dip to the switch of intercalation dominated to plating dominated current is therefor not possible.

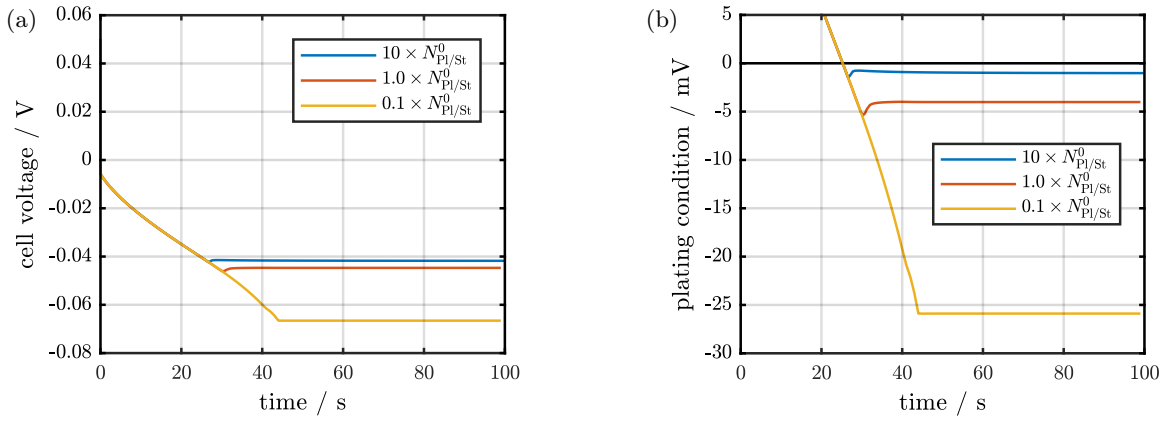

Figure 5.31.: (a) The cell voltage for the variation of the plating reaction rate constant i^0_{PLEL}. (b) The plating condition at the anode-separator-interface for the variation of the rate constant i^0_{PLEL}

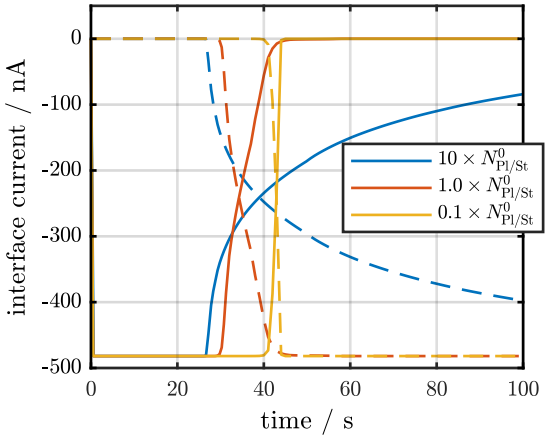

Figure 5.32.: The current fraction divided onto the intercalation and plating reaction. A longer coexistence of both reactions is apparent for a larger plating rate constant.

The spatial distribution of the SEI thickness along the through direction is not easily accessible to measurements. Therefor no information about the distribution exists. It is well established, that a fresh interface between lithium metal and the electrolyte results in a enhanced growth of the solid electrolyte interphase. The strong growth of lithium metal at the separator-interface, as observed with the presented plating model, should result in-homogeneous SEI growth and could allow for a better understanding and prediction of loss of dissolved lithium.

5.6. Impact of local inhomogeneities on lithium plating

The postmortem analysis of heavily degraded lithium-ion cells showed that on electrode level a inhomogeneous degradation behavior seems to exist [82, 79, 83]. If one assumes, that the active material behaves electrochemical identical throughout the whole electrode, local variation of the structural

properties - such as porosity - of the electrodes or separator could be the source of inhomogeneous lithium plating or SEI growth. The electrochemical simulation of lithium-ion batteries on microstructure level with the framework BEST is only possible within a certain domain size. The number of possible discretization volumes is limited by the memory size and a practicable simulation runtime. Hence, a electrode with in the range of the observed degradation inhomogeneities can not be resolved. As an approximation the microstructure is modified such, that one part can be given different electrochemical parameters. Starting with a empty electrode the full lithiation is investigated. Different operation and system conditions are varied. The modified microstructure, as shown in fig. 4.16, consists of a inner and outer region. The impact of a local variation on cell performance and lithium plating is investigated by the modification of different parameters of the inner region.

5.6.1. Electronic conductivity

The electronic conductivity of the solid electrode was varied at global and local level. For the electrochemical parameters used in this work and the given size of the microstructure no impact on the global cell voltage and local plating onset was found. A larger impact on the cell performance is expected on cell level or very large cut-outs of microstructures.

5.6.2. Rate constant of direct intercalation

In this section, the rate constant of the direct intercalation was varied for the complete electrode and only for the inner part of the modified electrode. The rate constant is multiplied by 0.1 and 10 with respect to the literature value. The cell voltages for two different global reaction rates and the local variation of the reaction rate during constant current lithiation with an high current can be seen in fig. 5.33(a). In table 5.2 the cases shown in this and subsequent sections are listed. The cell voltage of

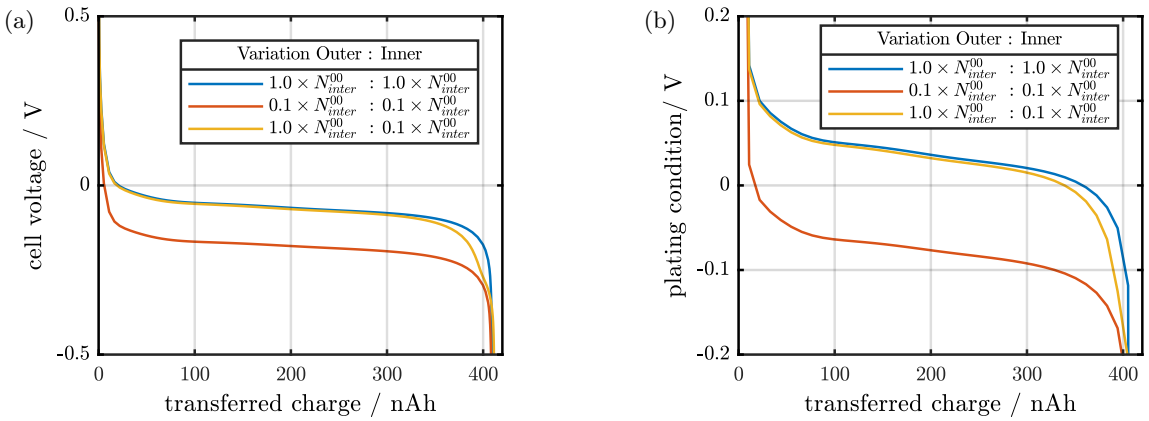

Figure 5.33.: Lithiation with $9mA/cm^2$ constant current at $298K$ ambient temperature: (a) The cell voltage for the variation of the intercalation rate constant. (b) Plating condition of the rate variation.

the inhomogeneous rate constant (case BV-3) changes from the homogeneous case with the literature

value for the rate constant (case BV-1) towards the cell voltage of the lower rate constant (case BV-2). This indicates, that a locally degraded electrode will result in earlier plating than a pristine one. This can be seen in the plating condition for the three different cases in fig. 5.33(b). The plating condition is reached at a earlier time for the locally decreased reaction rate than for the homogeneous case (see fig. 5.33(b)). A globally decreased intercalation rate leads to a high plating risk already shortly after start of lithiation.

Table 5.2.: List of the different rate variations used for inhomogeneous simulations.

Case	Varied parameter	value	variation location
intercalation rate variation			
BV-1	N^{00}_{Inter}	$1.0 \times N^{00}_{\text{Inter,lit}}$	global
BV-2	N^{00}_{Inter}	$0.1 \times N^{00}_{\text{Inter,lit}}$	global
BV-3	N^{00}_{Inter}	$0.1 \times N^{00}_{\text{Inter,lit}}$	inner part
plating rate variation			
PL-1	$N^{00}_{\text{Pl/St}}$	$0.1 \times N^{00}_{\text{Pl/St,ref}}$	inner part
PL-2	$N^{00}_{\text{Pl/St}}$	$1.0 \times N^{00}_{\text{Pl/St,ref}}$	global
PL-3	$N^{00}_{\text{Pl/St}}$	$10 \times N^{00}_{\text{Pl/St,ref}}$	inner part

When the rate constant of the intercalation rate is smaller in the inner part than the outer part, a inhomogeneous distribution of the state of charge after $200nAh$ charge transferred occurs. The inner

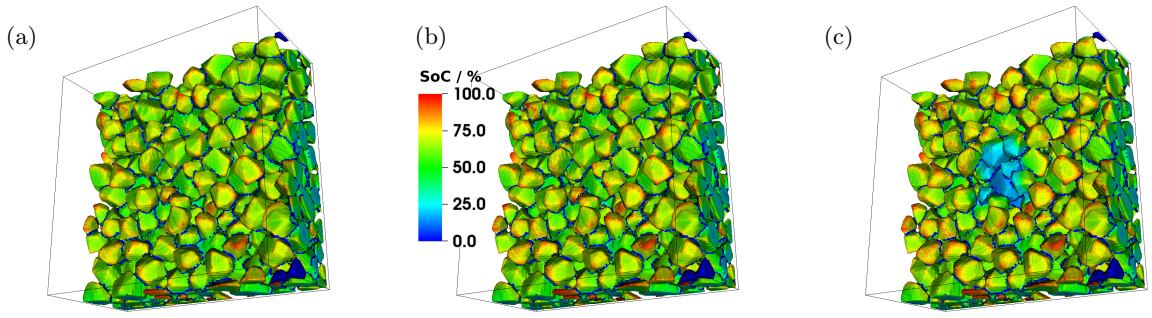

Figure 5.34.: The state of charge (SoC) of anode at 200nAh for the cases (a) BV-1, (b) BV-2 and (c) BV-3 (see table 5.2). The binder and unconnected particles appear blue.

region of the electrode is less utilized for intercalation and thus resulting in an earlier plating onset. The active material is representing graphite, which exhibits a volumetric change during lithiation with lithium. The concentration gradient between different regions of the electrode will result in increased structural stress in the boundary between these regions. This can decrease the contact between electrode particles and as a result decrease the electronic connection or even lead to loss of active material.

The simulation of the cases BV-1 and BV-3 are repeated with the plating model enabled. The cell voltage is shown in combination with the previous simulations in fig. 5.35(a). The case of inhomogeneous rate constant (BV-3) exhibits, as expected from the plating condition in fig. 5.33(b), an earlier plating onset. The cell voltage for BV-1 and BV-3 are shifted along the x-axis so they overlap at a potential of $-110\,\text{mV}$ (see fig. 5.35(b)). Little to no deviation can be seen between the plated curves. This

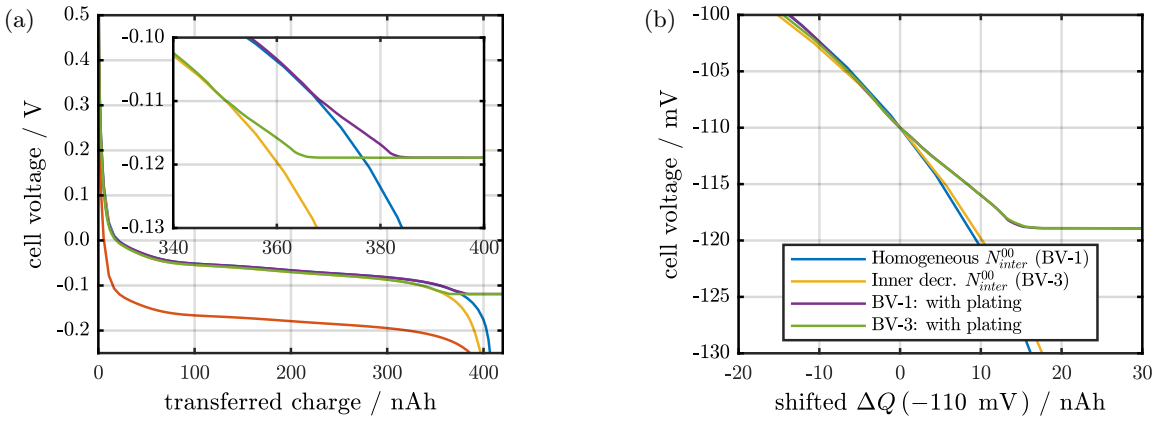

Figure 5.35.: (a) Comparison of the cell voltage for case BV-1 and BV-3 with plating enabled. (b) The cell voltages are shifted along the x-axis to allow for a comparison of the general shape.

indicates, that the spatial distribution of the plating is not strongly impacted. The average thickness of the plated lithium can be found in fig. 5.36(a).The earlier onset of plating for case BV-3 is apparent. The average thickness is split shown separately for the inner and outer part of the electrode. The

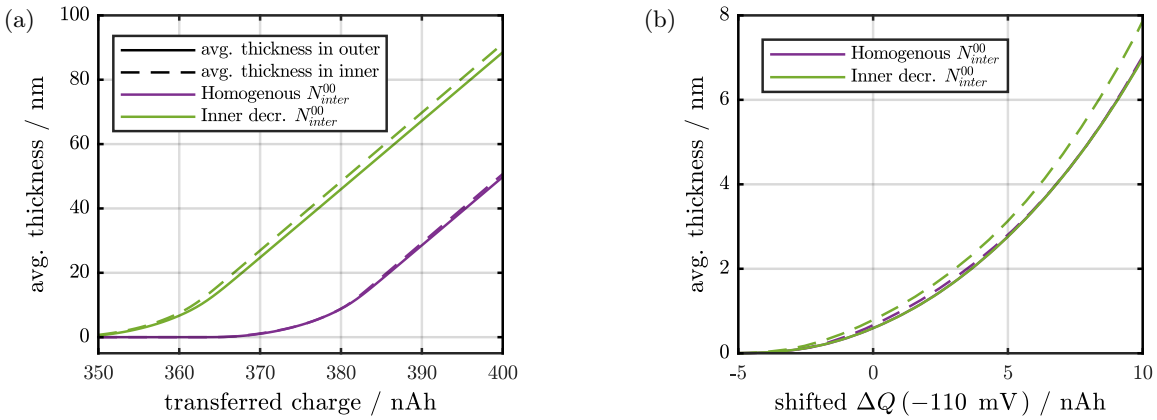

Figure 5.36.: (a) The average thickness of plated lithium split into outer and inner region. (b) The average thickness with shifted x-axis (same values as in fig. 5.35(b)).

locally decreased reaction rate (case BV-3) results in a slightly thicker lithium deposition in the inner part. For better comparison the average thickness is shifted (see fig. 5.36(b)) with the same factor as used in fig. 5.35(b). The shifted average thickness of the outer part phases show no difference. Only the modified phase shows a stronger increase in plated lithium than the majority. Thus, it can be said, that a local decrease of the intercalation rate constant N^{00}_{Inter} leads to a increase of plated lithium in that region.

Even so the plating simulations describe only reversible degradation, some insight can be extracted. The solid-electrolyte-interphase is known to impact the intercalation reaction. It is quite common to include the impact of an existing SEI-layer on the intercalation reaction by the addition of an resistance

term to the overpotential of the intercalation [4]:

$$\eta_{\text{inter}}^{\text{SEI}} = \varphi_{\text{El}} - \phi_{\text{So}} - U_{0,\text{so}} - i_{\text{inter}} \cdot R_{\text{SEI}} \tag{5.4}$$
$$\eta_{\text{inter}}^{\text{SEI}} = \eta_{\text{inter}} - i_{\text{inter}} \cdot R_{\text{SEI}}$$

This modified overpotential is then used in the calculation of the exchange current, usually a Butler-Volmer like expression:

$$i_{\text{inter}}^{\text{w SEI}} = i_0 \cdot \left[\exp\left(\frac{F\eta_{\text{inter}}^{\text{w SEI}}}{2 \cdot RT}\right) - \exp\left(-\frac{F\eta_{\text{inter}}^{\text{w SEI}}}{2 \cdot RT}\right)\right] \tag{5.5}$$

This approach was used by [4] to investigate the impact of lithium plating on cell performance and by [139] to predict SEI growth. The resistance term $i_{\text{inter}} \cdot R_{\text{SEI}}$ leads to a higher overpotential η_{inter} compared to a reaction without SEI. In the previous simulations the impact of a local variation of the intercalation rate constant was investigated. It can be seen, that a decrease in the rate constant results in a locally earlier plating onset. A short approximation is done under the assumptions of intercalation through SEI and an overpotential as in eq. (5.4). For intercalation the exchange current i_{inter} is smaller than zero with an overpotential below zero. The SEI-resistance term in eq. (5.5) can be extracted to the rate constant as follows.

$$i_{\text{inter}}^{\text{w SEI}} = i_0 \cdot \left[\exp\left(\frac{F\eta_{\text{inter}}^{\text{w SEI}}}{2 \cdot RT}\right) - \exp\left(-\frac{F\eta_{\text{inter}}^{\text{w SEI}}}{2 \cdot RT}\right)\right] \tag{5.6}$$
$$i_{\text{inter}}^{\text{w SEI}} = i_0 \cdot \left[\exp\left(\frac{F\eta_{\text{inter}}^{\text{w SEI}}}{2 \cdot RT}\right) - \exp\left(-\frac{F\eta_{\text{inter}}}{2 \cdot RT}\right) \cdot \exp\left(\frac{F}{2 \cdot RT} i_{\text{inter}} R_{\text{SEI}}\right)\right] \tag{5.7}$$
$$i_{\text{inter}}^{\text{w SEI}} = \frac{i_0}{\exp\left(-\frac{F \cdot i_{\text{inter}} R_{\text{SEI}}}{2 \cdot RT}\right)} \cdot \left[\exp\left(\frac{F\eta_{\text{inter}}^{\text{w SEI}}}{2 \cdot RT}\right) \cdot \exp\left(-\frac{F \cdot i_{\text{inter}} R_{\text{SEI}}}{2 \cdot RT}\right) - \exp\left(-\frac{F\eta_{\text{inter}}}{2 \cdot RT}\right)\right] \tag{5.8}$$

We can neglect the positive exponential function under the assumption, that $|i_{\text{inter}} \cdot R_{\text{SEI}}| < |\eta_{\text{inter}}|$ and since the overpotential $\eta_{\text{inter}}^{\text{w SEI}}$ is below zero:

$$i_{\text{inter}}^{\text{w SEI}} \approx -\frac{i_0}{\exp\left(-\frac{F \cdot i_{\text{inter}} R_{\text{SEI}}}{2 \cdot RT}\right)} \cdot \left[\exp\left(-\frac{F\eta_{\text{inter}}}{2 \cdot RT}\right)\right] \tag{5.9}$$

This approximation is similar in shape as the Tafel approximation of a Butler-Volmer without SEI-resistance [33]:

$$i_{\text{inter}}^{\text{w/o SEI}} \approx -i_0 \cdot \left[\exp\left(-\frac{F\eta_{\text{inter}}}{2 \cdot RT}\right)\right] \tag{5.10}$$

For a given intercalation current i_{inter} the additional term $\exp\left(\frac{F \cdot i_{\text{inter}} R_{\text{SEI}}}{2 \cdot RT}\right)$ can be seen as reduction of the rate constant i_0. The local variation of the rate constant in this section could therefor be interpreted as a local variation of SEI thickness. Through the SEI resistance this induces a local variation of the overpotential. The simulations with different local rate constants show clearly, that a local variation of the SEI leads to a locally different degradation behavior. E.g a thicker SEI leads to a smaller rate constant. The extension of the presented plating model to include SEI growth should hopefully be able to investigate this feedback in more detail.

5.6.3. Rate constant of lithium plating

The rate constant of the plating reaction $i^{00}_{\mathrm{Pl/St}}$ is also locally varied. The different variation cases are listed in table 5.2. The variation of the plating rate constant only becomes apparent in the cell voltage (see fig. 5.37(a)) after onset of plating. Increasing the rate constant for the inner region leads to a

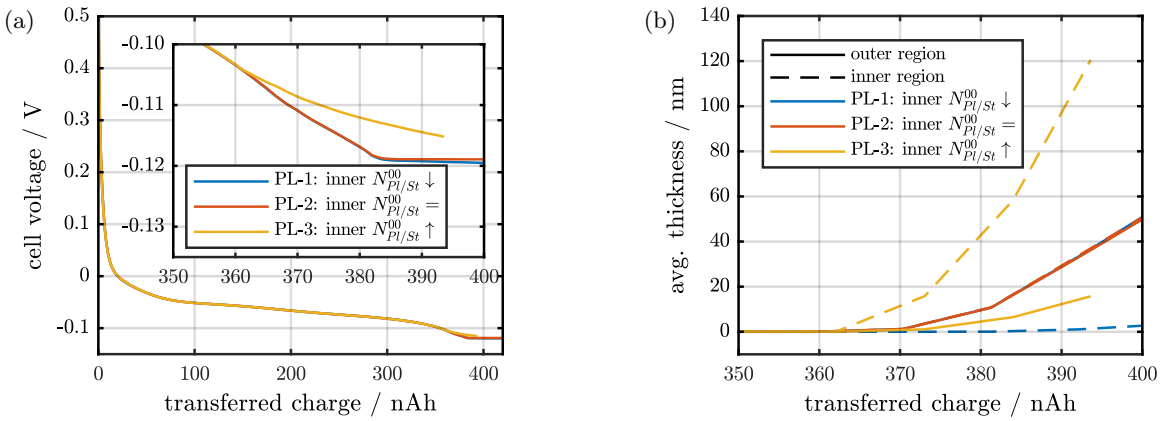

Figure 5.37.: (a) The local variation of the rate constant of the plating reaction has a large impact on the overall cell voltage. (b) A locally higher or lower plating rate constant can result in a locally thick plated lithium layer or even in a nearly unplated surface. The inner and outer value of the homogeneous plating rate and the outer value of the locally decreased plating rate overlap.

larger cell voltage. The slope of the cell voltage changes and the dominant switch towards constant value vanishes. The local decrease of the rate constant does not result in a large deviation from the homogeneous case. Both variations cause a significant variance in the thickness of plated lithium for the inner as well as the outer region (see fig. 5.37(b)). The inner sector exhibits a three times thicker average lithium film than the homogeneous case. The outer region shows a halved thickness.Decreasing the rate constant of the inner part results in a nearly unplated electrode, without an visible impact on the outer region. It is apparent, that a local variation in reaction rate for intercalation or plating has an large impact on degradation.

In fig. 5.38 the average thickness of plated lithium in through direction for the three plating rate variations around 400 nAh are shown. The lithium thickness is largest at the separator interface for all cases. The lithium plating remains very small in the region of the locally decreased plating constant, while the outer part of the microstructure still behaves like the homogeneous case. The increase of the plating rate constant int he inner part result in a four times thicker lithium film at the separator film. At the same time, the electrode surface close to the current collector is largely free of plated lithium. The average thickness for the locally increased plating rate is nearly 0.5 µm thick and therefore in the order of the discretization volume. The simulation can hence only be seen as approximations. A lithium growth in this magnitude would lead to pore blockage. The change of the plating rate for a fraction of the total electrode surface also influences the outer part of the electrode. The active surface of the inner region represents 16.7 % of the total surface area (see table 4.15). These results clearly show, that local variations can heavily impact the overall cell performance and indicate the importance of

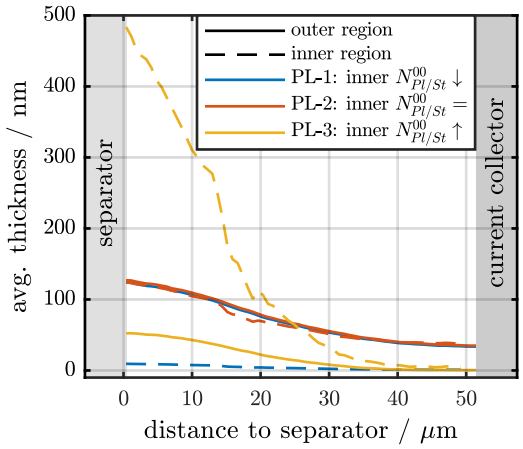

Figure 5.38.: The spatial distribution of the average thickness of plated lithium at roughly 400 nAh charge transfered. The variation of the local plating constant leads to a clear inhomogeneous plating distribution.

electrochemical transport models, which spatially resolve the microstructure. The spatial distribution

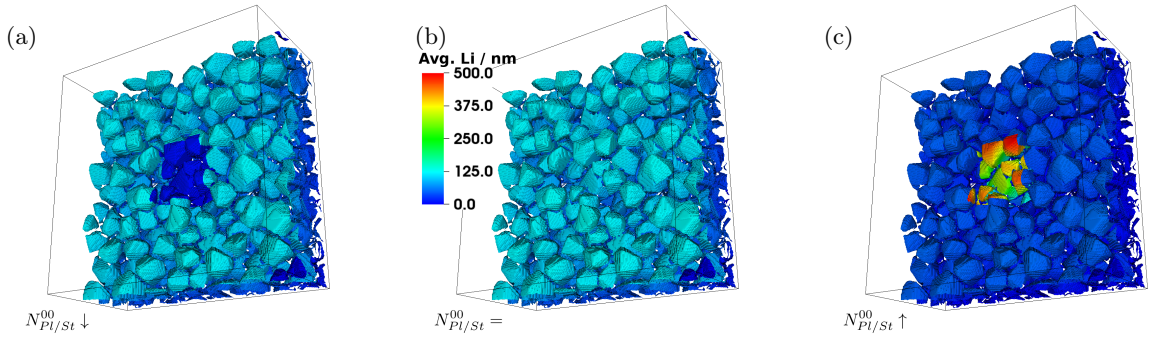

Figure 5.39.: The spatial distribution of plated lithium for the three variations are shown here. The rate constant of the inner part is (a) smaller (PL-1), (b) equal (PL-2) or (c) larger than the bulk value (PL-3).

of the average lithium thickness around 400 nAh is plotted in fig. 5.39. The color scale is identical for all three plots. The locally varied rate constant of the plating reaction increases from (a) over (b) to (c). A smaller reaction rate results in a thinner lithium film in the inner part (see fig. 5.39(a)). For the case of identical rate constant in the inner and outer region (see fig. 5.39(b)) a homogeneous film distribution is visible. The comparison to the locally decreased value shows, that the outer region behaves nearly identical for both cases. This can also be seen in fig. 5.38. The increase of the rate constant in the inner region (see fig. 5.39(c)) results in a four times thicker lithium film as compared to the homogeneous case. The largest film thickness can be found at the parts of the inner particles close to the separator (dark red in fig. 5.39(c)).

The spatial distribution of the current through the electrolyte-solid-interface attributed to the intercalation reaction in fig. 5.40 shows clearly, that the locally increased rate constant of the plating reaction impacts the surrounding electrode. The local decrease of the plating rate constant can be seen analogous

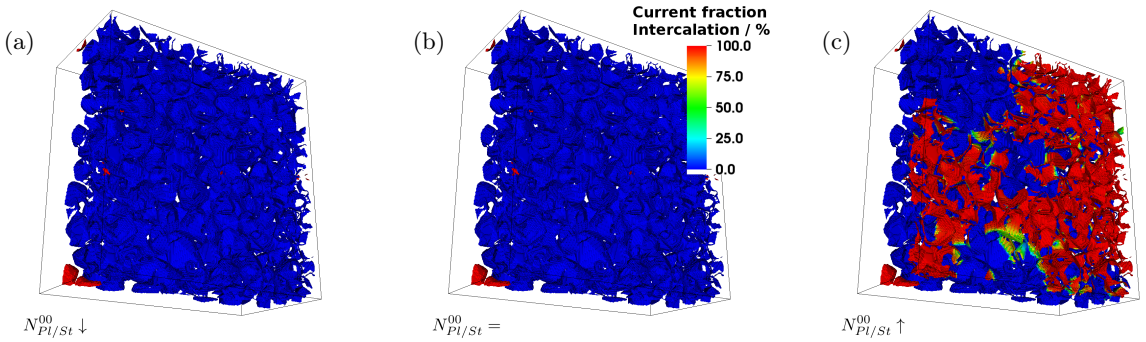

Figure 5.40.: The fraction of the current through the electrolyte-solid-interface attributed to intercalation seen from the current-collector side. The rate constant of the inner part is (a) smaller (PL-1), (b) equal (Pl-2) or (c) larger than the outer value (Pl-3). The unconnected particle is visible in red at the lower left in all images.

to the discussion for the reduction of the intercalation rate constant: A decreased local rate constant corresponds to an increase in local SEI thickness. The local decrease of the rate constant of the plating reaction, on the other hand, resulted in a lower local lithium deposition. A locally thicker SEI will hamper the deposition of lithium. Thus protecting the anode from plating. A cracking of SEI or other processes resulting in a fresh surface between graphite and electrolyte will locally favor lithium plating. This highlights the complexity of the interplay of the SEI and the plating reaction. The extension of the plating model to include the growth of SEI, as mentioned earlier, together with the parameterization of the system on experimental data are sensible next steps (see chapter 6). A local variation of the plating reaction rate and the intercalation reaction rate and explicit simulations were omitted in this work. The results of the previous variation simulations indicate, that a locally enhanced or hindered plating will occure depending on the relation between the rate constants of the plating and intercalation reaction. A cooperation with experimentalists to parameterize the model system on a defined battery system with known components is planned [140].

5.7. Plating and stripping during operation

So far only the plating process was investigated with the surface model. In this section the impact of a local variation of the plating reaction rate during a constant current lithiation and delithiation is simulated. The switch from lithation to delithiation occurs at $t = 730\,\mathrm{s}$. The simulation consists of four regions: Intercalation, plating, stripping and deintercalation. The reaction rate $N^{00}_{\mathrm{Pl/St,inner}}$ is varied according to table 5.2. The cell voltages are shown in fig. 5.41(a). The insets show magnifications of the plating and stripping regions. The plating inset shows the same information as fig. 5.37(a). The cases PL-1 and PL-2 exhibit no large differences for the whole lithiation-delithiation cycle. The simulation for the PL-3 variation (local rate increase) ends early due to walltime limitations. The locally increased rate results in a very inhomogeneous plating distribution. This leads to smaller time steps and thus to a longer calculation duration. The decrease of runtime is a numerical challenge to be tackled. A possible approach is a domain decomposition. Selected parts of the system would be

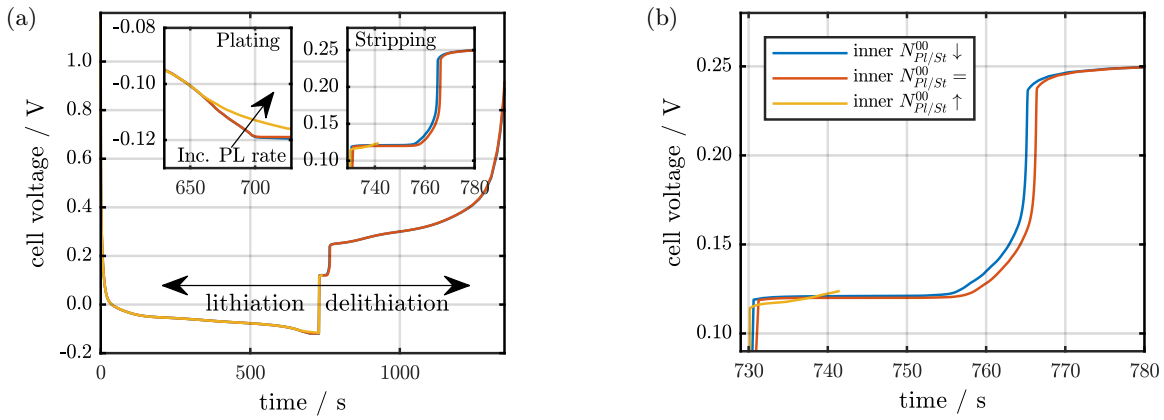

Figure 5.41.: (a) The cell voltages for the constant current charge and discharge with variation of inner plating rate. The insets show the plating and stripping region. (b) The stripping plateau of the locally increased reaction rate $N^{00}_{\mathrm{Pl/St}}$ seems to exhibit a more sloped behavior.

solved on a shorter timescale than others. Other runtime optimization options exist and need to be implemented. But the vast changes in the simulation framework needed were beyond the frame of this thesis. Nevertheless, the plating simulations with locally increased reaction rate allow for first insights. Figure 5.41(b) shows the cell voltage during the striping plateau. The cases $N^{00}_{\mathrm{Pl/St}} =$ and $N^{00}_{\mathrm{Pl/St}}\downarrow$ exhibit very similar shapes. The difference is a small shift along the x-axis. Part of the shift of the plateau is caused by small variations in the time steps. The case $N^{00}_{\mathrm{Pl/St}}\uparrow$ shows a slope right from the start of stripping. This is in contrast to the constant voltage part of the other two cases. A sloped stripping plateau is also observed in experiments [141]. This could indicate, that lithium deposition is usually very inhomogeneous and localized. The combination of dedicated experiments, microstructure data of the used electrode and plating simulations could allow for a better understanding.

The surface coverage is shown for the outer and inner region in fig. 5.42(a). A complete coverage of

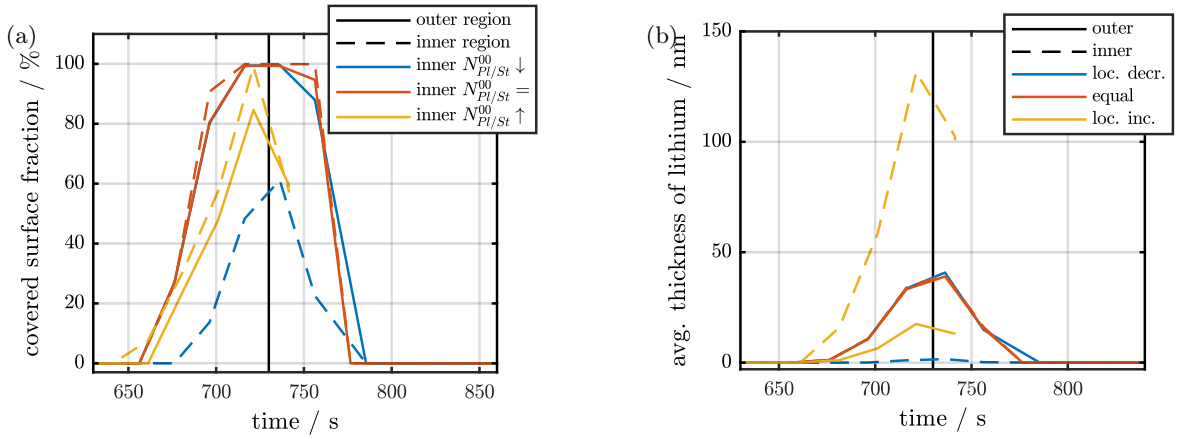

Figure 5.42.: (a) The amount of surface covered by plated lithium for the inner and outer region. (b) The average thickness of plated lithium in the inner and outer region.

the surface with lithium exists only for the homogeneous rate constant. Roughly 50 % of the inner

region is covered by lithium for a decreased rate constant $N^{00}_{\mathrm{Pl/St}}\downarrow$. While the outer region exhibits a similar behavior as the homogeneous case $N^{00}_{\mathrm{Pl/St}}=$. The increase of the reaction rate $N^{00}_{\mathrm{Pl/St}}\uparrow$ results in less surface area covered. In combination with the average lithium thickness in the two regions (see fig. 5.42(b)) it becomes clear, that the local increase leads to a thicker lithium film on less covered surface. The locally decreased case $N^{00}_{\mathrm{Pl/St}}\downarrow$ exhibits a surface coverage on the inner region with a film thickness close to monolayer thickness.

Figure 5.43(a) contains the amount of plated lithium expressed as corresponding charge per area of current collector. The charge transferred during the existence of the stripping plateau of cases $N^{00}_{\mathrm{Ch.Int.}}\downarrow$

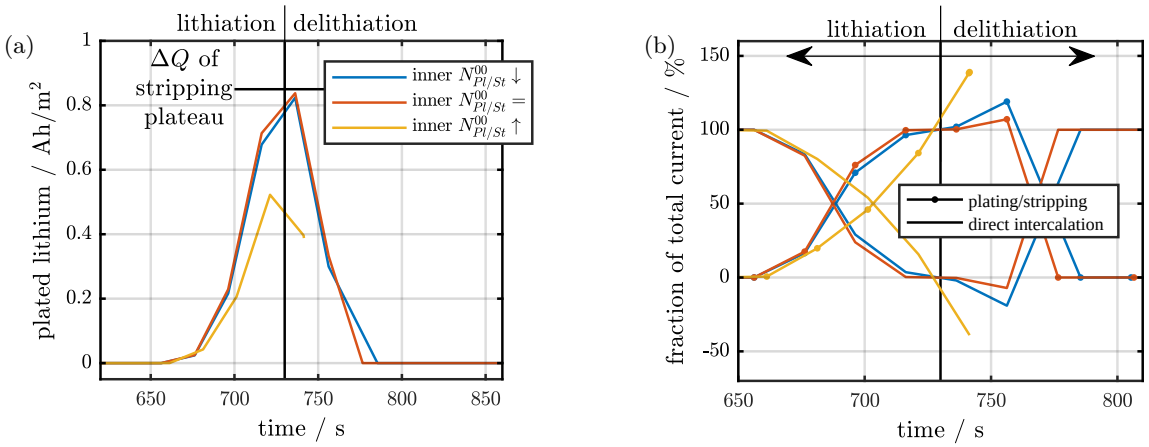

Figure 5.43.: (a) The amount of plated lithium expressed as corresponding charge per area of current collector. (b) The contributions of intercalation and plating/stripping to the total current flux through the battery. A negative fraction during delithiation corresponds to a net lithiation.

and $N^{00}_{\mathrm{Ch.Int.}}=$ is indicated through a horizontal line. The amount of plated lithium for the three cases was calculated using the spatial output of the framework BEST. This output is saved only for a fraction of the successful time steps, since the size of one snapshot is in the order of GB. For the homogeneous case the coverage of the surface with plated lithium is already complete at the last output step (see fig. 5.42(a)). For the constant applied current a linear growth of thickness is expected. It can therefore be assumed, that the real thickness of the plated lithium film is quite higher than the amount estimated by the stripping plateau. The distribution of the current flux onto the two relevant reactions is shown in fig. 5.43(b). A negative current fraction during delithiation indicates, that lithiation is taking place. A net intercalation during stripping occurs for all simulations. The locally increased plating rate leads to a net intercalation during the whole stripping phase. A circle current of nearly 50 % of the applied current is occurring during the delithiation for the locally increased plating constant. This current is flowing between different parts of the porous anode without contributing to the current flow from negative to positive electrode. A closed loop of current flux generates a magnetic dipole. A change in magnetic field can be detected using a magnetic field sensor (e.g. hall-sensor). The author is not aware of any literature regarding the detection of time dependent magnetic fields during battery operation. The distribution of the current fluxes is quite complex. It is therefor suspected, that the

overall magnetic field is counterbalanced. Closed loops of current flux inside a lithium-ion battery can also occur during the relaxation of a blend electrode.

Part of the 3D distribution of the lithium concentration inside the electrolyte is shown fig. 5.44 during lithium plating close to the current switch towards delithation. The electrolyte domain is split along the

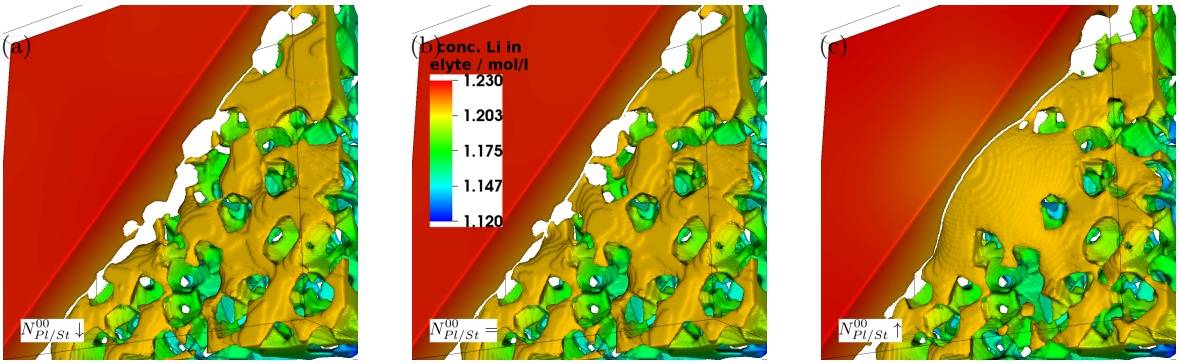

Figure 5.44.: The spatial distribution of the lithium concentration in the electrolyte is split along 1.21 mol/l. The rate constant of the inner part is (a) smaller (PL-1), (b) equal (Pl-2) or (c) larger than the outer value (Pl-3).

concentration of 1.21 mol/l. The homogeneous case exhibits a quite even front (see fig. 5.46(b)). The local increase of reaction rate $N^{00}_{\mathrm{Pl/St}}$ in the inner part leads to an increased lithium consumption. Thus lowering the concentration in the electrolyte around the inner region. This pushes the equiconcentration plane of 1.21 mol/l towards the counter electrode, which is visible as dome in fig. 5.44(c). The inverse occurs for the local rate decrease $N^{00}_{\mathrm{Pl/St}}\downarrow$. The equiconcentration plane is pulled into the porous phase and therefor less visible in fig. 5.44(a). The cases of inhomogeneous reaction rate both exhibit a slightly larger spread in lithium concentration in the electrolyte than the homogeneous case.

The spatial distribution of the lithium concentration in the electrolyte during the stripping of the plated lithium is shown in fig. 5.45. The locally decreased plating rate $N^{00}_{\mathrm{Pl/St}}\downarrow$ (see fig. 5.45(a)) results in an less active region for the inner part. The lithium concentration is hence lower in the inner region than for the homogeneous case (see fig. 5.45(b)). The case $N^{00}_{\mathrm{Pl/St}}\uparrow$ (see fig. 5.45(c)) exhibits a local maxima

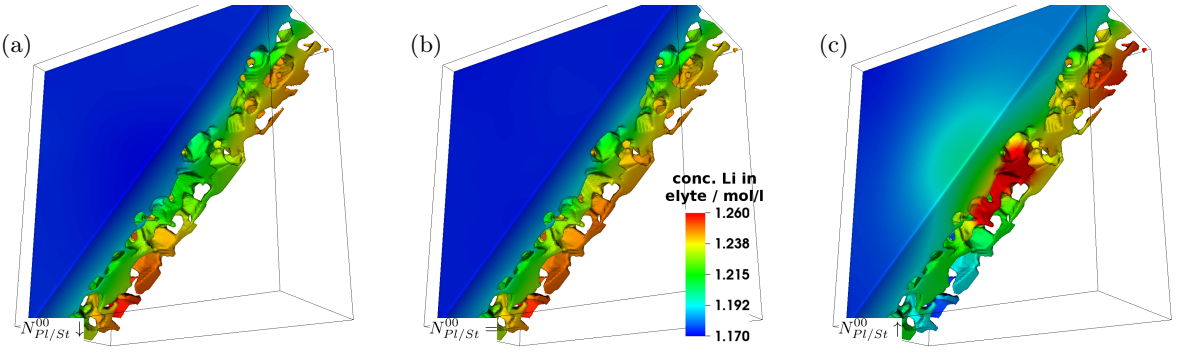

Figure 5.45.: The spatial distribution of the lithium concentration in the electrolyte during delithiation and stripping. The rate constant of the inner part is (a) smaller (PL-1), (b) equal (Pl-2) or (c) larger than the outer value (Pl-3).

in the concentration close to the largest amount of plated lithium. This effect was already seen with

the volume model (see fig. 5.13). The current flux during stripping can form closed loops, as indicated by the net intercalation in fig. 5.43(b). The impact of the net intercalation on the lithium concentration in the electrolyte can be seen in the lower left part of fig. 5.45(c). There is a local minimum in the concentration, which is in contrast to the local maximum for the other two cases (see fig. 5.45(a) and fig. 5.45(b)).

The localized change in reaction constant is also visible in the current flux through the cell (see fig. 5.46). The integral curves (streamlines) of the current density are plotted as two-colored lines for a matrix

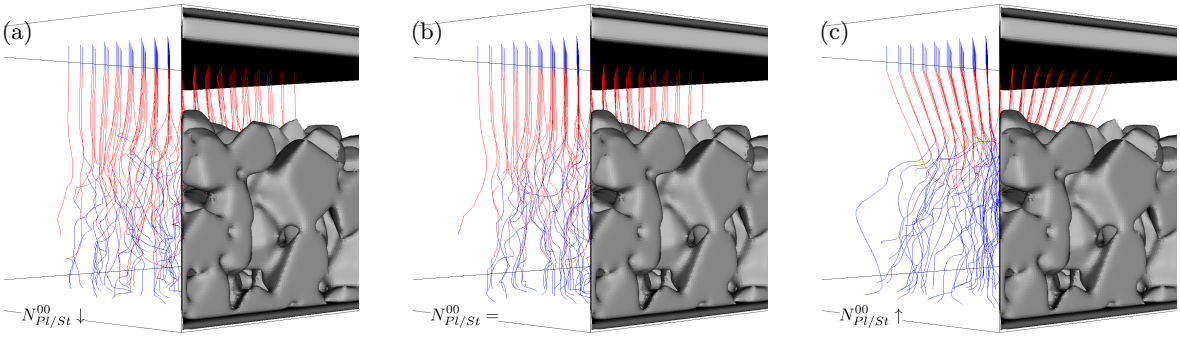

Figure 5.46.: Integral curves (streamlines) of the current density field inside the battery at the last saved step before switch to delithiation. The rate constant of the inner part is (a) smaller (PL-1), (b) equal (Pl-2) or (c) larger than the outer value (Pl-3).

of 10×10 starting points opposite the inner region. The blue parts of the streamlines indicate, that the current flows through a solid phase (active material or current collector). The red parts indicate electrolyte. The homogeneous case (see fig. 5.46(b)) exhibit parallel streamlines from the counter electrode towards the porous graphite. The transition of the current flux from electrolyte phase into the solid phase occurs at various depths in the graphite electrode. The local increase of the reaction rate (see fig. 5.46(c)) shows a strong focus of the streamlines towards the inner region. The transition from electrolyte into solid is strongly localized to the region at the separator. The decrease of rate constant $N^{00}_{\mathrm{Pl/St}}\downarrow$ leads to avoidance of the inner region. The streamlines in the center are redirected towards the outer region. The streamlines were obtained using the integral curve operator of the visualization tool VisIt [142].

The homogeneity of the reaction constant of the plating reaction $N^{00}_{\mathrm{Pl/St}}$ has a huge impact on the spatial distribution of lithium plating. A local variation of the plating rate constant influences the electrochemical simulation in the complete electrode. The high local thickness of plated lithium can increase the loss of active lithium due to the growth of SEI at the lithium-electrolyte-interface. The local variation of the plating rate has a strong impact on the plating onset feature in the cell voltage. Thorough analysis of experimental measurements could maybe result in the detection of this feature.

6. Summary and outlook

This dissertation introduced a new model, which describes lithium plating in lithium-ion batteries. The model allows a competition between intercalation and lithium deposition. This is in contrast to other known models. The plated lithium is included into a thermodynamically consistent transport theory as an additional surface equation. It was implemented into the simulation framework BEST. This allowed plating and stripping simulations within spatially resolved microstructures. Other known models, such as the model of Arora [4], work on the basis of a volume averaged microstructure. The impact of spatially varying properties on the plating behavior was investigated.

The electrochemical situation, which enables lithium plating, is called plating condition. The time dependent behavior during charging a full-cell is investigated. The part of the negative electrode close to the separator is the region, where lithium plating will first occur. The onset of condition, which favors lithium plating, depends on the applied current and the temperature inside the battery. The region of possible plating increases from the separator into the electrode as a front. It was shown, that for higher currents a larger spread of the plating condition occurs. This means, that small regions experience a higher risk of plating than the majority of the electrode. A lower temperature leads to the similar spread.

The impact of an existing lithium deposition on the local electrochemical situation and cell behavior was investigated through a simple model. The simple model includes a dedicated lithium phase. The phase was distributed throughout an anode microstructure. The plated lithium was stripped in a half-cell setup. While plated lithium is dissolved, the known stripping plateau can be observed in the cell voltage. The electrode can exhibit a net intercalation during the presence of plated lithium, even so the applied current enforces a delithiation. For a given distribution of plated lithium, the net current can be lithiation or delithiation depending on the value of the applied current. This observation has consequences on the accuracy of the differential voltammetry (DV). The method is often used to estimate the amount of plated lithium by determining the length of the stripping plateau. The presence of a net lithiation or delithiation, depending on the applied current, can result in an underestimation or overestimation of the amount of plated lithium.

The developed plating model allowed the simulation of lithium deposition during lithiation and the stripping during delithiation of a graphite electrode. The complete coverage of an electrode by a plated lithium film results in a constant anode voltage. Simulations in half-cell setup showed a deviation from the open-circuit dominated cell voltage at the onset of plating. The change in the cell voltage is relatively small and is therefore probably not noted in the experimental cell voltage. The influence of localized variations of reaction rates on the lithium deposition behavior were investigated. If the

intercalation reaction is hampered, the deposition of lithium plating throughout the electrode occurs sooner than for a homogeneous intercalation reaction. The rate constant of the plating reaction $N^{00}_{\text{Ch.Int.}}$ exhibits a stronger impact on the distribution of the plated lithium. A variation can result in a very inhomogeneous and strongly localized lithium film. This inhomogeneous film suppresses the constant anode voltage, since no complete surface coverage occurs. A closer investigation, where the onset of plating could be seen in an experimental full cell is suggested. The subsequent stripping of plated lithium was also investigated. The well known stripping plateau can be seen, regardless of the homogeneity of the plated lithium film. The inhomogeneous film results in a larger slope in the cell voltage during lithium stripping. A sloped stripping plateau is also observed experimentally. Thus it is suspected, that the experimental observations indicate a inhomogeneous lithium deposition. The local variations of the reaction rates can be translated into the influence of a SEI. A local thickness variation of the SEI can strongly influence the deposition of plated lithium. The combination of the SEI model and the plating model could help to investigate the SEI growth due to lithium plating.

The 3D spatially resolved simulations need structural data to construct the microstructure of electrodes. The availability of realistic or real microstructure data is limited due to the high acquisition costs. Virtual microstructures can also be generated using a computer through stochastic structure models. The electrochemical similarity of real microstructures and virtual microstructures, which were created through a stochastic model, was shown. This loosens the 3D spatially resolved simulations from the dependence on tomography data. The electrochemical validated model could be used to create new microstructures with defined geometrical parameters, such as porosity and tortuosity. The optimization of an electrode structure regarding suppression of lithium plating is now possible in combination with the developed plating model.

The presented model has several possible points for extension. The temperature of a lithium-ion cell varies during operation. Some experiments indicate, that the onset of lithium plating can result in a visible change of the local cell temperature [143]. Latz *et al.* [7] were able to show, that a large part of the heat production results from the irreversible Joule heat. The source of Joule heat is an electric current passing a resistance, such as the interface between solid and electrolyte. A change of the dominant reaction pathway, as shown in this work, should induce a specific feature in the heat production. Extending the plating model to include thermal feedback would allow for dedicated simulations with reference to these experimental observations. The thoroughly parameterization of this transport model [7] as done by Cabañero *et al.* [140] is an excellent basis for these studies.

The plating model includes only reversible degradation processes. The growth of a solid-electrolyte-interphase is one of the most important irreversible loss mechanisms. The model of Single *et al.* [144] describes the morphology evolution of a SEI on a nanoporous scale. Since the resolution of the microscopic structure model is larger than the one used in the SEI-model, the reduced growth equation (see eq. (10) in [144]) could be incorporated into the microscopic transport model and lithium plating framework. The reduced growth equation depends on the current thickness of the SEI d_{SEI} and the potential difference between the SEI and the electrolyte $\Delta\Phi_{\text{EC}}$.

The electrochemical impedance spectroscopy (EIS) is a common technique for health and degradation estimation of lithium-ion batteries. The electrochemical simulation of an impedance requires the modeling of the electrochemical doublelayer [145, 146, 147]. The combination of the presented plating model and a double layer theory would allow for the investigation of impedance spectra of degraded batteries [75]. Possible candidates are the often used model as presented by Ong *et al.* [145] and the thermodynamically consistent model by Lück *et al.* [35].

The new plating model introduced additional electrochemical parameters, which need to be determined. The rate constant of the plating reaction $N^{00}_{\mathrm{Pl/St}}$ and of the chemical intercalation $N^{00}_{\mathrm{Ch.Int.}}$ are crucial for a good predictive power of the plating model. Two basic approaches can be used to estimate their values: Either first principle and molecular dynamics calculations, or specific experiments.

The nudged elastic band method, kinetic Monte Carlo simulations or Density Functional Theory are candidates to identify the rate constants and the anodic transfer numbers. These methods are already used in the literature to investigate similar electrochemical questions. The nudged elastic band method is applied to the lithium diffusion inside the SEI [148]. First principle calculations are used to calculate the nucleation of lithium on a graphene sheet [149]. Temel *et al.* [150] employ kinetic Monte Carlo simulations to calculate parameters of catalytic CO oxidation at solid interfaces. The review by Franco [151] lists different techniques and approaches.

The small dip and the constant cell voltage after the start of lithium plating is a feature, which is also reported experimentally [137, 143]. The level of the constant cell voltage depends on the covered surface, plated by lithium, and the homogeneity of deposition, as was shown in this work. Parametrizing the electrochemical model using experiments without lithium plating would allow the determination of the plating rate constant $N^{00}_{\mathrm{Pl/St}}$ with specific plating experiments. Measuring the constant voltage level during plating and stripping for different applied currents can help to estimate the anodic transfer number $\alpha_{\mathrm{a}}^{\mathrm{Pl/St}}$ similar to [152]. The chemical intercalation requires a more complex experiment. One proposed possibility is shown in fig. 6.1. The lithium-graphite cell is held at zero current while the

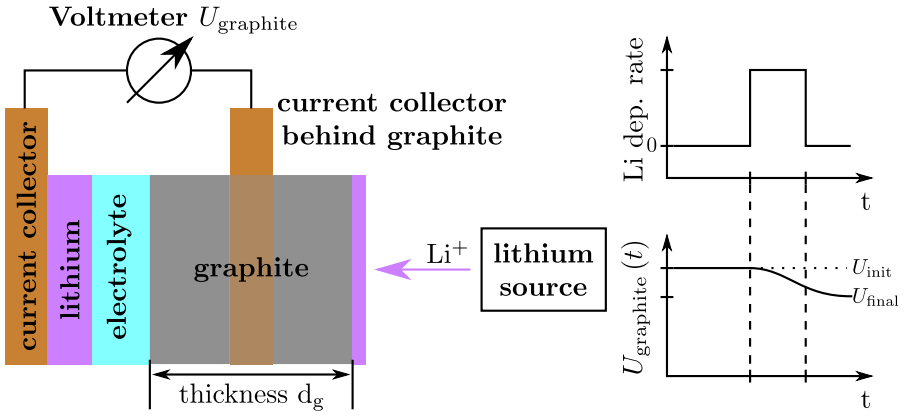

Figure 6.1.: Proposed experiment to obtain more information about the rate constant. (left) the experimental setup consisting of the electrochemical cell and the lithium source is shown. (right) The expected response function $U_{\mathrm{graphite}}(t)$ after a pulsed lithium deposition contains information about the lithium diffusion coefficient inside the graphite and the chemical intercalation rate.

potential difference between the graphite and the lithium U_{graphite} is observed. Lithium is brought from the right side on the surface of the graphite. Depending on the chemical intercalation rate, the incoming lithium accumulates on the surface or is immediately intercalated. The concentration gradient in the graphite results in a diffusion of lithium to the electrolyte interface and hence in a change of the measured cell voltage U_{graphite}. The lithium is deposited only for a certain time and the cell voltage is measured as a function of time. A lithium source could be chemical vapor deposition (CVD). CVD was suggested to be used to create active materials, current collectors, separators or a protective coating for active materials [153]. It is not clear if CVD can be used in combination with a operating electrochemical cell.

The implementation of the transport model and the surface plating model should be optimized to reduce the simulation runtime, the required amount of memory, and increase the numerical stability. The most promising step to reduce runtime is the change from *calculate-everytime-when-needed* to *calculate-once-and-remember*. The current implementation calculates the conservation equations for each discretization volume separately. For each volume the lithium and current fluxes, and their derivatives are calculated. Every discretization volume shares interfaces with other volumes. Therefore each flux calculation between two neighboring volumes is calculated twice. The suggested step would calculate the fluxes once and keep them stored in the memory. Thus reducing the calculations needed.

A. Numerical

The discretization using finite volumes and the approach for the numerical solution of the presented transport model ist explained with a bit more details.

A.1. Discretization

In the following the steps involved in the discretization are shown for a simple spatial domain where only a mass balance equation in the shape of eq. (2.5) needs to be solved. The mass balance of the concentration c was defined in eq. (3.12):

$$0 = \frac{\partial\, c}{\partial\, t} - \boldsymbol{\nabla N} \tag{A.1}$$

Let the 1D domain consist of two different subdomains Ω_1 and Ω_2, with $e_h \in \Omega_1$ and $e_j, e_j \in \Omega_2$. The main domain is discretized by cell centered finite volumes: The spatial domain Ω is divided into a polygonal mesh ($\Omega = \Sigma_{i=1}^{N} e_i$) with each cell e_i being a polyhedron. In fig. A.1 the discretization of a simple 1D domain is shown. The different terms used to describe the discretization process are shown explanatory in this figure. The discretization cell e_i is described by the center x_i, the thickness in

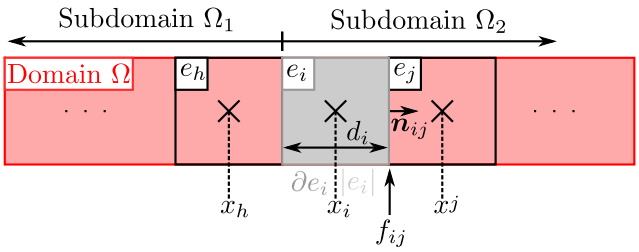

Figure A.1.: Cell centered finite volumes for a simple 1D domain Ω (red). The cell e_i (grey) is specified by the center x_i, the outer surface ∂e_i and the volume $|e_i|$. The interface between neighboring cells (e.g. e_i and e_j) is denoted by f_{ij} with the surface normal $\boldsymbol{n}_{ij}$.

one direction d_i, the outer surface ∂e_i and the volume $|e_i|$. The interface area between cell e_i and a neighboring cell e_j is named f_{ij} and has a surface normal $\boldsymbol{n}_{ij}$, which points from i into j.

The mass balance equation (eq. (3.12)) is integrated over the volume of a cell e_i and the time t:

$$0 = \int_{t_n}^{t_{n+1}} \int_{e_i} \left[\frac{\partial\, c}{\partial\, t} + \boldsymbol{\nabla N} \right] dx\; dt \tag{A.2}$$

Using the divergence theorem and expanding the integrals one obtains

$$0 = \int_{e_i} c(x, t_{n+1}) dx - \int_{e_i} c(x, t_n) dx + \int_{t_n}^{t_{n+1}} \int_{\partial e_i} \boldsymbol{N} \cdot \boldsymbol{n}_{\mathrm{A}} \, dA \, dt \tag{A.3}$$

With the definition of the lithium flux, this leads to

$$0 = \int_{e_i} c(x, t_{n+1}) dx - \int_{e_i} c(x, t_n) dx - \int_{t_n}^{t_{n+1}} \int_{\partial e_i} D \boldsymbol{\nabla} c \cdot \boldsymbol{n}_{\mathrm{A}} \, dA \, dt \tag{A.4}$$

The cell e_i can share interfaces with cells of different domains, which need a different treatment: $\partial e_i = \sum_{h \in \Omega_1} f_{ih} + \sum_{j \in \Omega_2} f_{ij}$. Therefore the last integral is split into a part for the interfaces with the same domain:

$$\begin{aligned} 0 = \int_{e_i} c(x, t_{n+1}) dx - \int_{e_i} c(x, t_n) dx - \overbrace{\int_{t_n}^{t_{n+1}} \int_{f_{ij}, j \in \Omega_2} D \boldsymbol{\nabla} c \cdot \boldsymbol{n}_{\mathrm{A}} \, dA \, dt}^{\text{same domain}} \\ \underbrace{+ \int_{t_n}^{t_{n+1}} \int_{f_{ih}, h \in \Omega_1} \boldsymbol{N} \cdot \boldsymbol{n}_{\mathrm{A}} \, dA \, dt}_{\text{different domains}} \end{aligned} \tag{A.5}$$

In the framework BEST a **backward Euler** method is employed to approximate the time integrals:

$$\begin{aligned} 0 = |e_i| \cdot (C(x) - c(x, t_n)) - (t_{n+1} - t_n) \cdot \int_{f_{ij}, j \in \Omega_2} D \boldsymbol{\nabla} C \cdot \boldsymbol{n}_{\mathrm{A}} \, dA \\ + (t_{n+1} - t_n) \cdot \int_{f_{ih}, h \in \Omega_1} \boldsymbol{N} \cdot \boldsymbol{n}_{\mathrm{A}} \, dA \end{aligned} \tag{A.6}$$

where C denotes the concentration for the time t_{n+1}. If the neighboring cell e_j is in the same domain as e_i the surface integral can be approximated by:

$$\int_{f_{ij}} D \boldsymbol{\nabla} c \cdot \boldsymbol{n}_{\mathrm{ij}} \, dA \approx f_{ij} \cdot D_{\frac{i+j}{2}} \frac{c(x_j, t) - c(x_i, t)}{x_j - x_i} \tag{A.7}$$

The subscript $\frac{i+j}{2}$ indicates the weighted harmonic average of the quantity at the interface between cell i and j. In the case of a diffusion coefficient this would be:

$$\begin{aligned} D_{\frac{i+j}{2}} &= \frac{d_i/2 + d_j/2}{\frac{d_i/2}{D(x_i)} + \frac{d_j/2}{D(x_j)}} \\ &= \frac{d_i + d_j}{\frac{d_i}{D(x_i)} + \frac{d_j}{D(x_j)}} \end{aligned} \tag{A.8}$$

with $D(x_i)$ the value of the diffusion coefficient at the center of cell i.

At the interface between two different domains one usually has a discontinuity of the primitive variable (under the assumption, that selection of domains is physically motivated). The interaction between these different domains is described using interface conditions. For the example system this interface

condition can be written as

$$\boldsymbol{N}_{\Omega_1} \cdot \boldsymbol{n} = \boldsymbol{N}_{\Omega_2} \cdot \boldsymbol{n} = \mathcal{N}\left(c_{\Omega_1}, c_{\Omega_2}\right) \tag{A.9}$$

where the scalar function $\mathcal{N}$ defines the exact interaction between the two domains. Hence the surface integral can be replaced by:

$$\int_{f_{ih}} N \cdot \boldsymbol{n}_{\mathrm{ih}}\, dA = f_{ih} \cdot \mathcal{N}\left(c_h, c_i\right) \tag{A.10}$$

The complete expression is hence:

$$0 = |e_i| \frac{C(x_i) - c(x_i)}{\Delta t} - \overset{\text{same D.}}{\sum_{j \in \Omega_2}} f_{ij} \cdot D_{\frac{i+j}{2}} \frac{c(x_j,t) - c(x_i,t)}{x_j - x_i} + \overset{\text{dif. D.}}{\sum_{h \in \Omega_1}} f_{ih} \cdot \mathcal{N}\left(c_h, c_i\right) \tag{A.11}$$

The application of the previously shown steps to the full battery system results in the following more general discretization of the governing equations eqs. (2.4) to (2.7):

$$\begin{aligned}
0 &= |e_i| \frac{C_{\mathrm{El}}(x_i) - c_{\mathrm{El}}(x_i)}{\Delta t} - \sum_{j \in El} f_{ij} \left(K^{\mathrm{A}}_{\mathrm{El}} \frac{C_{\mathrm{El}}(x_j) - C_{\mathrm{El}}(x_i)}{x_j - x_i} + K^{\mathrm{B}}_{\mathrm{El}} \frac{\Phi_{\mathrm{El}}(x_j) - \Phi_{\mathrm{El}}(x_i)}{x_j - x_i} \right) \\
&\quad + \sum_{h \in So} f_{ih} \cdot \mathcal{N}\left(C_h, C_i, \Phi_h, \Phi_i\right) \\
0 &= |e_i| \frac{C_{\mathrm{So}}(x_i) - c_{\mathrm{So}}(x_i)}{\Delta t} - \sum_{j \in So} f_{ij} \left(K^{\mathrm{A}}_{\mathrm{So}} \frac{C_{\mathrm{So}}(x_j) - C_{\mathrm{So}}(x_i)}{x_j - x_i} \right) \\
&\quad + \sum_{h \in El} f_{ih} \cdot \mathcal{N}\left(C_h, C_i, \Phi_h, \Phi_i\right) \\
0 &= - \sum_{j \in El} f_{ij} \left(K^{\mathrm{C}}_{\mathrm{El}} \frac{C_{\mathrm{El}}(x_j) - C_{\mathrm{El}}(x_i)}{x_j - x_i} + K^{\mathrm{D}}_{\mathrm{El}} \frac{\Phi_{\mathrm{El}}(x_j) - \Phi_{\mathrm{El}}(x_i)}{x_j - x_i} \right) \\
&\quad + \sum_{h \in So} f_{ih} \cdot \mathcal{J}\left(C_h, C_i, \Phi_h, \Phi_i\right) \\
0 &= - \sum_{j \in So} f_{ij} \left(K^{\mathrm{D}}_{\mathrm{So}} \frac{\Phi_{\mathrm{So}}(x_j) - \Phi_{\mathrm{So}}(x_i)}{x_j - x_i} \right) + \sum_{h \in El} f_{ih} \cdot \mathcal{J}\left(C_h, C_i, \Phi_h, \Phi_i\right)
\end{aligned} \tag{A.12}$$

with the factors in the electrolyte

$$K^{\mathrm{A}}_{\mathrm{El}} = D^{El}_{\frac{i+j}{2}} + \kappa^{El}_{\frac{i+j}{2}} \cdot \frac{t_{+,\frac{i+j}{2}} \cdot \left(1 - t_{+,\frac{i+j}{2}}\right)}{F^2} \left(\frac{\partial \mu_{\mathrm{El}}}{C_{\mathrm{El}}} \right)_{\frac{i+j}{2}} \tag{A.13}$$

$$K^{\mathrm{B}}_{\mathrm{El}} = \kappa^{El}_{\frac{i+j}{2}} \cdot \frac{t_{+,\frac{i+j}{2}}}{F} \tag{A.14}$$

$$K^{\mathrm{C}}_{\mathrm{El}} = \kappa^{El}_{\frac{i+j}{2}} \tag{A.15}$$

$$K^{\mathrm{D}}_{\mathrm{El}} = \frac{\left(1 - t_{+,\frac{i+j}{2}}\right)}{F} \left(\frac{\partial \mu_{\mathrm{El}}}{C_{\mathrm{El}}} \right)_{\frac{i+j}{2}} \tag{A.16}$$

and in the solid

$$K_{\mathrm{So}}^{\mathrm{A}} = D_{\frac{i+j}{2}}^{So} \tag{A.17}$$

$$K_{\mathrm{So}}^{\mathrm{D}} = \sigma_{\frac{i+j}{2}}^{So} \tag{A.18}$$

A.2. Numerical solution of nonlinear equation system

A.2.1. Linearization

The discretized system in eq. (A.12) is a system of algebraic equations with included nonlinearities in the form

$$0 = F_{\mathrm{MBE,El}} \tag{A.19}$$

$$0 = F_{\mathrm{MBE,So}} \tag{A.20}$$

$$0 = G_{\mathrm{CCE,El}} \tag{A.21}$$

$$0 = G_{\mathrm{CCE,El}} \tag{A.22}$$

The system is influenced by the strong nonlinear nature of the system and hence a linearization is applied to the system. The system $\boldsymbol{F}$ is extended using the first order of the Taylor series around point $\boldsymbol{x}_0$:

$$\boldsymbol{F}(\boldsymbol{x}) \approx \boldsymbol{F}(\boldsymbol{x}_0) + \boldsymbol{J}(\boldsymbol{x}_0) \cdot (\boldsymbol{x} - \boldsymbol{x}_0) \tag{A.23}$$

with $\boldsymbol{J}(\boldsymbol{x}_0)$ being the Jacobian matrix of the system $\boldsymbol{F}(\boldsymbol{x}) = (f_1, ..., f_n)$ with the unknowns $\boldsymbol{x} = (x_1, ..., x_n)$. The Jacobian matrix is defined as:

$$\boldsymbol{J} = \frac{d\ \boldsymbol{F}}{d\ \boldsymbol{x}} = \left[\frac{\partial\ \boldsymbol{F}}{\partial\ x_1}\ ...\ \frac{\partial\ \boldsymbol{F}}{\partial\ x_n}\right] = \begin{pmatrix} \frac{\partial\ F_1}{\partial\ x_1} & \cdots & \frac{\partial\ F_1}{\partial\ x_n} \\ \vdots & \ddots & \vdots \\ \frac{\partial\ F_n}{\partial\ x_1} & \cdots & \frac{\partial\ F_n}{\partial\ x_n} \end{pmatrix} \tag{A.24}$$

This linearization scheme is applied to the full set of algebraic equations (eqs. (A.19) to (A.22)).

A.2.2. Newton's method

The next step is the determination of the solution. The Newton's method [104] is applied to find the root of the algebraic equations. In general the initial value for the unknowns $\boldsymbol{x}_0$ does not fulfill the system. Hence the iterative Newton's method is used. The next solution $\boldsymbol{x}_1$ is calculated to satisfy the following equation:

$$\boldsymbol{F}(\boldsymbol{x}_0) + D\boldsymbol{F}(\boldsymbol{x}_0) \cdot (\boldsymbol{x}_1 - \boldsymbol{x}_0) = 0 \tag{A.25}$$

This equation can be solved for the next step solution $\boldsymbol{x}_1$ to

$$\boldsymbol{x}_1 = \boldsymbol{x}_0 - \left(\boldsymbol{J}\left(\boldsymbol{x}_0\right)\right)^{-1} \boldsymbol{F}\left(\boldsymbol{x}_0\right) \tag{A.26}$$

After obtaining the next step, the solution is tested if it fulfills the equation system with wished accuracy. If the wished accuracy is not reached, the same step is repeated, with the previous solution $\boldsymbol{x}_1$ as initial value. This can be repeated until the solution is found or one decides to stop looking for it.

Using eq. (A.26) for obtaining the numerical solution needs the inverse of the Jacobian matrix to be determined, which is quite computational expensive. Instead the root of the following system is solved:

$$\boldsymbol{J}\left(\boldsymbol{x}_0\right) \Delta\boldsymbol{x} = -\boldsymbol{F}\left(\boldsymbol{x}_0\right) \tag{A.27}$$

the Jacobian matrix $\boldsymbol{J}\left(\boldsymbol{x}_0\right)$ and the vector $-\boldsymbol{F}\left(\boldsymbol{x}_0\right)$ are known. Hence the solution to this equation can be found efficiently and accurately. With the resulting solution $\Delta\boldsymbol{x}$ one can estimate the solution via

$$\boldsymbol{x}_1 = \boldsymbol{x}_0 + \Delta\boldsymbol{x} \tag{A.28}$$

The calculation of the solution $\Delta\boldsymbol{x}$ is repeated until a solution $\boldsymbol{x}_i$ with an acceptable accuracy is found.

To obtain a time transient solution of a given system these steps are repeated, while increasing the system time. In fig. A.2(a) the general flow diagram for the solution of the *classical* system is shown. After setting all concentrations to their initial values, the pure potential system is solved to obtain a consistent potential distribution. Now the transient simulation starts with the first time step. Every time step follows the same rule: Solve eq. (A.27) and test the result for target accuracy.

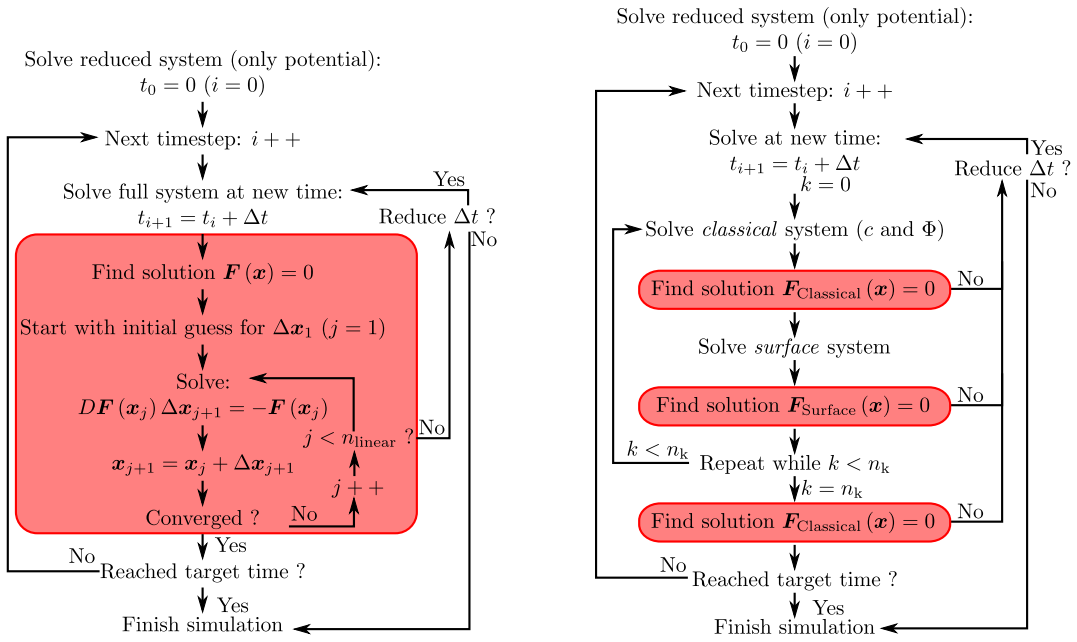

(a) Flow diagram for the *classical* and coupled surface system.

(b) Flow diagram for the decoupled surface system.

Figure A.2.: Flow diagram for finding a solution of the system.

Two different tolerances are used to test for convergence:

1. relative difference in solution $\Delta \boldsymbol{x}_{j+i}$: $\frac{\Delta \boldsymbol{x}_{j+1}}{\boldsymbol{x}_j} <$ Threshold for rel. solution
2. absolute norm of function $\boldsymbol{F}$: $|\boldsymbol{F}(\boldsymbol{x}_{j+1})| <$ Threshold for abs. function

B. Notes

B.1. Color convention

Most of the graphics underlie a certain color convention for the distinct materials. Each element of the periodic table is assigned to a certain color. The assignment is defined by the Jmol[1] package, which is an open-source Java viewer for chemical structures. The molecule color of a structure is obtained by mixing the color of the underlying atoms according to the chemical composition[2]. The used colors in this work are listed in table B.1 with RGB24-representation[3] in hexadecimal form.

Table B.1.: Color list of used colors in this work.

Material	Color	Example
Lithium	CC80FF	
Copper	C88033	
Aluminium	BFA6A6	
Flourine	90E050	
Phosphorus	FF8000	
Graphite C_6	909090	
Graphite LiC_6	988EA0	
LMO $LiMn_2O_4$	DB3D65	
LMO $LiMn_2O_4$ with conductive agent (C_6)	C05B74	
SEI as Li_2CO_2	DB4974	

One exception is the representation of electrolyte: the color for electrolyte was chosen to be cyan (00FFFF) to allow for a contrast between the solid phases and the electrolyte (e.g. in fig. 2.3). The virtual phase of external boundary conditions (see fig. 2.3) was set to green (008000).

[1] See http://jmol.sourceforge.net/jscolors
[2] The mixing can be done with an applet on the web page http://trycolors.com/.
[3] See https://en.wikipedia.org/wiki/RGB_color_model

C. Publications and conferences

Publications

First author

- Hein, Simon ; Latz, Arnulf: Lithium Plating and Stripping in the Framework of a 3D Electrochemical Model. In: ECS Trans. 69 (2015), oct, Nr. 1, 3–5. [154]
- Hein, Simon ; Latz, Arnulf: Influence of local lithium metal deposition in 3D microstructures on local and global behavior of Lithium-ion batteries. In: Electrochim. Acta 201 (2016), may, 354–365. [12]
- Hein, Simon ; Feinauer, Julian ; Westhoff, Daniel ; Manke, Ingo ; Schmidt, Volker ; Latz, Arnulf: Stochastic microstructure modeling and electrochemical simulation of lithium-ion cell anodes in 3D, In: J. Power Sources. 336 (2016) 161–171. [121]
- Hein, Simon; Latz, Arnulf: An electrochemical model of lithium plating and stripping in lithium-ion batteries. In: Phys. Chem. Chem. Phys. *submitted* [155]

Part

- Westhoff, Daniel ; Feinauer, Julian ; Kuchler, Klaus ; Mitsch, Tim ; Hein, Simon ; Latz, Arnulf ; Schmidt, Volker: Parametric stochastic 3D model for the microstructure of anodes in lithium-ion power cells, In: Comput. Mater. Sci. 126 (2016) 453–467. [119]
- Westhoff, Daniel ; Feinauer, Julian ; Hein, Simon ; Rave, Stephan ; Schmidt, Sebastian ; Zausch, Jochen ; Iliev, Oleg ; Latz, Arnulf ; Ohlberger, Mario ; Schmidt, Volker: MULTIBAT: Unified workflow for fast electrochemical 3D simulations of lithium-ion cells combining virtual stochastic microstructures, electrochemical degradation models and model order reduction. In: Journal of Computational Science *accepted* [136]
- Danner, Timo; Singh; Madhav; Hein, Simon; Kaiser, Jörg; Hahn, Horst; Latz, Arnulf: Thick electrodes for Li-ion batteries: A model based analysis, In: J. Power Sources. 334 (2016) 191–201. [8]
- M.A. Cabanero, J. Altmann, L. Gold, N. Boaretto, J. Müller, S. Hein, et al., Investigation on the temperature dependence of lithium plating in commercial Li-ion batteries, In Electrochimica Acta *submitted* [140]

Conferences

Talks

1. 2016 - Modval in Lausanne (Switzerland)
2. 2015 - ISE topical in Saint Malo (France)
3. 2015 - ECS in Phoenix (USA)

Poster

1. 2017 - AABC in Mainz (Germany)
2. 2014 - Modval in Winterthur (Switzerland)
3. 2014 - UECT in Ulm (Germany)

Part

1. 2017 - Kraftwerk Batterie in Aachen (Germany); Poster: Thomas Waldmann (ZSW)
2. 2016 - Kraftwerk Batterie in Münster (Germany); Poster: Stefan Schindler (HIU)
3. 2015 - Modval in Freiburg (Germany); Talk: Arnulf Latz (DLR)

Bibliography

[1] Staff, Guardian: *Tesla to build world's biggest lithium ion battery in South Australia.* https://www.theguardian.com/australia-news/2017/jul/07/tesla-to-build-worlds-biggest-lithium-ion-battery-in-south-australia. Version: August 1 2017

[2] Younicos: *WEMAG BATTERY PARK SUCCESSFULLY BLACK STARTS GRID.* https://www.younicos.com/wemag-battery-park-successfully-black-starts-grid-first-attempt/. Version: September 1 2017

[3] Winter, Martin ; Passerini, Stefano: Lithium ion batteries as key component for energy storage in automotive and stationary applications. In: *INTELEC, Int. Telecommun. Energy Conf.* (2011), S. 1–3. http://dx.doi.org/10.1109/INTLEC.2011.6099839. – DOI 10.1109/INTLEC.2011.6099839. – ISBN 9781457712494

[4] Arora, Pankaj ; Doyle, Marc ; White, Ralph E.: Mathematical Modeling of the Lithium Depotision Overcharge Reaction in Lithium-Ion Batteries Using Carbon-Based Negative Electrodes. In: *J. Electrochem. Soc.* 146 (1999), Nr. 10, 3543–3553. http://dx.doi.org/10.1149/1.1392512. – DOI 10.1149/1.1392512

[5] Tippmann, Simon ; Walper, Daniel ; Balboa, Luis ; Spier, Bernd ; Bessler, Wolfgang G.: Low-temperature charging of lithium-ion cells part I: Electrochemical modeling and experimental investigation of degradation behavior. In: *J. Power Sources* 252 (2014), apr, 305–316. http://dx.doi.org/10.1016/j.jpowsour.2013.12.022. – DOI 10.1016/j.jpowsour.2013.12.022. – ISSN 03787753

[6] ITWM: *BEST - Battery and Electrochemistry Simulation Tool.* https://www.itwm.fraunhofer.de/de/abteilungen/sms/produkte-und-leistungen/best-battery-and-electrochemistry-simulation-tool.html. Version: 2017-12-13

[7] Latz, Arnulf ; Zausch, Jochen: Multiscale modeling of lithium ion batteries: thermal aspects. In: *Beilstein J. Nanotechnol.* 6 (2015), apr, 987–1007. http://dx.doi.org/10.3762/bjnano.6.102. – DOI 10.3762/bjnano.6.102. – ISSN 2190–4286

[8] Danner, Timo ; Singh, Madhav ; Hein, Simon ; Kaiser, Jörg ; Hahn, Horst ; Latz, Arnulf: Thick electrodes for Li-ion batteries: A model based analysis. In: *J. Power Sources* 334 (2016), dec, 191–201. http://dx.doi.org/10.1016/j.jpowsour.2016.09.143. – DOI 10.1016/j.jpowsour.2016.09.143. – ISSN 03787753

[9] Ebner, Martin ; Geldmacher, Felix ; Marone, Federica ; Stampanoni, Marco ; Wood, Vanessa: X-Ray Tomography of Porous, Transition Metal Oxide Based Lithium Ion Battery Electrodes. In: *Adv. Energy Mater.* 3 (2013), Nr. 7, 845–850. http://dx.doi.org/10.1002/aenm.201200932. – DOI 10.1002/aenm.201200932. – ISSN 16146832

[10] Feinauer, Julian ; Brereton, Tim ; Spettl, Aaron ; Weber, Matthias ; Manke, Ingo ; Schmidt, Volker: Stochastic 3D modeling of the microstructure of lithium-ion battery anodes via Gaussian random fields on the sphere. In: *Comput. Mater. Sci.* 109 (2015), 137–146. http://dx.doi.org/10.1016/j.commatsci.2015.06.025. – DOI 10.1016/j.commatsci.2015.06.025. – ISBN 0927–0256

[11] Petzl, Mathias ; Danzer, Michael A.: Nondestructive detection, characterization, and quantification of lithium plating in commercial lithium-ion batteries. In: *J. Power Sources* 254 (2014), may, 80–87. http://dx.doi.org/10.1016/j.jpowsour.2013.12.060. – DOI 10.1016/j.jpowsour.2013.12.060. – ISSN 03787753

[12] Hein, Simon ; Latz, Arnulf: Influence of local lithium metal deposition in 3D microstructures on local and global behavior of Lithium-ion batteries. In: *Electrochim. Acta* 201 (2016), may, 354–365. http://dx.doi.org/10.1016/j.electacta.2016.01.220. – DOI 10.1016/j.electacta.2016.01.220. – ISSN 00134686

[13] Scrosati, B ; Abraham, KM ; Schalkwijk, Walter van ; Hassoun, Jusef: *Lithium batteries: advanced technologies and applications*. Wiley, 2013

[14] Lenfant, P.: Primary lithium batteries in europe — an industrial and commercial fact. In: *J. Power Sources* 14 (1985), Nr. October, 251–254. http://dx.doi.org/10.1016/0378-7753(85)88038-1. – DOI 10.1016/0378–7753(85)88038–1. – ISBN 6135000882708

[15] Yoshio, Masaki ; Brodd, Ralph J. ; Kozawa, Akiya ; Yoshio, Masaki (Hrsg.) ; Brodd, Ralph J. (Hrsg.) ; Kozawa, Akiya (Hrsg.): *Lithium-ion batteries: Science and technologies*. New York, NY : Springer New York, 2009. – 1–452 S. http://dx.doi.org/10.1007/978-0-387-34445-4. http://dx.doi.org/10.1007/978-0-387-34445-4. – ISBN 9780387344447

[16] Brandt, K: Historical development of secondary lithium batteries. In: *Solid State Ionics* 69 (1994), Nr. 3-4, S. 173–183. http://dx.doi.org/10.1016/0167-2738(94)90408-1. – DOI 10.1016/0167–2738(94)90408–1. – ISBN 01672738

[17] Goodenough, John B. ; Kim, Youngsik: Challenges for rechargeable Li batteries. In: *Chem. Mater.* 22 (2010), feb, Nr. 3, 587–603. http://dx.doi.org/10.1021/cm901452z. – DOI 10.1021/cm901452z. – ISBN 0897–4756

[18] Yazami, R. ; Touzain, Ph: A reversible graphite-lithium negative electrode for electrochemical generators. In: *J. Power Sources* 9 (1983), Nr. 3, S. 365–371. http://dx.doi.org/10.1016/0378-7753(83)87040-2. – DOI 10.1016/0378–7753(83)87040–2. – ISBN 0378–7753

[19] Sony: *Keywords to understanding Sony Energy Devices*. http://www.sonyenergy-devices.co.jp/en/keyword/. Version: 2016-08-03

[20] Nagaura, T. ; Tozawa, K.: Lithium ion rechargeable battery. In: *Prog. Batter. Sol. Cells* 9 (1990), S. 209

[21] Rogers, John A. ; Maznev, Alex A. ; Banet, Matthew J. ; Nelson, Keith A.: *Optical Generation and Characterization of Acoustic Waves in Thin Films: Fundamentals and Applications*. 2nd. John Wiley & Sons, Inc., 2000. – 117–157 S. http://dx.doi.org/10.1146/annurev.matsci.30.1.117. http://dx.doi.org/10.1146/annurev.matsci.30.1.117. – ISBN 0471043729

[22] Tarascon, Jean-Marie ; Armand, M: Issues and challenges facing rechargeable lithium batteries. In: *Nature* 414 (2001), nov, Nr. 6861, 359–367. http://dx.doi.org/10.1038/35104644. – DOI 10.1038/35104644. – ISSN 0028–0836

[23] Latz, Arnulf ; Zausch, Jochen ; Iliev, Oleg: Modeling of species and charge transport in Li–Ion Batteries based on non-equilibrium thermodynamics. In: *Berichte des Fraunhofer ITWM* 190 (2010), Nr. 190. http://link.springer.com/chapter/10.1007/978-3-642-18466-6_39

[24] Vu, Anh ; Qian, Yuqiang ; Stein, Andreas: Porous Electrode Materials for Lithium-Ion Batteries - How to Prepare Them and What Makes Them Special. In: *Adv. Energy Mater.* 2 (2012), Nr. 9, 1056–1085. http://dx.doi.org/10.1002/aenm.201200320. – DOI 10.1002/aenm.201200320. – ISSN 16146832

[25] Spahr, Michael E. ; Goers, Dietrich ; Leone, Antonio ; Stallone, Salvatore ; Grivei, Eusebiu: Development of carbon conductive additives for advanced lithium ion batteries. In: *J. Power Sources* 196 (2011), Nr. 7, 3404–3413. http://dx.doi.org/10.1016/j.jpowsour.2010.07.002. – DOI 10.1016/j.jpowsour.2010.07.002. – ISSN 03787753

[26] Dougassa, Yvon R. ; Jacquemin, Johan ; El Ouatani, Loubna ; Tessier, Cécile ; Anouti, Mérièm: Viscosity and Carbon Dioxide Solubility for LiPF6, LiTFSI, and LiFAP in Alkyl Carbonates: Lithium Salt Nature and Concentration Effect. In: *J. Phys. Chem. B* 118 (2014), apr, Nr. 14, 3973–80. http://dx.doi.org/10.1021/jp500063c. – DOI 10.1021/jp500063c. – ISSN 1520–5207

[27] Forestier, Coralie ; Grugeon, Sylvie ; Davoisne, Carine ; Lecocq, Amandine ; Marlair, Guy ; Armand, Michel ; Sannier, Lucas ; Laruelle, Stéphane: Graphite electrode thermal behavior and solid electrolyte interphase investigations: Role of state-of-the-art binders, carbonate additives and lithium bis(fluorosulfonyl)imide salt. In: *J. Power Sources* 330 (2016), 186–194. http://dx.doi.org/10.1016/j.jpowsour.2016.09.005. – DOI 10.1016/j.jpowsour.2016.09.005. – ISSN 03787753

[28] Novák, Petr ; Müller, Klaus ; Santhanam, K. S. V. ; Haas, Otto: Electrochemically Active Polymers for Rechargeable Batteries. In: *Chem. Rev.* 97 (1997), Nr. 1, 207–282. http://dx.doi.org/10.1021/cr941181o. – DOI 10.1021/cr941181o. – ISBN 0009–2665

[29] Marom, Rotem ; Amalraj, S. F. ; Leifer, Nicole ; Jacob, David ; Aurbach, Doron: A review of advanced and practical lithium battery materials. In: *J. Mater. Chem.* 21 (2011), Nr. 27, S. 9938. http://dx.doi.org/10.1039/c0jm04225k. – DOI 10.1039/c0jm04225k. – ISBN 0959–9428

[30] Nitta, Naoki ; Wu, Feixiang ; Lee, Jung T. ; Yushin, Gleb: Li-ion battery materials: Present and future. In: *Mater. Today* 18 (2015), Nr. 5, 252–264. http://dx.doi.org/10.1016/j.mattod.2014.10.040. – DOI 10.1016/j.mattod.2014.10.040. – ISBN 1369–7021

[31] Bruce, Peter G. ; Saidi, M. Y.: The mechanism of electrointercalation. In: *J. Electroanal. Chem.* 322 (1992), Nr. 1-2, S. 93–105. http://dx.doi.org/10.1016/0022-0728(92)80069-G. – DOI 10.1016/0022–0728(92)80069–G. – ISBN 0022–0728

[32] Bruce, Peter G. ; Saidi, M. Y.: A two-step model of intercalation. In: *Solid State Ionics* 51 (1992), Nr. 3-4, S. 187–190. http://dx.doi.org/10.1016/0167-2738(92)90198-X. – DOI 10.1016/0167–2738(92)90198–X. – ISBN 0167–2738

[33] Newman, John ; Thomas-Alyea, Karen E.: *Electrochemical systems*. 3rd editio. John Wiley & Sons, 2004. – ISBN 978–0–471–47756–3

[34] Latz, Arnulf ; Zausch, Jochen: Thermodynamic derivation of a Butler–Volmer model for intercalation in Li-ion batteries. In: *Electrochim. Acta* 110 (2013), nov, 358–362. http://dx.doi.org/10.1016/j.electacta.2013.06.043. – DOI 10.1016/j.electacta.2013.06.043. – ISSN 00134686

[35] Lück, Jessica ; Latz, Arnulf: Theory of reactions at electrified interfaces. In: *Phys. Chem. Chem. Phys.* 18 (2016), Nr. 27, 17799–17804. http://dx.doi.org/10.1039/C6CP02681H. – DOI 10.1039/C6CP02681H. – ISSN 1463–9076

[36] Latz, Arnulf ; Zausch, Jochen: Thermodynamic consistent transport theory of Li-ion batteries. In: *J. Power Sources* 196 (2011), mar, Nr. 6, 3296–3302. http://dx.doi.org/10.1016/j.jpowsour.2010.11.088. – DOI 10.1016/j.jpowsour.2010.11.088. – ISSN 03787753

[37] ITWM: *CoRheos - Complex Rheology Solver*. www.itwm.fraunhofer.de/de/abteilungen/sms/komplexe-fluide-und-mehrphasenstroemung.html. Version: 2017-12-13

[38] Less, G. B. ; Seo, J. H. ; Han, S. ; Sastry, A. M. ; Zausch, Jochen ; Latz, Arnulf ; Schmidt, Sebastian ; Wieser, C. ; Kehrwald, D. ; Fell, S.: Micro-Scale Modeling of Li-Ion Batteries: Parameterization and Validation. In: *J. Electrochem. Soc.* 159 (2012), Nr. 6, A697–A704. http://dx.doi.org/10.1149/2.096205jes. – DOI 10.1149/2.096205jes. – ISSN 00134651

[39] Braithwaite, Jeffrey W.: Corrosion of Lithium-Ion Battery Current Collectors. In: *J. Electrochem. Soc.* 146 (1999), Nr. 2, S. 448. http://dx.doi.org/10.1149/1.1391627. – DOI 10.1149/1.1391627. – ISSN 00134651

[40] Lu, Peng ; Li, Chen ; Schneider, Eric W. ; Harris, Stephen J.: Chemistry, impedance, and morphology evolution in solid electrolyte interphase films during formation in lithium ion batteries. In: *J. Phys. Chem. C* 118 (2014), Nr. 2, S. 896–903. http://dx.doi.org/10.1021/jp4111019. – DOI 10.1021/jp4111019. – ISBN 1932–7447

[41] Dasgupta, Sankar ; Jacobs, James K.: *CURRENT COLLECTOR FOR LITHIUM ION BATTERY*. 1996

[42] Arora, Pankaj ; White, Ralph E. ; Doyle, Marc: Capacity Fade Mechanisms and Side Reactions in Lithium-Ion Batteries. In: *J. Electrochem. Soc.* 145 (1998), Nr. 10, 3647. http://dx.doi.org/10.1149/1.1838857. – DOI 10.1149/1.1838857. – ISBN 0013–4651

[43] Yang, Li ; Xiao, Ang ; Lucht, Brett L.: Investigation of solvation in lithium ion battery electrolytes by NMR spectroscopy. In: *J. Mol. Liq.* 154 (2010), Nr. 2-3, 131–133. http://dx.doi.org/10.1016/j.molliq.2010.04.025. – DOI 10.1016/j.molliq.2010.04.025. – ISBN 01677322

[44] Morita, Masayuki ; Asai, Yoshiko ; Yoshimoto, Nobuko ; Ishikawa, Masashi: A Raman spectroscopic study of organic electrolyte solutions based on binary solvent systems of ethylene carbonate with low viscosity solvents which dissolve different lithium salts. In: *J. Chem. Soc. Faraday Trans.* 94 (1998), Nr. 23, S. 3451–3456. http://dx.doi.org/10.1039/a806278a. – DOI 10.1039/a806278a. – ISBN 1364–5455

[45] Borodin, Oleg ; Smith, Grant D.: Quantum Chemistry and Molecular Dynamics Simulation Study of Dimethyl Carbonate: Ethylene Carbonate Electrolytes Doped with LiPF 6. In: *J. Phys. Chem. B* 113 (2009), Nr. 6, 1763–1776. http://dx.doi.org/10.1021/jp809614h. – DOI 10.1021/jp809614h. – ISBN 1520–6106

[46] Xu, Kang ; Lam, Y. ; Zhang, Sheng S. ; Jow, T R. ; Curtis, T.B.: Solvation Sheath of Li+ in Nonaqueous Electrolytes and Its Implication of Graphite/Electrolyte Interface Chemistry. In: *J. Phys. Chem. C* 111 (2007), may, Nr. 20, 7411–7421. http://dx.doi.org/10.1021/jp068691u. – DOI 10.1021/jp068691u. – ISSN 1932–7447

[47] Xu, Kang: "Charge-Transfer" Process at Graphite/Electrolyte Interface and the Solvation Sheath Structure of Li[sup +] in Nonaqueous Electrolytes. In: *J. Electrochem. Soc.* 154 (2007), Nr. 3, A162. http://dx.doi.org/10.1149/1.2409866. – DOI 10.1149/1.2409866. – ISBN 0013–4651

[48] Enoki, Toshiaki ; Endo, Morinobu ; Suzuki, Masatsugu: *Graphite Intercalation Compounds and Applications*. 2003. – 456 S. http://site.ebrary.com/lib/alltitles/docDetail.action?docID=10266491. – ISBN 9780195128277

[49] Dahn, J. R. ; Zheng, T. ; Liu, Y. ; Xue, J. S.: Mechanisms for Lithium Insertion in Carbonaceous Materials. In: *Science (80-.).* 270 (1995), Nr. 5236, S. 590–593. http://dx.doi.org/10.1126/science.270.5236.590. – DOI 10.1126/science.270.5236.590. – ISBN 0036–8075

[50] Fong, Rosamaria ; Sacken, Ulrich von ; Dahn, J. R.: Studies of Lithium Intercalation into Carbons Using Nonaqueous Electrochemical Cells. In: *J. Electrochem. Soc.* 137 (1990), Nr. 7, 2009. http://dx.doi.org/10.1149/1.2086855. – DOI 10.1149/1.2086855. – ISSN 00134651

[51] Safari, M. ; Delacourt, C.: Modeling of a Commercial Graphite/LiFePO4 Cell. In: *J. Electrochem. Soc.* 158 (2011), Nr. 5, A562–A571. http://dx.doi.org/10.1149/1.3567007. – DOI 10.1149/1.3567007. – ISSN 00134651

[52] Moon, Janghyuk: Ab initio and kinetic Monte Carlo simulation study of lithiation in c- and a-silicon. In: *J. Power Sources* 272 (2014), 1010–1017. http://dx.doi.org/10.1016/j.jpowsour.2014.09.004. – DOI 10.1016/j.jpowsour.2014.09.004. – ISSN 03787753

[53] Ohzuku, Tsutomu ; Iwakoshi, Yasunobu ; Sawai, Keijiro: Formation of Lithium-Graphite Intercalation Compounds in Nonaqueous Electrolytes and Their Application as a Negative Electrode for a Lithium Ion (Shuttlecock) Cell. In: *J. Electrochem. ...* 140 (1993), Nr. 9, 1–9. http://jes.ecsdl.org/content/140/9/2490.short

[54] Fuller, Thomas F. ; Doyle, Marc ; Newman, John: Simulation and Optimization of the Dual Lithium Ion Insertion Cell. In: *J. Electrochem. Soc.* 141 (1994), Nr. 1, 1–10. http://dx.doi.org/10.1149/1.2054684. – DOI 10.1149/1.2054684. – ISBN 0013–4651

[55] Dahn, J. R.: Phase diagram of LixC6. In: *Phys. Rev. B* 44 (1991), nov, Nr. 17, 9170–9177. http://dx.doi.org/10.1103/PhysRevB.44.9170. – DOI 10.1103/PhysRevB.44.9170. – ISBN 0163–1829

[56] Sethuraman, Vijay a. ; Hardwick, Laurence J. ; Srinivasan, Venkat ; Kostecki, Robert: Surface structural disordering in graphite upon lithium intercalation/deintercalation. In: *J. Power Sources* 195 (2010), Nr. 11, S. 3655–3660. http://dx.doi.org/10.1016/j.jpowsour.2009.12.034. – DOI 10.1016/j.jpowsour.2009.12.034. – ISBN 0378–7753

[57] Qi, Yue ; Harris, Stephen J.: In Situ Observation of Strains during Lithiation of a Graphite Electrode. In: *J. Electrochem. Soc.* 157 (2010), Nr. 6, S. A741. http://dx.doi.org/10.1149/1.3377130. – DOI 10.1149/1.3377130. – ISBN 0013–4651

[58] Qi, Yue ; Guo, Haibo ; Hector, Louis G. ; Timmons, Adam: Threefold Increase in the Young's Modulus of Graphite Negative Electrode during Lithium Intercalation. In: *J. Electrochem. Soc.* 157 (2010), Nr. 5, A558–A566. http://dx.doi.org/10.1149/1.3327913. – DOI 10.1149/1.3327913. – ISSN 0013–4651, 1945–7111

[59] Job, G ; Herrmann, F: Chemical potential—a quantity in search of recognition. In: *Eur. J. Phys.* 27 (2006), Nr. 2, S. 353–371. http://dx.doi.org/10.1088/0143-0807/27/2/018. – DOI 10.1088/0143–0807/27/2/018. – ISBN 0143–0807

[60] Madelung, Otfried: *Heidelberger Taschenbücher*. Bd. 109: *Festkörpertheorie II*. Berlin, Heidelberg : Springer Berlin Heidelberg, 1972. http://dx.doi.org/10.1007/978-3-642-65413-8. http://dx.doi.org/10.1007/978-3-642-65413-8. – ISBN 978–3–540–05866–3

[61] Riess, I: What does a voltmeter measure? In: *Solid State Ionics* 95 (1997), Nr. 3-4, S. 327–328. http://dx.doi.org/10.1016/S0167-2738(96)00542-5. – DOI 10.1016/S0167–2738(96)00542–5. – ISSN 01672738

[62] Vetter, J. ; Novák, Petr ; Wagner, M. R. ; Veit, C. ; Möller, K.-C. ; Besenhard, J. O. ; Winter, Martin ; Wohlfahrt-Mehrens, Margret ; Vogler, C. ; Hammouche, A.: Ageing mechanisms in lithium-ion batteries. In: *J. Power Sources* 147 (2005), sep, Nr. 1-2, 269–281. http://dx.doi.org/10.1016/j.jpowsour.2005.01.006. – DOI 10.1016/j.jpowsour.2005.01.006. – ISSN 03787753

[63] Lin, H.-p. ; Chua, D ; Salomon, M ; Shiao, H-C ; Hendrickson, M ; Plichta, E ; Slane, S: Low-Temperature Behavior of Li-Ion Cells. In: *Electrochem. Solid-State Lett.* 4 (2001), Nr. 6, A71. http://dx.doi.org/10.1149/1.1368736. – DOI 10.1149/1.1368736. – ISBN 10990062

[64] Legrand, N. ; Knosp, B. ; Desprez, P. ; Lapicque, F. ; Raël, S.: Physical characterization of the charging process of a Li-ion battery and prediction of Li plating by electrochemical modelling. In: *J. Power Sources* 245 (2014), jan, 208–216. http://dx.doi.org/10.1016/j.jpowsour.2013.06.130. – DOI 10.1016/j.jpowsour.2013.06.130. – ISSN 03787753

[65] Tang, Maureen ; Albertus, Paul ; Newman, John: Two-Dimensional Modeling of Lithium Deposition during Cell Charging. In: *J. Electrochem. Soc.* 156 (2009), Nr. 5, A390–A399. http://dx.doi.org/10.1149/1.3095513. – DOI 10.1149/1.3095513. – ISBN 0013–4651

[66] Li, Zhe ; Huang, Jun ; Yann Liaw, Bor ; Metzler, Viktor ; Zhang, Jianbo: A review of lithium deposition in lithium-ion and lithium metal secondary batteries. In: *J. Power Sources* 254 (2014), 168–182. http://dx.doi.org/10.1016/j.jpowsour.2013.12.099. – DOI 10.1016/j.jpowsour.2013.12.099. – ISBN 03787753

[67] Rauh, R. D.: Some observations on the attack of esters by lithium. Version: 1975. http://oai.dtic.mil/oai/oai?verb=getRecord&metadataPrefix=html&identifier=ADA006746. 1975 (February). – Forschungsbericht

[68] Rauh, R. D.: Passive-Lithium Secondary Batteries. Version: 1975. http://oai.dtic.mil/oai/oai?verb=getRecord&metadataPrefix=html&identifier=ADA006748. 1975 (February). – Forschungsbericht

[69] Peled, E.: Film forming reaction at the lithium/electrolyte interface. In: *J. Power Sources* 9 (1983), Nr. 3, S. 253–266. http://dx.doi.org/10.1016/0378-7753(83)87026-8. – DOI 10.1016/0378–7753(83)87026–8. – ISBN 0378–7753

[70] Bonino, F. ; Scrosati, B. ; Selvaggi, A. ; Evans, J. ; Vincent, C. A.: Electrode processes at the lithium-polymer electrolyte interface. In: *J. Power Sources* 18 (1986), Nr. 1, S. 75–81. http://dx.doi.org/10.1016/0378-7753(86)80103-3. – DOI 10.1016/0378–7753(86)80103–3. – ISSN 03787753

[71] Shu, Z X. ; McMillan, RS S. ; Murray, JJ: Electrochemical intercalation of lithium into graphite. In: *J. Electrochem. ...* 140 (1993), Nr. 4, 922–927. http://dx.doi.org/10.1149/1.2056228. – DOI 10.1149/1.2056228. – ISSN 0013–4651

[72] Scrosati, Bruno: Lithium Rocking Chair Batteries: An Old Concept? In: *J. Electrochem. Soc.* 139 (1992), Nr. 10, S. 2776. http://dx.doi.org/10.1149/1.2068978. – DOI 10.1149/1.2068978. – ISBN 0013–4651

[73] Smart, M. C. ; Ratnakumar, B. V.: Effects of Electrolyte Composition on Lithium Plating in Lithium-Ion Cells. In: *J. Electrochem. Soc.* 158 (2011), Nr. 4, A379–A389. http://dx.doi.org/10.1149/1.3544439. – DOI 10.1149/1.3544439. – ISBN 0013–4651

[74] Petzl, Mathias ; Kasper, Michael ; Danzer, Michael A.: Lithium plating in a commercial lithium-ion battery – A low-temperature aging study. In: *J. Power Sources* 275 (2014), nov, 799–807. http://dx.doi.org/10.1016/j.jpowsour.2014.11.065. – DOI 10.1016/j.jpowsour.2014.11.065. – ISSN 03787753

[75] Schindler, Stefan ; Bauer, Marius ; Petzl, Mathias ; Danzer, Michael A.: Voltage relaxation and impedance spectroscopy as in-operando methods for the detection of lithium plating on graphitic anodes in commercial lithium-ion cells. In: *J. Power Sources* 304 (2016), 170–180. http://dx.doi.org/10.1016/j.jpowsour.2015.11.044. – DOI 10.1016/j.jpowsour.2015.11.044. – ISSN 03787753

[76] Zhang, Sheng S.: The effect of the charging protocol on the cycle life of a Li-ion battery. In: *J. Power Sources* 161 (2006), oct, Nr. 2, 1385–1391. http://dx.doi.org/10.1016/j.jpowsour.2006.06.040. – DOI 10.1016/j.jpowsour.2006.06.040. – ISSN 03787753

[77] Zhang, Sheng S. ; Xu, Kang ; Jow, T R.: Study of the charging process of a LiCoO2-based Li-ion battery. In: *J. Power Sources* 160 (2006), oct, Nr. 2, 1349–1354. http://dx.doi.org/10.1016/j.jpowsour.2006.02.087. – DOI 10.1016/j.jpowsour.2006.02.087. – ISSN 03787753

[78] Harris, Stephen J. ; Timmons, Adam ; Baker, Daniel R. ; Monroe, Charles W.: Direct in situ measurements of Li transport in Li-ion battery negative electrodes. In: *Chem. Phys. Lett.* 485 (2010), jan, Nr. 4-6, 265–274. http://dx.doi.org/10.1016/j.cplett.2009.12.033. – DOI 10.1016/j.cplett.2009.12.033. – ISSN 00092614

[79] Waldmann, Thomas ; Hogg, Björn-Ingo ; Kasper, Michael ; Grolleau, Sébastien ; Couceiro, César G. ; Trad, Khiem ; Matadi, Bramy P. ; Wohlfahrt-Mehrens, Margret: Interplay of Operational Parameters on Lithium Deposition in Lithium-Ion Cells: Systematic Measurements with Reconstructed 3-Electrode Pouch Full Cells. In: *J. Electrochem. Soc.* 163 (2016), Nr. 7, A1232–A1238. http://dx.doi.org/10.1149/2.0591607jes. – DOI 10.1149/2.0591607jes. – ISSN 0013–4651

[80] Burns, J. C. ; Stevens, D. a. ; Dahn, J. R.: In-Situ Detection of Lithium Plating Using High Precision Coulometry. In: *J. Electrochem. Soc.* 162 (2015), Nr. 6, A959–A964. http://dx.doi.org/10.1149/2.0621506jes. – DOI 10.1149/2.0621506jes. – ISSN 0013–4651

[81] Zinth, Veronika ; Lüders, Christian von ; Hofmann, Michael ; Hattendorff, Johannes ; Buchberger, Irmgard ; Erhard, Simon ; Rebelo-Kornmeier, Joana ; Jossen, Andreas ; Gilles, Ralph: Lithium plating in lithium-ion batteries at sub-ambient temperatures investigated by in situ neutron diffraction. In: *J. Power Sources* 271 (2014), 152–159. http://dx.doi.org/10.1016/j.jpowsour.2014.07.168. – DOI 10.1016/j.jpowsour.2014.07.168. – ISSN 03787753

[82] Ghanbari, N. ; Waldmann, Thomas ; Kasper, M. ; Axmann, Peter ; Wohlfahrt-Mehrens, Margret: Detection of Li Deposition by Glow Discharge Optical Emission Spectroscopy in Post-Mortem Analysis. In: *ECS Electrochem. Lett.* 4 (2015), Nr. 9, A100–A102. http://dx.doi.org/10.1149/2.0041509eel. – DOI 10.1149/2.0041509eel. – ISSN 2162–8726

[83] Waldmann, Thomas ; Iturrondobeitia, Amaia ; Kasper, Michael ; Ghanbari, Niloofar ; Aguesse, Frédéric ; Bekaert, Emilie ; Daniel, Lise ; Genies, Sylvie ; Gordon, Isabel J. ; Löble, Matthias W. ; De Vito, Eric ; Wohlfahrt-Mehrens, Margret: Review—Post-Mortem Analysis of Aged Lithium-Ion Batteries: Disassembly Methodology and Physico-Chemical Analysis

Techniques. In: *J. Electrochem. Soc.* 163 (2016), Nr. 10, A2149–A2164. http://dx.doi.org/10.1149/2.1211609jes. – DOI 10.1149/2.1211609jes. – ISSN 0013–4651

[84] Brissot, Claire ; Rosso, Michel ; Chazalviel, J.-N. ; Baudry, P ; Lascaud, Stephane: In situ study of dendritic growth in lithium/PEO-salt/lithium cells. In: *Electrochim. Acta* 43 (1998), apr, Nr. 10-11, 1569–1574. http://dx.doi.org/10.1016/S0013-4686(97)10055-X. – DOI 10.1016/S0013–4686(97)10055–X. – ISSN 00134686

[85] Yamaki, Jun-ichi ; Tobishima, Shin-ichi ; Hayashi, Katsuya ; Nemoto, Yasue ; Arakawa, Masayasu: A consideration of the morphology of electrochemically deposited lithium in an organic electrolyte. In: *J. Power Sources* 74 (1998), aug, Nr. 2, 219–227. http://dx.doi.org/10.1016/S0378-7753(98)00067-6. – DOI 10.1016/S0378–7753(98)00067–6. – ISSN 03787753

[86] Steiger, Jens ; Richter, Gunther ; Wenk, Moritz ; Kramer, Dominik ; Mönig, Reiner: Comparison of the Growth of Lithium Filaments and Dendrites Under Different Conditions. In: *Electrochem. commun.* 50 (2014), nov, 11–14. http://dx.doi.org/10.1016/j.elecom.2014.11.002. – DOI 10.1016/j.elecom.2014.11.002. – ISSN 13882481

[87] Bai, Peng ; Li, Ju ; Brushett, Fikile R. ; Bazant, Martin Z.: Transition of lithium growth mechanisms in liquid electrolytes. In: *Energy Environ. Sci.* (2016), 13–17. http://dx.doi.org/10.1039/C6EE01674J. – DOI 10.1039/C6EE01674J. – ISSN 1754–5692

[88] Lu, Languang ; Han, Xuebing ; Li, Jianqiu ; Hua, Jianfeng ; Ouyang, Minggao: A review on the key issues for lithium-ion battery management in electric vehicles. In: *J. Power Sources* 226 (2013), 272–288. http://dx.doi.org/10.1016/j.jpowsour.2012.10.060. – DOI 10.1016/j.jpowsour.2012.10.060. – ISBN 0378–7753

[89] Monroe, Charles W. ; Newman, John: Dendrite Growth in Lithium/Polymer Systems. In: *J. Electrochem. Soc.* 150 (2003), Nr. 10, A1377–A1384. http://dx.doi.org/10.1149/1.1606686. – DOI 10.1149/1.1606686. – ISSN 00134651

[90] Horstmann, Birger ; Hein, Simon ; Latz, Arnulf: Modeling Lithium Stripping and Plating. In: *Meet. Abstr.* MA2014-04 (2014), jun, Nr. 4, 629. http://ma.ecsdl.org/content/MA2014-04/4/629.abstract

[91] Meibuhr, Stuart G.: Electrode Studies in Nonaqueous Electrolytes. In: *J. Electrochem. Soc.* 117 (1970), Nr. 1, 56. http://dx.doi.org/10.1149/1.2407438. – DOI 10.1149/1.2407438. – ISSN 00134651

[92] Scarr, Robert F.: Kinetics of the Solid Lithium Electrode in Propylene Carbonate. In: *J. Electrochem. Soc.* 117 (1970), Nr. 3, S. 295–299. http://dx.doi.org/10.1149/1.2407497. – DOI 10.1149/1.2407497. – ISSN 00134651

[93] Crowther, Owen ; West, Alan C.: Effect of Electrolyte Composition on Lithium Dendrite Growth. In: *J. Electrochem. Soc.* 155 (2008), Nr. 11, A806. http://dx.doi.org/10.1149/1.2969424. – DOI 10.1149/1.2969424. – ISSN 00134651

[94] Metzger, M. ; Marino, C. ; Sicklinger, J. ; Haering, D. ; Gasteiger, Hubert A.: Anodic Oxidation of Conductive Carbon and Ethylene Carbonate in High-Voltage Li-Ion Batteries Quantified by On-Line Electrochemical Mass Spectrometry. In: *J. Electrochem. Soc.* 162 (2015), Nr. 7, A1123–A1134. http://dx.doi.org/10.1149/2.0951506jes. – DOI 10.1149/2.0951506jes. – ISBN 0013–4651

[95] Jana, Aniruddha ; Ely, David R. ; García, R. E.: Dendrite-separator interactions in lithium-based batteries. In: *J. Power Sources* 275 (2015), 912–921. http://dx.doi.org/10.1016/j.jpowsour.2014.11.056. – DOI 10.1016/j.jpowsour.2014.11.056. – ISBN 03787753

[96] Chazalviel, J.-N. N.: Electrochemical aspects of the generation of ramified metallic electrodeposits. In: *Phys. Rev. A* 42 (1990), Nr. 12, 7355–7367. http://dx.doi.org/10.1103/PhysRevA.42.7355. – DOI 10.1103/PhysRevA.42.7355. – ISBN 1050–2947

[97] Rosso, Michel ; Chassaing, Elisabeth ; Fleury, Vincent ; Chazalviel, J.-N. Jean-Noël ; Vincent, Fleury ; Chazalviel, J.-N. Jean-Noël ; Fleury, Vincent: Shape evolution of metals electrodeposited from binary electrolytes. In: *J. Electroanal. Chem.* 559 (2003), nov, 165–173. http://dx.doi.org/10.1016/S0022-0728(02)01269-X. – DOI 10.1016/S0022–0728(02)01269–X. – ISSN 15726657

[98] Tan, Jinwang ; Ryan, Emily M.: Computational study of electro-convection effects on dendrite growth in batteries. In: *J. Power Sources* 323 (2016), 67–77. http://dx.doi.org/10.1016/j.jpowsour.2016.05.012. – DOI 10.1016/j.jpowsour.2016.05.012. – ISSN 03787753

[99] Doyle, Marc ; Fuller, Thomas F. ; Newman, John: Modeling of galvanostatic charge and discharge of the lithium/polymer/insertion cell. In: *J. Electrochem. Soc.* 140 (1993), Nr. 6, 1526–1533. http://jes.ecsdl.org/content/140/6/1526.short

[100] Perkins, Roger D. ; Randall, Alfred V. ; Zhang, Xiangchun ; Plett, Gregory L.: Controls oriented reduced order modeling of lithium deposition on overcharge. In: *J. Power Sources* 209 (2012), jul, 318–325. http://dx.doi.org/10.1016/j.jpowsour.2012.03.003. – DOI 10.1016/j.jpowsour.2012.03.003. – ISSN 03787753

[101] Single, Fabian ; Horstmann, Birger ; Latz, Arnulf: Revealing SEI Morphology: In-Depth Analysis of a Modeling Approach. In: *J. Electrochem. Soc.* 164 (2017), Nr. 11, E3132–E3145. http://dx.doi.org/10.1149/2.0121711jes. – DOI 10.1149/2.0121711jes. – ISSN 0013–4651

[102] Wieser, Michael E. ; Coplen, Tyler B.: Atomic weights of the elements 2009 (IUPAC Technical Report). In: *Pure Appl. Chem.* 83 (2010), Nr. 2, 2012. http://dx.doi.org/10.1351/PAC-REP-10-09-14. – DOI 10.1351/PAC–REP–10–09–14. – ISBN 0033–4545

[103] Greenwood, Norman N. ; Earnshaw, A: *Chemie der Elemente*. Wiley-VCH, 1990. – 5–8 S. – ISBN 9783527261697

[104] Meister, Andreas: *Numerik linearer Gleichungssysteme*. Wiesbaden : Springer Fachmedien Wiesbaden, 2015. http://dx.doi.org/10.1007/978-3-658-07200-1. http://dx.doi.org/10.1007/978-3-658-07200-1. – ISBN 978–3–658–07199–8

[105] Cormen, Thomas H. ; Leiserson, Charles E. ; Rivest, Ronald L. ; Stein, Clifford: *Introduction to Algorithms*. Massachusetts Institute of Technology, 2009. – 235 S. – ISBN 9780262033848

[106] Brune, Harald: Microscopic view of epitaxial metal growth: Nucleation and aggregation. In: *Surf. Sci. Rep.* 31 (1998), may, Nr. 3-4, S. 125–229. http://dx.doi.org/10.1016/S0167-5729(99)80001-6. – DOI 10.1016/S0167–5729(99)80001–6. – ISSN 01675729

[107] Tornberg, Anna-Karin ; Engquist, Björn: Regularization techniques for numerical approximation of PDEs with singularities. In: *J. Sci. Comput.* 19 (2003), Nr. 1/3, 527–552. http://dx.doi.org/10.1023/A:1025332815267. – DOI 10.1023/A:1025332815267. – ISSN 08857474

[108] Langtangen, Hans P. ; Pedersen, Geir K.: *Scaling of Differential Equations*. Cham : Springer International Publishing, 2016. http://dx.doi.org/10.1007/978-3-319-32726-6. http://dx.doi.org/10.1007/978-3-319-32726-6. – ISBN 978–3–319–32725–9

[109] Taiwo, Oluwadamilola O. ; Finegan, Donal P. ; Gelb, Jeff ; Holzner, Christian ; Brett, Daniel J L. ; Shearing, Paul R.: The use of contrast enhancement techniques in X-ray imaging of lithium???ion battery electrodes. In: *Chem. Eng. Sci.* 154 (2016), 27–33. http://dx.doi.org/10.1016/j.ces.2016.04.023. – DOI 10.1016/j.ces.2016.04.023. – ISSN 00092509

[110] Liu, Zhao ; Chen-Wiegart, Yu-chen K. ; Wang, Jun ; Barnett, Scott A. ; Faber, Katherine T.: Three-Phase 3D Reconstruction of a LiCoO2 Cathode via FIB-SEM Tomography. In: *Microsc. Microanal.* (2016), 1–9. http://dx.doi.org/10.1017/S1431927615015640. – DOI 10.1017/S1431927615015640. – ISSN 1431–9276

[111] Math2Market: *GeoDict*. www.geodict.com. Version: 2015

[112] Horiba: *Particle Size Analysis of Battery Materials*. http://www.horiba.com/scientific/products/particle-characterization/applications/battery/. Version: 2016-08-25

[113] Park, Jonghyun ; Lu, Wei ; Sastry, Ann M.: Numerical Simulation of Stress Evolution in Lithium Manganese Dioxide Particles due to Coupled Phase Transition and Intercalation. In: *J. Electrochem. Soc.* 158 (2011), Nr. 2, S. A201. http://dx.doi.org/10.1149/1.3526597. – DOI 10.1149/1.3526597. – ISSN 00134651

[114] Huang, H. ; Chen, C. H. ; Perego, R. C. ; Kelder, E. M. ; Chen, L. ; Schoonman, J. ; Weydanz, W. J. ; Nielsen, D. W.: Electrochemical characterization of commercial lithium manganese oxide powders. In: *Solid State Ionics* 127 (2000), Nr. 1-2, S. 31–42. http://dx.doi.org/10.1016/S0167-2738(99)00057-0. – DOI 10.1016/S0167–2738(99)00057–0. – ISBN 0167–2738

[115] Pfaffmann, Lukas ; Jaiser, Stefan ; Müller, Marcus ; Scharfer, Philip ; Schabel, Wilhelm ; Bauer, Werner ; Scheiba, Frieder ; Ehrenberg, Helmut: New method for binder and carbon black detection at nanometer scale in carbon electrodes for lithium ion batteries. In: *J. Power Sources* 363 (2017), 460–469. http://dx.doi.org/10.1016/j.jpowsour.2017.07.102. – DOI 10.1016/j.jpowsour.2017.07.102. – ISSN 03787753

[116] MULTIBAT: *BMBF-Project: MULTIBAT (05M13CLA)*. https://www.uni-muenster.de/AMM/num/ohlberger/research/projects/MULTIBAT/

[117] Mitsch, Tim ; Krämer, Yvonne ; Feinauer, Julian ; Gaiselmann, Gerd ; Markötter, Henning ; Manke, Ingo ; Hintennach, Andreas ; Schmidt, Volker: Preparation and Characterization of Li-ion Graphite Anodes using Synchrotron Tomography. In: *Materials (Basel).* (2014), S. 1–21. http://dx.doi.org/10.3390/ma7064455. – DOI 10.3390/ma7064455. – ISBN 4917630905697

[118] Gaiselmann, Gerd ; Tötzke, Christian ; Manke, Ingo ; Lehnert, Werner ; Schmidt, Volker: 3D microstructure modeling of compressed fiber-based materials. In: *J. Power Sources* 257 (2014), 52–64. http://dx.doi.org/10.1016/j.jpowsour.2014.01.095. – DOI 10.1016/j.jpowsour.2014.01.095. – ISSN 03787753

[119] Westhoff, Daniel ; Feinauer, Julian ; Kuchler, Klaus ; Mitsch, Tim ; Hein, Simon ; Latz, Arnulf ; Schmidt, Volker: Parametric stochastic 3D model for the microstructure of anodes in lithium-ion power cells. In: *Comput. Mater. Sci.* 126 (2016), 453–467. http://dx.doi.org/10.1016/j.commatsci.2016.09.006. – DOI 10.1016/j.commatsci.2016.09.006. – ISSN 0927–0256

[120] Gaiselmann, Gerd ; Neumann, Matthias ; Schmidt, Volker ; Pecho, Omar ; Hocker, Thomas ; Holzer, Lorenz: Quantitative relationships between microstructure and effective transport properties based on virtual materials testing. In: *AIChE J.* 60 (2014), jun, Nr. 6, 1983–1999. http://dx.doi.org/10.1002/aic.14416. – DOI 10.1002/aic.14416. – ISBN 9783902661548

[121] Hein, Simon ; Feinauer, Julian ; Westhoff, Daniel ; Manke, Ingo ; Schmidt, Volker ; Latz, Arnulf: Stochastic microstructure modeling and electrochemical simulation of lithium-ion cell anodes in 3D. In: *J. Power Sources* 336 (2016), dec, 161–171. http://dx.doi.org/10.1016/j.jpowsour.2016.10.057. – DOI 10.1016/j.jpowsour.2016.10.057. – ISSN 03787753

[122] Doyle, Marc ; Newman, John ; Gozdz, Antoni S. ; Schmutz, Caroline N. ; Tarascon, Jean-Marie: Comparison of Modeling Predictions with Experimental Data from Plastic Lithium Ion Cells. In: *J. Electrochem. Soc.* 143 (1996), Nr. 6, 1890. http://dx.doi.org/10.1149/1.1836921. – DOI 10.1149/1.1836921. – ISBN 9781450307192

[123] Morgan, M: Electrical conduction in amorphous carbon films. In: *Thin Solid Films* 7 (1970), Nr. l, S. 313–323. http://dx.doi.org/10.1016/0040-6090(71)90049-6. – DOI 10.1016/0040–6090(71)90049–6

[124] Langer, J. ; Epp, V ; Heitjans, P ; Mautner, F A. ; Wilkening, M: Lithium motion in the anode material LiC6 as seen via time-domain 7Li NMR. In: *Phys. Rev. B - Condens. Matter Mater. Phys.* 88 (2013), Nr. 9, S. 1–9. http://dx.doi.org/10.1103/PhysRevB.88.094304. – DOI 10.1103/PhysRevB.88.094304. – ISSN 10980121

[125] Chandrasekaran, Rajeswari ; Fuller, Thomas F.: Analysis of the Lithium-Ion Insertion Silicon Composite Electrode/Separator/Lithium Foil Cell. In: *J. Electrochem. Soc.* 158 (2011), Nr.

8, A859–A871. http://dx.doi.org/10.1149/1.3589301. – DOI 10.1149/1.3589301. – ISBN 0013–4651

[126] Jow, T R. ; Marx, Michelle B. ; Allen, Jan L.: Distinguishing Li+ Charge Transfer Kinetics at NCA/Electrolyte and Graphite/Electrolyte Interfaces, and NCA/Electrolyte and LFP/Electrolyte Interfaces in Li-Ion Cells. In: *J. Electrochem. Soc.* 159 (2012), Nr. 5, A604. http://dx.doi.org/10.1149/2.079205jes. – DOI 10.1149/2.079205jes. – ISBN 9781607682295

[127] Du, Wenbo ; Gupta, Amit ; Zhang, Xiangchun ; Sastry, Ann M. ; Shyy, Wei: Effect of cycling rate, particle size and transport properties on lithium-ion cathode performance. In: *Int. J. Heat Mass Transf.* 53 (2010), Nr. 17-18, 3552–3561. http://dx.doi.org/10.1016/j.ijheatmasstransfer.2010.04.017. – DOI 10.1016/j.ijheatmasstransfer.2010.04.017. – ISBN 00179310

[128] Srinivasan, Venkat ; Newman, John: Design and Optimization of a Natural Graphite/Iron Phosphate Lithium-Ion Cell. In: *J. Electrochem. Soc.* 151 (2004), Nr. 10, S. A1530. http://dx.doi.org/10.1149/1.1785013. – DOI 10.1149/1.1785013. – ISBN 0013–4651

[129] Buchberger, Irmgard ; Seidlmayer, Stefan ; Pokharel, Aneil ; Piana, Michele ; Hattendorff, Johannes ; Kudejova, Petra ; Gilles, Ralph ; Gasteiger, Hubert A.: Aging Analysis of Graphite/LiNi 1/3 Mn 1/3 Co 1/3 O 2 Cells Using XRD, PGAA, and AC Impedance. In: *J. Electrochem. Soc.* 162 (2015), Nr. 14, A2737–A2746. http://dx.doi.org/10.1149/2.0721514jes. – DOI 10.1149/2.0721514jes. – ISSN 0013–4651

[130] Reimers, Jan N. ; Shoesmith, M. ; Lin, Y. S. ; Valoen, Lars O.: Simulating High Current Discharges of Power Optimized Li-Ion Cells. In: *J. Electrochem. Soc.* 160 (2013), Nr. 10, A1870–A1884. http://dx.doi.org/10.1149/2.094310jes. – DOI 10.1149/2.094310jes. – ISBN 0013–4651

[131] Ghanbari, Niloofar ; Waldmann, Thomas ; Kasper, Michael ; Axmann, Peter ; Wohlfahrt-Mehrens, Margret: Inhomogeneous Degradation of Graphite Anodes in Li-Ion Cells: A Postmortem Study Using Glow Discharge Optical Emission Spectroscopy (GD-OES). In: *J. Phys. Chem. C* 120 (2016), oct, Nr. 39, 22225–22234. http://dx.doi.org/10.1021/acs.jpcc.6b07117. – DOI 10.1021/acs.jpcc.6b07117. – ISSN 1932–7447

[132] Valoen, Lars O. ; Reimers, Jan N.: Transport Properties of LiPF[sub 6]-Based Li-Ion Battery Electrolytes. In: *J. Electrochem. Soc.* 152 (2005), Nr. 5, A882–A891. http://dx.doi.org/10.1149/1.1872737. – DOI 10.1149/1.1872737. – ISSN 00134651

[133] Tanaka, Nanako ; Bessler, Wolfgang G.: Numerical investigation of kinetic mechanism for runaway thermo-electrochemistry in lithium-ion cells. In: *Solid State Ionics* 262 (2014), sep, 70–73. http://dx.doi.org/10.1016/j.ssi.2013.10.009. – DOI 10.1016/j.ssi.2013.10.009. – ISSN 01672738

[134] Väyrynen, Antti ; Salminen, Justin: Lithium ion battery production. In: *J. Chem. Thermodyn.* 46 (2012), S. 80–85. http://dx.doi.org/10.1016/j.jct.2011.09.005. – DOI 10.1016/j.jct.2011.09.005. – ISBN 00219614

[135] Zheng, Honghe ; Tan, Li ; Liu, Gao ; Song, Xiangyun ; Battaglia, Vincent S.: Calendering effects on the physical and electrochemical properties of Li[Ni1/3Mn1/3Co1/3]O2 cathode. In: *J. Power Sources* 208 (2012), 52–57. http://dx.doi.org/10.1016/j.jpowsour.2012.02.001. – DOI 10.1016/j.jpowsour.2012.02.001. – ISBN 03787753

[136] Westhoff, Daniel ; Feinauer, Julian ; Hein, Simon ; Rave, Stephan ; Schmidt, Sebastian ; Zausch, Jochen ; Iliev, Oleg ; Latz, Arnulf ; Ohlberger, Mario ; Schmidt, Volker: MULTI-BAT: Unified workflow for fast electrochemical 3D simulations of lithium-ion cells combining virtual stochastic microstructures, electrochemical degradation models and model order reduction. In: *J. Comput. Sci.* (accepted)

[137] Guyomard, D. ; Tarascon, Jean-Marie: Li Metal-Free Rechargeable LiMn204 / Carbon Cells: Their Understanding and Optimization. In: *Sci. Technol.* 139 (1992), Nr. 4, S. 937–948. http://dx.doi.org/10.1149/1.2069372. – DOI 10.1149/1.2069372. – ISBN 0013–4651

[138] Liu, Yinghu ; Xue, J. S. ; Zheng, Tao ; Dahn, J. R.: Mechanism of lithium insertion in hard carbons prepared by pyrolysis of epoxy resins. In: *Carbon N. Y.* 34 (1996), Nr. 2, S. 193–200. http://dx.doi.org/10.1016/0008-6223(96)00177-7. – DOI 10.1016/0008–6223(96)00177–7. – ISBN 0008–6223

[139] Pinson, Matthew B. ; Bazant, Martin Z.: Theory of SEI Formation in Rechargeable Batteries: Capacity Fade, Accelerated Aging and Lifetime Prediction. In: *J. Electrochem. Soc.* 160 (2013), dec, Nr. 2, A243–A250. http://dx.doi.org/10.1149/2.044302jes. – DOI 10.1149/2.044302jes. – ISBN 0013–4651

[140] Cabañero, Maria A. ; Altmann, Johannes ; Gold, Lukas ; Boaretto, Nicola ; Müller, Jana ; Hein, Simon ; Zausch, Jochen ; Kallo, Josef ; Latz, Arnulf: Investigation on the temperature dependence of lithium plating in commercial Li-ion batteries. In: *Electrochim. Acta* (2017)

[141] Ratnakumar, B. V. ; Smart, M. C.: Lithium Plating Behavior in Lithium-Ion Cells. In: *ECS Trans.* 25 (2010), Nr. 36, 241–252. http://ecst.ecsdl.org/content/25/36/241.short

[142] Childs, Hank ; Brugger, Eric ; Whitlock, Brad ; Meredith, Jeremy ; Ahern, Sean ; Pugmire, David ; Biagas, Kathleen ; Miller, Mark ; Harrison, Cyrus ; Weber, Gunther H. ; Krishnan, Hari ; Fogal, Thomas ; Sanderson, Allen ; Garth, Christoph ; Bethel, E W. ; Camp, David ; Rübel, Oliver ; Durant, Marc ; Favre, Jean M. ; Navrátil, Paul: VisIt: An End-User Tool For Visualizing and Analyzing Very Large Data. Version: 2012. https://wci.llnl.gov/simulation/computer-codes/visit. In: *High Perform. Vis. Extrem. Sci. Insight.* 2012, 357–372

[143] Downie, L. E. ; Krause, L. J. ; Burns, J. C. ; Jensen, L. D. ; Chevrier, V. L. ; Dahn, J. R.: In Situ Detection of Lithium Plating on Graphite Electrodes by Electrochemical Calorimetry. In: *J. Electrochem. Soc.* 160 (2013), feb, Nr. 4, A588–A594. http://dx.doi.org/10.1149/2.049304jes. – DOI 10.1149/2.049304jes. – ISSN 0013–4651

[144] Single, Fabian ; Horstmann, Birger ; Latz, Arnulf: Dynamics and morphology of solid electrolyte interphase (SEI). In: *Phys. Chem. Chem. Phys.* 18 (2016), Nr. 27, 17810–17814. http://dx.doi.org/10.1039/C6CP02816K. – DOI 10.1039/C6CP02816K. – ISSN 1463–9076

[145] Ong, Irene J. ; Newman, John: Double-Layer Capacitance in a Dual Lithium Ion Insertion Cell. In: *J. Electrochem. Soc.* 146 (1999), Nr. 12, 4360. http://dx.doi.org/10.1149/1.1392643. – DOI 10.1149/1.1392643. – ISBN 0013–4651

[146] Ecker, Madeleine ; Gerschler, Jochen B. ; Vogel, Jan ; Käbitz, Stefan ; Hust, Friedrich ; Dechent, Philipp ; Sauer, Dirk U.: Development of a lifetime prediction model for lithium-ion batteries based on extended accelerated aging test data. In: *J. Power Sources* 215 (2012), S. 248–257. http://dx.doi.org/10.1016/j.jpowsour.2012.05.012. – DOI 10.1016/j.jpowsour.2012.05.012. – ISBN 0378–7753

[147] Delacourt, C. ; Ridgway, P. L. ; Srinivasan, V. ; Battaglia, V.: Measurements and Simulations of Electrochemical Impedance Spectroscopy of a Three-Electrode Coin Cell Design for Li-Ion Cell Testing. In: *J. Electrochem. Soc.* 161 (2014), Nr. 9, A1253–A1260. http://dx.doi.org/10.1149/2.0311409jes. – DOI 10.1149/2.0311409jes. – ISSN 0013–4651

[148] Shi, Siqi ; Lu, Peng ; Liu, Zhongyi ; Qi, Yue ; Hector, Louis G. ; Li, Hong ; Harris, Stephen J.: Direct calculation of Li-ion transport in the solid electrolyte interphase. In: *J. Am. Chem. Soc.* 134 (2012), Nr. 37, S. 15476–15487. http://dx.doi.org/10.1021/ja305366r. – DOI 10.1021/ja305366r. – ISBN 1520–5126 (Electronic)\r0002–7863 (Linking)

[149] Liu, Mingjie ; Kutana, Alex ; Liu, Yuanyue ; Yakobson, Boris I.: First-principles studies of Li nucleation on graphene. In: *J. Phys. Chem. Lett.* 5 (2014), Nr. 7, S. 1225–1229. http://dx.doi.org/10.1021/jz500199d. – DOI 10.1021/jz500199d. – ISSN 19487185

[150] Temel, Burcin ; Meskine, Hakim ; Reuter, Karsten ; Scheffler, Matthias ; Metiu, Horia: Does phenomenological kinetics provide an adequate description of heterogeneous catalytic reactions? In: *J. Chem. Phys.* 126 (2007), Nr. 20. http://dx.doi.org/10.1063/1.2741556. – DOI 10.1063/1.2741556. – ISBN 0021–9606

[151] Franco, Alejandro A.: Multiscale modelling and numerical simulation of rechargeable lithium ion batteries: concepts, methods and challenges. In: *Rsc Adv.* 3 (2013), Nr. 32, S. 13027–13058. http://dx.doi.org/10.1039/c3ra23502e. – DOI 10.1039/c3ra23502e. – ISSN 2046–2069

[152] Sequeira, C ; Hooper, a: The study of lithium electrode reversibility against (PEO)xLiF3CSO3 polymeric electrolytes. In: *Solid State Ionics* 9-10 (1983), S. 1131–1138. http://dx.doi.org/10.1016/0167-2738(83)90142-X. – DOI 10.1016/0167–2738(83)90142–X. – ISSN 01672738

[153] Wang, Xinran ; Yushin, Gleb: Chemical vapor deposition and atomic layer deposition for advanced lithium ion batteries and supercapacitors. In: *Energy Environ. Sci.* 8 (2015), Nr. 7, 1889–1904. http://dx.doi.org/10.1039/C5EE01254F. – DOI 10.1039/C5EE01254F. – ISSN 1754–5692

[154] Hein, Simon ; Latz, Arnulf: Lithium Plating and Stripping in the Framework of a 3D Electrochemical Model. In: *ECS Trans.* 69 (2015), oct, Nr. 1, 3–5. http://dx.doi.org/10.1149/06901.0003ecst. – DOI 10.1149/06901.0003ecst. – ISBN 9781607685395

[155] Hein, Simon ; Latz, Arnulf: An electrochemical model of lithium plating and stripping in lithium-ion batteries. In: *Phys. Chem. Chem. Phys.* (submitted)

Acknowledgment

First and foremost I want to thank everyone who supported me during the conferral of my doctorate. Without you this work would not be as it is.

I want to thank my doctoral supervisor Prof. Arnulf Latz for his excellent supervision and all the fruitful and productive discussion over the years. I would like to thank Prof. Axel Groß for agreeing to act as examiner. I thank all members of the modeling group at the DLR, past and current, for the great time. Special thanks go to Dr. Jochen Zausch for the aid with the usage and development of BEST. I would like to thank all project partners of the MULTIBAT project for the pleasant collaboration and the German Ministry of Education and Research (BMBF) for funding this work. The authors acknowledge support by the state of Baden-Württemberg through bwHPC and the German Research Foundation (DFG) through grant no INST 40/467-1 FUGG.

I thank my family and my girlfriend Carola for their constant support.

Teile dieser Dissertation wurden bereits in folgenden Fachartikeln veröffentlicht:

- Hein, Simon ; Latz, Arnulf: Lithium Plating and Stripping in the Framework of a 3D Electrochemical Model. In: ECS Trans. 69 (2015), oct, Nr. 1, 3–5. [154]
- Hein, Simon ; Latz, Arnulf: Influence of local lithium metal deposition in 3D microstructures on local and global behavior of Lithium-ion batteries. In: Electrochim. Acta 201 (2016), may, 354–365. [12]
- Hein, Simon ; Feinauer, Julian ; Westhoff, Daniel ; Manke, Ingo ; Schmidt, Volker ; Latz, Arnulf: Stochastic microstructure modeling and electrochemical simulation of lithium-ion cell anodes in 3D, In: J. Power Sources. 336 (2016) 161–171. [121]

Name: Simon Hein Matrikelnummer: 827197

Erklärung

Ich erkläre, dass ich die Arbeit selbständig verfasst und keine anderen als die angegebenen Quellen und Hilfsmittel verwendet habe.

Ulm, den .....

Simon Hein

Europass Curriculum Vitae

Personal information

Surname(s) / First name(s)	**Hein, Simon**
Date of birth	1987

Conferral of Doctorate

Date	since Mai 2013
Title of qualification awarded	Doktor rer. nat. (ISCED 6)
Name of university	Fakultät für Naturwissenschaften Universität Ulm Albert-Einstein-Allee 11, D-89081 Ulm

Studies

Date	October 2006 – November 2012
Title of qualification awarded	Diplom Physiker (ISCED 5A)
Name of university	Fakultät für Physik und Astronomie Julius-Maximilians-Universität Würzburg Sanderring 2, D-97070 Würzburg
Date	August 2009 – August 2010
Title of qualification awarded	Master of Science Physics (ISCED 5A)
Name of university	Physics and Astronomie University of New Mexico Albuquerque, NM 87131, USA

Conferences

Talks	ModVal 13, Lausanne (CH), 2016
	228th ECS Meeting, Phoenix (USA), 2015
	17th ISE Topical Meeting, Saint-Malo (F), 2015
Poster	AABC, Mainz (D), 2017
	ModVal 11, Winterthur (CH), 2014
	14th UECT, Ulm (D), 2014

Publications

Hein, S.; Latz, A. - Phys. Chem. Chem. Phys.(2018) (*submitted*).

Hein, S.; *et al.* - J. Power Sources 336 (2016), 161-171.

Hein, S.; Latz, A. - Electrochim. Acta 201 (2016), 354–365.

Hein, S.; Latz, A. - ECS Trans. 69 (2015), Nr. 1, 3–5.